



**HAL**  
open science

# Electrical fluctuations and heat flow in a quantum composite circuit

Émile Sivré

► **To cite this version:**

Émile Sivré. Electrical fluctuations and heat flow in a quantum composite circuit. Mesoscopic Systems and Quantum Hall Effect [cond-mat.mes-hall]. Université Paris Saclay (COMUE), 2019. English. NNT : 2019SACLS548 . tel-02798535

**HAL Id: tel-02798535**

**<https://theses.hal.science/tel-02798535v1>**

Submitted on 5 Jun 2020

**HAL** is a multi-disciplinary open access archive for the deposit and dissemination of scientific research documents, whether they are published or not. The documents may come from teaching and research institutions in France or abroad, or from public or private research centers.

L'archive ouverte pluridisciplinaire **HAL**, est destinée au dépôt et à la diffusion de documents scientifiques de niveau recherche, publiés ou non, émanant des établissements d'enseignement et de recherche français ou étrangers, des laboratoires publics ou privés.

# Electrical fluctuations and heat flow in a quantum composite circuit

Thèse de doctorat de l'Université Paris-Saclay  
préparée à l'université Paris Sud

École doctorale n°564 Physique en Île-de-France (EDPIF)  
Spécialité de doctorat: Physique

Thèse présentée et soutenue à Palaiseau, le 16/12/2019, par

**Émile Sivré**

Composition du Jury :

<b>Marco Aprili</b> Directeur de recherche, CNRS (LPS, UMR-8502)	Président
<b>Adeline Crépieux</b> Maître de conférences, Université d'Aix-Marseille (CPT, UMR-7332)	Rapporteuse
<b>Clemens Winkelmann</b> Maître de conférences, Institut Néel (NEEL, UPR-2940)	Rapporteur
<b>Pascal Degiovanni</b> Directeur de recherche, CNRS (LPENSL, UMR-5672)	Examineur
<b>Gwendal Fève</b> Professeur, ENS Paris (LPENS, UMR-8023)	Examineur
<b>Frédéric Pierre</b> Directeur de recherche, CNRS (C2N, UMR-9001)	Directeur de thèse
<b>Anne Anthore</b> Maître de conférences, Université Paris Diderot (C2N, UMR-9001)	Encadrante



---

This work is supported by a public grant overseen by the French National Research Agency (ANR) as part of the “Investissements d’Avenir” program (Labex NanoSaclay, reference: ANR-10-LABX-0035)

---

## Remerciement :

Je souhaite tout d'abord remercier Anne Anthore et Frédéric Pierre, mes deux co-directeurs de thèse, pour avoir accepté que j'effectue ma thèse dans leur équipe de recherche. J'ai grandement apprécié votre passion pour la physique, vous êtes tous les deux des modèles pour moi, que ce soit en termes de rigueur scientifique, de vos savoirs faire respectif, où des exigences que vous vous posez à vous-même. Je souhaite ensuite remercier les membres du Jury : Adeline Crépieux et Clemens Winkelmann pour avoir accepté d'être rapporteur de ma thèse, ainsi que Marco Aprili, Pascal Degiovanni et Gwendal Feve. Je vous remercie aussi pour les questions très intéressantes, et parfois challenging, que vous m'avez posées pendant ma soutenance de thèse. Un grand merci à mon compagnon de manip, Hadrien Duprez, avec qui la discussion est si facile qu'elle fait émerger des tonnes d'idées, que ce soit en physique ou à propos de plein d'autres choses tout aussi passionnantes. Un grand merci à Ulf Gennser et Rebekah D'Arcy pour la relecture de ma thèse. Merci à Zubair et François pour vos conseils sur l'utilisation de ce fameux échantillon (RIP fameux échantillon), et sur plein d'autres sujet. Merci aussi à toutes les personnes que j'ai côtoyées au sein du C2N pendant ces trois ans : Rebeca, Abdel, Yong, Dominique, Quan, Jeremy, Pierre, Clément, Marie, Florian, Ludivine, Arnaud, Raphaëlle, et plein d'autres. Merci à Francesca Chiodi et Gilles Montambaux pour avoir accepté d'être respectivement marraine et tuteur scientifique de ma thèse. Merci à l'équipe STM pour votre retour sur l'idée farfelue que j'ai eu à propos de STM pendant ma soutenance :-p. Merci aux organisateurs des journées des doctorants, contribuer à l'organisation de ces événements avec vous était une expérience très sympathique. Merci à l'afreubo, qui m'a permis de tirer une réflexion profonde sur les notions intriquées de mélodie et de bruit, tous les lundis soir. Merci aux "BTK", j'espère que nos liens d'amitié resteront solides encore longtemps malgré nos nombreuses divergences en matière de start-up nation, de liberté individuelle, et de comment doit se tenir une bonne soirée (no comment). Merci aux "chatons" aussi (ah c'est relou les privées joke dans les remerciements...). Merci à tous mes amis depuis toujours, et en particulier ceux qui sont dispos le vendredi soir pour aller découvrir tous les bars de Paris, ou pour faire une petite partie de starcraft, ou pour faire des soirées jeux, ou pour faire de la musique, ou pour refaire le monde, ou d'autre chose que la

---

bienséance m'empêche de nommer. Merci à mes deux sœurs, Mathilde et Melanie.  
Merci à mes parents.

---

*“Je préfère ceux qui n’y arrivent pas pour la bonne et simple raison que je n’y arrive pas très bien, moi-même. Et que dans l’ensemble l’humour et l’inventivité se situent plutôt de notre côté. Quand on n’a pas ce qu’il faut pour se la péter, on est souvent plus créatifs. Je suis plutôt King Kong que Kate Moss, comme fille.”*

Virginie Despentes, *King Kong Théorie*

# Contents

<b>Contents</b>	<b>7</b>
<b>Introduction</b>	<b>9</b>
<b>1 Experimental techniques</b>	<b>17</b>
1.1 Introduction . . . . .	18
1.2 How to reach very low temperatures in a mesoscopic circuit . . . . .	18
1.3 Presentation of a hybrid and highly tunable quantum circuit . . . . .	20
<b>2 Noise measurements</b>	<b>35</b>
2.1 Introduction . . . . .	36
2.2 Fundamental sources of noise . . . . .	36
2.3 Cross-correlations and auto-correlations in a composite circuit . . . . .	41
<b>3 Dynamical Coulomb blockade</b>	<b>51</b>
3.1 Introduction . . . . .	52
3.2 Modelisation of the environment . . . . .	53
3.3 Single electron tunneling theory . . . . .	55
3.4 Mapping with a Tomonaga-Luttinger liquid . . . . .	57
3.5 Predictions for the local sine-Gordon model . . . . .	63
<b>4 Out-of-equilibrium noise in a quantum circuit</b>	<b>67</b>
4.1 Introduction . . . . .	68
4.2 Current noise as a function of voltage bias . . . . .	69
4.3 Shot noise induced by a temperature difference across a quantum point contact . . . . .	79



<b>5</b>	<b>Electronic heat flow in a composite quantum circuit</b>	<b>87</b>
5.1	Introduction . . . . .	89
5.2	Electronic heat flow through quantum circuits . . . . .	90
5.3	Predictions for heat flow in composite quantum-circuits . . . . .	92
5.4	Observation of the electronic heat flow in a ballistic circuit . . . . .	102
5.5	Observation of the electronic heat flow in a non-ballistic quantum circuit . . . . .	114
5.6	Conclusion . . . . .	119
<b>A</b>	<b>Refinement about electrons temperature determination</b>	<b>125</b>
A.1	Electronic base temperature determination including ac voltage . . .	125
A.2	Heating contribution by ac voltage . . . . .	126
<b>B</b>	<b>Conductance Formulae</b>	<b>127</b>
<b>C</b>	<b>Résumé en français</b>	<b>129</b>
<b>D</b>	<b>Abbreviations and symbols</b>	<b>137</b>
	<b>Bibliography</b>	<b>139</b>

# Introduction

Through the reduction of the size of electrical circuits and the experimental temperature, driven by the progress in nano-fabrication and cryogenic techniques, new quantum phenomena emerge. These result from quantum confinement [1; 2], or interference effects [3; 4], in combination with the Coulomb interaction [5]. The consequences are wide-ranging, and show-up in electrical conductance and electrical fluctuations, as well as via thermal effect [6–8]. The general aim of this experimental thesis is to shed light on fluctuations in the current and on electronic heat flow in a quantum composite circuit, assembled from several elementary components. The implemented test-bed circuit consists of a small metallic island connected to the outside world by several elementary quantum channels each individually fully tunable. We address the electrical and thermal properties of the overall circuit. Because of the interplay between Coulomb correlations and charge granularity, these cannot be straightforwardly inferred from the properties of each individual component. Diverse phenomena can develop depending on the circuit configuration, from the emblematic Coulomb blockade of the electrical conduction at low voltage and low temperature [5; 9] to exotic charge Kondo physics [10–12].

In the first chapter, we describe the sample, explain how it is characterized, and how the conductance and the current noise are measured in practice.

In chapter 2, we detail how the current fluctuations coming from different sources can be separately determined using complementary measurement of both auto-correlations and cross-correlations of electrical fluctuations. After briefly reviewing the scattering theory of noise [13–16], we establish the relations that will be used along the thesis in order to distinguish current fluctuations according to their sources.

In chapter 3, we review the theoretical predictions for a quantum dissipative cir-

cuit, which consist here of a non-ballistic quantum channel connected in series with a linear resistance. In such a circuit, the granular transfers of charge combined with the Coulomb interaction lead to a decrease of the conductance of the overall circuit at low voltage and low temperature [5]. This so-called dynamical Coulomb blockade (DCB) can be addressed theoretically using a mapping onto a Tomonaga Luttinger liquid (TLL) with a single impurity [17].

In the chapter 4, we experimentally investigate the current noise in a quantum dissipative circuit. We start by considering the noise resulting from a dc voltage bias. A predicted form of fluctuation-dissipation relation between variations of the conductance with voltage and variations of the shot noise [17], both versus the voltage, is here established experimentally. Then, using the same circuit with balanced voltages heating up the island, we measure a shot noise across a non-ballistic channel resulting from a pure thermal bias. A good agreement is observed with the theory [14; 16], as also recently shown using an atomic contact [18].

In chapter 5, we investigate the heat flowing through several channels from the small metallic island toward cold electrodes. We start by investigating the case where all channels are ballistic (in contrast to the setting of the device in chapter 4, where one of the channels is not ballistic). Performing the experiment in a regime where the coupling to phonons is negligible gives us access to the total electronic heat flow, and thereby allows us to observe the recently predicted [19] systematic heat Coulomb blockade of one ballistic channel at low voltage and temperature. Pursuing this investigation beyond the ballistic limit, we observe a different heat flow mechanism involving a combination of both the electron partition through a non-ballistic channel and the Coulomb interaction, in agreement with a model derived in this thesis.

A large part of the work in this thesis has been done in collaboration with another PhD student, Hadrien Duprez, who arrived one year after me. We decided together that my thesis would include the results concerning current noise and heat flow in circuits. Hadrien Duprez's thesis will include our more recent works concerned with electronic Mach-Zehnder interferometers, whose published article and submitted preprint are provided in the end of the manuscript.

## Summary

In this thesis, we explore the quantum laws governing the transport in a small electrical circuit. To reveal these quantum behaviors, our experiments are performed at low temperatures, on small conductors. In this context, the Coulomb interaction combined with the granularity of the charge often leads to a violation of the classical laws of impedances composition. The charging energy of the circuit nodes creates correlations between the interconnected coherent conductors that have a profound influence on transport. It is well established that these correlations can greatly reduce the electrical conductance, a phenomenon referred to as dynamical Coulomb blockade. However, their influence on current fluctuations and the flow of heat remains barely explored experimentally. This thesis is a first step beyond simple electrical conductance in the experimental study of composite quantum circuits. The test-bed circuit studied, represented in figure C.1, consists of a micrometer-sized metallic island connected to several elementary quantum channels of conduction. The number of channels as well as their individual transmissions are precisely adjustable. This simple circuit includes a single node formed by a metallic island whose important charging energy  $E_C \equiv e^2/2C \simeq k_B \times 0.3\text{K}$  ( $C$  is its capacitance) can be made much larger than thermal and electrical energies given our base temperature  $T_0 \approx 8\text{ mK}$ . The tools at our disposal for this investigation are conductances and current noise measurements. Electronic noise in the circuit comes from different sources: shot noise from the granular transfer of charge through non-ballistic quantum conduction channels, and Johnson-Nyquist noise from the thermal agitation of electrons. Both depend on the applied voltages since these also result in a Joule heating of the central metallic island. By simultaneously performing measurements of auto-correlations and cross-correlations of electrical fluctuations, we are able to distinguish the different sources of noise, and thus to determine separately the temperature rise of the central metallic island ( $T_\Omega - T_0$ ), the shot noise through the non-ballistic channels and the heat flow. This thesis presents four results obtained by this approach, two of which are related to measurements of current fluctuations and two others to heat flow as further described below. These results advance our understanding of fluctuations, electrical and thermal transport in composite quantum circuit. Furthermore, we expect that the advanced noise measurement strategies

combining auto- and cross-correlations pioneered in this thesis will open the path to new investigations of the quantum law of transport and provide novel insights into complex systems such as the fractional quantum Hall state.

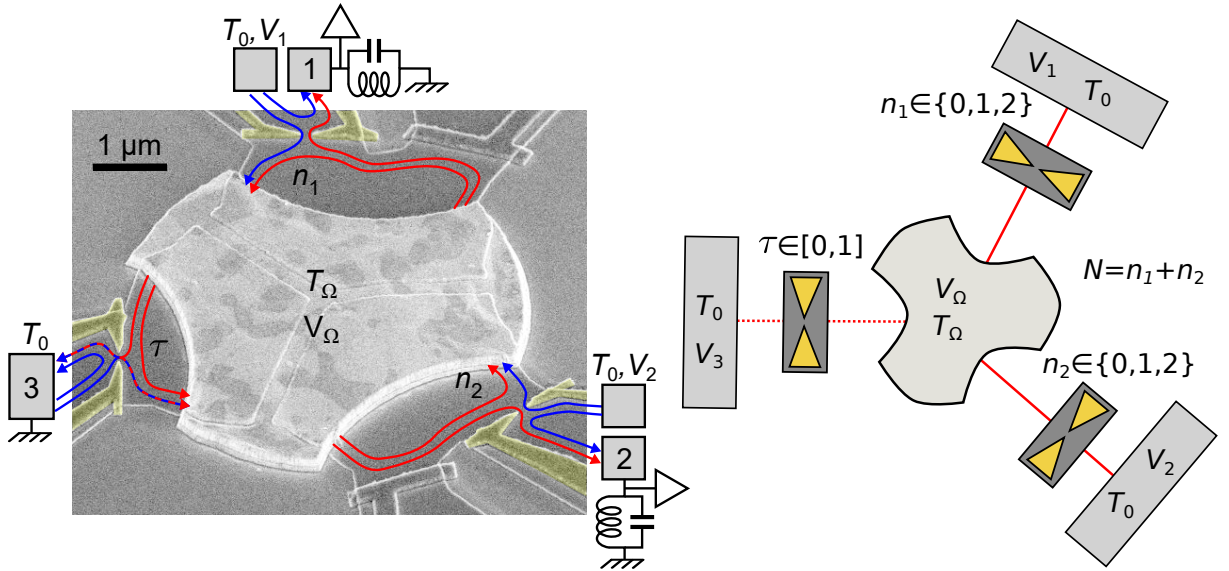


Figure 1: **False color micrograph (left) and diagram (right) representing the test-bed sample measured during this thesis.** A metallic island is in contact with three separate branches formed in a two-dimensional electron gas located 105 nm below the surface. The connection with large contacts (represented by rectangles) is controlled by field effect using gates (represented in yellow) coupled capacitively, thus forming quantum point contacts. The sample is immersed in a perpendicular magnetic field corresponding to the quantum hall effect at a filling factor of  $\nu = 2$ . The current therefore propagates along two chiral edge channels (lines with arrows). On the configuration shown on the left, electrodes 1 and 2 are each connected by a perfectly transmitted channel while electrode 3 is connected by a channel partially transmitted through the quantum point contact.

## Out-of-equilibrium noise in a dissipative quantum circuit

### Shot noise in the presence of dynamical Coulomb blockade

We explore here the shot noise induced by a voltage bias in a dissipative quantum circuit and its relation with the electrical conductance when a single channel is in series with a linear resistance. The voltage bias dependence of the two observables are theoretically predicted to be connected by a type of fluctuation dissipation relation [17]. Accordingly, the circuit is adjusted by field effect to have one conduction channel characterized by a fully adjustable transmission probability in series with a linear resistance formed by  $N$  ballistic channels in parallel, thereby emulating a resistance  $R_{env} = R_K/N$  with  $R_K = h/e^2 \simeq 25.8 \text{ k}\Omega$  the resistance quantum and  $N \in \{2, 3\}$ . The conductance of such a circuit is renormalized at low temperature and low voltage ( $eV, k_B T \ll NE_C$ , with  $V$  the voltage applied to the large electrode connected to the non-ballistic channel) by the dynamical Coulomb blockade phenomenon (DCB): due to Coulomb interactions, the granularity of the charge makes it possible to excite the electromagnetic modes of the environment formed by its capacitance and the resistance  $R_{env}$ , which prevents low energy charge transfers and thus reduces the conductance. In addition, at low energy ( $eV, k_B T \ll NE_C$ ) this circuit with a single non-ballistic channel is described by the Tomonaga-Luttinger (TLL) liquid theory of interaction parameter  $K = 1/(1 + R_{env}/R_K)$  as theoretically [17] and experimentally [20; 21] demonstrated.

Here, the measured noise is first compared to the predictions from the scattering theory [13], which is a non-interacting theory into which we inject the measured renormalized value of the conductance by DCB. These noise predictions are found to provide a good approximation to the data. They also allow us to compute and subtract a relatively small but non-negligible thermal noise contribution that enables a precise comparison of the measured noise with the TLL predictions only available at zero temperature for the noise. At our resolution, the measurements do not allow to distinguish between predictions of the scattering theory using the renormalized conductance and these of the TLL theory: although different, the two approaches give quantitatively very close results. However, we could establish the fluctuation-dissipation relation predicted specifically in the framework of the TLL theory, connecting the variation of the conductance as a function of voltage with

the variation of shot noise as a function of voltage. These results constitute a new step in the investigation of current fluctuations in Tomonaga-Luttinger liquids and in composite quantum circuits ruled by the Coulomb interaction.

**Article:**

E.Sivre, H. Duprez, A.Anthore, A. Aassime, F.D. Parmentier, A. Cavanna, A. Ouerghi, U. Gennser, and F. Pierre. (in preparation)

**Shot noise induced by a temperature difference**

In this experiment, we directly test the predictions from the scattering theory for the shot noise induced solely by a temperature difference, in the absence of a dc voltage difference. The circuit is adjusted in the same way as in the previous experiment (one non-ballistic channel,  $N$  ballistic channels). The difference is that balanced voltages of opposite signs are applied only across the ballistic channels such, that the central metallic island is heated up by Joule effect without any dc voltage difference across the imperfectly transmitted channel. Using auto-correlation and cross-correlation measurements of current fluctuations, we are able to observe the shot noise induced by the temperature difference across the imperfect channel, separately from the Johnson-Nyquist noise. Although predicted since a long time, this “thermal shot noise” has been measured for the first time only very recently, in an atomic contact [18]. We consolidate here the results of [18] by using a quantum contact point (QPC) with a single channel of known transmission probability, thus allowing for a direct comparison with the theory. The quantitative agreement of our measurements with predictions further establishes the scattering theory for the noise [13].

**Published article:**

E.Sivre, H. Duprez, A.Anthore, A. Aassime, F.D. Parmentier, A. Cavanna, A. Ouerghi, U. Gennser, and F. Pierre. Electronic heat flow and thermal shot noise in quantum circuits. *Nat. Commun.*10, 5638 (2019)

## Heat flow in a composite circuit

### Heat Coulomb blockade of one ballistic channel

The objective is here to investigate the thermal impedance composition rules for several ballistic channels connected in parallel to a small floating circuit node. Accordingly, the circuit is set so that the central island is connected only by  $N$  ballistic channels ( $N \in \{2, 3, 4, 5\}$ ). A dc voltage is applied to heat the central island. By energy conservation, in the stationary regime the total outgoing heat flow is equal to the well-known power injected in the island by the Joule effect. From the thermal noise measurement, we deduce the electron temperature  $T_\Omega$  in the metallic island. Thereby, we have the total heat flow as a function of temperature. This total heat flow includes two contributions: the electronic heat flow through the conduction channels connected to the island, and the heat transfer from electrons to phonons within the island. By focusing on very low temperatures ( $T_\Omega < 25$  mK), where heat transfers to phonons become negligible, we observe a new form of Coulomb blockade that applies specifically to the flow of electronic heat exiting the metallic island, while the electrical conductance is not affected. Our finding is in agreement with the theory [19], but in violation of the widespread Wiedemann-Franz's law. This reduction of the heat flow corresponds to the systematic suppression of a single electronic channel for heat transport, regardless of the total number of ballistic channels  $N$ . The correlations between the channels that lead to such a selective reduction of heat flow result from the absence of charge accumulation in the metallic island over the entire thermal frequency range ( $\omega \lesssim k_B T_\Omega / h$ ), which is imposed when the charging energy  $E_C$  is large enough ( $N E_C \gg k_B T_\Omega$ ). For higher temperatures, we could separate the electronic heat flow from the non-negligible heat transfer to phonons by exploiting that the latter depends only on the temperature and not on the number of connected channels. This allowed us to validate the theory also beyond the low temperature regime, along the crossover towards an absence of heat Coulomb blockade at high temperatures.

#### Published article:

E.Sivre, A.Anthore, F.D. Parmentier, A. Cavanna, U. Gennser, A. Ouerghi, Y. Jin and F. Pierre. Heat Coulomb blockade of one ballistic channel. *Nat.Phys.* **14**, 145-



148 (2018)

**Heat flow enhanced by thermal shot noise and Coulomb interaction**

The investigation of the thermal impedance composition rules is here pushed one step further, by including in the circuit one non-ballistic channel. Exploiting on the previously established knowledge in the ballistic case allows us to determine the heat transfers from electrons to phonons within the central metallic island (which does not depend on the configuration of the circuit). We thereby obtained the electronic heat transfer through  $N + 1$  channels ( $N \in \{2, 3, 4\}$ ), one of which is characterized by an intermediate transmission probability. Remarkably, the presence of the partially transmitted channel gives rise to an additional contribution to the electronic heat flow. This phenomenon results from a combined effect of the Coulomb interaction and of the “thermal shot noise” associated with the temperature difference across the imperfectly transmitted channel. A very good quantitative agreement is observed between the data and novel theoretical predictions obtained by extending the Fokker-Planck approach of [19].

**Published article:**

E.Sivre, H. Duprez, A.Anthore, A. Aassime, F.D. Parmentier, A. Cavanna, A. Ouerghi, U. Gennser, and F. Pierre. Electronic heat flow and thermal shot noise in quantum circuits. *Nat. Commun.*10, 5638 (2019)

**Other published works not discussed in this thesis:**

H. Duprez, E.Sivre, A.Anthore, A. Aassime, A. Cavanna, A. Ouerghi, U. Gennser, and F. Pierre. Macroscopic electron quantum coherence in a solid-state circuit. *PRX* **9**, 021030 (2019)

H. Duprez, E.Sivre, A.Anthore, A. Aassime, A. Cavanna, U. Gennser, and F. Pierre. Transferring the quantum state of electrons across a metallic island with Coulomb interaction. *Science* **366**(6470), 1243-1247 (2019)

# Chapter 1

## Experimental techniques

### Contents

---

<b>1.1</b>	<b>Introduction</b>	<b>18</b>
<b>1.2</b>	<b>How to reach very low temperatures in a mesoscopic circuit</b>	<b>18</b>
<b>1.3</b>	<b>Presentation of a hybrid and highly tunable quantum circuit</b>	<b>20</b>
1.3.1	Sample description	21
1.3.2	Transport measurements	26
1.3.3	Sample settings in this thesis	29

---

## 1.1 Introduction

The purpose of this thesis is to investigate experimentally the behavior of a quantum circuit in the non-equilibrium regime. To this aim, we need to perform noise and conductance measurements with a high resolution. In this chapter we describe: the way we proceed to reach an electronic temperature smaller than 10 mK in the sample; the different elements constitutive of the sample; and the different measurement procedures which will be used.

## 1.2 How to reach very low temperatures in a mesoscopic circuit

The sample is inserted into a commercial cryogen-free dilution refrigerator (Oxford instruments) of base temperature below 10 mK. In contrast to systems involving additional cooling such as nuclear demagnetization, a dilution refrigerator can be operated at a stable temperature over long periods of times, which is crucial for the experiments which will be described in this thesis. The refrigerator contains different parts, which allow us to reach different steps in temperature:

- **The pulse tube cooler:** To reach the temperature of 4 K the operation of the refrigerator is based on a two-stage pulse tube technology involving the compression and adiabatic expansion of helium.
- **The dilution circuit:** A mixture of  ${}^3\text{He}$ – ${}^4\text{He}$  circulates in a closed loop. The lowest temperature achieved in the mixing chamber is based on evaporation cooling of  ${}^3\text{He}$ .

The principle of evaporation cooling of  ${}^3\text{He}$  is now explained. At low temperature, a  ${}^3\text{He}$ – ${}^4\text{He}$  mixture will separate in two phases: a rich phase with a very high concentration in liquid  ${}^3\text{He}$  and a dilute phase composed of super-fluid  ${}^4\text{He}$  and liquid  ${}^3\text{He}$  ( $\approx 6\%$   ${}^3\text{He}$  at  $T = 0$  K). When pumping the dilute phase, the  ${}^3\text{He}$  is preferentially removed, because of its lower boiling temperature as described below. In order to restore the equilibrium  ${}^3\text{He}$  concentration,  ${}^3\text{He}$  atoms from the  ${}^3\text{He}$  rich phase are transferred into the dilute phase. This process being endothermic,

it absorbs heat from the surroundings, leading to a decrease of the temperature. To remove only  ${}^3\text{He}$  from the dilute phase, the mixing chamber is connected to a still, which is at a temperature of approximately 0.8 K, where the  ${}^3\text{He}$  is distilled from the  ${}^4\text{He}$  due to the difference in vapor pressure at the liquid/gas interface. In practice, the vapor pumped in the dilution circuit is almost entirely made of  ${}^3\text{He}$ . Whereas commercial dilution refrigerators readily achieve temperatures of the mixing chamber lower than 10 mK, the pertinent value in a mesoscopic circuit is the temperature of the electrons. The strong coupling of the device to the measurement lines connected to instruments at room temperature, the weak coupling to phonons in the substrate, and microwave heating, make it very difficult to thermalize the electrons below 10 mK. In the implementation used in this thesis:

- High frequency filtering and initial thermalization of the electrical lines are performed with resistive microcoaxial cables. The photon modes propagating through the electrical lines, which are responsible to extrinsic source of noise and heating are then drastically attenuated [22].
- The sample is protected against spurious high energy photons by two shields at base temperature.
- Inside the inner shield, the thermal anchoring of each measurement line is realized by dipping copper wires coated with thin insulating layer into a conductive silver epoxy together with a thermalized copper braid.

The electronic base temperature in the device reaches value as low as 7.5 mK in the experiments which will be presented. Note that even lower temperature have been achieved using this apparatus [23] but at a lower magnetic field than in the experiments presented here : in presence of high magnetic field, the vibration of the pulse tube are responsible of energy dissipation by Eddy currents.

### 1.3 Presentation of a hybrid and highly tunable quantum circuit

The circuit used in this thesis is composed of a small metallic island connected to the external world by three short coherent quantum conductors. This circuit has been made by François Parmentier and it has been used for several other experiments [11; 12; 21; 23; 24]. A false color micrograph of the sample is provided in Fig.1.1. In the following we present all the constitutive elements of this sample.

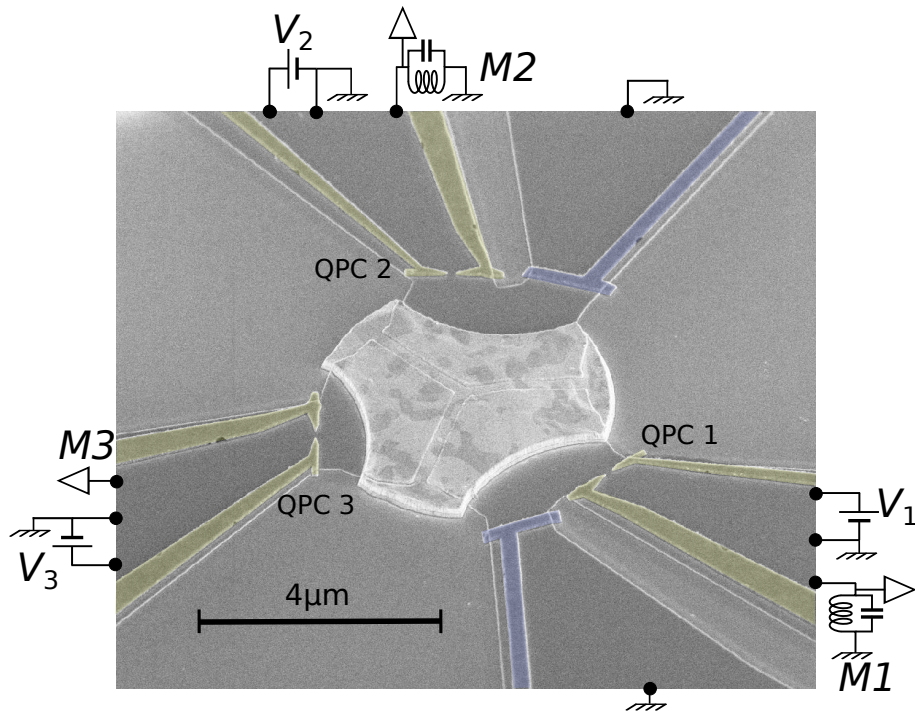


Figure 1.1: **False color micrograph of the sample**

A metallic island (light gray) is connected through a 2D electrons gas (dark gray) to several contacts (represented here by black points). When applying a high magnetic field, we reach the quantum Hall regime and the electrons propagate along the edge of the 2DEG in one or several edge channels. The edge channels can be biased using the voltage source  $V_1$ ,  $V_2$  and  $V_3$ . The noise measuring circuits are represented schematically by an LC circuit and a voltage amplifier. The yellow gates are deposited on top of the 2D electrons gas in order to create quantum point contacts by field effects.

### 1.3.1 Sample description

#### 2D electrons gas (2DEG)

One of the basic ingredients of the circuit is a 2D electron gas (dark gray in Fig.1.1). Electrons are confined in the vertical dimension, leading to a quantization of the energy levels associated with this degree of freedoms. At low temperature, when  $k_B T$  is lower than the gap between Fermi energy and first excited energy level, the movement of electrons along the vertical axis is frozen in the quantum ground state. We use a heterojunction formed of GaAs and AlGaAs. The layer of the AlGaAs semiconductor is doped with silicium, which has the effect to add free electrons. To minimize their energies, the free electrons move in the GaAs, but they are still attracted by the remaining positive ion in the AlGaAs. They end up trapped at the interface between the two layers (see figure 1.2). The 2DEG has been grown by molecular-beam epitaxy techniques by Ulf Gennser, Antonella Cavanna and Abdelkarim Ouerghi at C2N. It is characterized by an electronic density of  $2.5 \times 10^{11} \text{ cm}^{-2}$  and a mobility of  $10^6 \text{ cm}^2 \text{V}^{-1} \text{s}^{-1}$ . It is buried 105 nm below the surface of the nanostructure.

#### Quantum Hall effect

All the experiment described in this thesis are performed in the integer quantum Hall regime (IQHR). The quantum Hall effect occurs when a 2DEG is subject to a strong perpendicular magnetic field [25]. From a classical point of view, the electrons follow cyclotron orbits. When treated quantum mechanically, these orbits are quantized and their energy levels take discrete values called Landau levels:  $E_n = (n + 1/2)\hbar\omega_c$  with  $\omega_c = eB/m^*$  the cyclotron frequency ( $e$  is the charge of the electrons,  $B$  is the magnetic field and  $m^*$  is the effective mass of electrons in the 2DEG). The number of filled Landau levels depends on the density of the electrons and on the magnetic field  $B$ . For a small density and high magnetic field, all the free electrons in the system populate only a few highly degenerate Landau levels. As schematically represented in figure 1.3, in the quantum Hall regime the Fermi energy crosses the filled Landau levels near the edges of the 2DEG, defining a finite number of chiral edge channels. Electrons near the Fermi energy propagate along these one-dimensional edge channels, which are protected from back-scattering by their chirality [26]. The

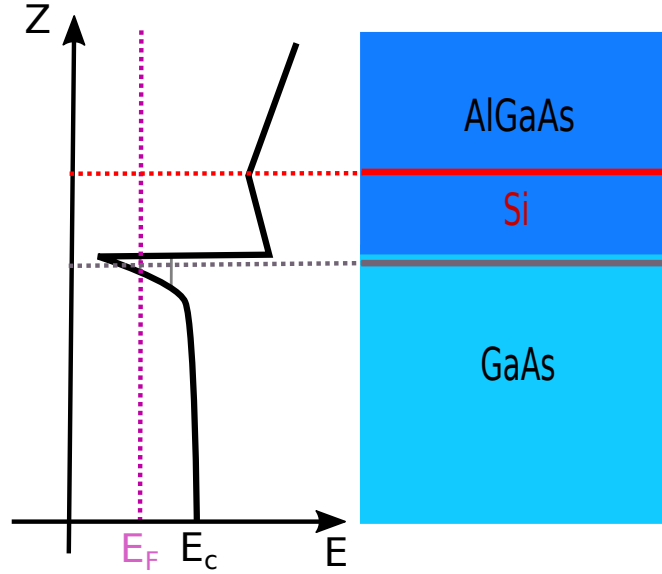


Figure 1.2: **2DEG formed in a GaAs/AlGaAs heterostructures.** Conduction band plot along the growth axis  $z$ : a quantum well traps the electrons provided by the doping layer at the interface between the GaAs and the AlGaAs. The dynamic of the trapped electrons along the axis  $z$  is frozen when the confinement is strong enough.

longitudinal resistance of the device is suppressed and the Hall resistance acquires a universal value given by  $\nu G_K$  with  $G_K = e^2/h$  the quantum of electrical conductance and  $\nu = \frac{h\bar{n}}{eB}$  the filling factor corresponding to the number of edge channels (two per Landau level due to the lifting of spin degeneracy by the Zeeman effect). The main measurements reported in this thesis have been done at a filling factor  $\nu = 2$ .

### Quantum point contact (QPC)

A quantum point contact is formed by depositing split gates on the surface of the heterojunction, above the 2DEG [1; 2]. In the micrograph of the figure 1.1, the split gates of the QPC are represented in yellow. When a negative DC voltage is applied to these split gates, the electron gas beneath is progressively depleted (the density of electrons changes locally). For a strong enough negative voltage, the electron gas is completely pinched off and the conductance through the QPC is null. By increasing the voltage, the width of the constriction is increased as well as the QPC

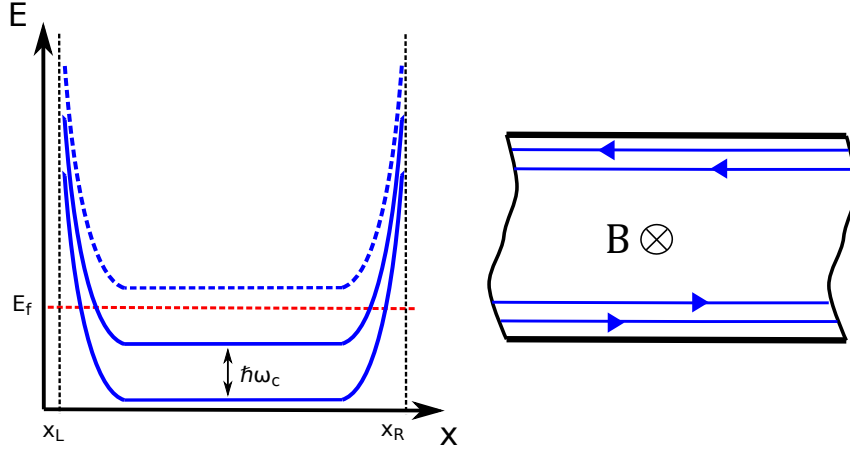


Figure 1.3: **Edge channels.** In the left panel the Landau levels are represented by blue lines. The confining potential which defines the sample increases the energy at the boundaries of the sample ( $x_L$  and  $x_R$ ). The Fermi energy crosses the Landau levels near the edge of the sample. In this case, there are two Landau levels crossed by the Fermi energy and then, as sketched in the right panel, there are two channels propagating along the edge of the sample. By changing the magnetic field, we can change  $\omega_c = eB/m$  and add or remove Landau level below the Fermi energy, and thus change the number of edge channels.

conductance. When the width of the constriction is of the order of half the Fermi wavelength (nearly 20 nm in our sample), only one transverse mode is available (two modes with spin). The maximum conductance through the constriction in this case is the quantum limit of electrical conductance  $G_K = e^2/h$ . This quantum limit is reached when back-scattering is negligible, for clean samples or thanks to the topological Quantum Hall protection. A conductance measurement through a QPC versus the split gates voltage is presented in figure 1.4. This measurement was done in the quantum Hall regime for a filling factor  $\nu = 4$ . At  $V_g = -0.6$  V, the conductance is zero. By increasing the voltage we can continuously increase the conductance until we reach a first plateau, and then the second, *etc*; each plateau corresponding to the full opening of one additional channel. Between the plateaus, the transmission value  $\tau(e^2/h)$  of the last channel can be tuned finely. A QPC is one of the basic building blocks of many quantum transport experiments, allowing us to emulate any short coherent conductor.



### Switch gates

Additional gates, colored in blue in the figure 1.1, are used as switches for bypassing the metallic island, allowing us to voltage bias directly the adjacent QPC. The conductance versus the bias gate voltage exhibits a larger plateau for these barring gates than for a QPC; however, the step between the plateaus are narrower. In this thesis, these gates are used mostly for thermometry (see section 1.3.3).

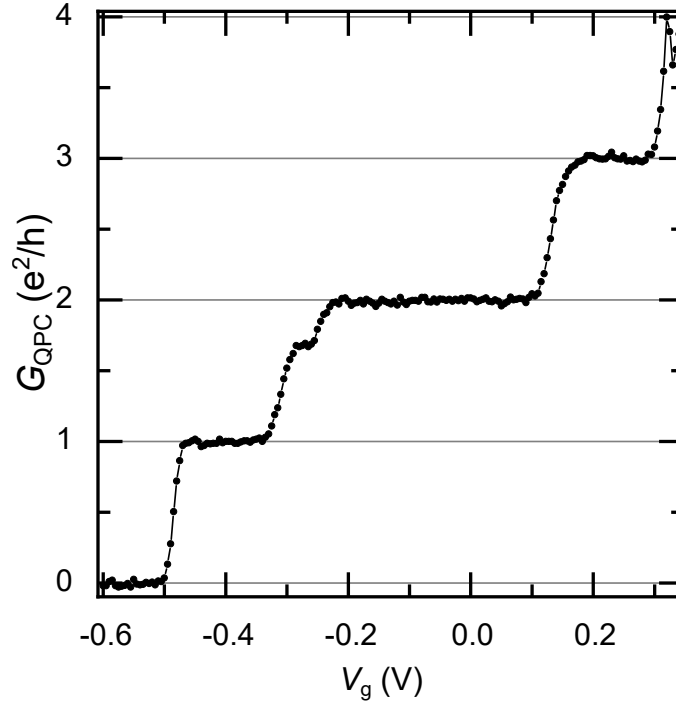


Figure 1.4: **Conductance of a QPC versus gate voltage.** This conductance measurement has been done at high magnetic field, corresponding to the integer quantum Hall regime at  $\nu = 4$ . Each channel is opened one by one and we can tune precisely the transmission probability  $\tau$  between each plateau.

### The central metallic island

The central metallic island (light gray in Fig.1.1) is a piece of metal which is diffused by thermal annealing in the Ga(Al)As heterojunction, forming an ohmic contact with the 2DEG. It is constituted of nickel, germanium and gold. Note that the 2DEG has been etched across the metallic island to ascertain that the electrons go through the

metal. For the different experiments presented in this thesis, some characteristics are required for the metallic island.

- Continuum of electron states: The energy level spacing inside the island must be negligible compared to the other relevant energy scale. The level spacing depends on the metal and the volume of the island. Based on the electronic density of gold (main component of the metallic island) and on the volume, we evaluate the level spacing to be  $\delta = k_B \times 0.2 \text{ } \mu\text{K}$ , well below the base temperature of the system ( $> 7 \text{ mK}$ ).
- Thermal electron distribution: Electrons in the island must follow a Fermi-Dirac distribution with temperature  $T_\Omega$ . This is expected since the average dwell times of the electrons in the island [27] is estimated to be much larger, by several orders of magnitude than the typical timescale for electron-electron inelastic collisions in similar metals (typically  $< 10 \text{ ns}$  [28]).
- Good island-2DEG contact: We need a very good connection between the metallic island and the 2DEG. It depends in particular on the length along which the 2DEG is in contact with the metal, and on the magnetic field. For each experiment reported in this thesis, the probability of reflection is of the order of one per thousand ( $\geq 99.9\%$  of incoming electrons are absorbed in the island).
- Relatively large charging energy: We will see that an important parameter of the metallic island is its charging energy  $E_C = e^2/2C$ . For observing the phenomena that we aim to investigate in this thesis, we need to work with temperatures and dc voltages inferior to this charging energy ( $k_B T, eV \ll E_C$ ). This energy depends on the geometry of the metallic island, and is obtained from Coulomb diamond measurements; its value is found to be equal to nearly  $k_B \times 300 \text{ mK}$  as further detailed in the corresponding section 1.3.3.

### 1.3.2 Transport measurements

#### Conductance measurements

Differential conductance measurements are performed by low frequency lock-in techniques (below 200 Hz). We use voltage sources connected in series with a 100-M $\Omega$  resistance in order to current-bias the sample at three different locations. Taking advantage of the well-defined quantum Hall resistance to grounded electrodes, the applied current is converted on-chip into a voltage independent of the device configuration:  $V_{\text{inj}} = \frac{R_K}{\nu} I_{\text{inj}}$  with  $R_K = h/e^2 \simeq 25.8 \text{ k}\Omega$  the resistance quantum. The contacts where we can inject both DC and ac voltages are represented by the black points connected to the voltage sources in the figure 1.1. For differential conductance measurements, we inject AC voltages of different frequencies on each contact. In the figure 1.1, the contacts where we measure the voltages at the three frequencies are located between the contact connected to LC tanks and the ground for the QPC 1 and 2 (not represented in figure 1.1 in order to simplify the schematics) and by the black points connected to an amplifier for the QPC 3. The conductance of the device can then be determined both from the reflected and transmitted current across the circuit. The specific formulae are recapitulated in the appendix B.

#### Calibrations for the conductance measurements

- **Injected voltages  $\times$  gain of low frequency amplifiers**

For each sources, the product of the injected ac voltage  $V_{\text{inj}}$  and the amplification gain of the nearby low frequency amplifier (not the noise amplifier) can be calibrated *in-situ* by closing the adjacent QPC: the voltage in the measurement contact is then the same as the injected one.

- **Relative gains of low frequency amplifiers**

In order to calibrate the gains of the conductance measurement lines, we set all the QPC to transmission  $\tau = 1$  (separately ascertained). In this configuration, the ratio of measured voltages gives the ratio of the gains. We take as a reference the voltage measured at the QPC 2. The gains are found independent of the frequency.

- **Parasitic offsets:**

The small instrumental offsets are calibrated by unplugging the voltage sources: the remaining voltages signals constitutes these offsets. For all the measurements, it is found to be inferior to  $10^{-10}$  V (in comparison, the injected signal is of the order of  $k_B T/e \approx 6.10^{-7}$  V). These offsets are not negligible when accurately measuring very weak signals.

### Noise measurements

The work described in the thesis relies heavily on noise measurements. In this section we describe briefly the experimental apparatus used to measure the noise with a very high resolution. In the circuit we measure the current fluctuations in two locations (indicated by black points connected to LC tanks in figure 1.1), we thus have two noise measurement lines. A noise measurement line is represented in the figure 1.5. First, the current fluctuations are converted into voltage fluctuations by a resonator consisting on the quantum Hall resistance  $R = h/\nu e^2$  in parallel with a LC tank. The LC tank consists of a superconducting inductance  $L \approx 400$   $\mu$ H and a capacitance  $C \approx 100$  pF which develops along the coaxial line. It leads to a resonance of frequency just below the MHz range. The bandwidth  $1/2\pi RC$  depends on the filling factor  $\nu$ . At the output of the RLC resonator, the voltage fluctuations are amplified using a cryogenic voltage amplifier working at a temperature of 4 K. The cryogenic amplifiers are based on homemade high-electron-mobility transistors (HEMT) [29] made by Yong Jin at the C2N. The best operating range of these amplifiers for our devices is just below the MHz range (motivating the use of an RLC resonator). At room temperature, the voltage fluctuations are further amplified using commercial amplifiers and they are sent to a spectrum analyzer (in our case a computer with a DAQ card) allowing us to calculate the power spectral density and cross-correlations.

### Gain calibration for the noise measurements

Here, we explain how we deduce the current noise in the circuit from the measured voltage noise.

- **Auto-correlation:**

The auto-correlated voltage noise measured in the output of the amplification

chain  $i$  (with  $i = 1$  or  $2$ ), behind the QPC  $i$ , is:

$$S_V^{mes}(w) = |G_i(w)|^2(S_V(w) + S_V^{amp}(w)) \quad (1.1)$$

with  $G_i(w)$  the gain of the amplifiers,  $S_V^{amp}(w)$  the noise added by the amplification chain and  $S_V(w)$  the voltage noise in the output of the RLC resonator:

$$S_V(w) = 4k_B T Re Z_{RLC_i}(w) + |Z_{RLC_i}(w)|^2 S_I(w) \quad (1.2)$$

The first term in equation 1.2 is the thermal noise emitted by the impedance of the RLC resonator  $Z_{RLC_i}(w)$ . The second term comes from the current fluctuations in the sample which are precisely the noise we want to measure. We then integrate  $S_V(w)$  over the  $RLC$  resonance on a bandwidth optimizing the signal to noise ratio. The excess current noise coming from the sample with respect to that at zero bias voltage ( $V=0$ ) is deduced from the formula:

$$\Delta S_I = \frac{1}{c_i} \int_{\omega_1}^{\omega_2} (S_V(V) - S_V(V=0)) dw \quad (1.3)$$

with

$$c_i = \int_{\omega_1}^{\omega_2} |G_i(w) Z_{RLC_i}(w)|^2 dw$$

The coefficient  $c_i$  is calibrated from the shot noise. At high voltage ( $eV \gg k_B T$ ) the current noise of a single quantum channel of transmission  $\tau$  is given by:

$$S_I^* = 2eV\tau(1 - \tau) + S_i^{offset}$$

Injecting this expression into equation 1.3 and fitting the resulting equation with measurements done in the adequate configuration of the device allows us to characterize  $c_i$ .

- **Cross-correlation:**

For identical resonators, the gain for the cross-correlated spectral density should be  $\sqrt{c_1 c_2}$  with  $c_1$  and  $c_2$  the gains characterizing the two amplification chains. However, a small difference between the resonators leads to a reduction with respect to  $\sqrt{c_1 c_2}$ . To calibrate this reduction, the sample is tuned with the QPC 3 closed and the other two QPCs opened. Then, by current conservation, the excess auto-correlation noises are equal to the absolute

value of the cross-correlation noise. This procedure allows us both to check that  $c_1$  and  $c_2$  are well characterized, and to evaluate precisely the gain for the cross-correlation noise. In the two different runs where this procedure was used, we found the value of  $\sqrt{c_1 c_2}/1.000$  for the first run and  $\sqrt{c_1 c_2}/1.007$  for the second run.

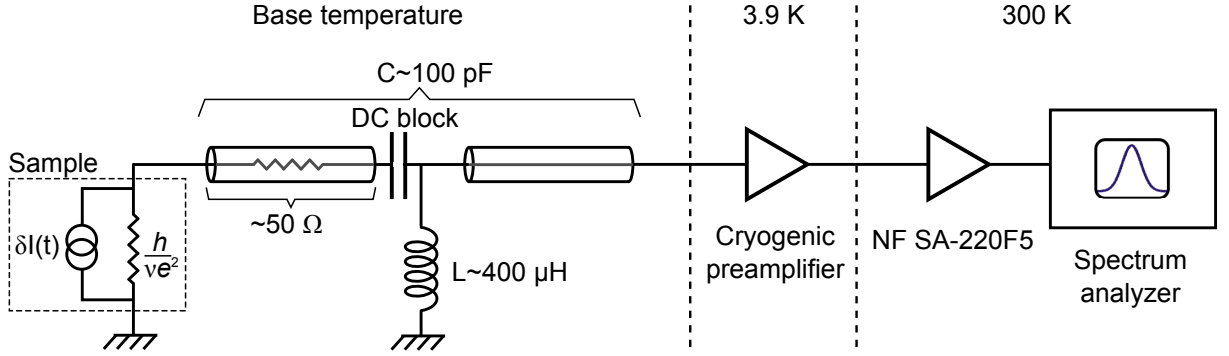


Figure 1.5: **Electrical diagram of the noise measurement line:** The current fluctuations are converted in voltage fluctuations using a RLC resonator of resonance frequency around the MHz. Then the voltage fluctuations are amplified using a cryogenic HEMT which works at a temperature of 4 K. The voltage fluctuations are again amplified at room-temperature and are analyzed with a spectrum analyzer.

### 1.3.3 Sample settings in this thesis

In this section we describe the different configurations of the sample used for this thesis. First, we deal with the configurations allowing us to characterize the system, and then we discuss the configurations used in the experiments themselves.

#### Determination of the base electronic temperature and amplifiers gain

For a short coherent conductor with a transmission  $\tau$  connecting two terminals, the excess power spectrum of the current fluctuation at zero frequency  $S_i$  can be derived using the scattering approach [13] :

$$\Delta S_i = \frac{e^2}{h} \left[ -4k_B T \tau (1 - \tau) + 2eV \tau (1 - \tau) \coth \left( \frac{eV}{2k_B T} \right) \right] \quad (1.4)$$

In this relation, the transmission  $\tau$  is assumed energy independent. Measuring this noise allows us to determine the electronic temperature  $T$  without the knowledge of the amplification chain [30]. In practice, we use the switch gates (represented in blue in figure 1.1 and 1.6) in order to directly voltage bias one of the QPCs (yellow in figure 1.1 and 1.6). In the figure 1.6, we show a raw measurement of the noise  $S_v^{mes}$  versus a bias voltage. Note the offset coming from both the amplification chain and the sample. When subtracting the offset, the data should follow the relation given for  $\Delta S_i$  in equation 1.4 times the factor  $c_i$  discuss in the previous section. In practice, fixing  $\tau \approx 1/2$  in order to maximize the signal, we fit the data using this equation with the factor  $c_i$ , the temperature, and an offset as free parameters. Averaging several sweeps allows us to determine precisely the gain of the amplification chain and the temperature (with a standard error of around 0.1 mK for the temperature). Typically, we perform such measurements both before and after the main experiment. The gains are found stable and are averaged from all the values measured during a cool down.

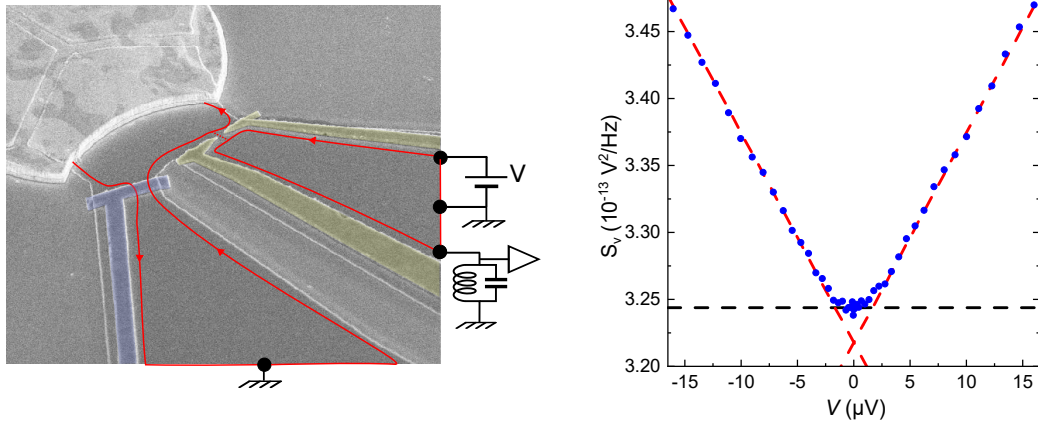


Figure 1.6: **Determination of the electronic temperature.** Left panel: configuration of the device for measuring the electronic base temperature and the gain of the amplifiers. This configuration is used for both QPC 1 and 2 simultaneously. Right panel: raw measurement of the noise versus dc voltage in the output of the amplification chain. The red dashed line indicates the shot noise limit  $2eV\tau(1 - \tau)$ . The black dashed line indicates the thermal noise limit. The offset comes from both the amplification chain and the sample.

### Charging energy characterization by Coulomb diamond measurements

The charging energy of the floating ohmic contact is determined by setting the device to a single electron transistor (SET) configuration (see Fig.1.7, left panel). To do this, one of the QPC is closed and the two others are set to the tunnel regime with transmission values  $\tau$  inferior to 0.1. In this configuration, the charge in the island is discretized. Sweeping the voltage of a lateral gates allows us to change the charge of the island and observe Coulomb oscillations. The 2D plot of the conductance of the device versus DC voltage applied to the circuit in the y-axis and the voltage applied to the lateral gate in the x-axis follows a pattern called Coulomb diamond on which the conductance is zero (see Fig.1.7, right panel). The height of the Coulomb diamond allows us to determine the charge energy of the metallic island using the relation  $E_C = eV_{diam}/2$  [31].

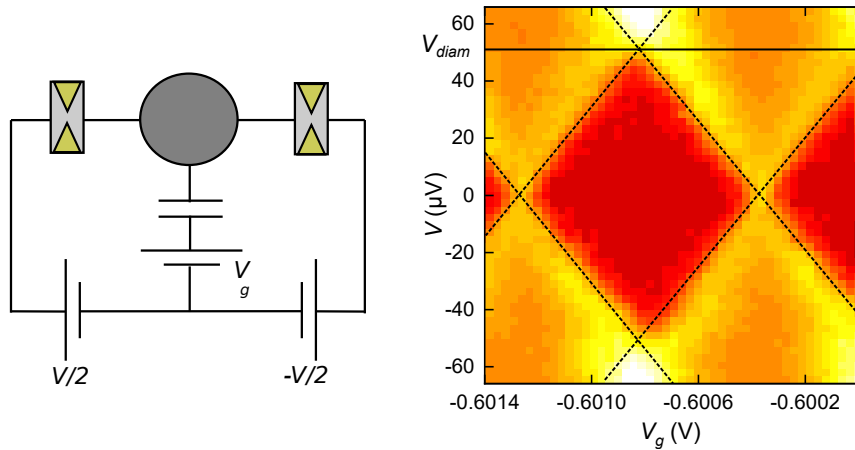


Figure 1.7: **Left:** a single electron transistor formed by a metallic island and two QPC tuned in the tunnel regime ( $\tau \ll 1$ ) **Right:** Coulomb diamond measurement. The color is red for vanishing conductance and become yellow when the conductance increases. The height of the diamond is equal to two times the charge energy, which gives here approximately  $E_C \approx 25.5 \mu\text{V}$ .

### Device tuned into a quantum dissipative circuit

The dynamical Coulomb blockade (DCB) manifests itself through the reduction of the conductance at low temperature and low voltage. It has been first studied



in circuit including a tunnel junction in series with a linear impedance [32; 33]. Here, we pursue the investigation of dynamical Coulomb blockade phenomena in a circuit composed of a one-dimensional short quantum conductor characterized by an arbitrary transmission probability  $\tau_\infty \in ]0, 1]$  (beyond the tunnel limit  $\tau_\infty \ll 1$ ), in series with an environment consisting of an ohmic impedance. To reproduce such a circuit with the device presented above, we tune one of the QPCs in the non-ballistic regime, where one channel is partially transmitted (it is usually the QPC 3 in figure 1.1, but control experiments have been done using the other QPCs). The other QPCs are tuned to the ballistic regime for respectively  $n_1$  and  $n_2$  channels. In this way, they act as a linear ohmic impedance of resistance  $R_K/N$  with  $N = n_1 + n_2$ .

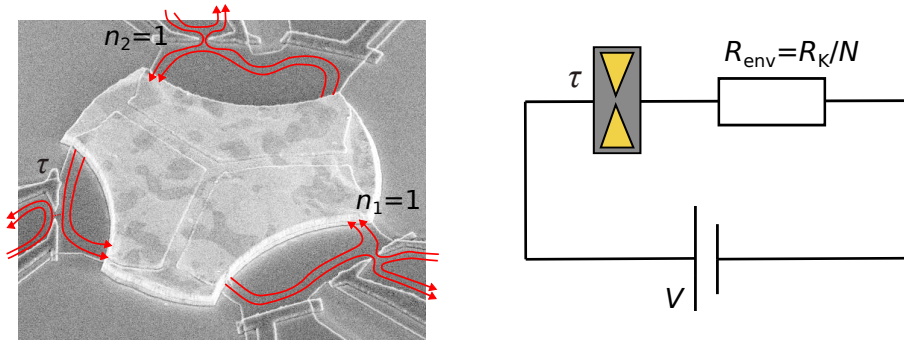


Figure 1.8: **Circuit in configuration "quantum dissipative circuit"**. Left: false color micrograph of the sample. The red lines represent the edge channels for the configuration "quantum dissipative circuit" with an impedance  $R_{\text{env}} = R_K/N$  with  $N = n_1 + n_2$  (here  $N = 2$ ). Right: equivalent electrical circuit.

### Dissipated Joule power and temperature bias

When we apply a voltage bias to a quantum conductor, we also dissipate a Joule power. Let us consider a quantum conductor of resistance  $R$  connecting two large reservoirs labeled 1 and 2, the total dissipated Joule power is:

$$P_J = \frac{(V_1 - V_2)^2}{R}$$

The Joule power is equally dissipated between the two reservoirs. The relation for the dissipated Joule power in one reservoir, which will be used in the following,

is then:

$$P_{J/\text{res}} = \frac{(V_1 - V_2)^2}{2R}$$

This dissipated Joule power heat up the elements of the circuit. The only ohmic contact impacted is the central metallic island: the other contacts are large enough to thermalize efficiently to the base temperature by electron-phonon coupling. For our experiments, this heating of the metallic island will be both a disadvantage and an advantage, depending on what we wish to do. It is a disadvantage when we are only concerned about the behavior in voltage: due to the heating, the system is not canonical as we would have preferred. Conversely it allows us to heat up the metallic island and apply a controlled temperature gradient. When the device is tuned to a quantum dissipative circuit, the procedure for applying a temperature gradient without voltage gradient to the non-ballistic channel is to bias the two environmental (ballistic) QPCs with voltages  $V_1$  and  $V_2$  such that  $n_1 V_1 = -n_2 V_2$ . Then, the average voltage in the central metallic island is null and the temperature of the central metallic island increases due to the Joule power  $J = n_1 V_1^2 / 2R_K + n_2 V_2^2 / 2R_K$  dissipated on it (figure 1.9).

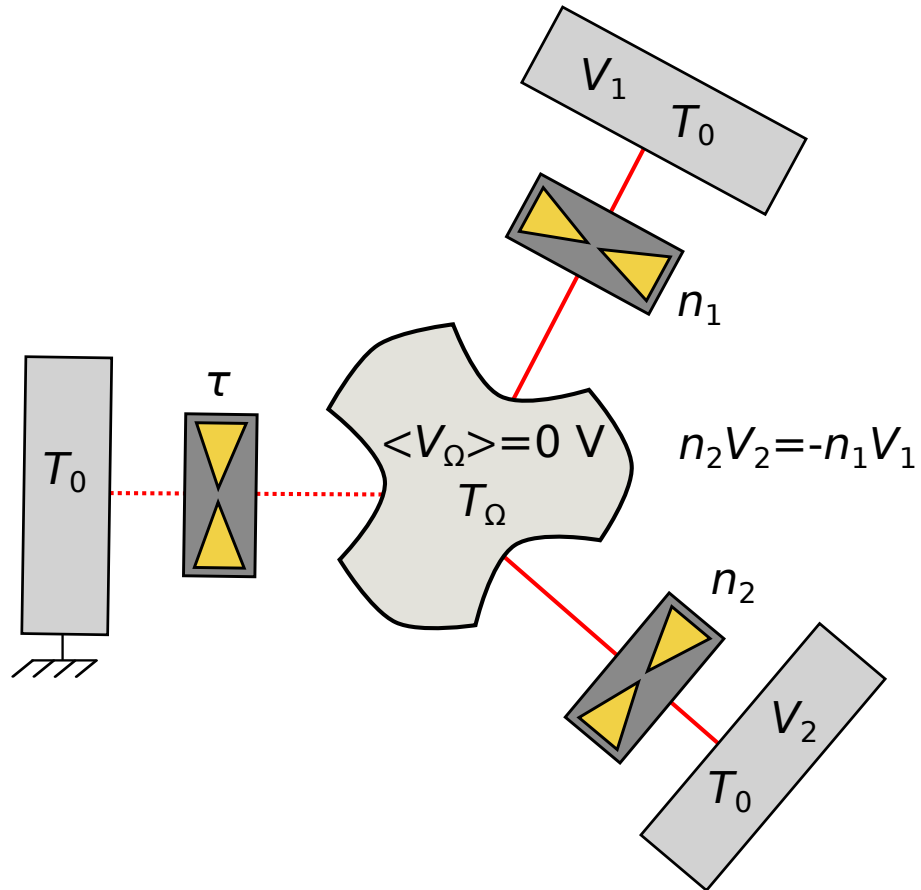


Figure 1.9: **Procedure in order to apply a thermal bias to a QPC.** We inject DC voltages  $V_1$  and  $V_2$  such that the voltage in the metallic island remains null. The dissipated Joule power has the effect of increasing the temperature of the metallic island  $T_\Omega$  above the base temperature  $T_0$ .

# Chapter 2

## Noise measurements

### Contents

---

<b>2.1</b>	<b>Introduction</b>	<b>36</b>
<b>2.2</b>	<b>Fundamental sources of noise</b>	<b>36</b>
2.2.1	Generality about current noise	36
2.2.2	The scattering theory of thermal and shot noises	38
<b>2.3</b>	<b>Cross-correlations and auto-correlations in a composite circuit</b>	<b>41</b>
2.3.1	Problematics	41
2.3.2	Relations between auto-correlations and cross-correlations	42
2.3.3	Excess thermal and shot noise in a quantum dissipative circuit	44
2.3.4	What should be measured behind the QPC 3?	47

---

## 2.1 Introduction

The objective in this chapter is to expose the method used to separate the noise contributions coming from different sources, namely the noise coming from the different reservoirs and the noise emitted from the electrons partition at the different QPCs. Measuring noise in an electrical circuit can be puzzling for someone unaccustomed to such measurements. To demystify this for the concerned reader, we start by explaining how the noise is characterized, and what information can be revealed by noise measurements. We then derive the relations which will be used throughout the thesis for the noise analysis.

## 2.2 Fundamental sources of noise

### 2.2.1 Generality about current noise

When measuring a current, the current noise consists of current fluctuations in time around the mean value of the signal. In signal processing, the noise is an unwanted disturbance of the signal. In contrast, in the study of mesoscopic circuits, it is a probe which reflects the thermal agitation and correlations of electrons. The current noise can be characterized by the power spectral density (sometimes called noise power), which is the Fourier transform at frequency  $w$  of the symmetrized current-current correlation function (we use the same convention for the Fourier transform as in ref [13]). In the following,  $\delta I_\alpha(t) = I_\alpha(t) - \langle I_\alpha \rangle$  denotes current fluctuations, *ie* departure from the mean value, measured in a contact labeled  $\alpha$ . The current-current correlation function is defined by:

$$\langle \delta I_x(t+t_0) \delta I_y(t_0) \rangle = \lim_{T \rightarrow \infty} \frac{1}{T} \int_{-T/2}^{T/2} \delta I_x(t+t_0) \delta I_y(t_0) dt_0 \quad (2.1)$$

Then, the power spectral density is given by:

$$S_{xy}(w) = \int_{-\infty}^{\infty} (\langle \delta I_x(t+t_0) \delta I_y(t_0) \rangle + \langle \delta I_y(t+t_0) \delta I_x(t_0) \rangle) e^{iwt} dt. \quad (2.2)$$

The power spectral density can be the auto-correlation of the current fluctuations ( $S_{xx}$ ), or the cross-correlation between the current fluctuations measured in different locations in the circuit ( $S_{xy}$  with  $x \neq y$ ). The fundamental sources of noise are the following:

- **The Johnson–Nyquist noise** comes from the thermal agitation of electrons [34]. At equilibrium, the thermal current power spectral density is found, based on the equipartition theorem [35], to be related to the resistance  $R$  and the temperature  $T$  of the system by the following formula:

$$S = 4k_{\text{B}}T/R. \quad (2.3)$$

This relation, measured for the first time by Johnson in 1927 [34], is valid only for small frequencies compared to  $k_{\text{B}}T/h$  ( $\approx 150$  MHz for the smallest base temperature reached for the experiments described in this thesis). Indeed, for larger frequencies, quantum effects have to be considering (in the same way as Planck’s law for the black-body radiation). At high frequency, the relation becomes [35]:

$$S(w) = \frac{2\hbar w/R}{\exp(\hbar w/k_{\text{B}}T) - 1}. \quad (2.4)$$

This relation can be derived in the more general framework of the fluctuation dissipation theorem [36]. Measuring the Johnson–Nyquist noise, and knowing the conductance -which can be determined by specific measurements- allows one to determine the temperature of the electrons. Note that in equation 2.4, the zero frequency limit gives a factor 2 instead of the factor 4 of equation 2.3: we need to symmetrize negative and positive frequency in order to recover equation 2.3.

- **The shot noise** originates from the discrete nature of electronic charge [37]. In devices such as a tunnel junction or a vacuum tube, the electrons are transmitted randomly and independently of each other: the transfers of electrons can then be described by Poisson statistics (used to analyze uncorrelated events in time). In this kind of device, the shot noise reaches the value  $S = 2eI$  (with  $I$  the average current and  $e$  the charge of electrons). This value changes in presence of correlations: for instance in a ballistic channel, the stream of electrons is completely correlated (in time) by the Pauli principle and the shot noise is suppressed [16; 38; 39]. Beyond the interest to investigate it for itself, the shot noise gives information about correlations which are not necessary available by low frequency conductance measurement [40; 41], and may allow one to probe the effect of Coulomb interaction [42]: for instance the noise is sensitive to the

charge of quasiparticles [43–45]. Note that in macroscopic samples, the shot noise is averaged out to zero by inelastic scatterings [46].

### 2.2.2 The scattering theory of thermal and shot noises

The noise in quantum conductors can be derived within the scattering approach, which relates the current to the scattering properties of electrons in the conductor [16]. The main assumption for this approach is that electrons cross the conductor without any loss of quantum coherence: they experience only elastic scattering. Here, we give the predicted current noise in the simple case of a quantum conductor connecting two large, voltage fixed electrodes labeled  $R$  and  $L$  for the right and left electrodes respectively. An electrode  $\alpha$  ( $\alpha \in \{L, R\}$ ) is characterized by a temperature  $T_\alpha$  and a chemical potential  $\mu_\alpha$ . The distribution function of electrons in each electrode is a Fermi distribution function:

$$f_\alpha(E) = \frac{1}{1 + \exp\left(\frac{E - \mu_\alpha}{k_B T_\alpha}\right)}. \quad (2.5)$$

The electrodes act as reservoirs for the electrons propagating across the quantum conductors. The quantum conductor can be decomposed in  $n$  transverse modes, each of them characterized by a probability of transmission  $\tau_n(E)$ .

At zero frequency, the power spectral density in the right reservoir is given by [14; 16]:

$$\begin{aligned} S_{RR} &= \frac{2e^2}{\pi\hbar} \int_{-\infty}^{\infty} \sum_n \tau_n(E) (f_L(E)(1 - f_L(E)) + f_R(E)(1 - f_R(E))) dE \\ &+ \frac{2e^2}{\pi\hbar} \int_{-\infty}^{\infty} \sum_n \tau_n(E) (1 - \tau_n(E)) (f_L(E) - f_R(E))^2 dE. \end{aligned} \quad (2.6)$$

The power spectral density in the left reservoir  $S_{LL}$  is identical due to charge conservation. The cross-correlation are  $S_{RL} = S_{LR} = -S_{LL} = -S_{RR}$  [16]. Up to the end of this section, we use:  $S \equiv S_{RR} = S_{LL} = -S_{RL} = -S_{LR}$

Assuming an energy independent transmission probability ( $\tau_n(E) = \tau_n$ ), the first term in the relation 2.6 does not depend on the voltage and depends only on the mean temperature  $\bar{T} = (T_L + T_R)/2$ . As a result:

$$S = 4k_B \bar{T} \sum_n \tau_n / R_K + \frac{2e^2}{\pi\hbar} \sum_n \tau_n (1 - \tau_n) \int_{-\infty}^{\infty} (f_L(E) - f_R(E))^2 dE. \quad (2.7)$$

This equation matches the Johnson-Nyquist noise discussed above at equilibrium, when  $\Delta T = \Delta V = 0$ , since  $f_L = f_R$  in that case. The second term can be interpreted as the non-equilibrium shot noise whose partition character is revealed by the characteristic factor  $\tau_n(1 - \tau_n)$ .

Equation 2.6 can also be rewritten as:

$$\begin{aligned}
 S &= \frac{2e^2}{\pi\hbar} \int_{-\infty}^{\infty} \sum_n \tau_n(E)^2 (f_L(E)(1 - f_L(E)) + f_R(E)(1 - f_R(E))) dE \\
 &+ \frac{2e^2}{\pi\hbar} \int_{-\infty}^{\infty} \sum_n \tau_n(E)(1 - \tau_n(E)) (f_L(E)(1 - f_R(E)) + f_R(E)(1 - f_L(E))) dE,
 \end{aligned} \tag{2.8}$$

which leads, for energy independent transmission probabilities:

$$\begin{aligned}
 S &= 4k_B\bar{T} \sum_n \tau_n^2 / R_K \\
 &+ \frac{2e^2}{\pi\hbar} \sum_n \tau_n(1 - \tau_n) \int_{-\infty}^{\infty} (f_L(E)(1 - f_R(E)) + f_R(E)(1 - f_L(E))) dE.
 \end{aligned} \tag{2.9}$$

The interest of this formulation, which mixes shot noise and thermal noise is that at increasingly high voltage compared to the temperature, the second term in the right-hand side of equation 2.9 progressively becomes independent of the temperature, in contrast with the second term in the right-hand side of equation 2.7. In the high voltage limit, the temperature effects are encapsulated in the first term of equation 2.9.

### Full low-frequency noise at homogeneous temperature $\Delta T = T_R - T_L = 0$

At thermal equilibrium  $\Delta T = 0$  and energy independent  $\tau_n$ , the second term in equation 2.7 is easily integrable:

$$S = 4k_B T \sum_n \tau_n / R_K + \frac{2eV}{R_K} \sum_n \tau_n(1 - \tau_n) \left( \coth \left( \frac{eV}{2k_B T} \right) - \frac{2k_B T}{eV} \right). \tag{2.10}$$

Note that this is the equation we use for thermometry (see the section 1.3.3). In the zero-temperature limit, it becomes:

$$S(T = 0) = 2eV \frac{\sum_n \tau_n(1 - \tau_n)}{R_K}. \tag{2.11}$$

This relation gives what is usually called shot noise. In the limit of low transparency  $\tau \ll 1$ , we recover the Poisson noise  $S = 2eI$  discussed above.



**Full low-frequency noise at zero voltage bias  $\Delta V = V_R - V_L = 0$**

From equation 2.7, we note that even at voltage equilibrium but in the presence of a temperature gradient  $\Delta T = T_L - T_R$ , there is a thermal shot noise induced by the partition of electrons through a partially transmitted channel. No analytical solution of the integral of equation 2.7 is currently available when a thermal gradient is applied to a quantum conductor. However, the integral can be calculated numerically. We can also perform a Taylor development in  $\Delta T$  of this expression, which result in [18]:

$$\frac{2e^2}{\pi\hbar} \int_{-\infty}^{\infty} \sum_n \tau_n(1-\tau_n)(f_L-f_R)^2 dE = \sum_n \tau_n(1-\tau_n)/R_K \left( \frac{k_B\Delta T^2}{\bar{T}} \left( \frac{\pi^2}{9} - \frac{2}{3} \right) \right) + o(\Delta T^2/\bar{T}^2). \quad (2.12)$$

## 2.3 Cross-correlations and auto-correlations in a composite circuit

### 2.3.1 Problematics

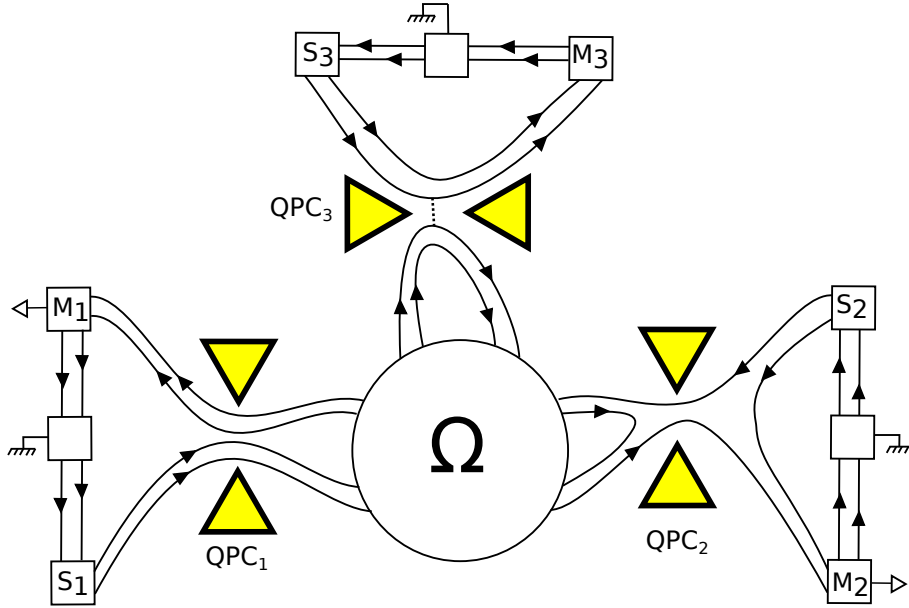


Figure 2.1: **Drawing of the sample.** Simplified representation of the sample:  $S_1$ ,  $S_2$  and  $S_3$  are voltage sources. We measure the current noise in the contacts  $M_1$  and  $M_2$  (not in  $M_3$ ). The QPCs are represented by the yellow triangles. The QPCs 1 and 2 let pass, respectively,  $n_1$  and  $n_2$  ballistic channels ( $n_1 = 2$  and  $n_2 = 1$  in this specific representation). The QPC 3 includes only one channel of transmission  $\tau$  between 0 and 1.

The noise measured in a quantum composite circuit constituted of several QPCs, contains contributions from all its elements. The objective is here to provide the relations connecting these sources of noise to the measured noise.

In the following, the current noise generated across a QPC  $i$  is denoted  $S_{qpci}$ . The circuit is tuned in a quantum dissipative circuit as explained in section 1.3.3: The QPC 1 and 2 let pass, respectively,  $n_1$  and  $n_2$  ballistic channels and the QPC 3 lets pass only one channel of arbitrary transmission probability  $\tau$ , as sketched in

the figure 2.1. Current fluctuations are measured in contacts  $M1$  and  $M2$  behind QPC 1 and 2, respectively. The presence of a floating metallic node results in a redistribution of the current noise generated at the different QPCs. All the contacts are assumed to be at the same temperature  $T_0$  except the central metallic island which is heated up by the Joule effect to a temperature  $T_\Omega$ . For ballistic channels, since there is no partition of electrons, the generated current noise is only the thermal noise  $S_{ball} = 4k_B\bar{T}/R_K$ , where  $\bar{T} = (T_\Omega + T_0)/2$  is the average temperature. From the noise measurements, we want to separately extract the temperature  $T_\Omega$ , and the noise  $S_{qpc3}$  generated across the QPC 3. In the case where  $n_1 = n_2$ , because the power spectral density in  $M1$  and  $M2$  are the same by symmetry, we need a different observable if we want to extract both  $T_\Omega$  and  $S_{qpc3}$ . For this purpose, we will use the cross-correlations between current fluctuations in  $M1$  and  $M2$ . We will see below that it gives the same information as a noise measurement in contact  $M3$  would have provided. As the noise is measured in the MHz range, we can neglect capacitive effects ( $C \approx 3.1$  fF  $\Rightarrow 1/R_K C \approx 10$  GHz  $\gg$  MHz). We first derive a very general formula for the different measurements, which is independent of the configuration of the device. Then we derive the formula connecting measurements to noise sources.

### 2.3.2 Relations between auto-correlations and cross-correlations

Let us start with a simple derivation allowing us to obtain a simple but robust formula about power spectral noise and cross correlation in the device. Assuming only that charge accumulation in the island is negligible at the measurement frequencies, by current conservation the sum of all current fluctuations in-going in contacts  $Mi$  ( $i \in \{1, 2, 3\}$ ) are equal to the sum of all current fluctuations emitted in the source contacts, whatever the configuration of the device:

$$\delta I_{M1} + \delta I_{M2} + \delta I_{M3} = \delta I_{S1} + \delta I_{S2} + \delta I_{S3} \quad (2.13)$$

Here,  $I_{S_i}$  are the current fluctuations out-going from the contact  $S_i$ , as sketched in figure 2.2.  $I_{M_i}$  are the current fluctuations in-going into the contact  $M_i$ . These current fluctuations depend on the thermal agitation in contact  $S1$ ,  $S2$ ,  $S3$  and in the central metallic island, and on the potential fluctuations of the floating metallic

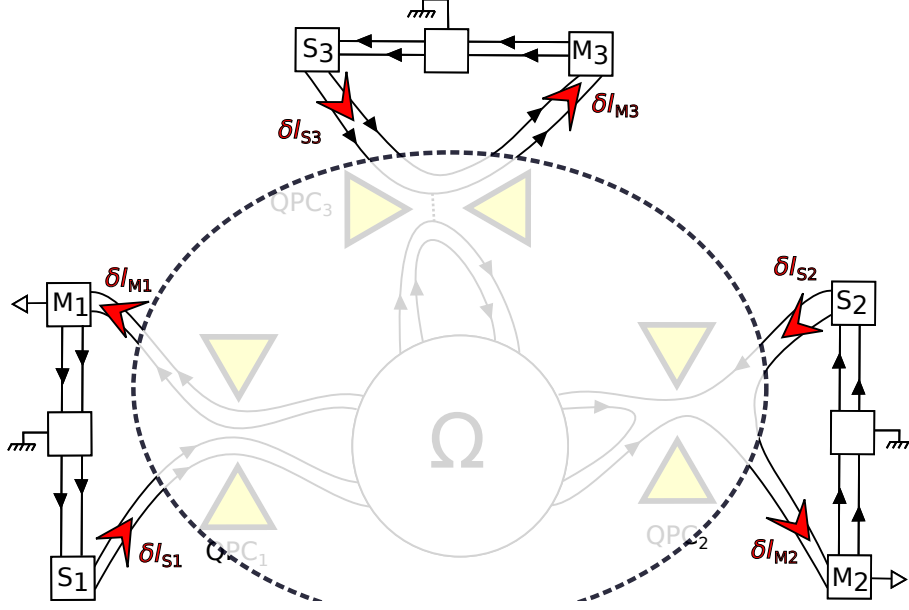


Figure 2.2: **Drawing of the sample.** Simplified representation of the sample: by current conservation, the out-going current fluctuations from the sources  $S1$ ,  $S2$  and  $S3$  are equal to the in-going current fluctuations in the contact  $M1$ ,  $M2$  and  $M3$ , whatever the configuration of the device, as long as the charge accumulation in the central part can be ignored.

island. From equation 2.13 we derive the correlation  $\langle \delta I_{M3}^2 \rangle$ . Using equation 2.2, we obtain:

$$S_{M3M3} \equiv \langle \delta I_{M3}^2 \rangle = S_{M1M1} + S_{M2M2} + 2S_{M1M2} + \sum_i S_{S_i S_i} - 2 \langle (\delta I_{M1} + \delta I_{M2}) \sum_i \delta I_{S_i} \rangle. \quad (2.14)$$

The last term can be written as:

$$2 \langle (\delta I_{M1} + \delta I_{M2}) \sum_i \delta I_{S_i} \rangle = 2 \sum_i^3 (G_{i1} + G_{i2}) S_{S_i S_i}, \quad (2.15)$$

where  $G_{ij}$  is the fraction of current emitted from contact  $S_i$  and impinging in the contact  $M_j$ . As the noise coming from the source contact involves only thermal noise at the same temperature, we can take it out  $S_{S_i S_i}$  of the sum. The conductance  $G_{ij}$  may depend of the voltage, however we have  $\sum_i^3 G_{ij} = \sum_j^3 G_{ij} = 1$  from current conservation and time reversal symmetries [47]. As the  $S_{S_i S_i}$  does not depend of the

voltage, when focusing on the excess noise we obtain:

$$\Delta S_{M_3M_3} = \Delta S_{M_1M_1} + \Delta S_{M_2M_2} + 2\Delta S_{M_1M_2}. \quad (2.16)$$

This relation indicates that although we only have two noise measurement lines allowing us to measure the noise in contact  $M_1$  and  $M_2$  only, cross-correlation between these two contacts makes it possible to obtain the missing information which will be brought by measuring the auto-correlation in the contact  $M_3$ . This relation indicates also that the role of the QPCs (with two tuned to the ballistic regime and one kept non-ballistic) can be inverted. Note that if one of the QPC is closed we will have:

$$\Delta S_{ii} = \Delta S_{jj} = -\Delta S_{ij}, \quad (2.17)$$

where we have replaced the notation  $M_iM_j$  by  $ij$ . Due to current conservation, all the measurements become redundant if one of the QPC is closed [40].

### 2.3.3 Excess thermal and shot noise in a quantum dissipative circuit

We now detail the formula allowing us to extract  $T_\Omega$  and  $S_{qpc3}$  from the excess power spectral density  $\Delta S_{11}$  and  $\Delta S_{22}$  and from the excess cross-correlation  $\Delta S_{12}$  for the configuration depicted in figure 2.1.  $N$  denote the number of ballistic channels ( $N = n_1 + n_2$ ).

No assumptions are made about the QPC 3, whose conductance is affected by DCB, and the noise is not presumed to follow the relations given by the scattering theory. For the QPC 1 and 2, which are tuned to have ballistic channels, we assume that the generated noise can be decomposed into the standard Johnson-Nyquist contributions from in-going and out-going channels:

$$S_{qpci} = S_{qpci}^{in} + S_{qpci}^{out}, \quad (2.18)$$

with

$$S_{qpci}^{in} = 2k_B T_0 n_i / R_K, \quad (2.19)$$

$$S_{qpci}^{out} = 2k_B T_\Omega n_i / R_K, \quad (2.20)$$

as the incoming (outgoing) current fluctuations along the  $n_i$  ballistic channels of QPC  $i$  are all emitted from the cold reservoirs (hot floating island).

First let us now consider how a single (isolated) current fluctuations  $\delta I_{qpc3}$  injected in the island from the QPC 3 manifests itself in the noise. At the MHz measurement frequencies where charge accumulation is negligible, the injected current is compensated by the total current from the resulting island's voltage fluctuations  $\delta V_\Omega = \delta I_{qpc3} R_K / (N + \tau)$ . As a result, a current  $\delta I_{qpc3} n_i / (N + \tau)$  is sent effectively simultaneously toward the measurement electrodes  $Mi$  with  $i \in \{1, 2\}$ . The auto-correlation signal resulting from this current fluctuations is then given by:

$$S_{ii}^{qpc3} = S_{qpc3} \frac{n_i^2}{(N + \tau)^2}. \quad (2.21)$$

The cross-correlation between current fluctuations in  $M1$  and  $M2$  originating from  $\delta I_{qpc3}$  are positive and given by:

$$S_{12}^{qpc3} = S_{qpc3} \frac{n_1 n_2}{(N + \tau)^2}. \quad (2.22)$$

Second, we consider a current fluctuations  $\delta I_{qpci}$  generated across QPC  $i$  ( $i \in \{1, 2\}$ ) of spectral density  $S_{qpci}$ . Similarly, it will result in  $Mj$ , with  $i \neq j$ , in the following auto-correlation signal:

$$S_{jj}^{qpci} = S_{qpci} \frac{n_j^2}{(N + \tau)^2}. \quad (2.23)$$

For  $Mi$  the situation is different, as generated current fluctuations toward  $Mi$  ( $\delta I_{qpci}^{out}$ ) and corresponding effectively simultaneously redistributed fluctuations ( $-\delta I_{qpci}^{out} n_i / (N + \tau)$ ) add up. Consequently, we need to consider separately out-going fluctuations emitted from the island across QPC  $i$  (see below). In contrast, the result from incoming current fluctuations ( $\delta I_{qpci}^{in}$ ) in the auto-correlation signal in  $Mi$  is obtained similarly to the noise generated at other QPCs:

$$S_{ii}^{qpci-in} = S_{qpci}^{in} \frac{n_i^2}{(N + \tau)^2}. \quad (2.24)$$

And the cross correlation is:

$$S_{12}^{qpci-in} = S_{qpci}^{in} \frac{n_i n_j}{(N + \tau)^2}. \quad (2.25)$$

Regarding the out-going current fluctuations  $\delta I_{qpci}^{out}$  thermally emitted from the island toward the contact  $Mi$ . These are partially compensated by the out-going

redistributed fluctuations  $-\delta I_{qpci}^{out} \frac{n_i}{N+\tau}$ . The net current impinging in electrode  $Mi$  is then  $\delta I_{qpci}^{out} (1 - \frac{n_i}{N+\tau})$  and the resulting noise is:

$$S_{ii}^{qpci-out} = S_{qpci}^{out} \left(1 - \frac{n_i}{N+\tau}\right)^2. \quad (2.26)$$

In the same way, the cross-correlation contribution is given by:

$$S_{12}^{qpci-out} = -S_{qpc1}^{out} \left(1 - \frac{n_1}{N+\tau}\right) \left(\frac{n_2}{N+\tau}\right) - S_{qpc2}^{out} \left(1 - \frac{n_2}{N+\tau}\right) \left(\frac{n_1}{N+\tau}\right). \quad (2.27)$$

Summing all the contributions we get for the auto-correlation:

$$S_{ii} = \frac{n_i^2}{(N+\tau)^2} (S_{qpc3} + S_{qpcj} + S_{qpci}^{in}) + \left(1 - \frac{n_i}{N+\tau}\right)^2 S_{qpci}^{out} + S_{offset}, \quad (2.28)$$

where  $S_{offset}$  corresponds to the thermal noise along the  $\nu - n_1$  channels reflected at the QPC 1 and along the  $\nu$  channels propagating from  $M1$  to the ground as well as the noise of the amplification chain. For the cross-correlation we have:

$$S_{12} = \frac{n_1 n_2}{(N+\tau)^2} (S_{qpc3} + S_{qpc1}^{in} + S_{qpc2}^{in}) - \left(1 - \frac{n_1}{N+\tau}\right) \frac{n_2}{N+\tau} S_{qpc1}^{out} - \left(1 - \frac{n_2}{N+\tau}\right) \frac{n_1}{N+\tau} S_{qpc2}^{out}. \quad (2.29)$$

Note that despite the fermionic statistic, the cross-correlations given by equation 2.29 may be positive (for instance at zero-temperature), as it can be expected [48] and measured [49] in presence of inelastic scattering. Focusing on the excess signal with respect to the applied voltage, one obtains from equations 2.19, 2.28 and 2.29 :

$$T_\Omega - T_0 = \frac{R_K}{2k_B} \left( \frac{\Delta S_{11}}{2n_1} + \frac{\Delta S_{22}}{2n_2} - \frac{\Delta S_{12}N}{2n_1 n_2} \right), \quad (2.30)$$

$$\Delta S_{qpc3} = (N+2\tau) \left( \frac{\Delta S_{11}}{2n_1} + \frac{\Delta S_{22}}{2n_2} \right) + \Delta S_{12} \frac{(N+\tau)^2 + \tau^2}{2n_1 n_2}. \quad (2.31)$$

Note that the determination of the excess temperature of the metallic island does not depend of the transmission probability across the non-ballistic channel.

As an illustration, we use these formulae, replacing  $\tau$  by the simultaneously measured differential conductance, in order to extract the excess temperature and the current noise from the non-ballistic QPC. We performed this illustrative measurement at a relative high base temperature of  $T_0 = 15.5$  mK in two different but equivalent configurations in the figure 2.3.3:

- Config. 1:** The voltage is applied behind the QPC 3, which is tuned in a non-ballistic regime with a transmission probability about 0.5 (it changes with voltage due to the strong renormalization of the conductance by the dynamical Coulomb blockade). The QPC 1 and 2 are tuned such that  $n_1 = n_2 = 1$ . In the top left panel we display  $\Delta S_{11}$ ,  $\Delta S_{22}$  and  $\Delta S_{12}$  as a function of the voltage. By symmetry,  $\Delta S_{11} = \Delta S_{22}$ . Using equation 2.30, we extract the excess temperature displayed in the left bottom panel as red triangle. Using equation 2.31, we extract the noise coming from the non-ballistic QPC displayed in the right bottom panel as red triangle
- Config. 2:** The voltage is applied behind the QPC 2, which is tuned in a non-ballistic regime within the same transmission probabilities than the QPC 3 in config. 1. The QPC 1 and 3 are tuned such that  $n_1 = n_3 = 1$ . In the top right panel we display  $\Delta S_{11}$ ,  $\Delta S_{22}$  and  $\Delta S_{12}$  as a function of the voltage. Using equations 2.30, 2.31 as well as equation 2.16, we extract the excess temperature and the noise coming from the non-ballistic QPC. The result is displayed as black triangles in the bottom left and the bottom right panel respectively.

### 2.3.4 What should be measured behind the QPC 3?

We will see in the following chapter that some theoretical predictions about the noise in the device deals with what would be measured behind the QPC 3 (seen from the metallic island) in electrode  $M3$ . To access experimentally to the excess noise we would have measured in electrode  $M3$ , we use equation 2.16:  $\Delta S_{33} = 2\Delta S_{12} + \Delta S_{11} + \Delta S_{22}$ . Injecting equations 2.19, 2.28 and 2.29, we obtain:

$$\Delta S_{33} = \frac{N\tau^2}{(N + \tau)^2} \frac{2k_B(T_\Omega - T_0)}{R_K} + \left(\frac{N}{N + \tau}\right)^2 \Delta S_{qpc3} \quad (2.32)$$

Now, following equation 2.6, let us decompose  $\Delta S_{qpc3}$  in a purely thermal term (Johnson-Nyquist noise) and a shot noise term:

$$\Delta S_{qpc3} = \frac{2k_B(T_\Omega - T_0)}{R_K} + \Delta S_{qpc3}^{sn} \quad (2.33)$$



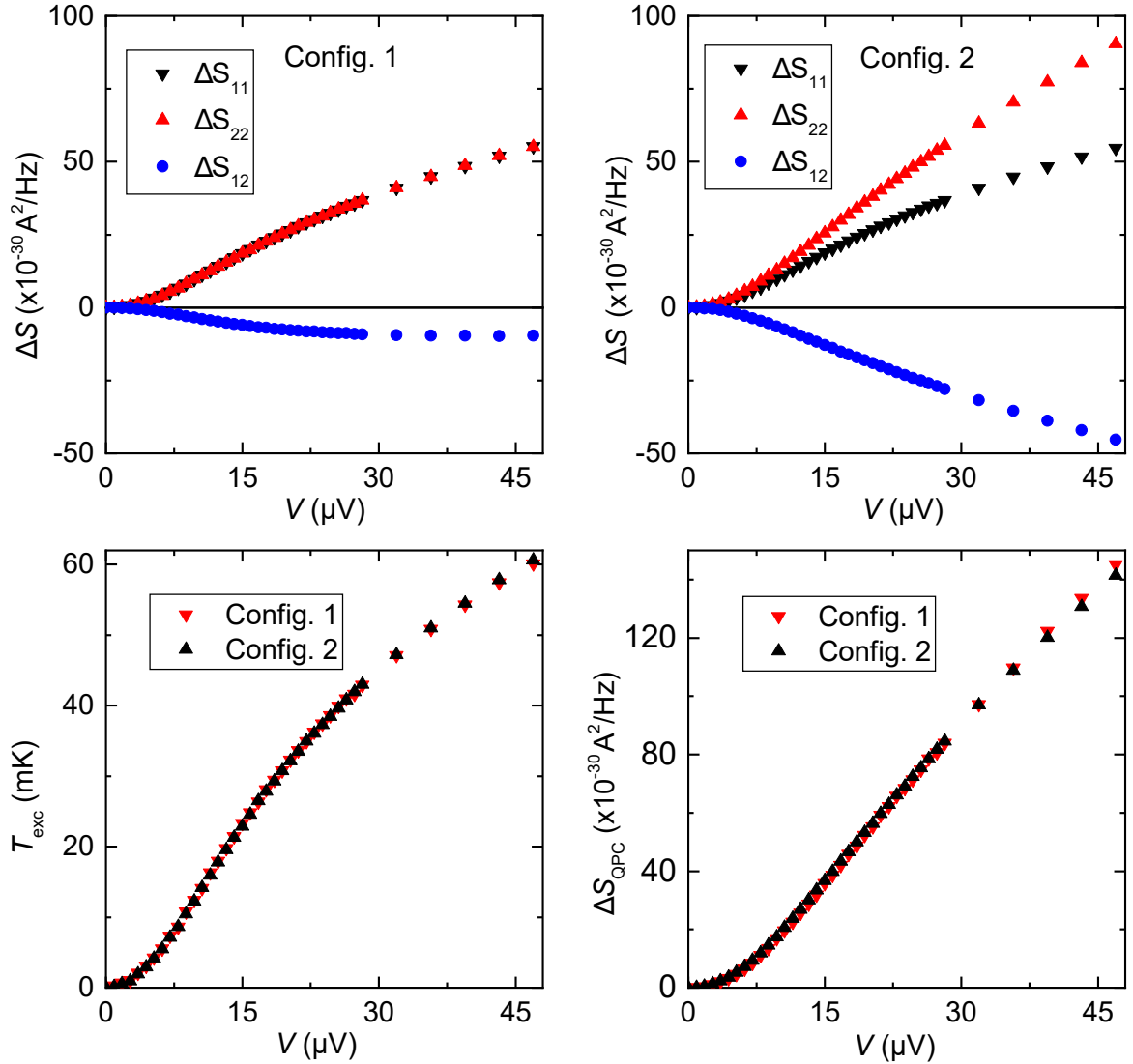


Figure 2.3: **Extraction of the excess temperature and of the noise from the non-ballistic QPC.** Left top panel: we display  $\Delta S_{11}$ ,  $\Delta S_{22}$  and  $\Delta S_{12}$  as voltage in the configuration 1 (see legends and text). Right top panel: we display  $\Delta S_{11}$ ,  $\Delta S_{22}$  and  $\Delta S_{12}$  as voltage in the configuration 2. Left bottom panel: we display the excess temperature for the two configurations obtained using equations 2.30 and 2.16. Right bottom panel: we display the spectral density of the noise originating from the non-ballistic QPC for the two configurations, obtained using equations 2.31 and 2.16.

Then, equation 2.32 can be recast as:

$$\Delta S_{33} = \frac{\tau N}{N + \tau} \frac{2k_B(T_\Omega - T_0)}{R_K} + \left( \frac{N}{N + \tau} \right)^2 \Delta S_{qpc3}^{sn}, \quad (2.34)$$

$$= G_{s,3} \frac{2k_B(T_\Omega - T_0)}{R_K} + \left( \frac{N}{N + \tau} \right)^2 \Delta S_{qpc3}^{sn}. \quad (2.35)$$

with  $G_{s,3}$  the conductance of the sample seen from the electrodes  $M3$ . The purely thermal term in the right-hand side of equation 2.34 corresponds to the one given by the fluctuation dissipation theorem applied to the overall sample. The other term corresponds to the shot noise from the QPC 3 times a factor which comes from the current redistribution in the metallic island.



# Chapter 3

## Dynamical Coulomb blockade

### Contents

---

<b>3.1</b>	<b>Introduction</b>	<b>52</b>
<b>3.2</b>	<b>Modelisation of the environment</b>	<b>53</b>
<b>3.3</b>	<b>Single electron tunneling theory</b>	<b>55</b>
3.3.1	Perturbation approach	55
3.3.2	Asymptotic limits:	56
<b>3.4</b>	<b>Mapping with a Tomonaga-Luttinger liquid</b>	<b>57</b>
3.4.1	Tomonaga-Luttinger liquid: the replacement of Fermi liquid in one dimension	57
3.4.2	Linearization of electronic excitation: the case of spinless electrons hopping on 1D lattice	58
3.4.3	Mapping to a Tomonaga Luttinger liquid	60
<b>3.5</b>	<b>Predictions for the local sine-Gordon model</b>	<b>63</b>
3.5.1	Predictions for certain interaction parameters	63
3.5.2	Zero-temperature predictions for the conductance for all interaction parameters	63
3.5.3	Prediction for the current noise	64

---

### 3.1 Introduction

A diffusive short quantum conductor embedded in a resistive circuit exhibits a drop of its electrical conductance at low voltage and low temperature, in violation of the classical laws of impedance composition [20; 50; 51]. An illustration of such a drop in the conductance is provided in figure 3.1. This quantum phenomena, the so-called dynamical Coulomb blockade (DCB), results from the excitations of the electromagnetic modes of the circuit by a charge pulse passing through the quantum conductors [5]. In this chapter, we review some theoretical developments on this phenomenon: we start by the quantum description of the environment, then we will deal with the well-established single electron tunneling theory which works for small transmission through the quantum conductor. We continue by describing a mapping between a quantum dissipative circuit composed of a single non-ballistic channel in series with an ohmic impedance, and a Tomonaga-Luttinger liquid with a single impurity [17]. This mapping allows us to describe the full crossover from a ballistic channel to a disconnected channel as the temperature is reduced [21; 52].

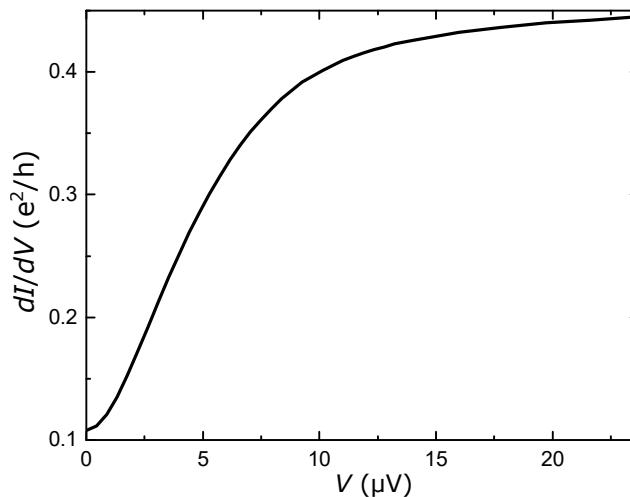


Figure 3.1: **Drop of the electrical conductance.** The black line displays measurement of the differential conductance as a function of the voltage in a device consisting of a single diffusive channel in series with an impedance  $R = h/e^2$ . The electronic temperature is approximately 8 mK.

## 3.2 Modelisation of the environment

The system we consider consists of a small quantum conductor connected to a dissipative electromagnetic environment. The coupling between these two parts changes the properties of the overall circuit. The main problem of addressing dissipation at the quantum level is that quantum mechanics usually deals with the Hamiltonian formalism, where the total energy of the system is a conserved quantity, whereas here we want to describe the mechanism which leads to an irreversible loss of energy. The idea introduced by Caldeira and Leggett [53] is to modelize the environment as an infinite set of LC oscillators in parallel. This model does not come from a microscopic description, but is a phenomenological approach.

In the following, we introduce the phase associated to a circuit:

$$\phi(t) = \frac{e}{\hbar} \int_{-\infty}^t V(t') dt', \quad (3.1)$$

where  $V$  is the voltage applied to the circuit. Each LC oscillator can be described quantum mechanically using the canonical commutation of the charge  $q$  and the phase  $\phi$ , which are conjugate variables:

$$[\phi, q] = ie \quad (3.2)$$

with the quantum Hamiltonian of a LC circuit:

$$H = \frac{q^2}{2C} + \frac{\phi^2}{2L} \quad (3.3)$$

which is that of a harmonic oscillator.

As illustrated in the figure 3.2, the quantum conductor can be decomposed into a pure conductor of resistance  $R = h/(e^2\tau)$  in parallel with a capacitor  $C$ . The relevant impedance of the environment is the parallel combination of this capacitance and the resistance of the circuit in which the quantum conductor is embedded:  $Z(\omega) = 1/(j\omega C + 1/R_{env})$ . The Hamiltonian describing the environment is then:

$$H_{env} = \frac{\delta Q^2}{2C} + \sum_n \left[ \frac{q_n^2}{2C_n} + \frac{(\delta\varphi - \varphi_n)^2}{2L_n} \right]. \quad (3.4)$$

$\delta Q$  and  $\delta\varphi$  are departure from the equilibrium value of the charge and of the phase of the capacitor  $C$ . The first term describes the charging energy of the quantum conductor. The second term describes  $R_{env}$  as an infinite sum of LC oscillators bilinearly

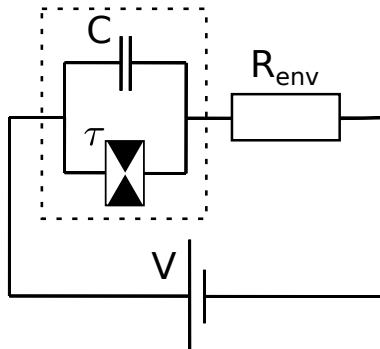


Figure 3.2: **A quantum conductor in series with a resistive environment.** The quantum conductor, inside the dashed frame, can be decomposed into a condenser  $C$  in parallel with a pure conductor of resistance  $R = h/(e^2\tau)$ . The relevant impedance of the environment  $Z(\omega)$  is the parallel combination of this capacitance and the resistance of the circuit in which the quantum conductor is embedded.

coupled to  $\delta\varphi$ . As detailed in the following the important quantity for the transport is the phase-phase correlation function  $J(t) = \langle [\delta\varphi(t) - \delta\varphi(0)]\delta\varphi(0) \rangle$  which is directly connected to the impedance  $Z(\omega)$  through the fluctuation dissipation theorem [5]:

$$J(t) = 2 \int_{-\infty}^{\infty} \frac{\Re[Z(\omega)]}{R_K} \frac{e^{-i\omega t} - 1}{1 - e^{-\hbar\omega/k_B T}} \frac{d\omega}{\omega} \quad (3.5)$$

### 3.3 Single electron tunneling theory

#### 3.3.1 Perturbation approach

The total Hamiltonian of the system described in the figure 3.2 can be written as:

$$H = H_r + H_l + H_{env} + H_T. \quad (3.6)$$

The two first terms describe the quasi-particles in the leads of the quantum conductor:

$$H_{r(l)} = \sum_{k,r(l)} \epsilon_{k,r(l)} c_{k,r(l)}^\dagger c_{k,r(l)}, \quad (3.7)$$

and  $H_T$  is the tunneling Hamiltonian from one lead to the other:

$$H_T = \sum_l T_{k,q} c_{k+q,r}^\dagger c_{k,l} e^{i\frac{e\varphi}{\hbar}}. \quad (3.8)$$

The operator  $e^{i\frac{e\varphi}{\hbar}}$  shifts the charge  $Q$  by  $e$  (as  $Q$  and  $\varphi$  are conjugate variables), which provides the coupling between the electrons in the electrodes with the electromagnetic degrees of freedom of the environment. The first attempt to capture the physics of the DCB was done using perturbation techniques: in the tunnel regime, when the transmission probability through all the elementary conduction channels is well below one, we can use the Fermi golden rule in order to estimate the transmission rate for an electron to tunnel through the junction and excite the electromagnetic modes of the environment [5]. According to the Fermi golden rule, the rates for transitions between an initial state  $|i\rangle$  and the final state  $|f\rangle$  is given by

$$\Gamma_{i \rightarrow f} = \frac{2\pi}{\hbar} |\langle f | H_T | i \rangle|^2 \delta(E_i - E_f). \quad (3.9)$$

The tunneling rate from one electrode to the other can be written as a convolution product involving the energy distribution in each electrode and the probability  $P(\Delta E)$  that the electromagnetic environment absorbs an energy  $\Delta E = E - E'$ :

$$\Gamma(V) = \frac{G_\infty}{e^2} \int f_l(E) [1 - f_r(E' + eV)] P(E - E') dE dE', \quad (3.10)$$

where  $f_l(E)$  and  $f_r(E)$  are the Fermi distribution in the left and the right lead respectively.  $P(\Delta E)$  is the Fourier transform of  $\exp(J(t))$  with  $J(t)$  the phase-phase correlation function which is given in equation 3.5, and  $G_\infty$  is the unrenormalized



conductance of the quantum conductor ( $G_\infty = \tau e^2/h$  for the single channel case illustrated in figure 3.2). The current flowing through the quantum conductor is then:

$$I(V) = e(\Gamma(V) - \Gamma(-V)), \quad (3.11)$$

The conductance of the quantum conductor, renormalized by Coulomb interaction, is:

$$G(V) \equiv \frac{dI(V)}{dV} = \frac{G_\infty}{e} \int f_l(E) \frac{d}{dV} [f_r(E' + eV) - f_r(E' - eV)] P(E - E') dE dE'. \quad (3.12)$$

This formula is valid as long as the transmission through the quantum conductor is much smaller than one. Notably, we can use different temperatures for each electrode and for the environment, allowing us to investigate theoretically the influence of a temperature bias in a dissipative circuit. This theory cannot be expanded beyond the tunnel regime.

### 3.3.2 Asymptotic limits:

At zero temperature and low voltage compared to the charging energy  $E_C = e^2/2C$  the conductance is given by [5]:

$$G(V) = G_\infty \frac{(2R_{\text{env}}/R_K + 1)(\pi/\exp(\gamma))^{2R_{\text{env}}/R_K}}{\Gamma(2 + 2R_{\text{env}}/R_K)} \left( R_{\text{env}}/R_K \frac{eV}{E_C} \right)^{2R_{\text{env}}/R_K}, \quad (3.13)$$

with  $\gamma \approx 0.5772$  the Euler's constant and  $\Gamma$  the gamma function. At zero voltage and low temperature compared to  $E_C$  it results in [54]:

$$G(T) = G_\infty \frac{\pi^{1/2+3R_{\text{env}}/R_K} \Gamma(1 + R_{\text{env}}/R_K)}{2\Gamma(3/2 + R_{\text{env}}/R_K)} \left( R_{\text{env}}/R_K \frac{k_B T}{E_C} \right)^{2R_{\text{env}}/R_K}. \quad (3.14)$$

In both cases, the conductance follows a power law in  $2R_{\text{env}}/R_K$ . Note that using these two previous equations, we can extract the temperature from the measurement of the conductance renormalization by DCB versus voltage [23].

## 3.4 Mapping with a Tomonaga-Luttinger liquid

A different approach, suggested by the power law behavior at small transmission, was found in order to treat the case of any value of transmission probabilities through a quantum conductor composed of a single channel and an environment composed of an arbitrary ohmic impedance. It was demonstrated that the Hamiltonian of the system is the same as the one of a Tomonaga-Luttinger liquid (TLL) with a single impurity [17]. This mapping allows one to exploit TLL theoretical developments to get a better understanding of the DCB phenomena. It also allows one to probe the TLL physics experimentally with engineered circuits [55].

### 3.4.1 Tomonaga-Luttinger liquid: the replacement of Fermi liquid in one dimension

Fermi liquid theory is a theoretical model of interacting fermions that describes the normal state of most metals at sufficiently low temperatures [56]. The basic result is that interacting fermions can be seen as non-interacting quasi-particles with renormalized parameters (for example the mass of electrons). Although this model gives a good description of a lot of systems, it fails to describe the behavior of interacting fermions in one dimension where interaction results in collective behavior, as illustrated in the figure 3.3. In 1981, Haldane [57] proposed the Luttinger liquid theory as a replacement for the Fermi liquid theory in one dimension. Following the idea developed in previous work from Tomonaga in 1950 [58] and Luttinger in 1963 [59], it consists of describing the low energy excitations in a one dimensional system as collective bosons modes. Luttinger liquids have generated a lot of interest, owing to their exotic properties and striking differences from Fermi liquids. An example of theoretical predictions that have already been observed are the spin-charge separation [60; 61], the fractionalization of injected charges [62–65], the behavior as a power law of the correlation functions which are associated with critical physics [66]. Note that the experimental investigation of TLL physics in 1D conductors is not easy since the impurities tends to localize the excitations [67].

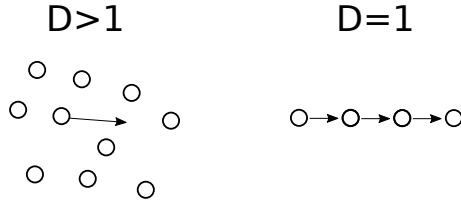


Figure 3.3: **High dimensional versus one dimensional system.** In the left, at high dimension, nearly free quasiparticle excitations are possible. In the right, in a one-dimensional interacting system, an individual electron cannot move without pushing all the electrons: only collective excitations can exist.

### 3.4.2 Linearization of electronic excitation: the case of spinless electrons hopping on 1D lattice

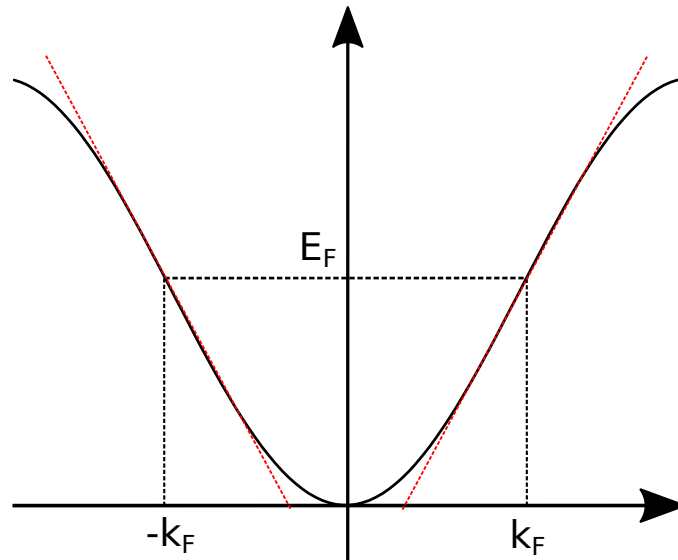


Figure 3.4: **Excitations spectrum of free spinless electrons hopping on 1D lattice.** When focusing on low energy excitations, the energy spectrum can be linearized near the Fermi points  $\pm k_F$  and it results in the straight red line.

Here, we review two key elements for describing a one-dimensional system: linearization of the energy spectrum and bosonization. Let us consider spinless electrons hopping on a 1D lattice with the following Hamiltonian [68]:

$$H = -t \sum_j c_j^\dagger c_{j+1} + \frac{V}{2} \sum_j c_j^\dagger c_j c_{j+1}^\dagger c_{j+1} + h.c. \quad (3.15)$$

$t$  is the hopping strength and  $V_{n-n}$  is the interaction strength between near-neighbor particles. For  $V_{n-n} = 0$ , the energy is given by  $E = -2t \cos(k)$  with  $k < \pi$  and is plotted in figure 3.4. When focusing on low energy excitations, we neglect high energy excitations, and those well below the Fermi level are blocked by the Pauli principle. We can thus linearize the energy spectrum near the Fermi points  $\pm k_F$ :  $\epsilon_k = v_F(k \mp k_F)$  with  $v_F = \left. \frac{\partial \epsilon_k}{\partial k} \right|_{\pm k_F}$  the Fermi velocity. This linearization leads to the introduction of two species of fermions: right moving fermions  $c_k^R = c_{k_F+k}$  and left moving fermions  $c_k^L = c_{-k_F+k}$ . The Hamiltonian becomes:

$$H = \sum_k v_F k (c_{R,k}^\dagger c_{R,k} - c_{L,k}^\dagger c_{L,k}). \quad (3.16)$$

The sum is performed using an arbitrary cutoff  $\Lambda$  in order to allow momentum between  $[k_F - \Lambda, k_F + \Lambda]$  (and the same thing for the opposite Fermi point). In this linear approximation, the dispersion relation of particle-hole excitations generated by  $c_{k+q}^\dagger c_k$  is simply given by  $E_k(q) = v_F q$  with  $q$  the momentum: the energy does not depend of  $k$ . One can write the Hamiltonian in this new basis. To do this we use the density fluctuations operator which is a superposition of particle-hole excitations:

$$\rho^\dagger(q) = \sum_k c_{k+q}^\dagger c_k. \quad (3.17)$$

In fact, deriving commutation relation of this operator, we can demonstrate its bosonic character [69]. Then, using the appropriate relation one can write the Hamiltonian of a spinless electrons hopping on 1D lattice in term of boson operators. Notably, the kinetic Hamiltonian, which is quadratic in terms of fermion modes, remains quadratic in terms of boson modes. Regarding the interaction term, it is quartic in term of fermion operators which make it difficult to diagonalize it. Now, in term of bosonic modes, it is given by [69]:

$$H_i = \frac{1}{2L} \sum_q V_{n-n}(q) \rho(q) \rho(-q). \quad (3.18)$$

It has also a quadratic form which allows to diagonalize it. This procedure of linearizing the energy spectrum and writing the Hamiltonian in term of bosonic modes, the so-called bosonization technique, is at the core of theoretical procedure when dealing with one-dimensional systems.

In term of bosonic fields  $\Pi = (\rho_R - \rho_L)$  and  $\nabla\phi = -\pi(\rho_R + \rho_L)$ , with  $\Pi$  and  $\phi$  which

are conjugate variables, the Hamiltonian of spinless electrons hopping on 1D lattice can be written as [69]:

$$H = \frac{U}{2\pi} \int \left[ K(\pi\Pi(x))^2 + \frac{1}{K}(\nabla\phi(x))^2 \right] dx, \quad (3.19)$$

which is the way this Hamiltonian is often written in the literature. It can be shown [69] that this Hamiltonian is more general and describes any gapless one-dimensional system, whether based on underlying fermionic, or bosonic particles [70]. The whole physics of TLL is embodied in two parameters: the dimensionless interaction parameter  $K$  and the velocity of density excitations  $U$ . These two parameters depend on the model and the value of interaction.  $K = 1$  means that we are dealing with free electrons,  $K > 1$  corresponds to attractive interactions and  $K < 1$  corresponds to repulsive interactions. The smaller  $K$  is, stronger are the repulsive interactions. For the observable that we are observing experimentally in this thesis, *ie* the differential conductance and the current noise, only the parameter  $K$  is relevant.

### 3.4.3 Mapping to a Tomonaga Luttinger liquid

Let us come back to the circuit: the mapping between the circuit and a TLL comes from the collective TLL excitations that can be described as bosonic density modes corresponding to the electromagnetic mode decomposition of the linear environment. First, we reformulate the Hamiltonian of the circuit in a different way as in section 3.3.1: the two formulations are equivalent but the one presented now is more natural for exploring the crossover from a near-ballistic to a disconnected channel. The Hamiltonian of the circuit can be rewritten as:

$$H = H_{QE} + H_I + H_{env} + H_c, \quad (3.20)$$

with  $H_{QE}$  the Hamiltonian of the unperturbed quantum channel:

$$H_{QE} = \sum_k \epsilon_k c_k^\dagger c_k, \quad (3.21)$$

$H_I$  is the Hamiltonian describing the impurity emulated by the QPC:

$$H_I = \sum_{k,k'} V(k - k') c_k^\dagger c_{k'}. \quad (3.22)$$

A small  $H_I$  corresponds to the initial near ballistic case.  $H_{env}$  is the Hamiltonian describing the environment which is given by the equation 3.4. The coupling between quasiparticles and the electromagnetic modes of the environment is given by:

$$H_c = -QV_{qc}, \quad (3.23)$$

with  $Q$  the charge transferred through the quantum conductor and  $V_{qc} \equiv V - \partial_t \hat{\Phi}$  the voltage across the quantum conductor, where  $\hat{\Phi}$  is a bosonic operator corresponding to the time integral of the voltage across the impedance. Using the approach of linearization of low energy excitations and bosonization, it can be shown that the first term describing left moving and right moving electrons through the unperturbed quantum channel corresponds to the TLL Hamiltonian (equation 3.19) for an interaction parameter  $K = 1$  (*ie* without interaction). At low frequency in front of the cutoff  $R_{env}C$ , it was demonstrated [17] that the sum of this Hamiltonian with  $H_{env}$  and  $H_c$  can be written as an effective Hamiltonian that corresponds to the one of the equation 3.19, with an interaction parameter  $K$  such that:

$$K = \frac{1}{1 + R_{env}/R_K}. \quad (3.24)$$

Details of this calculation can be found in the thesis of Sebastien Jezouin [71]. In the limit of small frequency in front of the cutoff  $1/R_{env}C$ , the total Hamiltonian of the circuit is:

$$H = \frac{U}{2\pi} \int \left[ K(\pi\Pi(x))^2 + \frac{1}{K}(\nabla\phi(x))^2 \right] dx + V_0 \left( -\frac{1}{\pi} \nabla\phi(x=0) + \frac{1}{\pi\alpha} \cos(2\phi(x=0)) \right). \quad (3.25)$$

The first term corresponds to the TLL Hamiltonian without scattering, and the second and third terms correspond to the barrier Hamiltonian expressed in terms of bosonic fields  $\phi$  and  $\Pi$ . Note that the second term induces a simple phase shift and can be ignored. In this equation,  $\alpha \approx 1/\Lambda$  is a high energy cutoff [69] (see section 3.4.2). This Hamiltonian corresponds to the local sine-Gordon model and it describes an infinite Luttinger liquid of interaction parameter  $K$ , with a single impurity leading to back-scattering. Notably, it is the same Hamiltonian as the one describing a QPC in the fractional quantum Hall regime for certain filling factors [67; 72]. The impurity is implemented by the single channel electronic contact, of scattering strength characterized by the unrenormalized transmission probability of

electrons  $\tau_\infty$ . The conductance of the device in absence of impurity is given by  $G = Ke^2/h$ . When adding the impurity, the system experiences a quantum phase transition from a metallic to an insulating state. At equilibrium, the crossover from one state to the other is predicted to follow a universal scaling flow characterized by a beta function  $\beta_K(G)$  which does not depend of the energy scale:

$$\frac{dG}{d\ln T} = \beta_K(G). \quad (3.26)$$

## 3.5 Predictions for the local sine-Gordon model

### 3.5.1 Predictions for certain interaction parameters

The sine-Gordon model has captured the attention of theoreticians as this model has been proposed to describe the edge states in fractional quantum Hall effect devices. Notably, it allows a connection with the quasiparticles introduced by Laughlin to explain the fractional quantum Hall effect [73]. The conductance of a system governed by the local sine-Gordon model as a function of both the temperature and the voltage, for the special cases of an interaction parameter  $K = 1/m$  with  $m$  an integer, was calculated using the thermodynamic Bethe ansatz (TBA) in references [67; 72]. For a given interaction parameter, the conductance is then described by three parameters: the voltage  $V$ , the temperature  $T$ , and a scaling energy  $k_B\tilde{T}_I$ , which depends on the impurity strength and on details of the high energy cutoff. The conductance could be cast as a function of  $T/\tilde{T}_I$  and  $eV/k_B\tilde{T}_I$ . In the device which is investigated in this thesis, the interaction parameters implemented are  $K = 2/3$  and  $K = 3/4$ ; we then need specific predictions not given in reference [67; 72]. The equilibrium predictions (zero voltage) for the conductance specific for the case  $K = 2/3$  are derived and compared with experimental data in [21]. Furthermore, we also have new equilibrium predictions for  $K = 3/4$  and  $K = 4/5$  [74] which are in good agreement with the corresponding data in [21].

### 3.5.2 Zero-temperature predictions for the conductance for all interaction parameters

The conductance was derived for all interaction parameters  $K$  (not only  $K = 1/m$ ) in the limit of  $T = 0$ . The differential conductance  $G \equiv dI/dV$  is calculated from the derivative of the current at  $T = 0$  in terms of two different power series for the regimes of high and low voltages, which together cover the full range of voltages



[67; 72]:

$$I(V) = \begin{cases} \frac{VKe^2}{h} \left[ 1 - K \sum_{n=1}^{\infty} a_n(K) \times \left( \frac{V}{V_I} \right)^{2n(K-1)} \right] \\ \frac{e^2V}{h} \sum_{n=1}^{\infty} a_n\left(\frac{1}{K}\right) \times \left( \frac{V}{V_I} \right)^{2n\left(\frac{1}{K}-1\right)}, \end{cases} \quad (3.27)$$

where the functions  $a_n(x)$  read:

$$a_n(x) = (-1)^{n+1} \frac{\sqrt{\pi} \Gamma(nx)}{2\Gamma(n)\Gamma\left(\frac{3}{2} + n(x-1)\right)}, \quad (3.28)$$

and with the scaling voltage  $V_I$  related to the temperature scale  $\tilde{T}_I$  through [72]:

$$eV_I = \frac{2\sqrt{\pi}\Gamma\left(\frac{1}{2(1-K)}\right)}{K\Gamma\left(\frac{K}{2(1-K)}\right)} k_B \tilde{T}_I. \quad (3.29)$$

For a direct comparison with experimental data, it is possible to eliminate the scaling energy  $k_B \tilde{T}_I$  (or equivalently  $eV_I$ ) by considering the logarithmic derivatives of the conductance  $dG/d \ln V$  or  $dG/d \ln T$  which do not depend on this parameter (it is the procedure used in reference [21] in order to investigate the zero voltage conductance). Note that the low voltage asymptotic behavior is given by the first order of the sum of the equation 3.27 and it is the same as the one found using a perturbation method in the tunnel limit in the first section of this chapter (equation 3.13).

### 3.5.3 Prediction for the current noise

The current noise resulting from the scattering at an impurity in a Tomonaga-Luttinger liquid has been calculated in references [43; 75; 76]. It is predicted that, at zero temperature, the shot noise  $S^{sn}$  in the limit of strong-backscattering limit (strong impurity) matches with what is expected from the tunneling of uncorrelated electrons (Poisson noise):

$$S^{sn} = 2eI, \quad (3.30)$$

with  $I$  the current flowing through the device and  $e$  the charge of the electron. In this case, the system can be interpreted as two Luttinger liquids with a small connection between them.

In the weak-backscattering limit, the noise is predicted to result from the uncorrelated tunneling of quasiparticles with fractional charge  $e^* = Ke$ , where we recall that  $K$  is the interaction parameter of the considered TLL:

$$S^{sn} = 2e^* I_{back}, \quad (3.31)$$

with  $I_{back}$  the backscattered current. Measurement of the slope of the noise versus voltage at high enough voltage allows one then to determine the charge of the quasiparticles. Such measurements have been performed for different filling factors in the fractional quantum Hall regime (FQHR)[44; 45]. Note the recent measurements of fractional charge in the FQHR using photo-assisted noise measurement [77] following prediction of reference [78], and using microwave photon detection [79].

Between the limits of weak and strong backscattering, a relation connecting the derivative of the zero-temperature current noise to the logarithmic derivative of the conductance has been proposed in reference [17], generalizing a result of reference [67]:

$$\frac{dG}{d \ln(V)} = \frac{1 - K}{Ke} \frac{dS^{sn}}{dV}. \quad (3.32)$$

This expression can be interpreted as an analog of the fluctuation-dissipation theorem for a Luttinger liquid at zero temperature [67]. Note that for  $K = 1$ , the left-hand side of this equation vanishes, as the conductance becomes voltage independent.



# Chapter 4

## Out-of-equilibrium noise in a quantum circuit

### Contents

---

<b>4.1</b>	<b>Introduction</b>	<b>68</b>
<b>4.2</b>	<b>Current noise as a function of voltage bias</b>	<b>69</b>
4.2.1	Conductance characterization of the circuit	69
4.2.2	Comparison of the measured current noise with the scattering theory of noise	73
4.2.3	Comparison of the measured current noise with prediction in the framework of the TLL mapping	75
4.2.4	Conclusion	78
<b>4.3</b>	<b>Shot noise induced by a temperature difference across a quantum point contact</b>	<b>79</b>
4.3.1	Previous measurements	79
4.3.2	Procedure for focusing on the $\Delta T$ -shot noise	81
4.3.3	Conclusion	83

---

## 4.1 Introduction

In this chapter, we measure the current noise in a dissipative quantum circuit firstly as a function of voltage bias, and secondly as a function of temperature bias. We use the circuit described in the chapter 2, tuned in order to have a single non-ballistic quantum channel characterized by a transmission  $\tau$  between zero and one, in series with ballistic quantum channels that emulate an ohmic environment.

The circuit in this condition can be described using the Tomonaga-Luttinger liquid theory, as seen in the previous chapter. One main objective is to test the predicted link between the noise and the renormalization of the conductance by the Coulomb interaction.

We first investigate the current noise versus voltage for two configurations of the “ballistic” QPC: one where two channels are ballistic, emulating a resistance of  $R_K/2$  corresponding to a TLL interaction parameter  $K = 2/3$ , and one where three channels are ballistic emulating a resistance of  $R_K/3$  and a TLL interaction parameter  $K = 3/4$ . For both configurations we note a good agreement at experimental accuracy with both the non-interacting scattering theory of noise, where the measured renormalized conductance is used, and with the prediction for a TLL with an impurity for the corresponding interaction parameter  $K$ . Indeed, the two predictions are close compared to measurement uncertainties. Moreover, we establish the link between voltage dependence of noise and conductance specifically (only) predicted in the TLL framework.

Then, we investigate the effect that a thermal bias has on the current noise. To do this we heat up the metallic island between the non-ballistic channel and the ballistic channels by applying voltages across the ballistic channels such that the average voltage in the metallic island remains zero. We thereby measure the shot noise produced by the resulting temperature gradient through the non-ballistic QPC, in the absence of a dc voltage. A good agreement with the scattering theory of noise is observed.

## 4.2 Current noise as a function of voltage bias

The work presented here is in the continuity with the work presented in the reference [21], performed in the team just before my arrival. In [21], the authors investigate the equilibrium and out-of-equilibrium behavior of the electrical conductance for different interaction parameters. The novelty here is the concomitant measurement of current fluctuations.

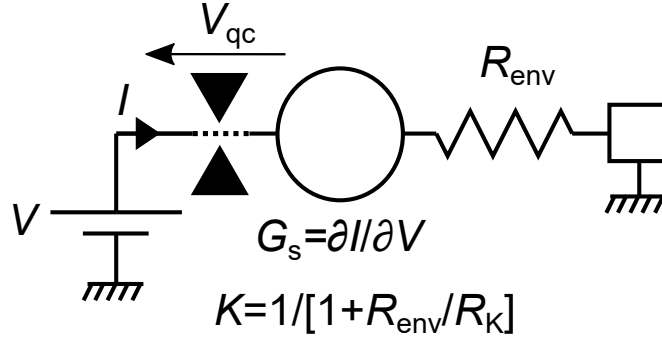


Figure 4.1: **Simple schematic of the sample.** The circuit is tuned as a quantum dissipative circuit, which consists here of a non-ballistic channel in series with a linear resistance  $R_{\text{env}}$ .

### 4.2.1 Conductance characterization of the circuit

First, we check if the conductance of the device follows the zero temperature universal curve predicted for a TLL with a single impurity [67]. For different settings of the non-ballistic QPC, we measure both the differential conductance and the current noise as explained in chapter 1. We perform this measurement for two different configurations of the environment:  $R_{\text{env}} = R_K/2$  and  $R_{\text{env}} = R_K/3$ , leading respectively to the TLL interaction parameters  $K = 2/3$  and  $K = 3/4$ . The dimensionless differential conductance  $G_s/K$  (in unit of  $e^2/h$ ), seen from the electrode  $M3$  (see figure 1.1,2.1 and simplified schematic in figure 4.1), versus the voltage is displayed for the two environments in the figure 4.2. In this experiment, the voltage is applied on electrode  $S3$  (see figure 1.1 and 2.1), behind the QPC 3 which is the one tuned in a non-ballistic regime. The open circles (full diamonds) correspond to  $R_{\text{env}} = R_K/2$  ( $R_{\text{env}} = R_K/3$ ). We observe that, as expected, the low voltage reduction of the

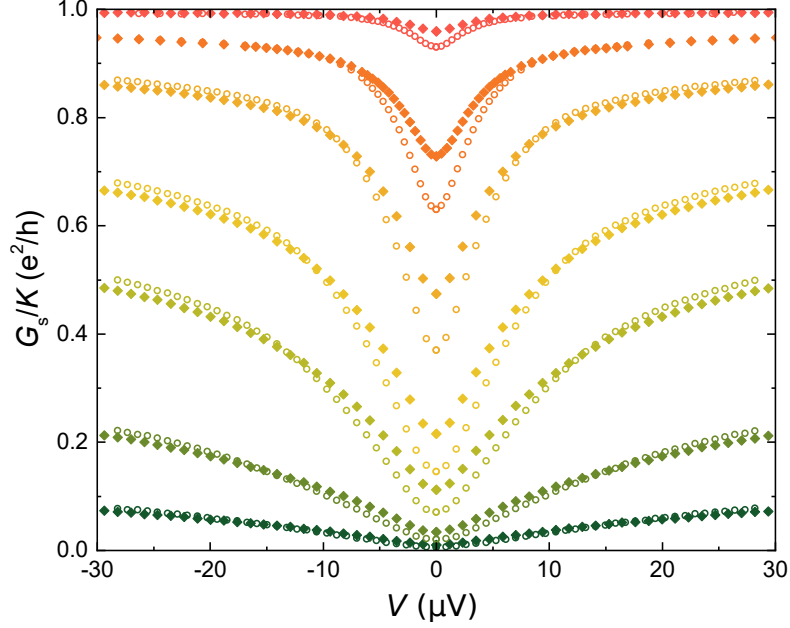


Figure 4.2: **Conductance of the device versus voltage.** The data points display the dimensionless differential conductance  $(G_s/K) R_K$ . The open circle (full diamond) points correspond to an environment  $R_{\text{env}} = R_K/2$  ( $R_{\text{env}} = R_K/3$ ). For a given setting of the environment, each color denotes a different configuration of the QPC.

conductance is less pronounced for a smaller resistance of the environment. We also observe that even for very weak impurity (transmission through the non-ballistic QPC very close to one) the conductance is notably affected by the DCB. As the behavior of the conductance at positive and negative voltages is symmetric, we average both in the following.

The excess temperature of the metallic island, resulting from the Joule heating when a voltage is applied to the circuit, is separately extracted using the formula derived in chapter 2, equation 2.30:

$$T_\Omega - T_0 = \frac{R_K}{2k_B} \left( \frac{\Delta S_{11}}{2n_1} + \frac{\Delta S_{22}}{2n_2} - \frac{N \Delta S_{12}}{2n_1 n_2} \right) \quad (4.1)$$

where we recall that  $\Delta S_{11}$  and  $\Delta S_{22}$  are excess current spectral densities measured in electrode  $M2$  and  $M1$ ,  $\Delta S_{12}$  are the cross-correlation,  $N = n_1 + n_2$  is the number

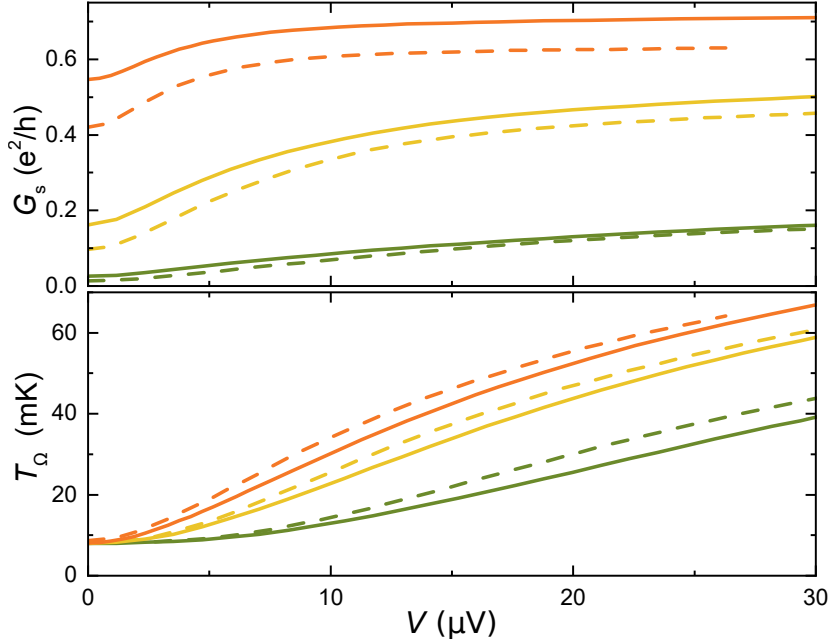


Figure 4.3: **Heating of the metallic island.** The temperature of the metallic island and the differential conductance of the sample (here not renormalized by  $K$ ) are displayed versus dc voltage in the top and in the bottom panel, respectively. The dashed (full) lines display data corresponding to  $K = 2/3$  ( $K = 3/4$ ). The different colors correspond to different tunings of the non-ballistic QPC (using the same color code as in the figure 4.2).

of ballistic channels constituting the environment, with  $n_1$  and  $n_2$  the number of ballistic channel through the QPC 1 and 2. For a base temperature of  $T_0 \approx 8$  mK, we present the temperature of the metallic island for the two configurations  $K = 2/3$  and  $K = 3/4$  in the bottom panel of figure 4.3, while the top panel displays the associated conductance. Since for a given voltage, the injected Joule power increases when the conductance of the device increases, the excess temperature of the metallic island is higher for transmission through the non-ballistic channel closer to one.

In the figure 4.4, for the same configuration as in figure 4.3, we display the differential conductance versus  $eV/k_B T_I$ .  $T_I = c_K \tilde{T}_I$  is the scaling temperature, which characterizes the strength of the impurity and depends on the setting of the non-ballistic channel.  $c_K$  is a coefficient chosen in order to respect the conventional criterion  $G_s(T/T_I = 1) = (Ke^2/h)/2$  at  $V = 0$  (in the same way as in reference [21]). For



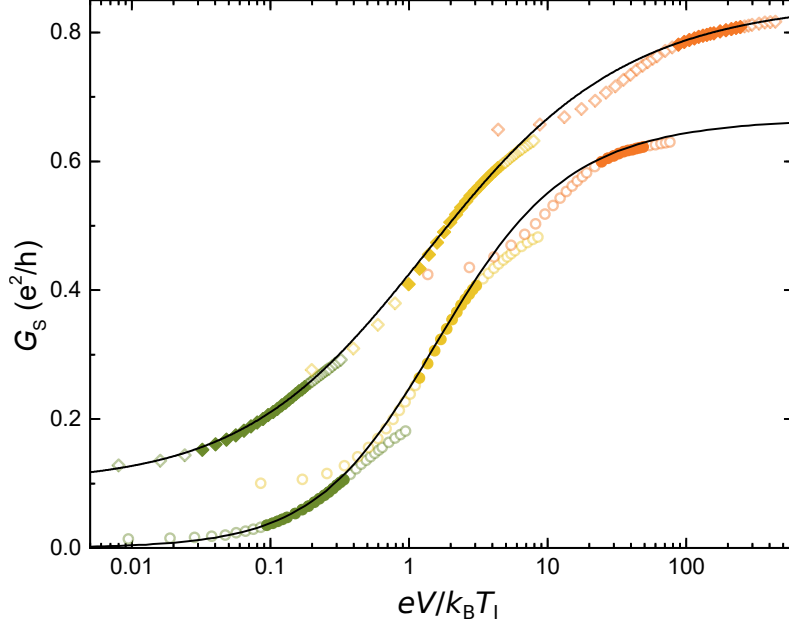


Figure 4.4: **Comparison of the conductance with the theoretical prediction.** The data points display the differential conductance versus  $eV/k_B T_1$ . The black lines are the theoretical predictions from [67]. The data are the same as in the previous figure (figure 4.3) with the same color codes. The full points correspond to  $6k_B \bar{T} < |eV| < h/(6R_{\text{env}}C)$  with  $\bar{T} = (T_\Omega + T_0)/2$ . For clarity, an offset of +0.1 is applied to the data and to the theoretical curve corresponding to  $K = 3/4$ .

each configuration,  $T_1$  is determined at zero dc voltage where it is predicted and measured that the conductance follows the equilibrium prediction for a TLL with a single impurity [21]. With  $T_1$  determined in the equilibrium regime, we can directly compare the data to the theoretical non-equilibrium prediction at zero temperature, which are drawn as black lines in the figure 4.4. This comparison was already done in [21] for  $K = 2/3$ . Here we also observe a good agreement between the data points and the theoretical curve at intermediate voltages, where a TLL behavior is expected, now including  $K = 3/4$ . For low voltages, deviations from zero temperature predictions come from the non-negligible temperature. The deviations at high voltages come from the capacitive cutoff ( $\approx h/(R_{\text{env}}C)$ ) above which the mapping to a TLL does not hold. From the figure 4.4 we assume in the following that our circuit is in the TLL regime and can be compared with the zero temperature prediction for

dc voltages  $V$  such that:

$$6k_{\text{B}}\bar{T} < |eV| < h/(6R_{\text{env}}C) \quad (4.2)$$

where  $\bar{T} = (T_{\Omega} + T_0)/2$ . In figure 4.4, the points for which this criterion is (not) respected are displayed as full (open) symbols.

## 4.2.2 Comparison of the measured current noise with the scattering theory of noise

The current noise associated with the theoretical predictions from the mapping to a TLL is the current noise which would be measured in electrode  $M3$  (see figure 1.1 and 2.1). In practice, we measure  $\Delta S_{11}$ ,  $\Delta S_{22}$  and  $\Delta S_{12}$  from which  $\Delta S_{33}$  can be deduced from charge conservation (see equation 2.16):  $\Delta S_{33} = 2\Delta S_{12} + \Delta S_{11} + \Delta S_{22}$ . Before comparing with the TLL prediction, we first compare the current noise to the prediction from the non-interacting scattering approach of noise (reviewed briefly in chapter 2). The excess noise is given by (equation 2.32 in chapter 2):

$$\Delta S_{33}^{\text{thy}} = \frac{2k_{\text{B}}(T_{\Omega} - T_0)}{R_{\text{K}}} \frac{N\tau^2}{(N + \tau)^2} + \left(\frac{N}{N + \tau}\right)^2 \Delta S_{\text{qpc3}}. \quad (4.3)$$

The first term in equation 4.3 is the thermal (Johnson-Nyquist) noise from the ballistic channels. In this first term we obtain  $\tau$  from the measured differential conductance. The second term is the excess noise from the QPC 3,  $\Delta S_{\text{qpc3}}$ , times a redistribution factor. This redistribution factor comes from the redistribution of the current fluctuations in the central metallic island (see chapter 2) and  $\tau$  is therefore also obtained from the measured differential conductance. According to the scattering theory, the noise from the QPC 3, which is open for only one channel, is given by the relation (equation 2.8 in chapter 2):

$$\begin{aligned} S_{\text{qpc3}}(V_{\text{qc}}, T_{\Omega}, T_0) &= \frac{2e^2}{\pi\hbar} \int_{-\infty}^{\infty} \tau(E)^2 [f_{\Omega}(E)(1 - f_{\Omega}(E)) + f_0(E)(1 - f_0(E))] dE \\ &+ \frac{2e^2}{\pi\hbar} \int_{-\infty}^{\infty} \tau(E)(1 - \tau(E)) [f_{\Omega}(E)(1 - f_0(E)) + f_0(E)(1 - f_{\Omega}(E))] dE, \end{aligned} \quad (4.4)$$

where  $V_{\text{qc}}$  is the dc voltage applied to the QPC 3. Each term of the integrand in the first integral of the right hand side of equation 4.4 is large only for energy close to

the voltage of the considered Fermi distribution, and becomes very small otherwise. Making the assumption that the value of  $\tau(E)$  is constant on the interval where the integrand is non-negligible, we replace  $\tau(E)$  by the fixed value  $\tau$  obtained from the measured differential conductance of the non-ballistic QPC. For the second integral in equation 4.4, the integrand is roughly constant for  $E \in [0, eV_{\text{qc}}]$  and vanishes exponentially outside this range. In this case, a more appropriate approximation is to replace  $\tau(E)$  by the dc conductance  $I/V_{\text{qc}}$ .

We display the total excess current noise as well as the theoretical prediction from equations 4.3 and 4.4 in figure 4.5 for  $R_{\text{env}} = R_K/2$  and figure 4.6 for  $R_{\text{env}} = R_K/3$ . We find, for both environments investigated here, a good agreement with the non-interacting theory.

We have to keep in mind that, here, we have injected the measured Coulomb renormalized conductance in the noise formula. In contrast, the TLL predictions give the complete behavior of the noise, without the need to inject the measured renormalized conductance.

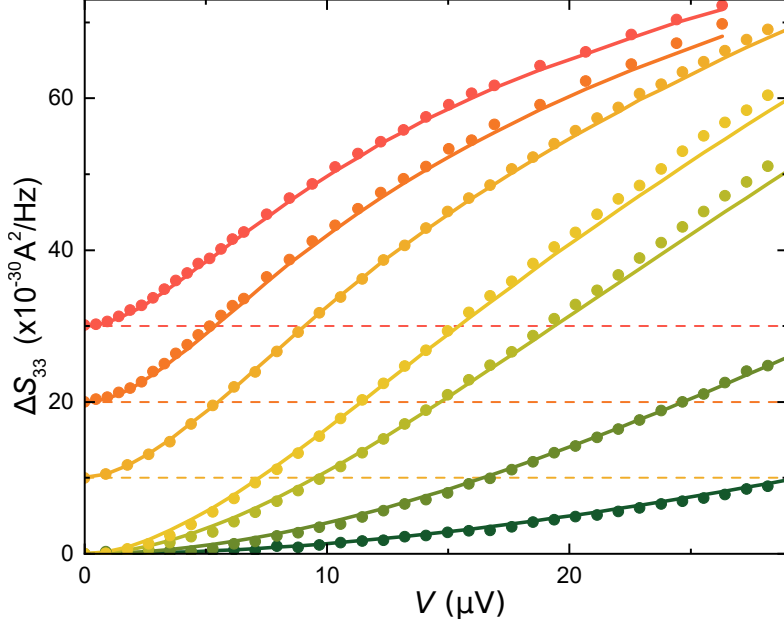


Figure 4.5: **Noise versus voltage for  $R_{\text{env}} = R_K/2$  ( $K = 2/3$ ).** The data points display the excess current noise  $S_{33}(V) - S_{33}(V = 0)$  versus the voltage for different tuning of the non-ballistic QPC. The lines display the predictions according to the scattering theory of noise. Offsets are added, indicated by the dashed lines, in order to improve the visibility.

### 4.2.3 Comparison of the measured current noise with prediction in the framework of the TLL mapping

Here, we will show that the voltage dependence of the noise is related to the voltage dependence of the conductance as predicted by the TLL theory. The current shot noise derivative by the voltage at  $T = 0$  is predicted to be related to the conductance by the following formula [17]:

$$\frac{1 - K}{eK^2} \frac{dS^{sn}}{dV} = \frac{dg}{d \ln V}, \quad (4.5)$$

where  $g = (G_s/K)R_K$  is the dimensionless conductance. Thus, this formula links the variation of the conductance by DCB to the variation of the noise. Furthermore, the right hand side of equation 4.5 is equal to the  $\beta$ -function describing the full

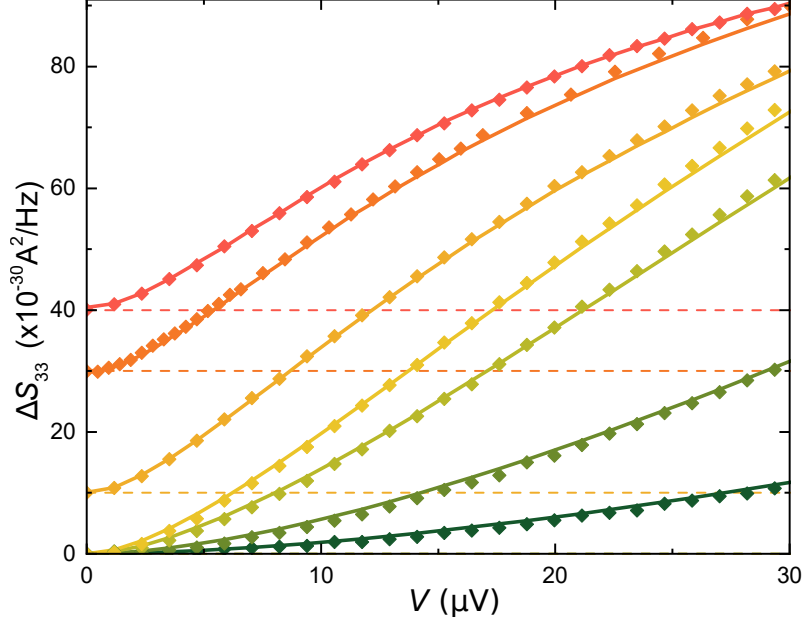


Figure 4.6: **Noise versus voltage for  $R_{\text{env}} = R_K/3$  ( $K = 3/4$ ).** The data points display the excess current noise  $S_{33}(V) - S_{33}(V = 0)$  versus the voltage for different tuning of the non-ballistic QPC. The lines display the prediction according to the scattering theory of noise. Offsets are added, indicated by the dashed lines, in order to improve the visibility.

scaling flow of the conductance crossover:

$$\frac{dg}{d \ln V} = \beta_K(g) \quad (4.6)$$

In order to investigate this relation, we display the discrete differentiation of the noise  $S_{33}$  by the voltage, times the factor  $(1 - K)/eK^2$ , as a function of the conductance in the figure 4.7, keeping only the data such that  $6k_B\bar{T} < eV < h/(6R_{\text{env}}C)$  (it is the same data as that displayed in figures 4.5 and 4.6). We also display the discrete differentiation of the dimensionless conductance,  $g = G_s/K$  in unit of  $e^2/h$ , by  $\ln(V)$  as colored lines, and the predicted  $\beta$ -function derived from the equations 3.27 as black line. Furthermore, we display the theoretical prediction from the scattering theory: the dashed lines in figure 4.7 displays  $\beta$ -functions-like derived using the relation 4.5 and the prediction from the scattering approach (at zero temperature),

keeping the conductance as voltage independent:

$$\begin{aligned} eK^2 \left( \frac{dS_{33}(V_{\text{qc}}, T = 0)}{dV} \right)_g &= \frac{1 - K}{eK^2} \left( \frac{d}{dV} \left[ 2eV_{\text{qc}}\tau(1 - \tau) \left( \frac{N}{N + \tau} \right)^2 \right] \right)_g \\ &= \frac{2(N - Kg)Kg(N(1 - Kg) - Kg)}{N^3}. \end{aligned} \quad (4.7)$$

Note that the non-interacting curve is very close to the TLL  $\beta$ -function: it explains the success of the scattering theory in our circuit despite the strong Coulomb interaction.

On the one hand, the conductance is found to follow the theoretical  $\beta$ -function, and this is not a surprise as it was already observed in figure 4.4. Note that the small deviations are more important in this representation. On the other hand, for both environments, we note that the noise data follow the theoretical  $\beta$ -function at low conductance, but detach from the theoretical curve as the conductance increases due to the resulting increase of heating. It can be quantitatively accounted for in the framework of the scattering theory: at non-zero temperature, the scattering approach gives the following relation for the noise:

$$\begin{aligned} S &= 2k_{\text{B}}(T_{\Omega} + T_0)/R_{\text{K}} \frac{G_{\text{s}}^2}{K} \\ &+ \left( \frac{N}{N + \tau} \right)^2 \frac{2e^2}{\pi\hbar} \int_{-\infty}^{\infty} \tau(E)(1 - \tau(E)) [f_{\Omega}(E)(1 - f_0(E)) + f_0(E)(1 - f_{\Omega}(E))] dE. \end{aligned} \quad (4.8)$$

This equation is calculated using equation 4.3 and equation 4.4, where we have replaced  $\tau(E)$  by  $\tau$  in the first integral on the right hand side. The standard approach for focusing on the  $\Delta V$ -shot noise is to focus on the excess noise, ignoring the thermal term. However, in our approach, when applying a voltage to the sample, we also heat up the central metallic island as a function of the voltage. Whereas the effect on the conductance is not overwhelming, it is the case for the noise where even in focusing on the excess noise, it has for effect to increase the first term in equation 4.8 (term which should be null at zero temperature). In the following we therefore subtract this term from the total noise, in order to investigate the shot noise versus voltage without being polluted by the temperature increase from the Joule effect, which would impede the comparison with the zero temperature prediction. Note that this thermal contribution at large voltage ( $eV \gg k_{\text{B}}T$ ) does not correspond

to the Johnson-Nyquist noise given by the fluctuation dissipation theorem (which is proportional to  $G_s$ , whereas the thermal contribution at large voltage is in  $G_s^2$ , see chapter 2). In figure 4.8 we display the result of this subtraction. When subtracting the thermal term of equation 4.8, the noise data fall down toward the predicted  $\beta$ -function as well as the experimental  $dg/d\ln V$ , experimentally highlighting the relation 4.5. However, the experimental resolution does not allow us to discriminate between the prediction from the non-interacting scattering theory (dashed lines) and the TLL predictions (full lines). In order to focus on the TLL relation between conductance variations and noise variations, we display in figure 4.9 the experimental  $dg/d\ln V$  versus  $[(1 - K)/eK^2] \times dS/dV$ , where we expect the points to follow the  $x = y$  line (black line).

Note that in the limit of weak back-scattering, it is expected that the noise is proportional to the charge of quasiparticles with fractional charge  $e^* = Ke$ . In principle, we may test this theoretical prediction for the data for which  $\tau$  is the closer to one. However, the shot noise signal is very weak compared to heating. Although the data seems consistent with  $e^* = Ke$  (not shown), further investigation is needed to ascertain a robust treatment of heating.

#### 4.2.4 Conclusion

In this section, we have investigated the current noise in an electronic dissipative quantum circuit. The motivation was to compare the noise measurement to the prediction for a Tomonaga Luttinger liquid with a single impurity. Remarkably, the theoretical prediction from the non-interacting scattering theory already constitutes a good approximation, provided the conductance renormalized by DCB is injected. In practice we do not have the experimental resolution for discriminating between the scattering theory as a function of renormalized conductance and the TLL predictions. However, in addition, the relation between voltage dependence of conductance and shot noise, which is a specific TLL prediction, could be established experimentally.

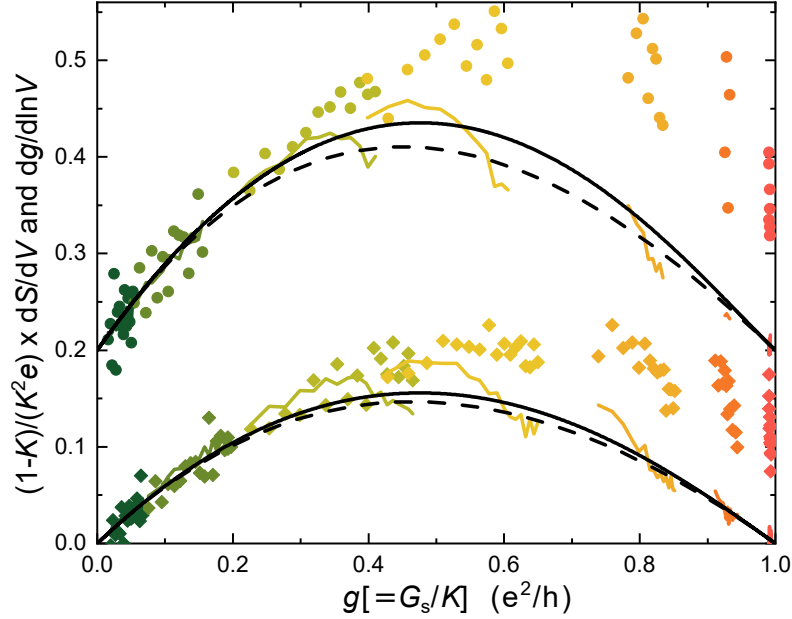


Figure 4.7: **Comparison with TLL beta function.** For a given setting of  $\tau$ , the full data points are a discrete voltage differentiation of the total noise times the factor  $(1 - K)/K^2e$ . The colored lines correspond to the measured  $dg/d\ln V$  with  $g = G_s/K$ . The TLL predictions are shown as full black lines. The dashed black lines display predictions from the scattering theory of noise (equation 4.7). For visibility, an offset of 0.2 is added to data and prediction corresponding to  $K = 2/3$ . The color code is the same as in the figure 4.2.

### 4.3 Shot noise induced by a temperature difference across a quantum point contact

#### 4.3.1 Previous measurements

Although predicted by the scattering theory of noise [13], a shot noise induced by a temperature gradient had never been measured until very recently [18]. In this paper, the authors investigate the noise specifically produced by a difference of temperature across an atomic contact. Although convincing, their measurements suffer from the fact that the number of open channels in the atomic contact is not ascertained. Here we perform measurements of this thermal shot noise through a



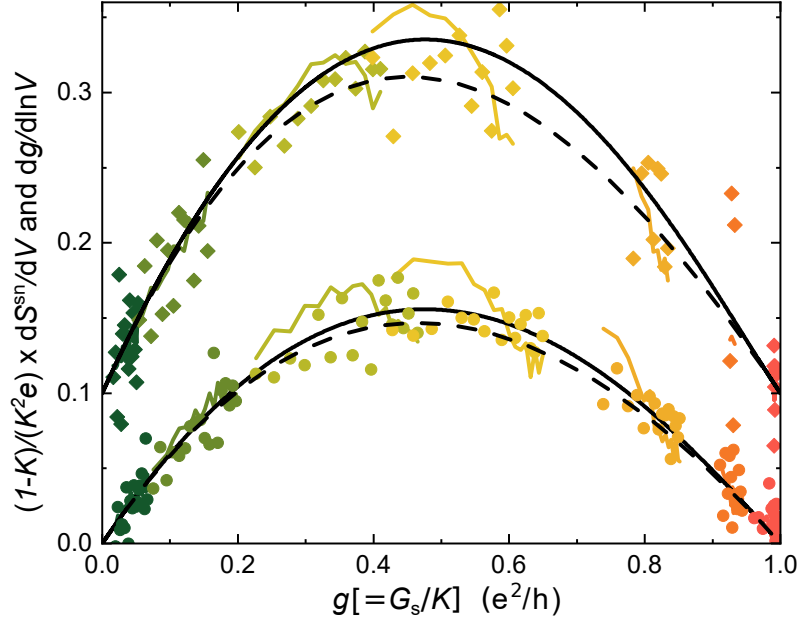


Figure 4.8: **Comparison of heatless noise with TLL beta function.** For a given setting of  $\tau$ , the full data points are a discrete voltage differentiation of the noise subtracted from the thermal term (see text), times the factor  $(1 - K)/K^2e$ . The colored lines correspond to the measured  $dg/d\ln V$  with  $g = G_s/K$ . The TLL predictions are shown as full black lines. The dashed black lines display predictions from the scattering theory of noise (equation 4.7). For visibility, an offset of 0.1 is added to data and prediction corresponding to  $K = 2/3$ . The color code is the same as in the figure 4.2.

single quantum channel with an adjustable transmission probability, using a QPC in the quantum Hall regime. We use the same configuration of the circuit as in the previous section, except for the voltage bias. A Joule power is injected through the ballistic channels connected to electrodes biased at voltages of opposite signs (electrodes  $S1$  and  $S2$  in figure 2.1), such that the average voltage of the metallic island remains null.

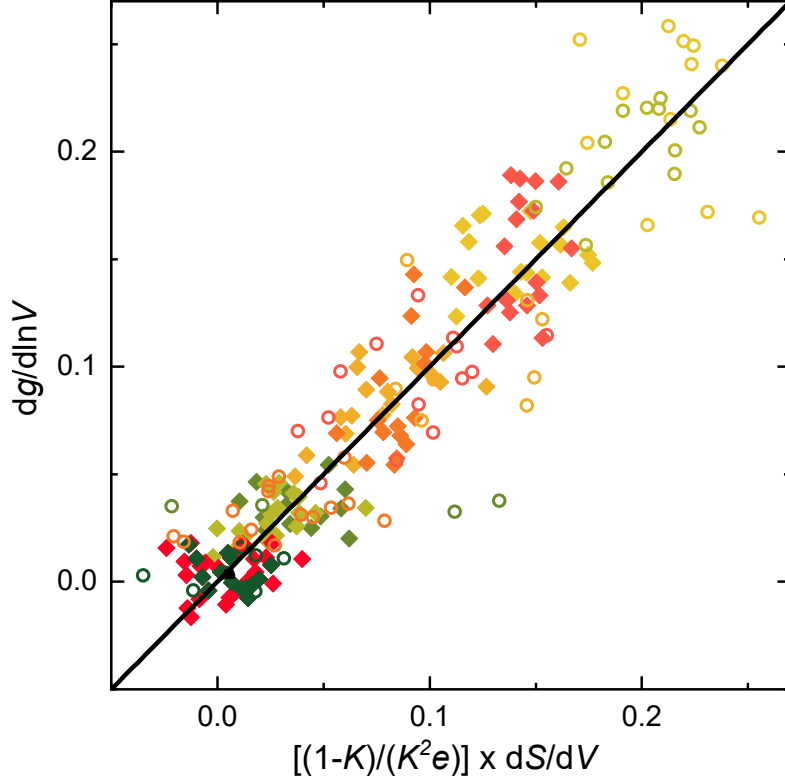


Figure 4.9:  $dg/d\ln V$  versus  $[(1-K)/eK^2] \times dS/dV$ . The open (full) points correspond to data for  $K = 2/3$  ( $K = 3/4$ ). The color code is the same as in the figure 4.2. The black lines correspond to the expected behavior  $dg/d\ln V = [(1-K)/eK^2] \times dS/dV$ .

### 4.3.2 Procedure for focusing on the $\Delta T$ -shot noise

The extraction of the island's temperature is performed in the same way as in the previous section, using equation 2.30 for different tunings of the non-ballistic QPC. We extract the excess noise source across the non-ballistic QPC using the equations 2.31 in chapter 3:

$$\Delta S_{\text{qpc}} = (N + 2\tau) \left( \frac{\Delta S_{11}}{2n_1} + \frac{\Delta S_{22}}{2n_2} \right) + \Delta S_{12} \frac{(N + \tau)^2 + \tau^2}{2n_1 n_2}, \quad (4.9)$$

with  $\Delta S_{11}$  ( $\Delta S_{22}$ ) the excess spectral density measured in electrodes 1 (2) and  $\Delta S_{12}$  the excess cross-correlations.  $\Delta S_{\text{qpc}}$  includes two contributions: the Johnson-Nyquist noise involving the average temperature of the electrodes 3 and the metallic

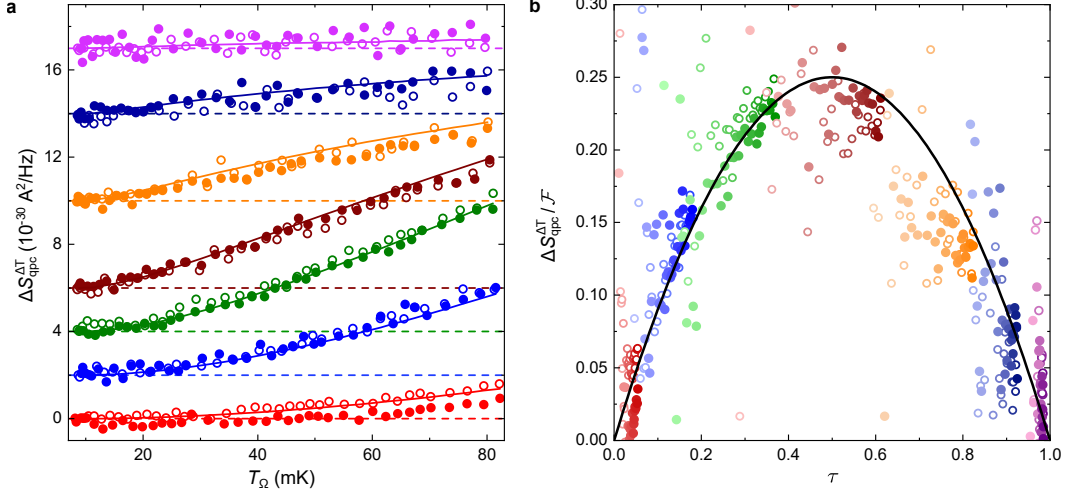


Figure 4.10:  $\Delta T$ -shot noise. Left panel: symbols represent the experimental QPC noise at  $N = 2$  from which the average thermal noise was removed. Measurements at different gate voltage tunings of the QPC are shifted vertically, with the applied offsets shown as horizontal dashed lines. Open and full symbols distinguish separate sequences of measurements. Continuous lines display predictions of equation 4.11. Right panel: the  $\tau(1 - \tau)$  partition signature is shown as a continuous line versus  $\tau$ . Symbols represent the experimental QPC noise from which the average thermal noise was removed, divided by the  $\tau$ -independent functions  $\mathcal{F}(T_\Omega, T_0)$ , which is the predicted thermal shot noise’s temperature dependence. A lighter (darker) symbol coloring indicates a small (large)  $T_\Omega - T_0$  corresponding to a higher (lower) experimental uncertainty.

island, and the thermal shot noise associated with the temperature difference. Following [18], we focus on the thermal shot noise by subtracting the “excess” Johnson-Nyquist noise given by the standard fluctuation dissipation formula:

$$\Delta S_{\text{qpc}}^{\Delta T} = \Delta S_{\text{qpc}} - 2k_{\text{B}}(T_\Omega - T_0)\tau/R_{\text{K}}, \quad (4.10)$$

For a base temperature of  $T_0 \approx 8\text{mK}$ , we display the result  $\Delta S_{\text{qpc}}^{\Delta T}$  in the left panel of the figure 4.10, adding offsets in order to distinguish each measurement. The colored lines correspond to the theoretical predictions of the scattering theory for the thermal shot noise, given by:

$$\Delta S_{\text{qpc}}^{\text{thy}} = \frac{2e^2}{\pi\hbar} \tau(1 - \tau) \int (f_0(E) - f_\Omega(E))^2 dE, \quad (4.11)$$

with  $f_0$  and  $f_\Omega$  the Fermi distribution of the electrons in the cold electrodes at temperature  $T_0$  and in the hot metallic island at temperature  $T_\Omega$  respectively, and where  $\tau$  is obtained from the simultaneously measured differential conductance renormalized by the DCB (note that  $I/V = dI/dV$  since there is no voltage bias applied to the non-ballistic QPC). The integration is performed numerically. We note that the predictions closely match the data. In the right panel of the figure 4.10 the data points represent the experimental shot noise renormalized by the predicted  $\tau$ -independent temperature function  $\mathcal{F} = \frac{2e^2}{\pi h} \int (f_0(E) - f_\Omega(E))^2 dE$ . In this panel, a lighter (darker) symbol coloring indicates a small (large)  $T_\Omega - T_0$  corresponding to a higher (lower) experimental uncertainty. The good agreement with  $\tau(1 - \tau)$  (black line) attests the partition origin of this shot noise induced by a difference of temperature.

We performed control measurements for other values of  $N$  ( $N = 3$  and  $N = 4$ ), shown in figure 4.11, where both demonstrate a good agreement with theoretical predictions. The measurements are also shown for a larger base temperature  $T_0 \approx 16$  mK in figure 4.12.

### 4.3.3 Conclusion

In this section, we have investigated the shot noise across a non-ballistic channel resulting from a pure thermal bias. A good agreement is observed with the scattering theory of noise [13], as also recently shown using an atomic contact [18], and despite the Coulomb renormalization of the conductance in our specific case. Our understanding of the non-equilibrium thermal noise will make it possible to address heat and noise in more complex quantum systems.

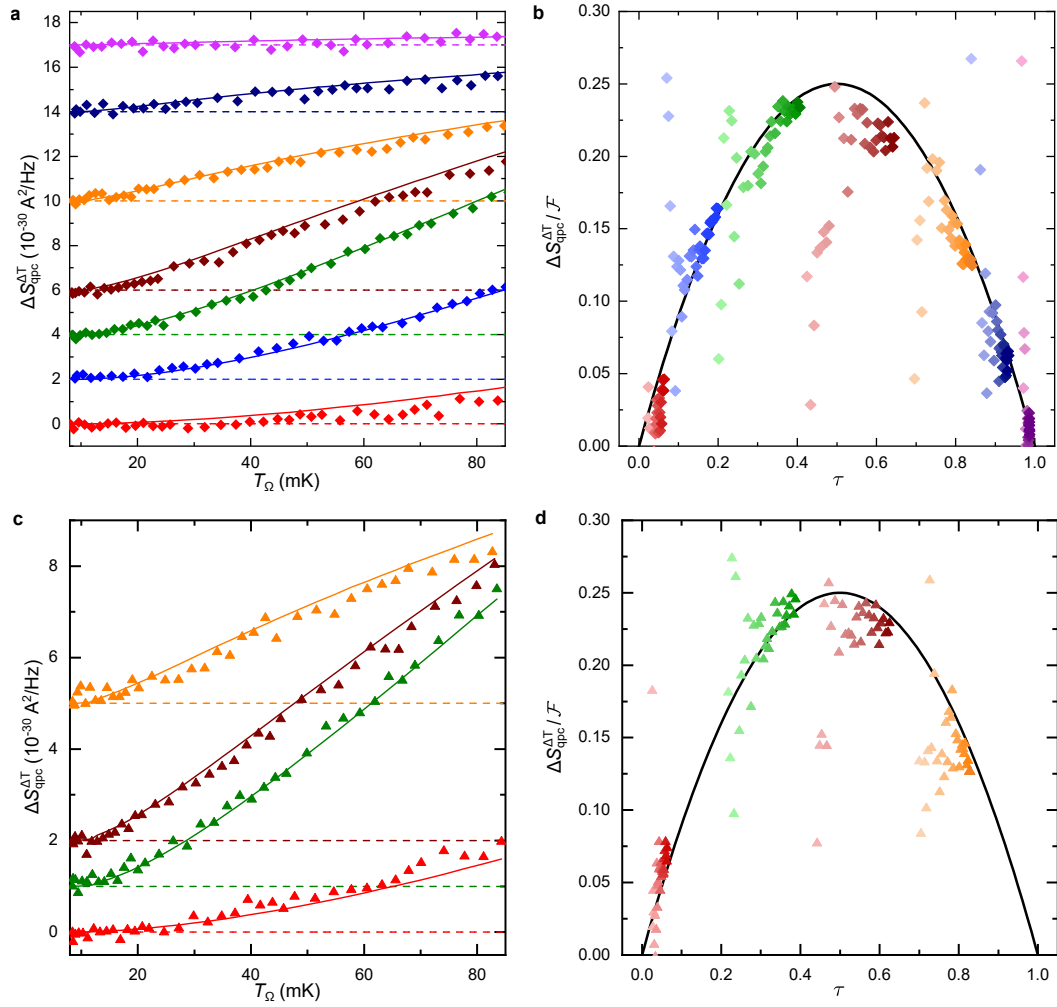


Figure 4.11: Control measurement for  $N = 3$  and  $N = 4$  at base temperature  $T_0 \approx 8$  mK.

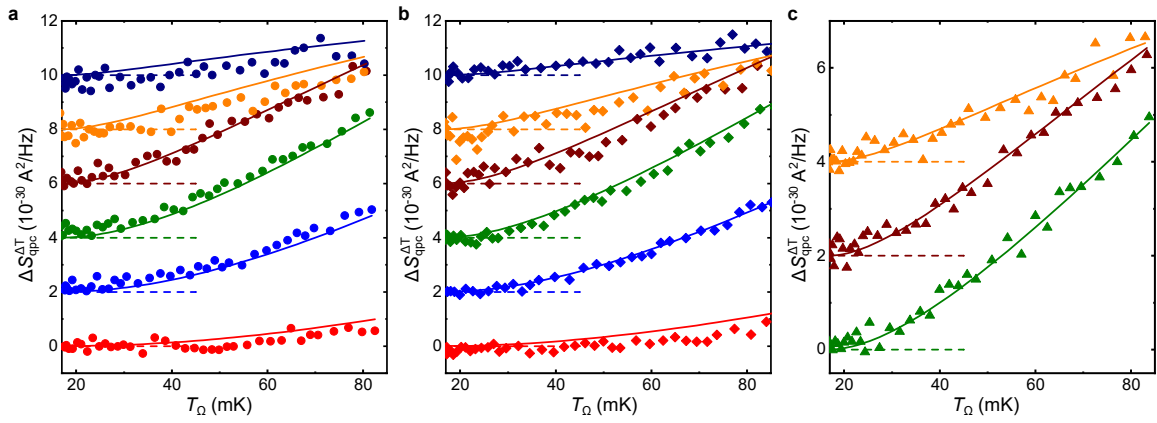


Figure 4.12: Control measurement at higher base temperature ( $T_0 \approx 16$  mK) for  $N = 2, 3$  and  $4$ .



# Chapter 5

## Electronic heat flow in a composite quantum circuit

### Contents

---

<b>5.1</b>	<b>Introduction</b>	<b>89</b>
<b>5.2</b>	<b>Electronic heat flow through quantum circuits</b>	<b>90</b>
5.2.1	Heat flow across a short quantum channel connected to large reservoirs	90
<b>5.3</b>	<b>Predictions for heat flow in composite quantum-circuits</b>	<b>92</b>
5.3.1	Heat Coulomb blockade prediction	92
5.3.2	Heat evacuation by electron-phonon coupling	100
<b>5.4</b>	<b>Observation of the electronic heat flow in a ballistic circuit</b>	<b>102</b>
5.4.1	Procedure to investigate heat flow	102
5.4.2	Experimental procedure	102
5.4.3	Observation of the heat Coulomb blockade of one ballistic channel on the electronic heat flow	104
5.4.4	Crossover from $(N - 1) \times J_Q^{\text{el}}$ to $N \times J_Q^{\text{el}}$	106
5.4.5	Electron-phonon coupling	108
5.4.6	Comparison of the theory with the raw noise data	110



5.4.7	Discussion about the heat Coulomb blockade of one ballistic channel . . . . .	111
<b>5.5</b>	<b>Observation of the electronic heat flow in a non-ballistic quantum circuit . . . . .</b>	<b>114</b>
5.5.1	Focusing on the electronic heat flow . . . . .	114
5.5.2	Results . . . . .	114
5.5.3	Comparison with predicted deviations from a Wiedemann-Franz increase of $J_Q$ . . . . .	117
<b>5.6</b>	<b>Conclusion . . . . .</b>	<b>119</b>

---

## 5.1 Introduction

In this chapter, we investigate the effect of Coulomb interaction upon the heat flow in a small quantum circuit. As the size of the sample and temperature of electrons decrease, quantum mechanics and Coulomb interaction become preponderant. As already seen in the previous chapter, the classical laws of electrical impedance composition may not apply anymore and we need to discover the new laws of electricity [20; 80]. The improvement in the experimental control of small circuit allow one now to investigate the heat flow at the nano-scale [6; 8; 81; 82]. Note also the recent measurement of fundamental temperature fluctuations in [83].

Here, we investigate the electronic heat flow, from a small metallic island of relatively important Coulomb charging energy, through several electronic quantum channels toward large cold reservoirs.

- First, we conduct this experiment in the case where all the channels are ballistic. For  $N = 1, 2, 3, 4$  and 5 ballistic channels connecting the metallic island, we directly observe the systematic heat Coulomb blockade of one ballistic channel at low temperature while the electrical conductance is unaffected (no blockade)[84], as recently predicted by theory [19].
- Then we investigate the electronic heat flow beyond the ballistic limit, with a controlled back-scattering in one of the channels. We observe an additional mechanism of the electronic heat flow, which involves both the Coulomb interaction and the shot noise through the non-ballistic channel.

## 5.2 Electronic heat flow through quantum circuits

### 5.2.1 Heat flow across a short quantum channel connected to large reservoirs

The heat flow through a quantum conductor connecting two large reservoirs, as represented in figure 5.1, can be calculated using the scattering theory [85; 86]. For a single quantum channel of an energy independent arbitrary transmission probability  $\tau$ , connecting two reservoirs with Fermi distribution  $f_L(E - eV_L, T_L)$  and  $f_R(E - eV_R, T_R)$  for the left and right reservoir respectively, the net heat current in reservoir R is given by (equation 16c in reference [85]):

$$\begin{aligned} J &= \frac{\tau}{h} \int (E - eV_R)(f_L(E - eV_L) - f_R(E - eV_R)) dE \\ &= \tau \frac{(V_R - V_L)^2}{2R_K} + \tau \frac{\pi^2 k_B^2}{6h} (T_L^2 - T_R^2) \end{aligned}$$

The first term is the Joule power dissipated when the channel is biased with a voltage  $\Delta V = V_R - V_L$ . The factor of 1/2 with respect to the total Joule power  $\Delta VI$  is because only one of the reservoirs is considered here. The second term is the heat flow  $J_{heat}$  which results from the difference of temperature  $\Delta T = T_L - T_R$  between the two reservoirs, and which can be related to the thermal conductance:

$$G^{th} = \lim_{\Delta T \rightarrow 0} J_{heat}/\Delta T = \pi^2 k_B^2 T \tau / 3h$$

The multi-channel case may be obtained by simply adding contributions of each independent channel. To my knowledge, a quantitative measurement of the heat flow in a simple QPC with an arbitrary transmission  $\tau \in ]0, 1[$  has never been reported before. Note however that relative variations of the thermal conductance, up to an unknown prefactor, were probed in [87], and an order of magnitude estimate was previously performed in [88].

#### Wiedemann-Franz law

Remarkably, the quantum result above for a non-interacting single channel is in agreement with the Wiedemann-Franz law broadly observed in classical conductor,

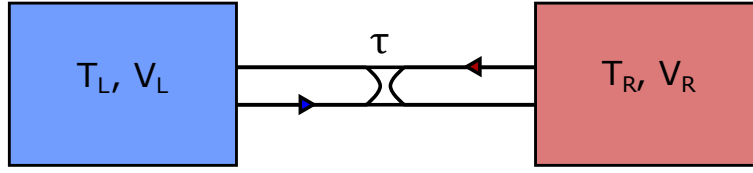


Figure 5.1: A single channel quantum conductor of electron transmission probability  $\tau$  connecting two large reservoirs, each of them characterized by a voltage and a temperature.

which states that the ratio between the electrical conductivity and the thermal conductivity in conductors is proportional to the temperature:

$$\frac{G_{\text{th}}}{G_{\text{el}}} = LT.$$

The proportionality constant  $L$ , called Lorenz number, is equal to:

$$L = \frac{\pi^2}{3} \left( \frac{k_{\text{B}}}{e} \right)^2.$$

### Quantum limit of heat flow

For a non-interacting ballistic quantum channel ( $\tau = 1$ ) the heat flow reaches the quantum limit of heat flow through a quantum conductor [82; 85; 86]:

$$J_{\text{Q}}^{\text{el}} = \frac{\pi^2 k_{\text{B}}^2}{6h} (T_{\text{L}}^2 - T_{\text{R}}^2). \quad (5.1)$$

In the same way as the quantum of electrical conductance, the quantum of thermal conductance  $G_{\text{Q}} = \pi^2 k_{\text{B}}^2 / 3h$  does not depend on the material constituting the conductor. Moreover, the quantum of thermal conductance is predicted [89] and measured to be the same for phonons [90], photons [91], and electrons [82]. However, we note the observation of half-integer thermal Hall conductance in the fractional quantum Hall regime at a filling factor  $\nu = 5/2$  [92], which may indicate the presence of non-abelian anyons at this particular filling factor.

## 5.3 Predictions for heat flow in composite quantum-circuits

In our device, we assume that heat is evacuated by two mechanisms: by electrons through the electronic channels and by the electron-phonon interaction in the metallic island,  $J_{\text{thy}}^{\text{heat}} = J_{\text{thy}}^{\text{el}} + J_{\text{thy}}^{\text{el-ph}}$ . In the work presented here we are interested in the first one: the electronic heat flow  $J_{\text{thy}}^{\text{el}}$ . Here we start by deriving the theoretical prediction for the electronic heat flow in the presence of Coulomb interaction. Then we will address the heat flow toward the cold phonons.

### 5.3.1 Heat Coulomb blockade prediction

In this section we derive the predictions for the electronic heat flow out-going from the metallic island through  $N$  ballistic channels and an additional channel of arbitrary transmission probability  $\tau \in [0, 1]$ . We use the same approach as the one used in [19] for ballistic systems. In Ref. 19, it is shown that the expressions of the currents found using the bosonization technique can be recovered using the semi-classical Langevin approach. Here we will use the Langevin approach. The idea of the derivation is as following:

- for each channel, we formulate the heat current in terms of high frequency electrical current fluctuations [19]. The current fluctuations in the circuit have for origin uncorrelated noise sources of thermal and partition origins;
- to derive the electrical current fluctuations in each channel, we need also to consider the charge and subsequent RC discharge of the metallic island. We first express the charge fluctuation  $\delta Q$  as a function of the uncorrelated noise sources;
- then, the electronic heat flow in each channel is calculated including the discharge current fluctuations  $\delta V_{\Omega}/R_K$  with  $\delta V_{\Omega} = \delta Q/C$ .

We first detail the calculation for ballistic channels where there is no partition noise, and subsequently for the non-ballistic channel where we need to consider the partition noise.

**Link between electronic heat flow and current fluctuations in a quantum channel**

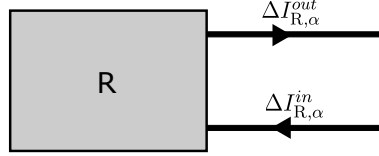


Figure 5.2: A reservoir  $R$  is connected to a quantum edge channel  $\alpha$ . The outgoing current fluctuations are denoted  $\Delta I_{R,\alpha}^{out}$ , and the in-going one are denoted  $\Delta I_{R,\alpha}^{in}$ .

The current fluctuations  $\Delta I_{R,\alpha}^{out}$  outgoing from a floating reservoir  $R$  of capacitance  $C$  in a chiral quantum channel  $\alpha$  (see figure 5.2) are given by:

$$\Delta I_{R,\alpha}^{out} = \delta I_{R,\alpha}^{th} + \frac{\delta Q}{R_K C}. \quad (5.2)$$

In this equation, the first term on the right side is a current Langevin source corresponding to the thermal electrons emitted from the reservoir  $R$  into the channel  $\alpha$ . In the following we assume that the thermal current Langevin source associated with different reservoirs or/and channels are uncorrelated ( $\langle \delta I_{R,\alpha}^{th} \delta I_{R',\alpha'}^{th} \rangle = 0$  if  $\alpha \neq \alpha'$  or  $R \neq R'$ ). The second term results from the fluctuation of the overall charge  $\delta Q$  of the reservoir. Note that voltage biased electrodes can be modeled by very large capacitances such that  $\delta Q/R_K C \rightarrow 0$ . The current noise spectral density associated with the thermal current fluctuations  $\delta I_{R,\alpha}^{th}$  emitted from a reservoir  $R$  at temperature  $T$  is given by [19]:

$$S_{R,\alpha}^{th}(\omega) = \frac{\hbar\omega/R_K}{-1 + \exp[\hbar\omega/k_B T]}. \quad (5.3)$$

In the following, in order to lighten the notation we replace  $S_{R,\alpha}^{th}(\omega)$  by  $S^{th}(T)$ . Note that this expression is the full, frequency dependent quantum noise, needed to compute the flow of heat (equation 5.4), in contrast with the low frequency relation used in the chapter 2 for the noise measured in the low-frequency MHz range ( $\hbar \times 1 \text{ MHz}/k_B \approx 50 \mu\text{K} \ll T$ ). Because of the chirality, a factor of 2 is missing compared to the relation 2.4 presented in the chapter 2. The heat flow propagating along the chiral channel, where the current  $\Delta I_{R,\alpha}^{out}$  is injected, is determined by integrating the

resulting current noise spectral density  $S_{R,\alpha}^{out}(\omega)$  [19]:

$$J_{R,\alpha}^{out} = \frac{\hbar}{2e^2} \int_{-\infty}^{\infty} [S_{R,\alpha}^{out}(\omega) - S_{\text{vacuum}}(\omega)] d\omega, \quad (5.4)$$

with  $S_{\text{vacuum}}(\omega)$  the vacuum fluctuations at zero temperature. In the same way, the incoming heat flow injected in the contact  $R$  from the channel  $\alpha$  is determined by integrating the current noise spectral density  $S_{R,\alpha}^{in}(\omega)$  associated with the incoming current fluctuations  $\Delta I_{R,\alpha}^{in}$ :

$$J_{R,\alpha}^{in} = \frac{\hbar}{2e^2} \int_{-\infty}^{\infty} [S_{R,\alpha}^{in}(\omega) - S_{\text{vacuum}}(\omega)] d\omega, \quad (5.5)$$

The net electronic heat flow out going from the reservoir  $R$  by the channel  $\alpha$  is then:

$$J_{\alpha}^{\text{el}} = J_{R,\alpha}^{out} - J_{R,\alpha}^{in} \quad (5.6)$$

For one ballistic channel connecting two reservoirs at temperatures  $T_L$  and  $T_R$  (for left and right reservoirs), the calculation of the net electronic heat flow leads to  $J^{\text{el}} = \frac{\pi^2 k_B^2}{6h} (T_L^2 - T_R^2)$ , recovering the quantum limit of heat flow  $J_Q^{\text{el}}$  defined in equation 5.1. The additional channel of transmission probability  $\tau \in [0, 1]$  brings about a few differences in comparison to the calculation performed in reference [19]: the symmetry between channels is broken and a partition noise emerges at the channel of transmission  $\tau$  when  $\tau \neq 0$  and 1. Note also that the in-situ transmission probability  $\tau$  depends on the temperatures due to dynamical Coulomb blockade. In practice we assume it is independent of the frequency and equal to the measured renormalized transmission probability.

### The island's charge fluctuations

In the following, we are considering the complete device used throughout this thesis (see a graphical representation in figure 5.3). The floating metallic island, labeled  $\Omega$ , is characterized by a temperature  $T_{\Omega}$ . The other electrodes, labeled  $E$ , are all large and at the same temperature  $T_0$  (as the other contacts are all voltage biased and at the same temperature  $T_0$ , it is equivalent to consider only one contact  $E$ ). Charge conservation allows us to determine the fluctuation  $\delta Q$  of the charge of the floating island:

$$i\omega\delta Q = \Delta I^{in} - \Delta I^{out}, \quad (5.7)$$

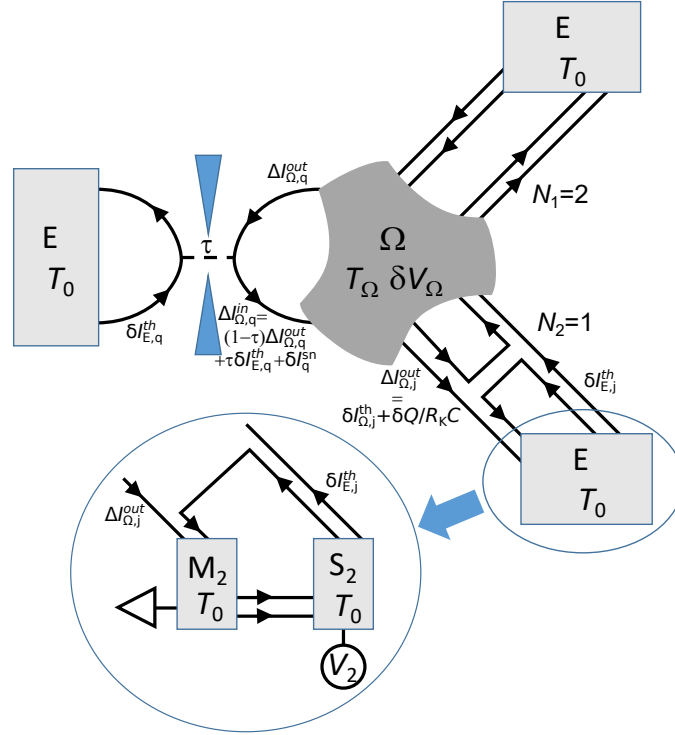


Figure 5.3: **Noise schematic.** Graphical representation of the different current and voltage fluctuations involve in the derivation of the heat flow.

with  $\Delta I^{in}$  and  $\Delta I^{out}$ , respectively, the total incoming and outgoing current fluctuations (summed over all channels). The corresponding island's voltage fluctuations  $\delta Q/C$  result in the emission of current fluctuations  $\delta Q/R_K C$  in each connected channel, which contribute to  $\Delta I^{out}$ :

$$\Delta I^{out} = \sum_{j=1}^N \delta I_{\Omega,j}^{th} + \delta I_{\Omega,q}^{th} + (N+1) \frac{\delta Q}{R_K C}, \quad (5.8)$$

with  $N$  the number of ballistic channels and  $q$  labeling the single non-ballistic channel. It also shows up in  $\Delta I^{in}$ , because of the  $(1-\tau)$  fraction of the current reflected at the non-ballistic QPC:

$$\Delta I^{in} = \sum_{j=1}^N \delta I_{E,j}^{th} + \tau \delta I_{E,q}^{th} + (1-\tau) \left[ \delta I_{\Omega,q}^{th} + \frac{\delta Q}{R_K C} \right] + \delta I_q^{sn}. \quad (5.9)$$

Note that  $\Delta I^{in}$  also includes an additional shot noise contribution  $\delta I_q^{sn}$  from the non-ballistic channel, as further discussed in the section “current fluctuations in the



non-ballistic channel". We now introduce  $\tau_\Omega$ , defined as the sum of the transmission probabilities of all the channels connected to the island:

$$\tau_\Omega = N + \tau.$$

Injecting equations 5.8 and 5.9 in equation 5.7, we deduce the charge variation as a function of the uncorrelated noise sources ( $\delta I_{E,j}^{th}$ ,  $\delta I_{\Omega,j}^{th}$ ,  $\delta I_q^{sn}$ ):

$$\frac{\delta Q}{R_K C} = \frac{1}{i\omega R_K C + \tau_\Omega} \left[ \sum_{j=1}^N (\delta I_{E,j}^{th} - \delta I_{\Omega,j}^{th}) + \tau (\delta I_{E,q}^{th} - \delta I_{\Omega,q}^{th}) + \delta I_q^{sn} \right]. \quad (5.10)$$

### Current fluctuations along the ballistic channels

The current fluctuations in-coming into the island from a ballistic channel  $j$  are equal to the current fluctuations emitted in this channel from electrode  $E$ , and they involve only thermal fluctuations:

$$\Delta I_{\Omega,j}^{in} = \delta I_{E,j}^{th}. \quad (5.11)$$

The corresponding current spectral density is:

$$S_{\Omega,j}^{in} \equiv \langle (\Delta I_{\Omega,j}^{in})^2 \rangle (\omega) = S^{th}(T_0), \quad (5.12)$$

with  $S^{th}(T_0)$  given equation 5.3. The current fluctuations out-going from the island  $\Omega$  in a ballistic channel  $j$  are given by:

$$\Delta I_{\Omega,j}^{out} = \delta I_{\Omega,j}^{th} + \frac{\delta Q}{R_K C}, \quad (5.13)$$

where we consider the voltage fluctuation of the metallic island. The corresponding current spectral density obtained using the expression of  $\delta Q$  given equation 5.10 is:

$$\begin{aligned} S_{\Omega,j}^{out} \equiv \langle (\Delta I_{\Omega,j}^{out})^2 \rangle (\omega) &= S^{th}(T_\Omega) - \frac{2\tau_\Omega}{(\omega R_K C)^2 + \tau_\Omega^2} [S^{th}(T_\Omega)] \\ &+ \frac{1}{(\omega R_K C)^2 + \tau_\Omega^2} [(\tau_\Omega - \tau(1 - \tau)) (S^{th}(T_\Omega) + S^{th}(T_0)) + S^{sn}] \end{aligned} \quad (5.14)$$

where we have introduced  $S^{sn} \equiv \langle (\Delta I_q^{sn})^2 \rangle (\omega)$ .

### Current fluctuations along the non-ballistic channel

(i) Current fluctuations in the  $\Omega$  side of the non-ballistic QPC

The current fluctuations in-going into the metallic island from the non-ballistic channel  $q$  are given by:

$$\Delta I_{\Omega,q}^{in} = \tau \delta I_{E,q}^{th} + (1 - \tau) \delta I_{\Omega,q}^{th} + (1 - \tau) \frac{\delta Q}{R_K C} + \delta I_q^{sn}, \quad (5.15)$$

where we have added the additional Langevin source  $\delta I_q^{sn}$  coming from the electrons partition. The corresponding spectral density obtained using the expression of  $\delta Q$  given equation 5.10 is:

$$\begin{aligned} S_{\Omega,q}^{in} &\equiv \langle (\Delta I_{\Omega,q}^{in})^2 \rangle (\omega) = \tau^2 S^{th}(T_0) + (1 - \tau)^2 S^{th}(T_\Omega) \\ &\quad + \frac{(1 - \tau)^2}{(\omega R_K C)^2 + \tau_\Omega^2} [(\tau_\Omega - \tau(1 - \tau))(S^{th}(T_\Omega) + S^{th}(T_0)) + S^{sn}] \\ &\quad + \frac{2(1 - \tau)\tau_\Omega}{(\omega R_K C)^2 + \tau_\Omega^2} [\tau S^{th}(T_0) - \tau(1 - \tau)(S^{th}(T_\Omega) + S^{th}(T_0)) + S^{sn}] \\ &\quad + S^{sn}. \end{aligned} \quad (5.16)$$

The current fluctuations out-going from the island  $\Omega$  in the non-ballistic channel  $q$  (before reaching the quantum point contact) are given by:

$$\Delta I_{\Omega,q}^{out} = \delta I_{\Omega,q}^{th} + \frac{\delta Q}{R_K C} \quad (5.17)$$

The corresponding current spectral density obtained is:

$$\begin{aligned} S_{\Omega,q}^{out} &\equiv \langle (\Delta I_{\Omega,q}^{out})^2 \rangle (\omega) = S^{th}(T_\Omega) - \frac{2\tau_\Omega}{(\omega R_K C)^2 + \tau_\Omega^2} [\tau S^{th}(T_\Omega)] \\ &\quad + \frac{1}{(\omega R_K C)^2 + \tau_\Omega^2} [(\tau_\Omega - \tau(1 - \tau))(S^{th}(T_\Omega) + S^{th}(T_0)) + S^{sn}] \end{aligned} \quad (5.18)$$

In principle, the knowledge of  $S_{\Omega,q}^{in}$  and  $S_{\Omega,q}^{out}$  is sufficient to calculate the net heat flow from equations 5.4, 5.5 and 5.6. However, as detailed in the next section, we also need to compute the current fluctuations on the other side of the QPC in order to straightforwardly determine  $S^{sn}$ .

(ii) Current fluctuations in the  $E$  side of the non-ballistic QPC

The transmitted current through the non-ballistic channel  $q$  impinging upon the electrodes  $E$  on the  $E$  side of the QPC is:

$$\Delta I_{E,q}^{in} = \tau \delta I_{\Omega,q}^{th} + (1 - \tau) \delta I_{E,q}^{th} - \delta I_q^{sn} + \tau \frac{\delta Q}{R_K C} \quad (5.19)$$

The associated current spectral density is given by:

$$\begin{aligned} S_{E,q}^{in} &\equiv \langle (\Delta I_{E,q}^{in})^2 \rangle (\omega) = \tau^2 S^{th}(T_\Omega) + (1 - \tau)^2 S^{th}(T_0) + S^{sn} \\ &\quad + \frac{2\tau\tau_\Omega}{(\omega R_K C)^2 + \tau_\Omega^2} \left[ -\tau S^{th}(T_\Omega) + \tau(1 - \tau) (S^{th}(T_0) + S^{th}(T_\Omega)) - S^{sn} \right] \\ &\quad + \frac{\tau^2}{(\omega R_K C)^2 + \tau_\Omega^2} \left[ (\tau_\Omega - \tau(1 - \tau)) (S^{th}(T_\Omega) + S^{th}(T_0)) + S^{sn} \right] \end{aligned} \quad (5.20)$$

The current out-going from the electrodes  $E$  is simply given by:

$$\Delta I_{E,q}^{out} = \delta I_{E,q}^{th} \quad (5.21)$$

The associated current spectral density is given by:

$$S_{E,q}^{out} \equiv \langle (\Delta I_{E,q}^{out})^2 \rangle (\omega) = S^{th}(T_0) \quad (5.22)$$

### Determination of $S^{sn}$

In the equations above, the only missing ingredient is the ‘‘shot noise’’  $S^{sn}$ . The required knowledge can be determined from global heat conservation:

$$J_q^{el} = J_{\Omega,q}^{out} - J_{\Omega,q}^{in} = J_{E,q}^{in} - J_{E,q}^{out} \quad (5.23)$$

Using equations 5.4,5.5,5.16,5.18 and 5.20,5.22, this condition imposes that:

$$\begin{aligned} \int_{-\infty}^{\infty} S^{sn} \times \left[ 1 + \frac{\tau_\Omega - \tau(1 - \tau) - 2\tau\tau_\Omega}{(\omega R_K C)^2 + \tau_\Omega^2} \right] d\omega = \\ \int_{-\infty}^{\infty} \tau(1 - \tau) \times \left[ 1 + \frac{\tau_\Omega - \tau(1 - \tau) - 2\tau\tau_\Omega}{(\omega R_K C)^2 + \tau_\Omega^2} \right] \times (S^{th}(T_\Omega) + S^{th}(T_0)) d\omega. \end{aligned} \quad (5.24)$$

This condition does not give the full shot noise, but only the part of the shot noise relevant for the calculation of the electronic heat flow. Note that this result is the same for a single channel without interaction.

### Net out-going electronic Heat flow

The net out-going heat flow through all the channels, using the previous equations (5.3, 5.4, 5.5, 5.12, 5.14, 5.16, 5.18, and 5.24), can be written as:

$$\begin{aligned}
 J_{\text{thy}}^{\text{el}} &= \sum_{j=1}^{N+1} (J_{\Omega,j}^{\text{out}} - J_{\Omega,j}^{\text{in}}) \\
 &= \tau_{\Omega} \frac{\pi^2 k_{\text{B}}^2}{6h} (T_{\Omega}^2 - T^2) - \tau_{\Omega} \frac{h(\tau_{\Omega} - \tau(1 - \tau))}{(2\pi R_{\text{K}} C)^2} \left[ \mathfrak{S} \left( \frac{h\tau_{\Omega}/R_{\text{K}} C}{2\pi k_{\text{B}} T_{\Omega}} \right) - \mathfrak{S} \left( \frac{h\tau_{\Omega}/R_{\text{K}} C}{2\pi k_{\text{B}} T} \right) \right],
 \end{aligned} \tag{5.25}$$

where we recall that  $\tau_{\Omega} = N + \tau$ , and with the function  $\mathfrak{S}$  given by:

$$\begin{aligned}
 \mathfrak{S}(x) &= \int_0^{\infty} \frac{z}{z^2 + x^2} \frac{1}{\exp(z) - 1} dz \\
 &= \frac{1}{2} \left[ \ln \left( \frac{x}{2\pi} \right) - \frac{\pi}{x} - \psi \left( \frac{x}{2\pi} \right) \right],
 \end{aligned} \tag{5.26}$$

with  $\psi(z)$  the digamma function. At  $\tau = 0$  or 1, Eq. 5.25 reduces to the expression derived for a ballistic system [19].

### Asymptotic behavior in ballistic case ( $\tau = 0, 1$ )

The function  $\mathfrak{S}$  has the asymptotic forms:

$$\mathfrak{S}(x \ll 1) \simeq \frac{\pi}{2x}, \quad \mathfrak{S}(x \gg 1) \simeq \frac{\pi^2}{6x^2},$$

with a crossover centered on  $x \approx 1$ . Note that the crossover from one asymptote to the other depends thus of the number of channels connected to the metallic island. At  $T, T_{\Omega} \ll NE_C/\pi k_{\text{B}}$  ( $x \gg 1$ ), Eq. 5.25 with  $\tau = 0$  therefore reduces to

$$J_{\text{thy}}^{\text{el}} \simeq (N - 1) \frac{\pi^2 k_{\text{B}}^2}{6h} (T_{\Omega}^2 - T_0^2) = (N - 1) \times J_{\text{Q}}^{\text{el}}, \tag{5.27}$$

with precisely one electronic ballistic channel effectively suppressed for heat conduction, whatever the total number  $N$  of ballistic channels.

At  $NE_C/\pi k_{\text{B}} \ll T_0, T_{\Omega}$  ( $x \ll 1$ ), Eq. 5.25 at  $\tau = 0$  becomes

$$J_{\text{thy}}^{\text{el}} \simeq N \frac{\pi^2 k_{\text{B}}^2}{6h} (T_{\Omega}^2 - T_0^2) - N \frac{E_{\text{C}} k_{\text{B}}}{2h} (T_{\Omega} - T_0), \tag{5.28}$$

which corresponds to a net reduction of the heat conductance ( $|T_0 - T_{\Omega}| \rightarrow 0$ ) per ballistic electronic channel by the fixed amount  $\Delta G_{\text{heat}}^{\text{el}} = E_{\text{C}} k_{\text{B}}/2h$  (always small

with respect to  $G_Q^{\text{th}}$  in the considered high-temperature limit).

At  $T_0 \ll NE_C/\pi k_B \ll T_\Omega$ , Eq. 5.25 at  $\tau = 0$  becomes

$$J_{\text{thy}}^{\text{el}} \simeq \frac{\pi^2 k_B^2}{6h} (NT_\Omega^2 - (N-1)T_0^2) - N \frac{E_C k_B}{2h} T_\Omega, \quad (5.29)$$

where the relative reduction due to heat Coulomb blockade progressively vanishes as  $T_\Omega$  increases.

In the figure 5.4 we show the theoretical prediction for a temperature  $T_0 = 8$  mK for different number of ballistic channels connected to the island. Note the different crossover temperature, given by  $NE_C/\pi k_B$ , for each configuration.

### Asymptotic behavior for $\tau \in ]0, 1[$

At low temperatures, Eq. 5.25 simplifies into:

$$J_{\text{thy}}^{\text{el}} \left( T_0, T_\Omega \ll \frac{\hbar\tau_\Omega}{k_B R_K C} \right) \simeq \left( \tau_\Omega - 1 + \frac{\tau(1-\tau)}{\tau_\Omega} \right) \times \frac{\pi^2 k_B^2}{6h} (T_\Omega^2 - T_0^2). \quad (5.30)$$

In this case, in addition to the systematic blockade of one ballistic channel ( $-1$  in the prefactor) with respect to the non-interacting case ( $\tau_\Omega$  in the prefactor), we find an additional contribution to the flow of heat, whose partition character is signaled by the characteristic  $\tau(1-\tau)$  dependence.

At high temperatures, Eq. 5.25 reduces to the non-interacting result matching the widespread Wiedemann-Franz law (without additional contribution from the partition noise):

$$J_{\text{thy}}^{\text{el}} \left( T_0, T_\Omega \gg \frac{\hbar\tau_\Omega}{k_B R_K C} \right) \simeq \tau_\Omega \frac{\pi^2 k_B^2}{6h} (T_\Omega^2 - T_0^2). \quad (5.31)$$

### 5.3.2 Heat evacuation by electron-phonon coupling

Assuming the metallic island can be described as a Fermi liquid with electrons at hot temperature  $T_\Omega$  and a phonons bath at the base temperature  $T_0$ , the standard formula used for modeling the transfers of heat toward the phonons is given by [93]:

$$J_{el-ph} = \Sigma \Omega (T_\Omega^\alpha - T_0^\alpha) \quad (5.32)$$

where  $\Omega$  is the volume of the metallic island, and  $\Sigma$  a constant parameter involving the electron-phonon coupling. The parameter  $\alpha$  depends of the disorder:

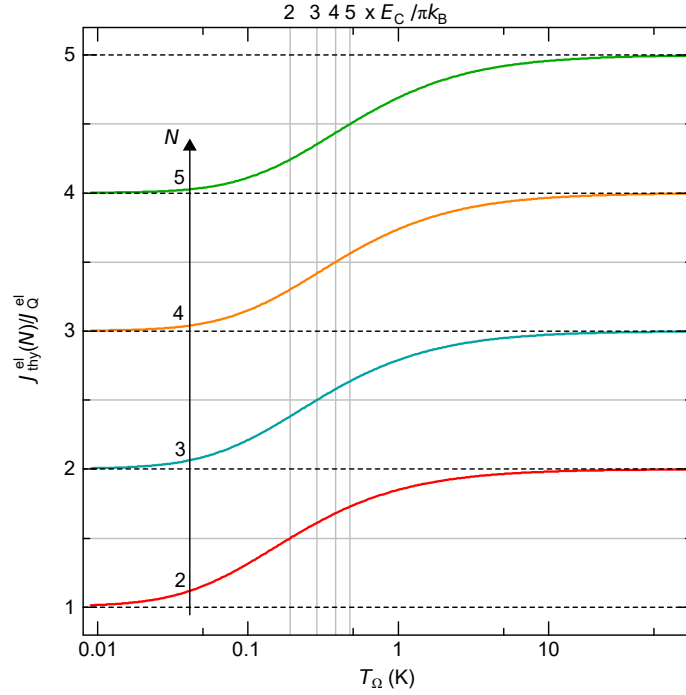


Figure 5.4: **Heat Coulomb blockade prediction for ballistic channels** Crossover from  $NJ_Q$  at  $T_{\Omega} \gg NE_C/\pi k_B$  to  $(N - 1)J_Q$  at  $T_{\Omega} \ll NE_C/\pi k_B$ . Colored continues lines display the theoretical prediction normalized by the quantum limit of heat flow per channel for different numbers  $N$  of ballistic channels and versus the metallic node temperature  $T_{\Omega}$ . The vertical dotted lines display the different thermal crossovers.

- In the case of a clean material with a phonon wavelength  $\lambda_{ph}$  well below the electron mean free path  $l_{el}$ , the heat transfer toward the phonons is predicted to follow a power law in  $T^5$  ( $\alpha = 5$ ) [93].
- In the disordered limit ( $\lambda_{ph} \gg l_{el}$ ), the heat flow toward phonons is expected to follow a power law in  $T^\alpha$  with  $\alpha$  between 4 and 6, depending of the nature of the disorder. Although most of the experiments measuring the transfers of heat between electrons and phonons found a result matching with the clean-limit case, other results are possible. For instance in reference [94], the authors have measured a heat flow in  $T^6$  as expected for “vibrating” disorder (defects moving together with the lattice atoms). In our case, the metallic island which is a diffused allow, is most likely not as clean as a pure metal.

## 5.4 Observation of the electronic heat flow in a ballistic circuit

First, we focus on the heat flow in the simplest ballistic limit, when only ballistic channels are connected to the metallic island.

### 5.4.1 Procedure to investigate heat flow

The approach used to measure the electronic heat flow is represented in figure 5.5. It is similar to the one introduced in order to measure the quantum limit of heat flow across an electronic channel [82]. A Joule power  $P_J$  is dissipated into the electronic fluid within the island. As a result the metallic island heats up to a steady-state electronic temperature  $T_\Omega$  above the base temperature  $T_0$  such that the dissipated Joule power and the net outgoing heat flow  $J_{heat}$  exactly compensate each other ( $J_{heat} = P_J$ ). The determination of  $T_\Omega$  through noise measurements therefore directly provides the heat flow-temperatures characteristics ( $J_{heat}(T_\Omega)$ ). The total heat flow is expected to contain two contributions:

$$J_{heat} = J^{el}(T_\Omega, T_0) + J^{el-ph}(T_\Omega, T_0)$$

$J^{el}$  is the heat current carried by electrons along the  $N$  connected ballistic channels and  $J^{el-ph}$  is an additional mechanism by which the heat is evacuated, which is attributed to coupling between electrons and phonons. In contrast to the previous work [82], the present measurement performed at low temperatures down to 8 mK allows for the direct observation of the electronic heat flow. Indeed, electronic heat flow is supposed to follow a power law in  $T^2$  whereas the heat flow by electron-phonon coupling should follow a power law in  $T^\alpha$  with  $\alpha$  between 4 and 6 [95]. At sufficiently low temperature, the heat flow by electron-phonon coupling may be negligible in comparison to the electronic heat flow, as we will see in the following.

### 5.4.2 Experimental procedure

First, we set all the QPCs in the ballistic regime with a total of  $N$  ballistic channels connecting the metallic island. To check that we are well in the ballistic regime, we measure the electrical conductance of the device  $G_S$  seen from the electrode  $M1$

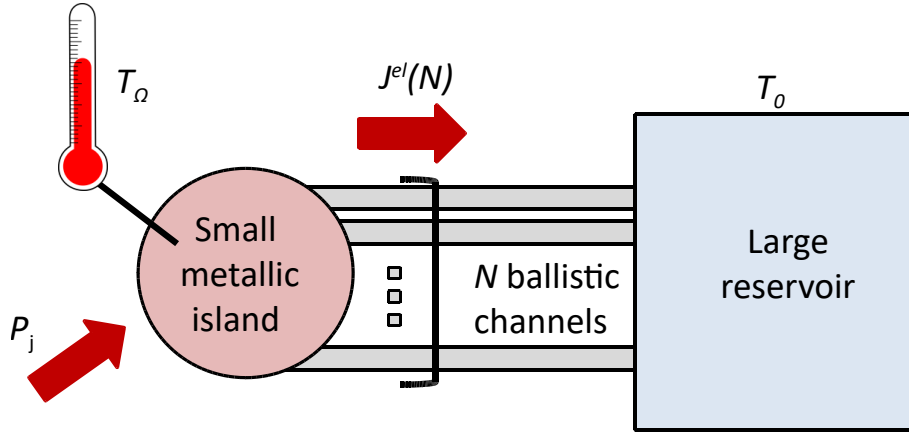


Figure 5.5: **Experimental principle:** We inject a well-known Joule power  $P_j$  in the metallic island by applying a dc voltage to the circuit. By energy conservation, the out-going electronic heat flow is equal to the injected Joule power. We measure the resulting temperature  $T_\Omega$  which allows us to determine the heat flow versus temperature characteristic. At very low temperature, the heat transfer toward the phonons is negligible in comparison to the electronic heat flow.

and  $G_P$  seen from the electrode  $M3$  versus the voltage applied to the electrode  $M3$  (see figure 1.1). These measurements are shown in the left panel of the figure 5.6. The four colors represent four different configurations, which are depicted by the following table:

$N$	$N_1$	$N_2$	$N_3$
2	1	0	1
3	1	1	1
4	1	2	1
5	2	2	1

with  $N_i$  the number of ballistic channels through the QPC  $i$  ( $i \in \{1, 2, 3\}$ ). As shown in the left panel of the figure 5.6, the electrical conductances are not affected by the applied voltage, as is expected for ballistic channels [96; 97]. At the same time, we measure the increase in the current noise impinging on electrode  $M1$ . The spectral density of this excess current noise is shown in the right panel of the figure 5.6. Since the channels are ballistic, there is no shot noise: the measured noise increase comes only from the augmentation of the temperature from the dissipated



Joule power. Note that we checked that when the QPCs are all closed, we do not observe any variation of the current noise spectral density versus the voltage applied in any electrode. This indicates that the source electrodes and the electrode where we measure the noise stay at the same base temperature. The only element of the circuit whose temperature is substantially increased is the central metallic island. In the right panel of the figure 5.6, the symmetric behavior in  $V$  is consistent with the absence of any thermo-electric effect, as expected for ballistic channels.

The following fluctuation dissipation relation [82; 98]:

$$(T_{\Omega} - T_0)2k_B G_S = S_{\text{exc}}, \quad (5.33)$$

allows us to determine the temperature increase in the metallic island (see chapter 2 for a derivation; here with a simplification arising from the fact that there is no shot-noise). The Joule power dissipated in the island is given by  $P_J = V^2 G_P / 2$ . Using these formulae and averaging for positive and negative voltages, we show in the figure 5.7 the augmentation of the temperature of the metallic island as a function of the injected Joule power. For a given Joule power injected, the different temperatures for the different configurations attest of the role of the electronic channel for the evacuation of heat: the greater is the number of channels, the better the heat is evacuated, and the lower is the temperature of the metallic island. At high injected Joule power, this difference tends to vanish: it is because the evacuation of heat by electron-phonon coupling becomes much higher than the electronic heat flow through the quantum electronic channels.

### 5.4.3 Observation of the heat Coulomb blockade of one ballistic channel on the electronic heat flow

We first observe the total heat flow at very low temperature, for a base temperature of  $T_0 = 8$  mK and a temperature of the metallic island  $T_{\Omega}$  below 25 mK. The result is shown in figure 5.8. The heat flow is shown versus squared temperature to directly compare with the quadratic power law expected for the electronic heat flow: the good agreement with straight lines indicates that the heat flow toward the cold phonons is negligible at these temperatures. The remarkable observation is the systematic suppression of one ballistic channel for the transport of heat. In contrast

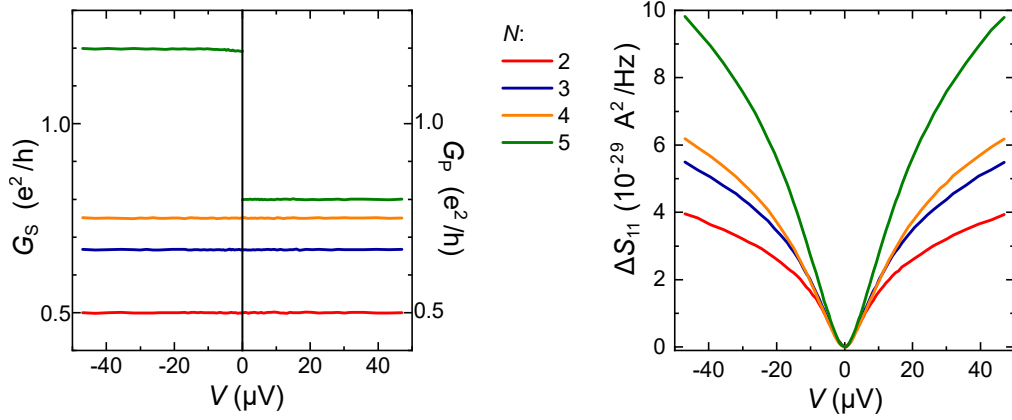


Figure 5.6: **Conductance and noise versus dc voltage.** The conductance of the sample seen from electrode  $M1$  where the noise is measured ( $G_S$ ) and seen from electrode  $M3$  where the voltage is applied ( $G_P$ ) are plotted in the left panel. The device electrical conductances  $G_{S,P}$  (lines, see text) match their expected quantum limited values independently of  $V$ : they are not reduced by Coulomb blockade. The right panel shows the excess noise measured in electrode  $M1$ , resulting from the augmentation of the temperature of the metallic island.

the electric current is not affected, in violation of the Wiedemann-Franz law. Indeed, the data match with the line corresponding to  $(N - 1)J_Q$ . This reduction of the overall electronic heat flow, which precisely obey the theoretical prediction derived in the previous section, is the main result of this section.

Control experiments of this observation are displayed in figure 5.9. First, we implement the case  $N = 2$  with 3 different configurations of the device, finding concordant measurements of the Coulomb blockade of the heat flow. Second, we perform the experiment at a twice higher temperature of the large reservoir  $T_0 = 16$  mK. In the two panels, the bottom dashed lines correspond to the low-temperature asymptotic limits of the theory, whereas the full black lines are the quantitative prediction of the heat Coulomb blockade. The top dashed line corresponds to the prediction for the electronic heat flow across two ballistic channels in the absence of the heat Coulomb blockade. We also perform the experiment at filling factor  $\nu = 3$  (data not shown).

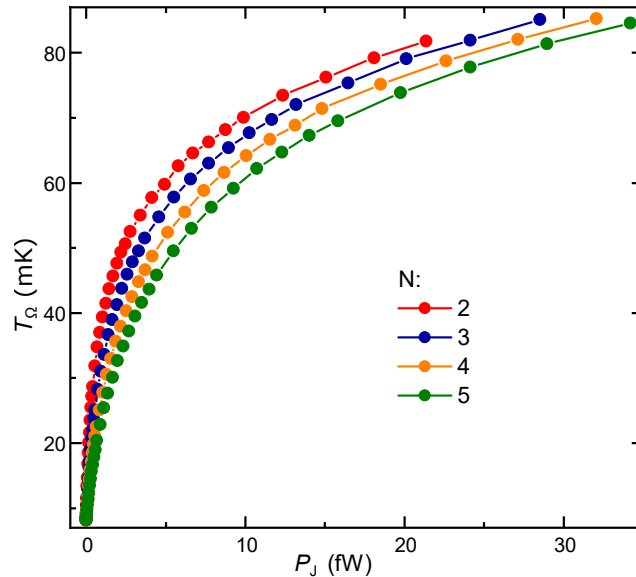


Figure 5.7: **Temperature versus injected Joule power.** The island electron temperature  $T_\Omega$  is plotted versus the dissipated Joule power  $P_J$ , for different numbers  $N$  of connected ballistic channels. It is obtained from the excess noise spectral density  $S_{\text{exc}}$  measured on electrode  $M1$ .

#### 5.4.4 Crossover from $(N - 1) \times J_Q^{\text{el}}$ to $N \times J_Q^{\text{el}}$

The purpose of this part is to compare our measurement with the theoretical predictions for the temperature dependence of the heat Coulomb blockade, which is expected to progressively cancel out as the temperature becomes much higher than  $NE_C/\pi k_B$ . The practical difficulty is that this crossover takes place on a temperature range where electron-phonon heat transfers are predominant in our device, which impedes a direct observation of the electronic heat flow to observe signatures of the heat Coulomb blockade crossover. We exploit the fact that the heat flow from the hot electrons in the metallic island at a given  $T_\Omega$  toward the cold surrounding phonons is independent of the number of channels connecting the metallic island, whereas the crossover around  $NE_C/\pi k_B$  depends on the number  $N$  of channels. Then, subtracting from the total heat flow  $J_{\text{heat}}(N, T_\Omega)$ , measured in one configuration, from the total heat flow  $J_{\text{heat}}(N_{\text{ref}}, T_\Omega)$  in another configuration used as a reference, allows us to cancel the phonon contribution:  $J_{\text{heat}}(N) - J_{\text{heat}}(N_{\text{ref}})$ .

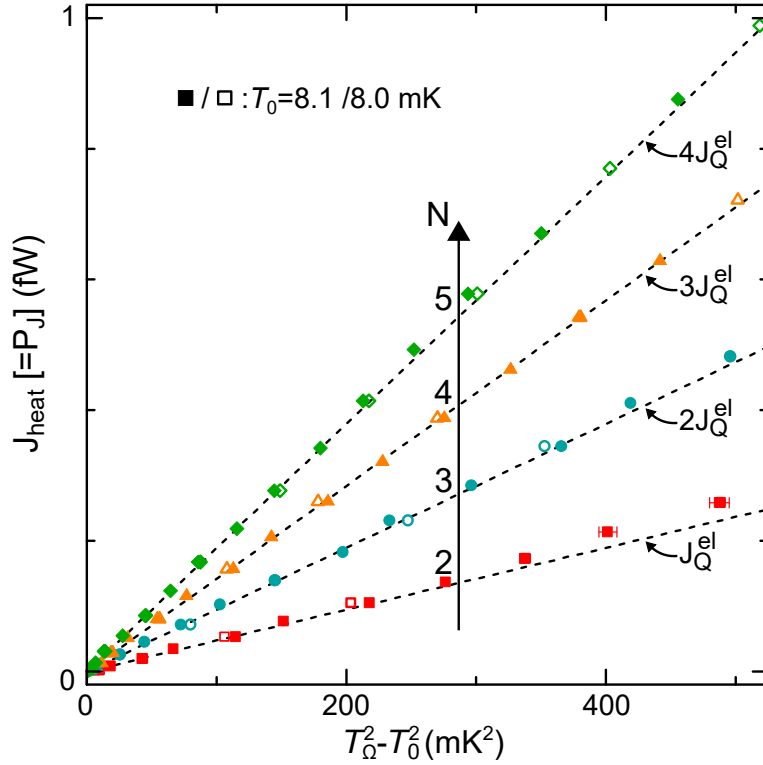


Figure 5.8: **Heat Coulomb blockade of one ballistic channel.** Symbols (statistical uncertainties shown when distinctly larger) represent the overall heat flow ( $J_{\text{heat}} = P_J$ ) displayed versus  $T_{\Omega}^2 - T^2$ , at low temperatures where electron-phonon interactions are negligible ( $T_{\Omega} < 25 \text{ mK}$ ). The nearby straight dashed lines show  $(N - 1) \times J_Q^{\text{el}}$ , corresponding to a systematic heat current suppression of  $1 \times J_Q^{\text{el}}$ .

The result is independent of the electron-phonon coupling and can be compared to  $J_{\text{thy}}^{\text{el}}(N, T_{\Omega}) - J_{\text{thy}}^{\text{el}}(N_{\text{ref}}, T_{\Omega})$ . The results using  $N_{\text{ref}} = 4$  and normalized by the quantum limit of heat flow for one channel are plotted in figure 5.10 as symbols. In this representation, a departure from  $(N - 4)$  signals a difference in the crossover. The quantitative prediction, given by equation 5.25 without any fitting parameter, is shown as continuous lines. For  $N - N_{\text{ref}} = -2$  ( $N = 2$ ,  $N_{\text{ref}} = 4$ ), the larger crossover signal follows the theoretical prediction up to  $T_{\Omega} \approx 60 \text{ mK}$  (right panel of figure 5.4 and figure 5.10). At higher temperature, the scatter of the data points rapidly increases due to the overwhelming subtracted electron-phonon contribution. This observation further establishes experimentally the full heat Coulomb blockade theory for ballistic channels at arbitrary temperatures, beyond the low-temperature

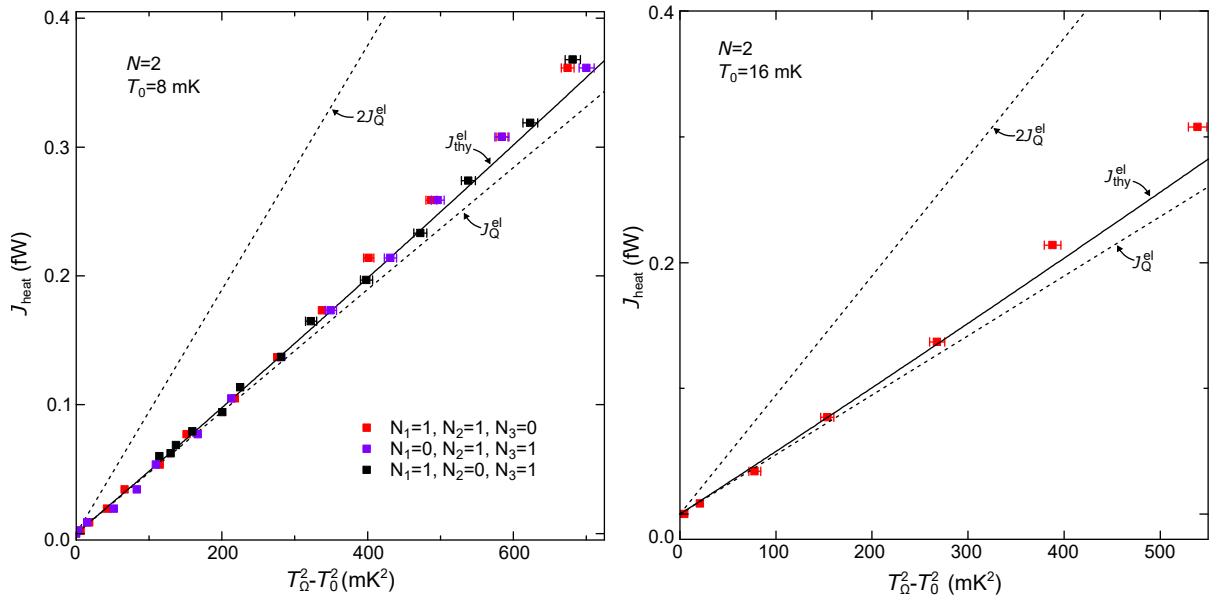


Figure 5.9: **Control experiments.** Left panel: control experiment at  $T_0 = 16$  mK. Right panel: Comparison of three device configurations implementing  $N=2$  (as detailed in the figure).

systematic suppression of one ballistic quantum channel.

### 5.4.5 Electron-phonon coupling

Having established the heat Coulomb blockade prediction for ballistic channels, we now use this prediction in order to investigate the additional mechanism for the dissipation of heat, which we attribute to the coupling between electrons and phonons. The figure 5.11 shows this additional contribution, obtained by subtracting the theoretical prediction for the electronic heat flow (equation 5.25) from the total heat flow. All the data collapse into a single curve, independently of the number  $N$  of electronics channels. It can be fitted by a simple power-law as expected for the heat flow toward the phonons [93]:

$$J^{el-ph} = \beta(T_\Omega^\alpha - T_0^\alpha) \quad (5.34)$$

We observe that the data correspond to an exponent of  $\alpha = 5.85$ , above the exponent of 5 characterizing the clean limit but in agreement with what can be expected for the heat evacuation through coupling between hot electron and cold phonon in the

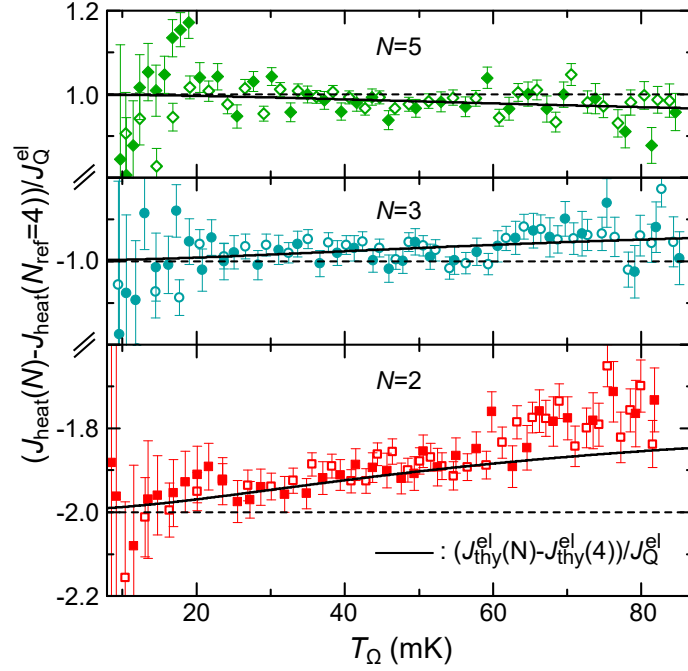


Figure 5.10: **Heat Coulomb blockade crossover.** Symbols (continuous lines) show the measured (predicted) heat current variation when changing  $N$  from  $N_{\text{ref}} = 4$  at fixed  $T_{\Omega}$ , renormalized by the quantum limit per channel  $J_{\text{Q}}^{\text{el}}$ . The crossover toward the low-temperature heat Coulomb blockade of one ballistic channel specifically shows as a difference with respect to the nearby horizontal dashed line, whereas electron-phonon thermal transfers are canceled out.

presence of disorder:  $\alpha \in [4, 6]$  [93]. The prefactor  $\beta = 39 \text{ nW/K}^{\alpha}$  is typical, given the volume of the metallic island (volume of  $\approx 3 \mu\text{m}^3$ ) and its composition: for the gold, which is the main constituent of the metallic island, the electron-phonon coupling constant is measured to be equal to  $2.4 \times 10^9 \text{ Wm}^{-3}\text{K}^{-5}$  for temperature between 80 mK and 1.2 K and assuming a  $T^5$  power law [99]. Note that the same power law (same exponent and same prefactor) is found in a verification experiment at the twice higher base temperature  $T_0 = 16 \text{ mK}$ . This verification ascertains that the temperature of the phonons is the same as the electron temperature in the cold reservoir that is measured by quantum shot noise for the electrons.

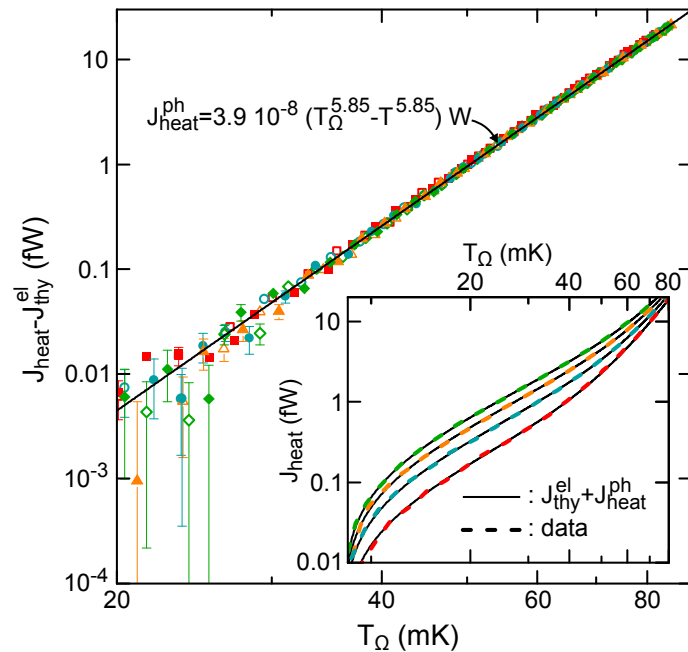


Figure 5.11: **Electron-phonon heat transfers.** Subtracting heat Coulomb blockade predictions, the displayed remaining part of the heat current (symbols) collapse onto a single curve for all  $N \in \{2, 3, 4, 5\}$ , fitted by a  $T_{\Omega}^{5.85}$  functional (line,  $J_{\text{heat}}^{\text{ph}}$ ). Inset, direct comparison between  $J_{\text{thy}}^{\text{el}} + J_{\text{heat}}^{\text{ph}}$  (black continuous lines) and measured total heat current  $J_{\text{heat}}$  (superimposed colored dashed lines).

#### 5.4.6 Comparison of the theory with the raw noise data

For completeness, we here compare directly the theory to the raw data in the figure 5.12. The noise predictions are obtained from the heat flow predictions. The noise data are the same as the one displayed in the figure 5.6 (right panel). Full lines display the theoretical noise derived using the fluctuation dissipation formula (equation 5.33), with the excess temperature determined from the heat Coulomb blockade theory (equation 5.25) and the electron-phonon coupling calibration (equation 5.34 with  $\alpha = 5.85$  and  $\beta = 39 \text{ nW/K}^{\alpha}$ ). Dashed lines display the theoretical noise derived without the electron-phonon coupling (which is only negligible at low island temperature, ie low bias voltages).

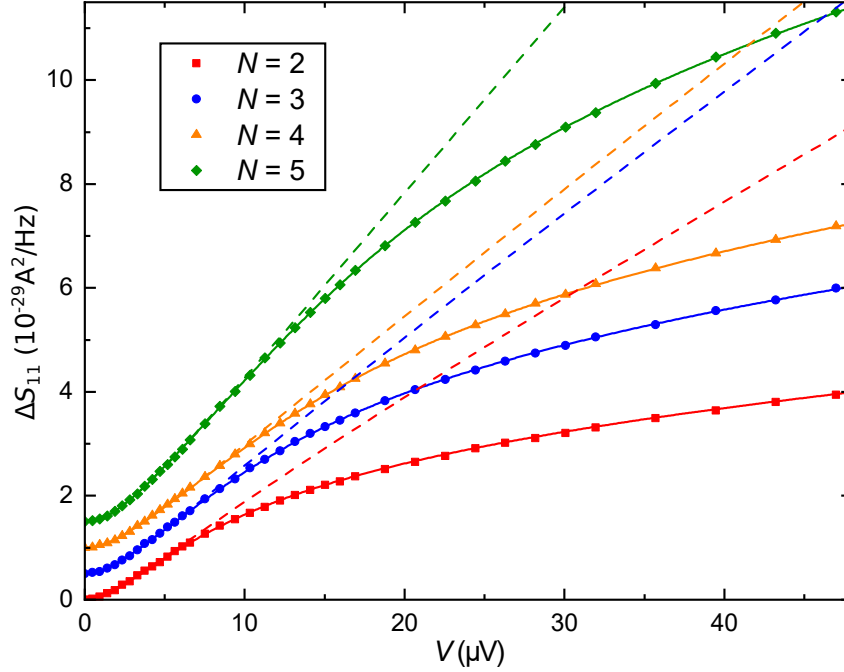


Figure 5.12: **Direct comparison raw data/theory.** In the main panel, we display as points the same raw data of the figure 5.6 (right panel) using the same color code. The colored full lines display the theoretical noise derived using the heat Coulomb blockade theory and the heat flow from electrons to phonons. The colored dashed lines display the theoretical noise without including the electron-phonon heat flow. Offsets are added in order to improve the visibility.

### 5.4.7 Discussion about the heat Coulomb blockade of one ballistic channel

#### Comparison with other experiments

In the previous experiment [82] performed in the team before my PhD, it was also attempted to determine the full electronic heat flow. However, the contribution of electron-phonon heat flow remained non-negligible in the previous experiment. Therefore, a power law in  $T^5$  ( $\alpha = 5$  in equation 5.34) was assumed ad hoc for modeling the transfers of heat from the hot electrons toward the cold phonons. Intriguingly, no heat Coulomb blockade was detected with this electron-phonon model. Re-analyzing these previous data without imposing a power law in  $T^5$ , we find that



they are compatible with the presently observed heat Coulomb blockade. The overall heat flow may be interpreted as the electronic heat flow reduce by the heat Coulomb blockade observed plus a heat flow toward the cold phonons following the standard relation  $\beta(T_e^\alpha - T_0^\alpha)$  with  $\alpha = 4.7$  and  $\beta = 27$  nW/K $^\alpha$ .

Other measurements of the heat flow which may give rise to heat Coulomb blockade have been reported in [92; 100]. In the reference [100], the main experiment, performed at a base temperature of around 11 mK, was done in the fractional quantum Hall regime. Although the electron-phonon contribution was assumed to be negligible, it is possible that the charging energy in their setup is too small, below  $k_B \times 10$  mK, for the heat Coulomb blockade to develop.

### **Why is exactly one channel blocked for the thermal transport?**

As further discussed in section 5.3.1, the suppression of precisely one quantum of thermal conductance for the transport of heat at low temperature can be explained by the fact that the Coulomb interaction introduces correlations between the different electronic channels. In a similar way as the dipole-charge separation for two interacting edge channels [101; 102], the  $N$  ballistic electronic channels can be mapped onto a single charge mode (for example, identical current fluctuations on all electronic channels) and  $N - 1$  independent neutral modes (for example, opposite current fluctuations on each of  $N - 1$  pairs of electronic channels). The charged mode is interacting with the charge of the metallic island whereas the neutral modes are totally decoupled from it. Therefore, in the limit of a low island capacitance where fluctuations of the overall island's charge are quenched because of the associated high charging energy, no heat can be evacuated in the form of electronic current fluctuations emitted along the single charge mode. However, heat evacuation through the  $(N - 1)$  neutral modes is not impacted by the Coulomb charging energy.

### **The one channel limit**

Note that this situation cannot be addressed in our device as we need more than one channel for heating-up the island by Joule effect and for determining the temperature by noise measurement. In the single channel case ( $N = 1$ ) the heat Coulomb blockade theory [19] predicts that the electronic heat flow is completely blocked at

low temperature. Because of the strong link between heat, entropy and information transfers [103], one may wonder if any quantum information is communicated between electrons in the connected channels and the many Fermi quasiparticles in the metallic island. The answer is no: remarkably, it is predicted [104] and now experimentally observed in an interferometer [105] that the quantum phase of incoming electrons is imprinted into the out-going electrons. I am co-first author of this experiment that will be presented in the PhD thesis of Hadrien Duprez.

## 5.5 Observation of the electronic heat flow in a non-ballistic quantum circuit

### 5.5.1 Focusing on the electronic heat flow

Now, one of the channels is set to an arbitrary transmission probability  $\tau \in [0, 1]$ , whereas the  $N$  other channels remain ballistic. This correspond to the “quantum dissipative circuit” configuration presented in section 1.3.3. In this configuration, the electrical conductance of the additional channel or arbitrary transmission probability  $\tau$  is affected by the dynamical Coulomb blockade and therefore depends on the temperature. The Joule power  $P_J$  is injected through ballistic channels connected to electrodes biased at voltage of opposite signs, such as the average voltage of the metallic island remains null. This allows for a pure temperature bias across the non-ballistic channel (without voltage bias), and also makes the injected Joule power independent of the renormalized  $\tau$ . In order to access to the electronic heat flow over a broader temperature range, we subtract from  $P_J$  the heat flow toward phonons  $J_{\text{el-ph}}$  separately calibrated with only ballistic channels (see figure 5.13). In practice, for each measurement of the heat flow which will be presented hereafter, we also performed a measurement at  $\tau = 1$  in order to calibrate the heat flow toward the cold phonons. As in the previous cooldown of the same sample, all the measurement at  $\tau \in \{0, 1\}$  collapse into a single curve very close to the one presented in the previous section. A fit performed on the ensemble of data shown in figure 5.13, gives a heat flow toward the phonons  $J_{\text{el-ph}} = 2.7 \times 10^{-8} (T_{\Omega}^{5.7} - T_0^{5.7})$ .

### 5.5.2 Results

In the previous section, it was shown that the thermal conductance from a small heated node connected to ballistic channels is reduced by precisely one quantum of thermal conductance at low temperature from what is expected according to the Wiedemann-Franz law. With such fixed reduction, the *increment* of the thermal conductance when *adding* an extra ballistic channel is still linear, in accordance with the Wiedemann-Franz law. Is it also the case when increasing continuously the transmission probability across an electronic channel from  $\tau = 0$  to 1? The answer

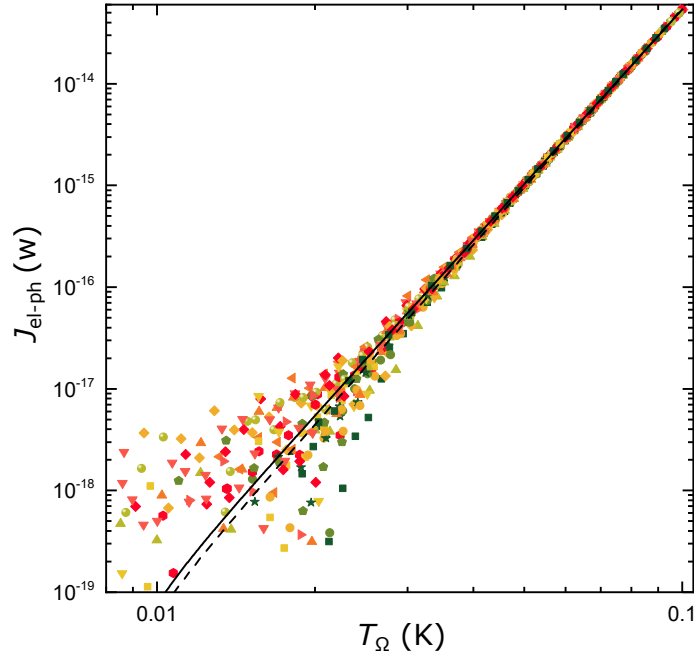


Figure 5.13: **Electron-phonon heat transfers.** Subtracting heat Coulomb blockade predictions, the displayed remaining part of the heat current (symbols) collapse onto a single curve for all  $N \in \{2, 3, 4\}$ , fitted by a  $T_{\Omega}^{5.7}$  functional (black full line). The dashed line correspond to the fit obtained in the previous section (in a different cooldown of the same sample).

is no, as predicted by our model in section 5.3.1, and as we will experimentally show now. In the figure 5.14 we present the measured electronic heat flow normalized by the quantum limit per channel, for different settings of the circuit, spanning the full range of  $\tau$  at  $N = 2$ . The two black thick lines display the heat Coulomb blockade prediction in the ballistic case for  $\tau = 0$  (bottom line), and  $\tau = 1$  (top line). The different settings of the non-ballistic QPC are encoded by the different colors. The dashed lines correspond to linear, Wiedemann-Franz-like, interpolations between ballistic predictions at  $N$  and  $N + 1$ , weighted respectively by  $1 - \tau$  and  $\tau$  measured for the corresponding data. The deviation from the dashed lines is particularly significant at intermediate  $\tau$ . This shows that the heat flow increases when increasing the transmission  $\tau$  does not reduce to a linear increase. In contrast, the novel predictions of equation 5.25 lie close to the data, without any adjustable parameter. Note that in our theoretical treatment, the dynamical Coulomb blockade

renormalization of the electron transmission probability  $\tau$  is considered separately: the renormalized  $\tau$  simultaneously measured is injected in equation 5.25. In the figures 5.15 and 5.16, we show similar measurement for  $N = 3$  and  $N = 4$  ballistic channels, presented in figure 5.15 and 5.16. We performed additional test at higher temperature  $T_0 = 16$  mK, shown in the figure 5.17 where all configurations ( $N=2,3$  and 4 ballistic channels) are plotted in the same panel.

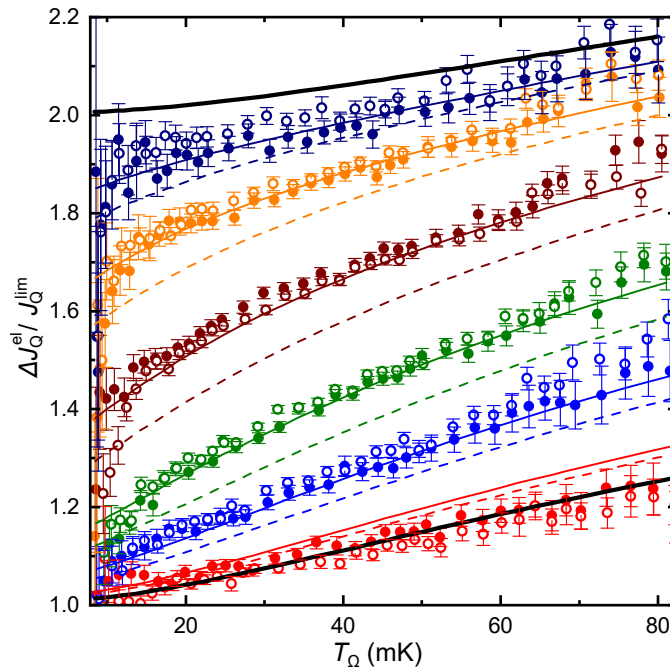


Figure 5.14: **Heat flow through  $N = 2$  ballistic and one partially transmitted channel.** Data points show the measured heat flow for 2 ballistic channels and different settings of  $\tau$ . The thick black lines display the Heat Coulomb blockade prediction for ballistic channels ( $N = 2$  for the bottom,  $N = 3$  for the top). The dashed lines are linear interpolations between ballistic predictions at  $N = 2$  and  $N = 3$  weighted respectively by  $\tau$  and  $1 - \tau$ . The full colored lines are the prediction derived in section 5.3.1, where we have injected the measured transmission probability of the QPC 3.

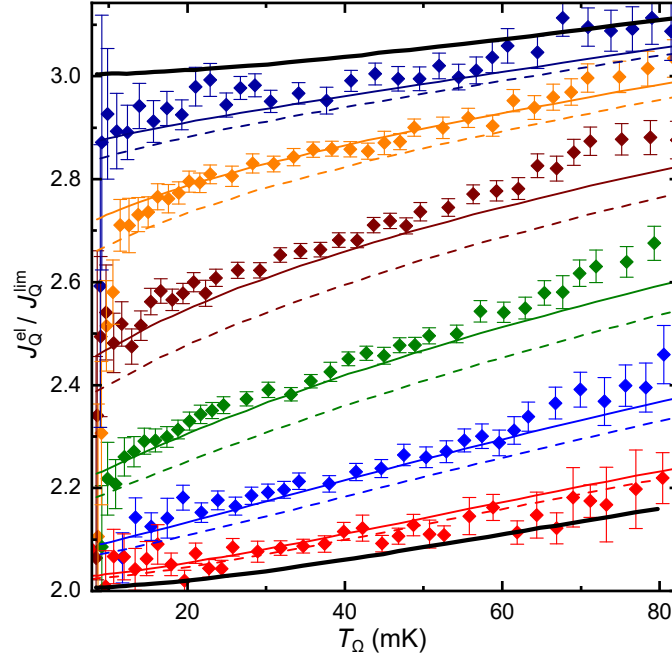


Figure 5.15: **Heat flow through  $N = 3$  ballistic and one partially transmitted channel.** Data points show the measured heat flow for 3 ballistic channels and different settings of  $\tau$ . The thick black lines display the Heat Coulomb blockade prediction for ballistic channels ( $N = 3$  for the bottom,  $N = 4$  for the top). The dashed lines are linear interpolations between ballistic predictions at  $N = 3$  and  $N = 4$  weighted respectively by  $\tau$  and  $1 - \tau$ . The full colored lines are the prediction derived in section 5.3.1 where we have injected the measured transmission probability of the QPC 3.

### 5.5.3 Comparison with predicted deviations from a Wiedemann-Franz increase of $J_Q$

At low temperatures  $T_\Omega, T_0 \ll h/k_B RC$ , the difference between the prediction and linear interpolation of the ballistic theory reads:

$$J_Q^{thy} - (N + \tau - 1) \times J_Q^{max} \approx \frac{\tau(1 - \tau)}{N + \tau} \times J_Q^{max}$$

Note that  $J_Q^{th} = 0$  for  $N = 0$  at low temperatures, whatever the value of  $\tau$ . Note also that the combined role of electron-partition and Coulomb interaction is attested by the  $\tau(1 - \tau)$  factor and by the fact that this difference progressively vanishes together

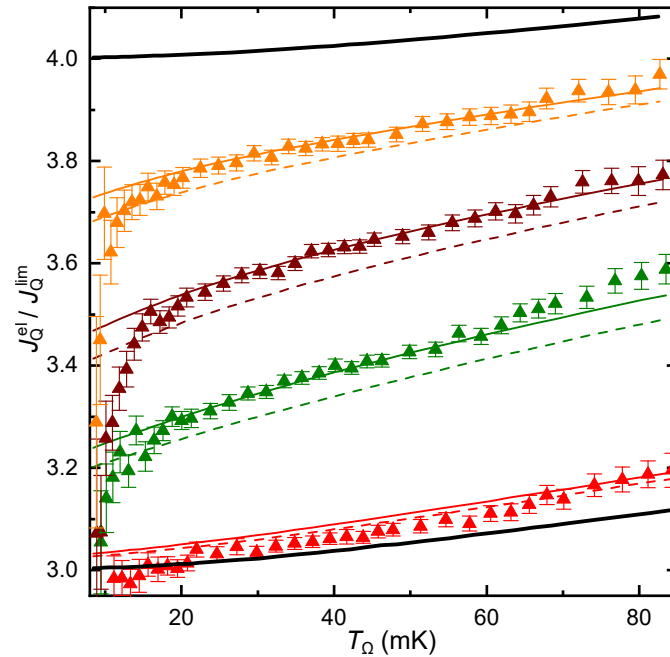


Figure 5.16: **Heat flow through  $N = 4$  ballistic and one partially transmitted channel.** Data points show the measured heat flow for 4 ballistic channels and different settings of  $\tau$ . The thick black lines display the Heat Coulomb blockade prediction for ballistic channels ( $N = 4$  for the bottom,  $N = 5$  for the top). The dashed lines are linear interpolations between ballistic predictions at  $N = 4$  and  $N = 5$  weighted respectively by  $\tau$  and  $1 - \tau$ . The full colored lines are the prediction derived in section 5.3.1 where we have injected the measured transmission probability of the QPC 3.

with Coulomb effects as the temperatures is increased. In the figures 5.18, 5.19 and 5.20 we display the electronic heat flow for respectively  $N = 2, 3,$  and  $4$  subtracted from the interpolation between ballistic predictions, normalized by the quantum limit of heat flow per channel. We plot only points for temperature  $T_\Omega$  between 20 and 60 mK where the statistical uncertainty are the smallest. The continuous line displays the low temperature prediction  $\tau(1 - \tau)/(N + \tau)$ .

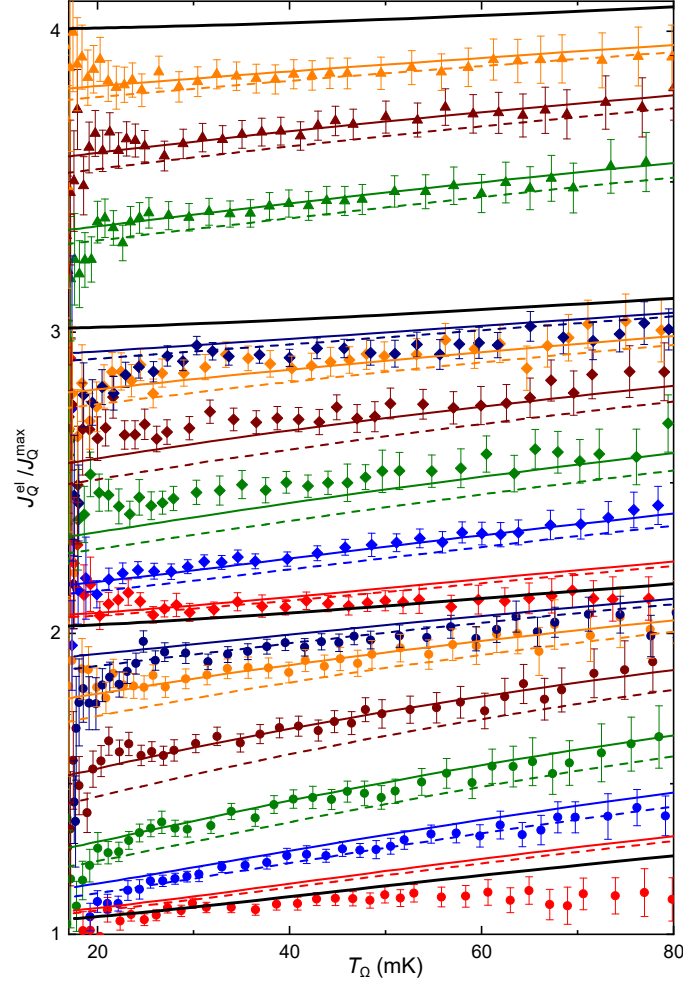


Figure 5.17: **Control experiment at a bath temperature of 16 mK.** Electronic heat flow for  $N = 2$  (circle), 3 (diamond) and 4 (triangle) ballistic channels. The higher statistical uncertainties compared to the scattering of the points, which seems similar to the measurements done at lower temperature, come from the determination with lower resolution of the bath temperature  $T_0$ .

## 5.6 Conclusion

In this chapter, we presented measurements of the electronic heat flow through circuits composed of several quantum channels. We observed two mechanisms influencing the heat flow in the presence of Coulomb interactions combined or not with shot noise. This leads to different deviations from the Wiedemann-Franz law. These discoveries advance our understanding of heat quantum transport and open



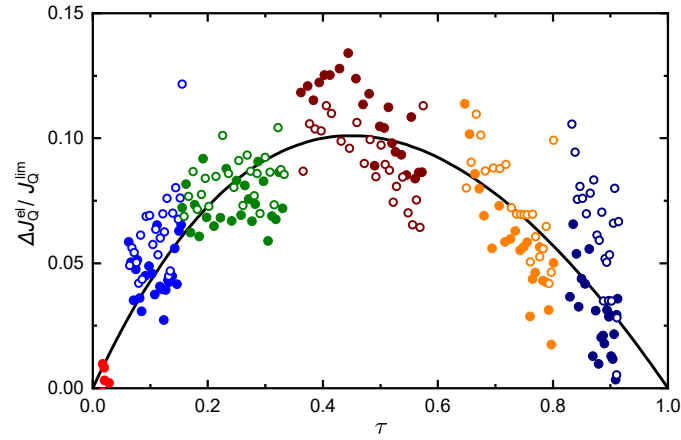


Figure 5.18: **Deviation from linear interpolation for  $N = 2$ .** The difference between the data points and the corresponding linear interpolations for  $N = 2$  ballistic channels, versus the transmission probability of the QPC 3 is plotted. The black line correspond to the asymptotic limit at  $T \ll h/k_B RC$ :  $\tau(1 - \tau)/(N + \tau)$ . Open and full symbols distinguish separate sequences of measurements.

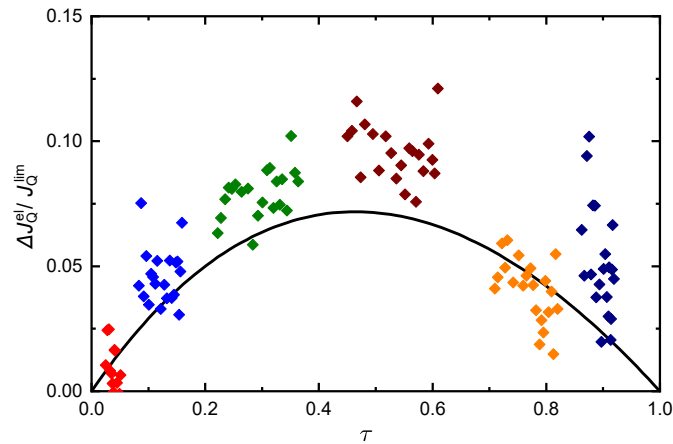


Figure 5.19: **Deviation from linear interpolation for  $N = 3$ .** The difference between the data points and the corresponding linear interpolations for  $N = 3$  ballistic channels, versus the transmission probability of the QPC 3 is plotted. The black line corresponds to the asymptotic limit at  $T \ll h/k_B RC$ :  $\tau(1 - \tau)/(N + \tau)$ .

new perspectives for managing heat in small nano-devices.

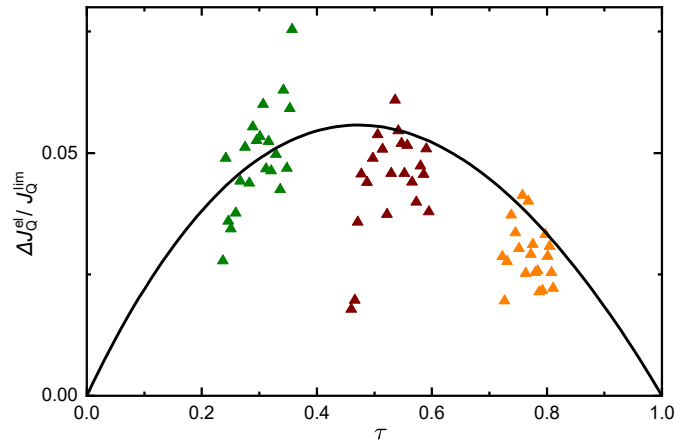


Figure 5.20: **Deviation from linear interpolation for  $N = 4$ .** The difference between the data points and the corresponding linear interpolations for  $N=4$  ballistic channels, versus the transmission probability of the QPC 3 is plotted. The black line corresponds to the asymptotic limit at  $T \ll h/k_B RC$ :  $\tau(1 - \tau)/(N + \tau)$ .



# Conclusion

In this thesis, we have investigated the shot noise and the heat flow in elementary quantum circuits composed of a few quantum channels connected to a single, small metallic node. In practice, three quantum point contacts formed by field effect in a 2D electron gas provide test-beds for arbitrary short quantum channels, and were connected to a micrometer-sized metallic island. Whereas quantum channels connected in parallel to voltage-biased electrodes are independent from one another, the Coulomb charging energy of the floating island/circuit node correlates the channels with a profound influence on transport. It is well-established that these correlations can strongly reduce the electrical conductance, the dynamical Coulomb blockade. However, experimental studies of their impact on shot-noise and heat flow remained wanting. This PhD work constitutes a first step in the experimental investigation of the influence of Coulomb interaction on the noise and heat transport of composite quantum circuits. Four main achievements can be singled out:

- The observation of a type of fluctuation-dissipation relation between the variation of the shot noise and the variation of the renormalized conductance as a function of bias voltage. This relation takes place in a quantum dissipative circuit composed of one non-ballistic quantum channel in series with a linear resistance, and was predicted in the connected Tomonaga-Luttinger liquid context.
- The observation of the ‘thermal’ shot noise solely induced by a temperature difference. Our work complements and strengthens the nearly simultaneous observation in atomic contacts [18], and directly establishes the predictions from the scattering theory of quantum transport.
- The observation of a new form of Coulomb blockade that only applies to heat in

ballistic circuits, whereas the dc electrical transport is not affected. This ‘heat Coulomb blockade’ manifests as the universal suppression of a single ballistic channel for the transport of heat, whatever the total number of channels.

- The observation of a new heat flow mechanism with non-ballistic channels, involving a combination of both the Coulomb interaction and the ‘thermal’ shot noise.

On the technical side, one crucial advance that made possible most of these achievements was the implementation of advanced noise measurement strategies combining simultaneous measurements of the auto- and cross-correlations of current fluctuations. The complementary information allowed us to distinguish between different sources of noise, namely the thermal emission from the heated-up metallic node and the shot-noise across non-ballistic channels. We expect that the developed methods will form the basis for further investigations of the quantum laws of heat, noise and thermoelectricity in circuits and may also help elucidating intriguing behaviors in the fractional quantum Hall regime. In this PhD work, only a single channel at most was not ballistic. The straightforward next step is to extend this investigation to circuits including several arbitrary channels, where the Coulomb-induced correlations between channels can give rise to exotic many-body phenomena such the multi-channel Kondo effect. Another future step will be to go beyond the short quantum channels presently studied. In channels formed by an interferometer or a resonant quantum dot, the energy corresponding to  $h$  (the Planck constant) over the electrons transit time, and the connected energy dependence of electrons’ transmission probabilities are expected to constitute novel important energy scales. Already, a remarkable achievement would be to demonstrate the quantum phase control of heat flow along an electronic Mach-Zehnder interferometer.

# Appendix A

## Refinement about electrons temperature determination

### A.1 Electronic base temperature determination including ac voltage

For precise measurement of the base temperature, the injected ac voltage used to simultaneously measure the transmission probability has an influence on the excess noise that should be included in the analysis. To take into account this effect, we add the contribution of the ac voltage in the formula equation 1.4. We use the Taylor development at order two in  $V_{ac}$ :

$$(V + V_{ac}) \coth\left(\frac{e(V + V_{ac})}{2k_B T}\right) \approx V \coth\left(\frac{eV}{2k_B T}\right) + \frac{eV_{ac}^2}{2k_B T} \left[-1 + \frac{eV}{2k_B T} \coth\left(\frac{eV}{2k_B T}\right)\right] \operatorname{cosh}^2\left(\frac{eV}{2k_B T}\right),$$

where  $V_{ac}$  is the RMS value of the injected voltage. In practice, the effect of the ac voltage would be to increase artificially the measured temperature by around 0.1 mK if its contribution was not included in the analysis.

## A.2 Heating contribution by ac voltage

Although weak, the injection of ac voltage ( $V^{ac} \approx 0.23 \mu\text{V}_{\text{rms}}$ ) in order to simultaneously determine the differential conductance of the sample heats up the small central metallic island above the base temperature measured by shot noise thermometry, even in absence of dc voltage. In order to determine this small increase of temperature, we measure the cross-correlation at zero dc voltage. The instrumental offset is calibrated before and after each measurement. The difference of offset between the calibration and the measurement is attributed to a heating of the metallic island whose excess temperature is given by the relation:

$$S_{12}(V = 0) = -2k_{\text{B}}T_{\text{exc}}/R_{\text{K}} \frac{n_1 n_2}{N + \tau} \quad (\text{A.1})$$

This formula comes straightforwardly from the fluctuation dissipation theorem (see chapter 2). The effect of shot noise is completely negligible for this small excess temperature, which is typically in the order of 0.3 mK (always below 0.6 mK). This small temperature difference is included in the experimental determination of  $T_{\Omega}$  for all experiments presented in this thesis, except the experiment concerning the heat flow through ballistic channels where only auto-correlation noise was measured. The effect of the ac voltage injected is also taking into account in order to determine the total dissipated Joule power using the relation:

$$P_J^{ac} = \sum_{i=1}^3 \frac{(V_i^{ac})^2}{2} G_{s,i}, \quad (\text{A.2})$$

where  $G_{s,i}$  is the conductance of the sample seen from electrode  $Mi$  and  $V_i^{ac}$  the ac voltage applied in electrode  $Si$  (see figure 1.1). In practice,  $P_J^{ac}$  is below 1% of the total Joule power injected for  $T_{\Omega} > 20$  mK.

# Appendix B

## Conductance Formulae

In the following, we note  $V_{i@f_j}$  the voltage measured in electrode  $i$  (see figure 1.1) at frequency  $j$ , and  $V_j$  the injected voltage, which is by current conservation, the sum of the three voltages measured at the same frequency  $f_j$ :  $V_j = \sum_{j=1}^3 V_{i@f_j}$ . We can calculate the conductance of the sample by two redundant ways: considering in one case the current transmitted through the sample or in the other case, the current reflected.

### Conductance from reflected current

By current conservation we have:

$$V_{i@f_i} \frac{\nu}{R_K} = V_i \frac{\nu}{R_K} - V_i \frac{G_{s,i}}{R_K}, \quad (\text{B.1})$$

with  $G_{s,i}$  the differential conductance of the sample seen from electrodes  $i$ . It leads to the relation:

$$G_{s,i} = \nu \left( 1 - \frac{V_{i@f_i}}{V_i} \right) \quad (\text{B.2})$$

### Conductance from the transmitted current

By current conservation we have:

$$V_i \frac{G_{s,i}}{R_K} = V_{j@f_i} \frac{\nu}{R_K} + V_{k@f_i} \frac{\nu}{R_K}, \text{ with } j, k \neq i \text{ and } j \neq k. \quad (\text{B.3})$$

Which leads to the relation:

$$G_{s,i} = \nu \left( \frac{V_{j@f_i} + V_{k@f_i}}{V_i} \right) \quad (\text{B.4})$$



### Conductance of each QPC

We note  $G_i$  the conductance of the QPC  $i$ . The conductance of the sample seen from electrode  $i$  as function of the conductance of each QPC is:

$$G_{s,i} = \frac{G_i(G_j + G_k)}{G_i + G_j + G_k} \quad (\text{B.5})$$

If none of the QPC is completely pinched off, once we have determined  $G_{s,i}$  for  $i = 1, 2, 3$  using equation [B.2](#) or [B.4](#), we can invert the equation system and find the conductance of each QPC.

# Appendix C

## Résumé en français

Dans cette thèse, nous explorons les lois quantiques régissant le transport dans un petit circuit électrique. Pour révéler ces comportements quantiques, nos expériences sont réalisées à basse température, sur de petits conducteurs. Dans ce contexte, l'interaction de Coulomb combinée à la granularité de la charge conduit souvent à une violation des lois classiques de la composition des impédances. L'énergie de charge des nœuds du circuit crée des corrélations entre les conducteurs cohérents interconnectés qui ont une profonde influence sur le transport. Il est bien établi que ces corrélations peuvent réduire considérablement la conductance électrique, un phénomène appelé blocage de Coulomb dynamique (DCB). Cependant, leur influence sur les fluctuations de courant et le flux de chaleur reste à peine explorée expérimentalement. Cette thèse est une première étape dans l'étude expérimentale, au-delà de la simple conductance électrique, des circuits quantiques composites. Le circuit étudié, représenté sur la figure C.1, est constitué d'un îlot métallique de taille micrométrique relié à plusieurs canaux de conduction quantiques élémentaires. Le nombre de canaux ainsi que leurs transmissions individuelles sont réglables avec précision. Ce circuit simple comprend un nœud unique formé par un îlot métallique dont l'importante énergie de charge  $E_C \equiv e^2/2C \simeq k_B \times 0,3\text{K}$  ( $C$  est sa capacité) peut être beaucoup plus grande que les énergies thermique et électrique, étant donné la température de base  $T_0 \approx 8\text{ mK}$ . Les outils à notre disposition pour cette étude sont les conductances et les mesures de bruit de courants. Le bruit électronique dans le circuit provient de différentes sources : le bruit de grenaille provient du transfert granulaire de charge à travers les canaux de conduction quantique non balistique

et le bruit de Johnson-Nyquist provient de l'agitation thermique des électrons. Les deux dépendent des tensions appliquées car l'application de ces tensions entraînent également un chauffage par effet Joule de l'îlot métallique central. En effectuant simultanément des mesures d'auto-corrélations et de corrélations croisées de fluctuations électriques, nous sommes en mesure de distinguer les différentes sources de bruit, et ainsi de déterminer séparément l'augmentation de température de l'îlot métallique central ( $T_\Omega - T_0$ ), le bruit de grenaille à travers les canaux non balistiques et le flux de chaleur. Cette thèse présente quatre résultats obtenus par cette approche, dont deux sont liés aux mesures des fluctuations de courant et deux autres au flux de chaleur comme décrit ci-dessous. Ces résultats font progresser notre compréhension des fluctuations de courant, du transport électrique et thermique dans un circuit quantique composite. En outre, nous nous attendons à ce que les stratégies avancées de mesure du bruit combinant des auto-corrélations et des corrélations croisées mises au point dans cette thèse ouvrent la voie à de nouvelles recherches sur les lois quantiques du transport et fournissent de nouvelles perspectives sur des systèmes complexes tels que les états de l'effet Hall quantique fractionnaire.

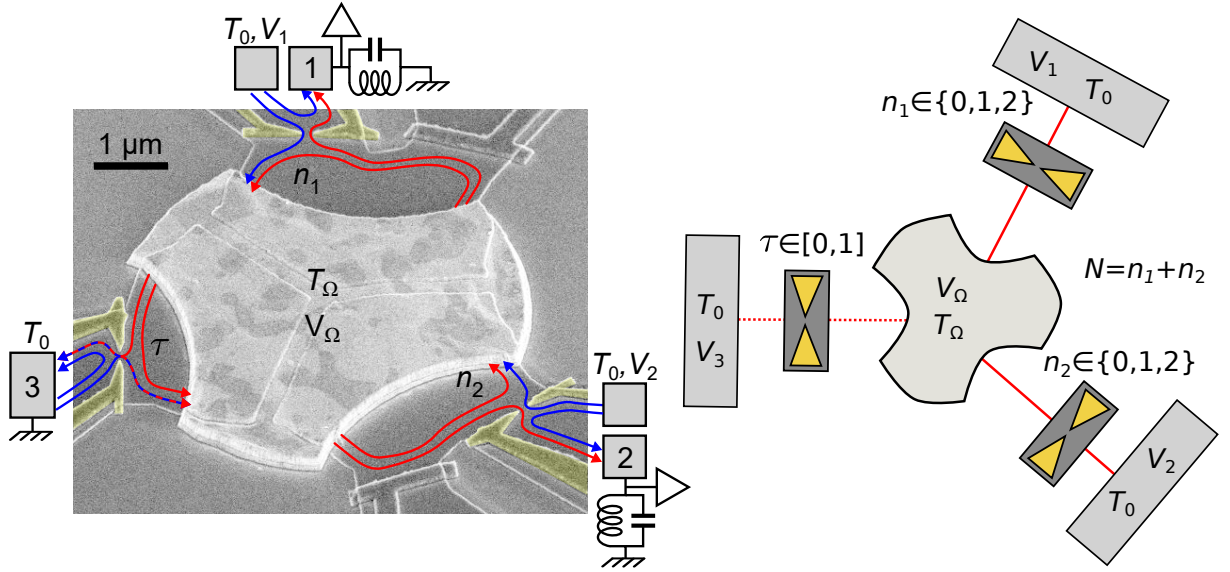


Figure C.1: **Micrographe en fausses couleurs (à gauche) et schéma (à droite) représentant l'échantillon mesuré au cours de cette thèse.** Un îlot métallique est en contact avec trois branches distinctes formées dans un gaz électronique bidimensionnel situé à 105 nm sous la surface. La connexion avec de grands contacts (représentés par des rectangles) est contrôlée par effet de champ à l'aide de grilles métallique (représentées en jaune) couplées capacitivement, formant ainsi des contacts ponctuels quantiques (QPC). L'échantillon est immergé dans un champ magnétique perpendiculaire correspondant à l'effet hall quantique avec un facteur de remplissage de  $\nu = 2$ . Le courant se propage donc le long de deux canaux de bord chiraux (lignes avec flèches). Sur la configuration illustrée à gauche, les électrodes 1 et 2 sont chacune connectées par un canal parfaitement transmis tandis que l'électrode 3 est connectée par un canal partiellement transmis par le contact ponctuel quantique.

## Bruit hors équilibre dans un circuit quantique dissipatif

### Bruit de grenaille en présence de blocage de Coulomb dynamique

Nous explorons ici le bruit de grenaille induit par une polarisation de tension dans un circuit quantique dissipatif et sa relation avec la conductance électrique lorsqu'un seul canal est en série avec une résistance linéaire. Il est prévu théoriquement que la dépendance en tension de polarisation des deux observables est liée par une relation

de type fluctuation-dissipation [17]. Le circuit est ajusté par effet de champ pour avoir un canal de conduction caractérisé par une probabilité de transmission entièrement réglable en série avec une résistance linéaire formée de  $N$  canaux balistiques en parallèle, émulant ainsi une résistance  $R_{env} = R_K/N$  avec  $R_K = h/e^2 \simeq 25,8$  k $\Omega$  le quantum de résistance et  $N \in \{2, 3\}$ . La conductance d'un tel circuit est renormalisée à basse température et à basse tension ( $eV$ ,  $k_B T \ll NE_C$ , avec  $V$  la tension appliquée à la grande électrode connectée au canal non balistique) par le phénomène de blocage dynamique de Coulomb (DCB): du fait des interactions coulombiennes, la granularité de la charge permet d'exciter les modes électromagnétiques de l'environnement formés par sa capacité et la résistance  $R_{env}$ , ce qui empêche les transferts de charges à faible énergie et réduit ainsi la conductance. De plus, à basse énergie ( $eV$ ,  $k_B T \ll NE_C$ ) ce circuit avec un seul canal non balistique est décrit par la théorie des liquides de Tomonaga-Luttinger (TLL) avec comme paramètre d'interaction  $K = 1/(1 + R_{env}/R_K)$ , comme théoriquement [17] et expérimentalement [20; 21] démontré.

Ici, le bruit mesuré est d'abord comparé aux prédictions de la théorie de diffusion [13], qui est une théorie sans interaction dans laquelle nous injectons la valeur renormalisée mesurée de la conductance par le DCB. Ces prévisions de bruit fournissent une bonne approximation des données. Ils nous permettent également de calculer et de soustraire une contribution relativement faible mais non négligeable du bruit thermique qui permet une comparaison précise du bruit mesuré avec les prédictions TLL uniquement disponibles à température nulle pour le bruit. A notre résolution, les mesures ne permettent pas de distinguer entre les prédictions de la théorie de diffusion utilisant la conductance renormalisée et celles de la théorie TLL : bien que différentes, les deux approches donnent des résultats quantitativement très proches. Cependant, nous pouvons établir la relation de fluctuation-dissipation prévue spécifiquement dans le cadre de la théorie TLL, reliant la variation de la conductance en fonction de la tension à la variation du bruit de grenaille en fonction de la tension. Ces résultats constituent une nouvelle étape dans l'étude des fluctuations de courant dans les liquides Tomonaga-Luttinger et dans les circuits quantiques composites régis par l'interaction de Coulomb.

**Article :**

E.Sivre, H.Duprez, A.Anthore, A. Aassime, F.D. Parmentier, A. Cavanna, A. Ouerghi, U. Gennser et F. Pierre. (en préparation)

### **Bruit de grenaille induit par une différence de température**

Dans cette expérience, nous testons directement les prédictions de la théorie de diffusion pour le bruit de grenaille induit uniquement par une différence de température, en l'absence d'une différence de tension continue. Le circuit est ajusté de la même manière que dans l'expérience précédente (un canal non balistique,  $N$  canaux balistiques). La différence est que des tensions équilibrées de signes opposés ne sont appliquées qu'à travers les canaux balistiques, de sorte que l'îlot métallique central est chauffé par effet Joule sans aucune différence de tension continue à travers le canal imparfaitement transmis. En utilisant des mesures d'auto-corrélation et de corrélation croisée des fluctuations de courant, nous pouvons observer le bruit de grenaille induit par la différence de température à travers le canal imparfait, séparément du bruit de Johnson-Nyquist. Bien que prévu depuis longtemps, ce "bruit de grenaille thermique" n'a été mesuré pour la première fois que très récemment, dans un contact atomique [18]. Nous consolidons ici les résultats de [18] en utilisant un QPC avec un seul canal de probabilité de transmission connue, permettant ainsi une comparaison directe avec la théorie. L'accord quantitatif de nos mesures avec les prédictions établit en outre la théorie de diffusion pour le bruit [13].

#### **Article publié :**

E.Sivre, H.Duprez, A.Anthore, A. Aassime, F.D. Parmentier, A. Cavanna, A. Ouerghi, U. Gennser et F. Pierre. Electronic heat flow and thermal shot noise in quantum circuits. *Nat. Commun.* **10**, 5638 (2019)

## Flux de chaleur dans un circuit composite

### Blocage de Coulomb de la chaleur d'un canal balistique

L'objectif est d'étudier les règles de composition d'impédance thermique pour plusieurs canaux balistiques connectés en parallèle à un petit nœud de circuit flottant. En conséquence, le circuit est réglé de sorte que l'îlot central n'est connecté que par des canaux balistiques  $N$  ( $N \in \{2, 3, 4, 5\}$ ). Une tension continue est appliquée pour chauffer l'îlot central. Par conservation de l'énergie, en régime stationnaire, le flux de chaleur sortant total est égal à la puissance, bien connue, injectée dans l'îlot par effet Joule. Par la mesure du bruit thermique, nous déduisons la température des électrons  $T_\Omega$  dans l'îlot métallique. Ainsi, nous déduisons le flux de chaleur total en fonction de la température. Ce flux de chaleur total comprend deux contributions : le flux de chaleur électronique à travers les canaux de conduction connectés à l'îlot et le transfert de chaleur des électrons aux phonons à l'intérieur de l'îlot. En nous concentrant sur les très basses températures ( $T_\Omega < 25$  mK), où les transferts de chaleur vers les phonons deviennent négligeables, nous observons une nouvelle forme de blocage de Coulomb qui s'applique spécifiquement au flux de chaleur électronique sortant de l'îlot métallique, tandis que la conductance électrique n'est pas affectée. Notre conclusion est en accord avec la théorie [19], mais en violation de la loi de Wiedemann-Franz. Cette réduction du flux thermique correspond à la suppression systématique d'un canal électronique unique pour le transport de chaleur, quel que soit le nombre total de canaux balistiques  $N$ . Les corrélations entre les canaux qui conduisent à une telle réduction sélective du flux de chaleur résultent de l'absence d'accumulation de charge dans l'îlot métallique sur toute la plage de fréquence thermique ( $\omega \lesssim k_B T_\Omega / h$ ), qui est imposée lorsque l'énergie de charge  $E_C$  est suffisamment grande ( $NE_C \gg k_B T_\Omega$ ). Pour des températures plus élevées, on peut séparer le flux de chaleur électronique du transfert de chaleur non négligeable vers les phonons en exploitant le fait que ce dernier ne dépend que de la température et non du nombre de canaux connectés. Cela nous a permis de valider la théorie également au-delà du régime des basses températures, le long du crossover vers une absence de blocage de Coulomb de la chaleur à haute température.

**Article publié :**

E.Sivre, A.Anthore, F.D. Parmentier, A. Cavanna, U. Gennser, A. Ouerghi, Y. Jin et F. Pierre. Heat Coulomb blockade of one ballistic channel. *Nat.Phys.* **14**, 145-148 (2018)

### **Flux de chaleur augmenté par le bruit de grenaille thermique et l'interaction de Coulomb**

L'étude des règles de composition d'impédance thermique est ici poussée un peu plus loin, en incluant dans le circuit un canal non balistique. L'exploitation des connaissances précédemment établies dans le cas balistique nous permet de déterminer les transferts de chaleur des électrons aux phonons à l'intérieur de l'îlot métallique central (qui ne dépend pas de la configuration du circuit). Nous avons ainsi obtenu le transfert de chaleur électronique via  $N + 1$  canaux ( $N \in \{2, 3, 4\}$ ), dont l'un est caractérisé par une probabilité de transmission intermédiaire. Remarquablement, la présence du canal partiellement transmis donne lieu à une contribution supplémentaire au flux de chaleur électronique. Ce phénomène résulte d'un effet combiné de l'interaction de Coulomb et du "bruit de grenaille thermique" associé à la différence de température à travers le canal imparfaitement transmis. Un très bon accord quantitatif est observé entre les données et les nouvelles prédictions théoriques obtenues en étendant l'approche de Fokker-Planck de [19].

#### **Article publié :**

E.Sivre, H.Duprez, A.Anthore, A. Aassime, F.D. Parmentier, A. Cavanna, A. Ouerghi, U. Gennser et F. Pierre. Electronic heat flow and thermal shot noise in quantum circuits. *Nat.Commun.* **10**, 5638 (2019)

#### **Autres travaux publiés non abordés dans cette thèse :**

H. Duprez, E.Sivre, A.Anthore, A. Aassime, A. Cavanna, A. Ouerghi, U. Gennser, and F. Pierre. Macroscopic electron quantum coherence in a solid-state circuit. *PRX* **9**, 021030 (2019)

H. Duprez, E.Sivre, A.Anthore, A. Aassime, A. Cavanna, U. Gennser, and F. Pierre.



Transferring the quantum state of electrons across a metallic island with Coulomb interaction. *Science* **366**(6470), 1243-1247 (2019)

# Appendix D

## Abbreviations and symbols

2DEG	Two dimensional electron gas
DCB	Dynamical Coulomb blockade
QHE	Quantum Hall effect
QPC	Quantum point contact
SET	Single electron transistor
TLL	Tomonaga-luttinger liquid

Table D.1: List of acronyms

$e \simeq 1.60 \times 10^{-19} \text{ C}$	Electron charge
$h \simeq 6.63 \times 10^{-34} \text{ J} \cdot \text{s}$	Planck constant
$\hbar = h/2\pi$	Reduced Planck constant
$k_B \simeq 1.38 \times 10^{-23} \text{ J/K}$	Boltzmann constant
$R_K = h/e^2 \simeq 25.8 \text{ k}\Omega$	Resistance quantum
$G_K = e^2/h$	Conductance quantum
$e^*$	Fractional charge
$C \simeq 3.1 \text{ fF}$	Capacitance of the metallic island
$E_C = e^2/2C$	Charging energy of the metallic island
$N$	Number of ballistic channels
$\tau$	Transmission probability of the non-ballistic channel
$T_0$	Electrons base temperature
$T_\Omega$	Electrons temperature in the central metallic island
$\nu$	Filling factor

Table D.2: List of symbols

## Bibliography

- [1] van Wees, B., van Houten, H., Beenakker, C., Williamson, J., Kouwenhoven, L., van der Marel, D., and Foxon, C. *Physical Review Letters* **60**(9), 848–850 February (1988).
- [2] Wharam, D., Thornton, T., Newbury, R., Pepper, M., Ahmed, H., Frost, J., Hasko, D., Peacock, D., Ritchie, D., and Jones, G. *J. Phys. C* **21**(8), L209–L214 (1988).
- [3] Webb, R. A., Washburn, S., Umbach, C., and Laibowitz, R. *Physical Review Letters* **54**(25), 2696 (1985).
- [4] Ji, Y., Chung, Y., Sprinzak, D., Heiblum, M., Mahalu, D., and Shtrikman, H. *Nature* **422**, 415–418 March (2003).
- [5] Grabert, H. and Devoret, M. H., editors. *Single charge tunneling*. Plenum, new york edition, (1992).
- [6] Giazotto, F. and Martínez-Pérez, M. J. *Nature* **492**(7429), 401–405 December (2012).
- [7] Pekola, J. P. *Nature Physics* **11**(2), 118 (2015).
- [8] Dutta, B., Peltonen, J. T., Antonenko, D. S., Meschke, M., Skvortsov, M. A., Kubala, B., König, J., Winkelmann, C. B., Courtois, H., and Pekola, J. P. *Physical review letters* **119**(7), 077701 (2017).
- [9] Nazarov, Y. *Sov. Phys. JETP* **68**(3), 561–566 (1989).
- [10] Matveev, K. A. *Sov. Phys. JETP* **72**, 892–899 (1991).
- [11] Iftikhar, Z., Jezouin, S., Anthore, A., Gennser, U., Parmentier, F., Cavanna, A., and Pierre, F. *Nature* **526**, 233–236 (2015).

- [12] Iftikhar, Z., Anthore, A., Mitchell, A., Parmentier, F., Gennser, U., Ouerghi, A., Cavanna, A., Mora, C., Simon, P., and Pierre, F. *Science* **360**, 1315–1320 (2018).
- [13] Blanter, Y. M. and Büttiker, M. *Phys. Rep.* **336**, 1–166 (2000).
- [14] Martin, T. and Landauer, R. *Physical Review B* **45**(4), 1742 (1992).
- [15] Büttiker, M. *Phys. Rev. B* **46**, 12485–12507 Nov (1992).
- [16] Büttiker, M. *Phys. Rev. Lett.* **65**, 2901–2904 Dec (1990).
- [17] Safi, I. and Saleur, H. *Phys. Rev. Lett.* **93**, 126602 Sep (2004).
- [18] Lumbroso, O. S., Simine, L., Nitzan, A., Segal, D., and Tal, O. *Nature* **562**(7726), 240 (2018).
- [19] Slobodeniuk, A. O., Levkivskiy, I. P., and Sukhorukov, E. V. *Physical Review B* **88**(16), 165307 (2013).
- [20] Jezouin, S., Albert, M., Parmentier, F., Anthore, A., Gennser, U., Cavanna, A., Safi, I., and Pierre, F. *Nat. Commun.* **4**, 1802 (2013).
- [21] Anthore, A., Iftikhar, Z., Boulat, E., Parmentier, F., Cavanna, A., Ouerghi, A., Gennser, U., and Pierre, F. *Physical Review X* **8**(3), 031075 (2018).
- [22] Glattli, D. C., Jacques, P., Kumar, A., Pari, P., and Saminadayar, L. *Journal of Applied Physics* **81**(11), 7350–7356 (1997).
- [23] Iftikhar, Z., Anthore, A., Jezouin, S., Parmentier, F., Jin, Y., Cavanna, A., Ouerghi, A., Gennser, U., and Pierre, F. *Nat. Commun.* **7**, 12908 (2016).
- [24] Jezouin, S., Iftikhar, Z., Anthore, A., Parmentier, F., Gennser, U., Cavanna, A., Ouerghi, A., Levkivskiy, I., Idrisov, E., Sukhorukov, E., Glazman, L., and Pierre, F. *Nature* **536**, 58–62 (2016).
- [25] Klitzing, K. v., Dorda, G., and Pepper, M. *Phys. Rev. Lett.* **45**, 494–497 Aug (1980).
- [26] Büttiker, M. *Phys. Rev. B* **38**, 9375–9389 Nov (1988).

## BIBLIOGRAPHY

---

- [27] Brouwer, P. and Büttiker, M. *EPL (Europhysics Letters)* **37**(7), 441 (1997).
- [28] Pierre, F., Gougam, A. B., Anthore, A., Pothier, H., Esteve, D., and Birge, N. O. *Phys. Rev. B* **68**, 085413 Aug (2003).
- [29] Dong, Q., Liang, Y. X., Ferry, D., Cavanna, A., Gennser, U., Couraud, L., and Jin, Y. *Applied Physics Letters* **105**(1), 013504 (2014).
- [30] Spietz, L., Lehnert, K. W., Siddiqi, I., and Schoelkopf, R. J. *Science* **300**(5627), 1929–1932 (2003).
- [31] Grabert, H. and Devoret, M. H., editors. *Single charge tunneling*. Plenum, new york edition, (1992).
- [32] Cleland, A. N., Schmidt, J. M., and Clarke, J. *Physica B: Condensed Matter* **165-166**, 979 – 980 (1990). LT-19.
- [33] Holst, T., Esteve, D., Urbina, C., and Devoret, M. *Physical review letters* **73**(25), 3455 (1994).
- [34] Johnson, J. B. *Phys. Rev.* **32**, 97–109 Jul (1928).
- [35] Nyquist, H. *Phys. Rev.* **32**, 110–113 Jul (1928).
- [36] Callen, H. B. and Welton, T. A. *Phys. Rev.* **83**, 34–40 Jul (1951).
- [37] Schottky, W. *Annalen der Physik* **362**(23), 541–567 (1918).
- [38] Kumar, A., Saminadayar, L., Glattli, D. C., Jin, Y., and Etienne, B. *Phys. Rev. Lett.* **76**, 2778–2781 Apr (1996).
- [39] Reznikov, M., Heiblum, M., Shtrikman, H., and Mahalu, D. *Physical Review Letters* **75**(18), 3340 (1995).
- [40] Beenakker, C. W. J. and Büttiker, M. *Phys. Rev. B* **46**, 1889–1892 Jul (1992).
- [41] Roche, P., Ségala, J., Glattli, D., Nicholls, J., Pepper, M., Graham, A., Thomas, K., Simmons, M., and Ritchie, D. *Physical review letters* **93**(11), 116602 (2004).

- [42] Birk, H., de Jong, M. J. M., and Schönenberger, C. *Phys. Rev. Lett.* **75**, 1610–1613 Aug (1995).
- [43] Fendley, P. and Saleur, H. *Physical Review B* **54**(15), 10845 (1996).
- [44] Saminadayar, L., Glattli, D. C., Jin, Y., and Etienne, B. *Phys. Rev. Lett.* **79**, 2526–2529 Sep (1997).
- [45] De-Picciotto, R., Reznikov, M., Heiblum, M., Umansky, V., Bunin, G., , and Mahalu, D. *Nature* **389**, 162–164 (1997).
- [46] de Jong, M. J. M. and Beenakker, C. W. J. *Phys. Rev. B* **51**, 16867–16870 Jun (1995).
- [47] Büttiker, M. *Phys. Rev. Lett.* **57**, 1761–1764 Oct (1986).
- [48] Texier, C. and Büttiker, M. *Phys. Rev. B* **62**, 7454–7458 Sep (2000).
- [49] Oberholzer, S., Bieri, E., Schönenberger, C., Giovannini, M., and Faist, J. *Physical review letters* **96**(4), 046804 (2006).
- [50] Altimiras, C., Gennser, U., Cavanna, A., Mailly, D., and Pierre, F. *Phys. Rev. Lett.* **99**(25), 256805–256808 Dec (2007).
- [51] Parmentier, F. D., Anthore, A., Jezouin, S., Gennser, U., Cavanna, A., and Pierre, F. *Nat. Phys.* **7**, 935–938 (2011).
- [52] Kane, C. and Fisher, M. *Phys. Rev. Lett.* **68**, 1220–1223 Feb (1992).
- [53] Caldeira, A. O. and Leggett, A. J. *Physical Review Letters* **46**(4), 211 (1981).
- [54] Odintsov, A. A., Falci, G., and Schön, G. *Phys. Rev. B* **44**, 13089–13092 Dec (1991).
- [55] Zamoum, R., Crépieux, A., and Safi, I. *Physical Review B* **85**(12), 125421 (2012).
- [56] Pines, D. and Nozières, P. *The Theory of Quantum Liquids*. CRC Press, (1966).

## BIBLIOGRAPHY

---

- [57] Haldane, F. M. *J. Phys. C* **14**, 2585–2609 (1981).
- [58] Tomonaga, S. *Prog. Theor. Phys.* **5**, 544–569 (1950).
- [59] Luttinger, J. *J. Math. Phys.* **4**(9), 1154–1162 (1963).
- [60] Jompol, Y., Ford, C. J. B., Griffiths, J. P., Farrer, I., Jones, G. A. C., Anderson, D., Ritchie, D. A., Silk, T. W., and Schofield, A. J. *Science* **325**(5940), 597–601 (2009).
- [61] Hashisaka, M., Hiyama, N., Akiho, T., Muraki, K., and Fujisawa, T. *Nat. Phys.* **13**, 559–562 (2017).
- [62] Steinberg, H., Barak, G., Yacoby, A., Pfeiffer, L., West, K., Halperin, B., and Le Hur, K. *Nat. Phys.* **4**, 116 (2008).
- [63] Prokudina, M. G., Ludwig, S., Pellegrini, V., Sorba, L., Biasiol, G., and Khrapai, V. S. *Phys. Rev. Lett.* **112**, 216402 May (2014).
- [64] Kamata, H., Kumada, N., Hashisaka, M., Muraki, K., and Fujisawa, T. *Nat. Nanotech.* **9**, 177–181 (2014).
- [65] Freulon, V., Marguerite, A., Berroir, J., Placais, B., Cavanna, A., Jin, Y., and Feve, G. *Nat. Commun.* **6**, 6854 (2015).
- [66] Klanjšek, M., Mayaffre, H., Berthier, C., Horvatić, M., Chiari, B., Piovesana, O., Bouillot, P., Kollath, C., Orignac, E., Citro, R., et al. *Physical review letters* **101**(13), 137207 (2008).
- [67] Fendley, P., Ludwig, A., and Saleur, H. *Phys. Rev. Lett.* **74**, 3005–3008 Apr (1995).
- [68] Galperin, Y. M. *Lecture Notes (Lund University Press, 1998)* (1998).
- [69] Giamarchi, T. *Quantum Physics in One Dimension*. Oxford University Press, (2003).
- [70] Caux, J.-S. and Smith, C. M. *Journal of Physics: Condensed Matter* **29**(15), 151001 (2017).



- [71] Jezouin, S. *Transport à travers un canal quantique élémentaire: action du circuit, quantification de la charge et limite quantique du courant de chaleur*. PhD thesis, Paris 6, (2014).
- [72] Fendley, P., Ludwig, A., and Saleur, H. *Phys. Rev. B* **52**, 8934–8950 Sep (1995).
- [73] Laughlin, R. B. *Physical Review Letters* **50**(18), 1395 (1983).
- [74] Boulat, E. *In preparation* (2019).
- [75] Kane, C. and Fisher, M. P. *Physical review letters* **72**(5), 724 (1994).
- [76] Fendley, P., Ludwig, A., and Saleur, H. *Physical review letters* **75**(11), 2196 (1995).
- [77] Kapfer, M., Roulleau, P., Santin, M., Farrer, I., Ritchie, D., and Glattli, D. *Science* **363**(6429), 846–849 (2019).
- [78] Crépieux, A., Devillard, P., and Martin, T. *Physical Review B* **69**(20), 205302 (2004).
- [79] Bisognin, R., Bartolomei, H., Kumar, M., Safi, I., Berroir, J.-M., Bocquillon, E., Plaçais, B., Cavanna, A., Gennser, U., Jin, Y., et al. *Nature communications* **10**(1), 1708 (2019).
- [80] Gabelli, J., Fève, G., Berroir, J.-M., Plaçais, B., Cavanna, A., Etienne, B., Jin, Y., and Glattli, D. *Science* **313**(5786), 499–502 (2006).
- [81] Cui, L., Jeong, W., Hur, S., Matt, M., Klöckner, J. C., Pauly, F., Nielaba, P., Cuevas, J. C., Meyhofer, E., and Reddy, P. *Science* **355**(6330), 1192–1195 (2017).
- [82] Jezouin, S., Parmentier, F. D., Anthore, A., Gennser, U., Cavanna, A., Jin, Y., and Pierre, F. *Science* **342**(6158), 601–604 (2013).
- [83] Karimi, B., Brange, F., Samuelsson, P., and Pekola, J. P. *arXiv preprint arXiv:1904.05041* (2019).

## BIBLIOGRAPHY

---

- [84] Sivre, E., Anthore, A., Parmentier, F., Cavanna, A., Gennser, U., Ouerghi, A., Jin, Y., and Pierre, F. *Nat. Phys.* **14**, 145–148 (2018).
- [85] Butcher, P. N. *J. Phys.: Condens. Matter* **2**(22), 4869–4878 (1990).
- [86] Sivan, U. and Imry, Y. *Phys. Rev. B* **33**, 551–558 Jan (1986).
- [87] Chiatti, O., Nicholls, J. T., Proskuryakov, Y. Y., Lumpkin, N., Farrer, I., and Ritchie, D. A. *Phys. Rev. Lett.* **97**, 056601–056604 Aug (2006).
- [88] Molenkamp, L. W., Gravier, T., van Houten, H., Buijk, O. J. A., Mabesoone, M. A. A., and Foxon, C. T. *Phys. Rev. Lett.* **68**, 3765–3768 Jun (1992).
- [89] Rego, L. and Kirczenow, G. *Phys. Rev. B* **59**(20), 13080–13086 (1999).
- [90] Schwab, K., Henriksen, E., Worlock, J., and Roukes, M. *Nature* **404**(6781), 974–977 (2000).
- [91] Meschke, M., Guichard, W., and Pekola, J. P. *Nature* **444**(7116), 187–190 November (2006).
- [92] Banerjee, M., Heiblum, M., Umansky, V., Feldman, D. E., Oreg, Y., and Stern, A. *Nature* **559**(7713), 205 (2018).
- [93] Wellstood, F. C., Urbina, C., and Clarke, J. *Phys. Rev. B* **49**, 5942–5955 Mar (1994).
- [94] Karvonen, J., Taskinen, L., and Maasilta, I. *Physical Review B* **72**(1), 012302 (2005).
- [95] Sergeev, A. and Mitin, V. *Physical Review B* **61**(9), 6041–6047 March (2000).
- [96] Kindermann, M. and Nazarov, Y. V. *Phys. Rev. Lett.* **91**(13), 136802–136805 Sep (2003).
- [97] Yeyati, A. L., Martin-Rodero, A., Esteve, D., and Urbina, C. *Phys. Rev. Lett.* **87**(4), 046802–046805 Jul (2001).
- [98] Blanter, Y. M. and Sukhorukov, E. V. *Phys. Rev. Lett.* **84**, 1280–1283 Feb (2000).

- [99] Echternach, P., Thoman, M., Gould, C., and Bozler, H. *Physical Review B* **46**(16), 10339 (1992).
- [100] Banerjee, M., Heiblum, M., Rosenblatt, A., Oreg, Y., Feldman, D. E., Stern, A., and Umansky, V. *Nature* **545**(7652), 75 (2017).
- [101] Bocquillon, E., Freulon, V., Berroir, J., Placais, B., Cavanna, A., Jin, Y., and Feve, G. *Nat. Commun.* **4**, 1839 (2013).
- [102] Levkivskiy, I. P. and Sukhorukov, E. V. *Phys. Rev. B* **78**, 045322 Jul (2008).
- [103] Caves, C. M. *Physical Review E* **47**(6), 4010 (1993).
- [104] Idrisov, E. G., Levkivskiy, I. P., and Sukhorukov, E. V. *Phys. Rev. Lett.* **121**, 026802 Jul (2018).
- [105] Duprez, H., Sivre, E., Anthore, A., Aassime, A., Cavanna, A., Gennser, U., and Pierre, F. *arXiv preprint arXiv:1902.07569* (2019).

# Heat Coulomb Blockade of One Ballistic Channel

E. Sivre,<sup>1</sup> A. Anthore,<sup>1,2</sup> F.D. Parmentier,<sup>1</sup> A. Cavanna,<sup>1</sup> U. Gennser,<sup>1</sup> A. Ouerghi,<sup>1</sup> Y. Jin,<sup>1</sup> and F. Pierre<sup>1,\*</sup>

<sup>1</sup>Centre de Nanosciences et de Nanotechnologies (C2N), CNRS,  
Univ Paris Sud-Université Paris-Saclay, 91120 Palaiseau, France

<sup>2</sup>Univ Paris Diderot-Sorbonne Paris Cité

Quantum mechanics and Coulomb interaction dictate the behavior of small circuits. The thermal implications cover fundamental topics from quantum control of heat to quantum thermodynamics, with prospects of novel thermal machines and an ineluctably growing influence on nanocircuit engineering<sup>1,2</sup>. Experimentally, the rare observations thus far include the universal thermal conductance quantum<sup>3–7</sup> and heat interferometry<sup>8</sup>. However, evidences for many-body thermal effects paving the way to markedly different heat and electrical behaviors in quantum circuits remain wanting. Here we report on the observation of the Coulomb blockade of electronic heat flow from a small metallic circuit node, beyond the widespread Wiedemann-Franz law paradigm. We demonstrate this thermal many-body phenomenon for perfect (ballistic) conduction channels to the node, where it amounts to the universal suppression of precisely one quantum of conductance for the transport of heat, but none for electricity<sup>9</sup>. The inter-channel correlations that give rise to such selective heat current reduction emerge from local charge conservation, in the floating node over the full thermal frequency range ( $\lesssim \text{temperature} \times k_B/h$ ). This observation establishes the different nature of the quantum laws for thermal transport in nanocircuits.

The non-interacting ‘scattering’ approach to quantum transport describes coherent conductors as a set of independent channels<sup>10,11</sup>. However, in circuits with small floating nodes, the Coulomb interaction induces inter-channel correlations, including among distinct conductors connected to the same node. Consequences are wide-ranging, from the emblematic ‘Coulomb blockade’ suppression of electrical conduction at low voltages and temperatures<sup>12–15</sup> to exotic ‘charge’ Kondo physics<sup>16,17</sup>. Remarkably, Coulomb effects can be profoundly different in the charge and heat sectors, in violation of the standard Wiedemann-Franz ratio between electronic conductances of heat and electricity ( $\pi^2 k_B^2 T/3e^2$  with  $e$  the elementary electron charge,  $k_B$  the Boltzmann constant,  $T$  the temperature). For ballistic conductors, along which electrons are never reflected backward, the electrical conductance  $G_{\text{elec}}$  is predicted<sup>18–20</sup> and found<sup>21–23</sup> immune against Coulomb blockade, essentially because charge flow is noiseless ( $G_{\text{elec}} = N \times G_Q^e$ , with  $N$  the number of channels,  $G_Q^e = e^2/h$  the electrical conductance quantum and  $h$  the Planck constant). Nonetheless, theory predicts<sup>9</sup> a universal suppression of the heat conductance  $G_{\text{heat}}$  across ballistic conductors connected to a

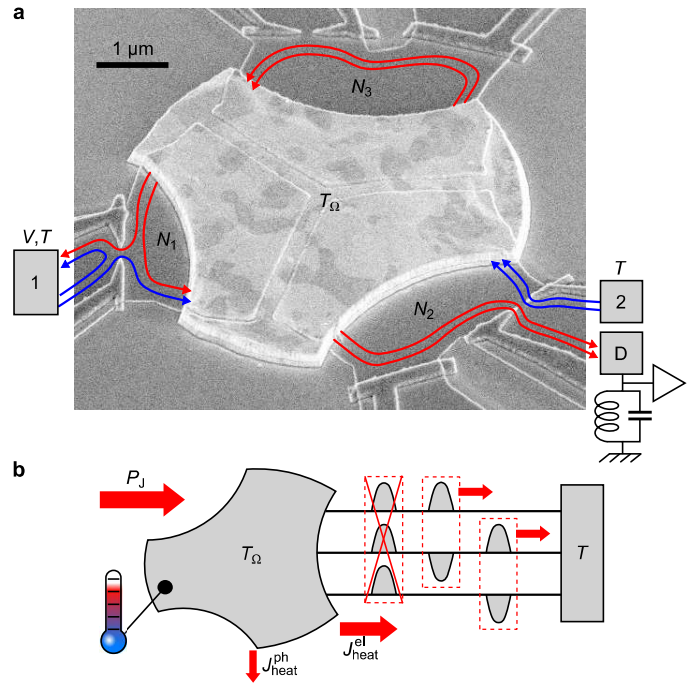


**Figure 1. Experimental setup.** **a**, Device micrograph. A small metallic island (brighter) is in galvanic contact with three distinct branches of a two-dimensional electron gas (darker grey; etched trenches visible underneath the island). The connection to large electrodes further away (represented by rectangles for branches 1 and 2) is controlled by field effect using capacitively coupled gates (grey with a bright delimitation). The sample is set in the integer quantum Hall regime at filling factor  $\nu = 2$ , where the current propagates along two chiral edge channels (lines with arrows). In the displayed configuration, electrodes 1, 2 and 3 are connected by, respectively, one, two and zero fully transmitted channels ( $N_1 = 1, N_2 = 2, N_3 = 0$ ). Applying a dc bias voltage  $V$  to electrode 1 dissipates the Joule power  $P_J$  into the island. The resulting temperature rise  $T_\Omega - T$  is determined from the measured increase of electrical fluctuations on electrode D. **b**, Heat flow schematic. Injected power and net outgoing heat current exactly compensate each other in the steady state ( $P_J = J_{\text{heat}}^{\text{el}} + J_{\text{heat}}^{\text{ph}}$ ). The  $N$  ballistic electronic channels (here  $N = 3$  shown as black lines) can be mapped onto one channel-symmetric charge mode suppressed by the heat Coulomb blockade (crossed symmetric charge pulses), and  $N - 1$  independent dipole (neutral) modes decoupled from the island’s charge (antisymmetric charge pulses).

small, floating circuit node by precisely one quantum of thermal conductance  $G_Q^h = \pi^2 k_B^2 T/3h$  ( $G_{\text{heat}} = (N - 1) \times G_Q^h$ ), as presently observed experimentally.

\* e-mail: frederic.pierre@u-psud.fr

This violation of the Wiedemann-Franz relation does not result from an energy dependent electronic density of states, nor from the high-pass energy filtering across single electron transistors<sup>24,25</sup>. We describe the underlying mechanism in the spirit of Ref. 9, specifically focusing on a metallic node connected to large voltage biased electrodes through a total of  $N$  ballistic channels (Fig. 1a,b). Electronic heat currents can be viewed as the propagation of electrical current fluctuations within a broad frequency bandwidth, extending up to the thermal cutoff  $\sim k_B T/h$ . For a voltage biased electrode, the emitted fluctuations result from the thermal broadening of the electron Fermi distribution. For a floating circuit node, charge conservation imposes that the thermal emission of a net charge through a current pulse is also accompanied by an opposite charge accumulation in the node. Such charge accumulation relaxes in the characteristic  $RC$  time (with  $R = 1/NG_Q^e$  here, and  $C$  the node geometrical capacitance), which suppresses the overall (net) charge fluctuations emitted from the node (thermal plus subsequent relaxation) at frequencies below  $\sim 1/RC$ . At low temperature  $k_B T \ll h/RC$  ( $k_B T \ll NE_C$  here, with  $E_C \equiv e^2/2C$  the node charging energy), where this suppression covers the full thermal frequency range, it can result in an important reduction of the total heat current. Note that the electrical fluctuations emitted from such a floating node were previously explored in the context of using a ‘voltage probe’ to emulate inelastic mechanisms within the scattering theory of quantum transport (see e.g. Ref. 26 and references within). An intuitive way to understand why, for ballistic conductors this reduction amounts universally to one heat transport channel, is to note<sup>9</sup> that  $N$  ballistic electronic channels can be mapped onto a single charge mode (e.g. identical current fluctuations on all electronic channels) and  $N - 1$  independent neutral modes (e.g. opposite current fluctuations on each of  $N - 1$  pairs of electronic channels), as schematically illustrated Fig. 1b. The  $N - 1$  ballistic neutral modes are completely decoupled from the global charge of the island, and therefore contribute each by one (universal) quantum of thermal conductance  $G_Q^h$ . In contrast, the electrical current fluctuations propagating along the single charge mode are directly connected with fluctuations of the node’s charge. Negligible charge accumulation in the node for frequencies  $\lesssim k_B T/h$  therefore completely blocks the charge mode and suppresses its contribution to heat transport, resulting in  $G_{\text{heat}} = (N - 1) \times G_Q^h$ .

The experiment expands on an approach introduced to measure the thermal conductance quantum across electronic channels<sup>5</sup>. In contrast to previous works<sup>5,6</sup>, the present implementation down to electronic temperatures of 8 mK (Methods) allows for the direct observation of the heat Coulomb blockade, which requires that energy transfers between electrons and phonons in the node remain negligible with respect to those through one ballistic channel. The device consists of a central metallic island (the circuit node, see Fig. 1a) separately connected to three large electrodes indexed by

$i \in \{1, 2, 3\}$  through, respectively,  $N_i$  ballistic quantum channels ( $N = N_1 + N_2 + N_3$ ). A Joule power  $P_J = V^2 G_P/2$  controlled by the dc voltage  $V$  applied to electrode 1 dissipates into the electronic fluid within the island (the remaining voltage generator power going into the large electrodes, see Methods), with electrodes 2 and 3 being grounded and  $G_P$  the corresponding conductance across the device (here,  $G_P = G_Q^e/[N_1^{-1} + (N_2 + N_3)^{-1}]$ ). As a result, the metallic island heats up to a steady-state electronic temperature  $T_\Omega > T$  (with  $T$  the base electronic temperature), such that  $P_J$  and net outgoing heat flow  $J_{\text{heat}}$  exactly compensate ( $P_J = J_{\text{heat}}$ ). The determination of  $T_\Omega$  through thermal noise measurements therefore directly provides the  $J_{\text{heat}} - (T_\Omega - T)$  characteristics. In general,  $J_{\text{heat}}$  is the sum of different contributions, including mainly the electronic heat current  $J_{\text{heat}}^{\text{el}}(N, T_\Omega, T)$  and thermal transfers to the substrate phonons  $J_{\text{heat}}^{\text{ph}}(T_\Omega, T)$ :  $J_{\text{heat}} \simeq J_{\text{heat}}^{\text{el}} + J_{\text{heat}}^{\text{ph}}$ . However, at  $T_\Omega < 20$  mK, the rapidly decreasing energy transfers toward phonons are found to become negligible such that  $P_J = J_{\text{heat}} \simeq J_{\text{heat}}^{\text{el}}$ .

The ballistic electronic channels are realized in a high-mobility Al(Ga)As two-dimensional electron gas (2DEG), tuned in the integer quantum Hall regime to the filling factor  $\nu = 2$  with an applied perpendicular magnetic field  $B \simeq 4.1$  T. Without loss of generality, we benefit from the topologically protected ballistic character of the chiral quantum Hall channels (lines with arrows in Fig. 1a). With  $\nu$  channels propagating along each edge, it is possible to adjust separately  $N_i \in \{0, 1, 2\}$  using the field effect. The device was tuned to  $N \in \{2, 3, 4, 5\}$  with at least one ballistic channel connecting the central island to both the large electrodes one and two ( $N_1 = 1$ ,  $N_2 \in \{1, 2\}$  and  $N_3 \in \{0, 1, 2\}$ , except for tests in Methods). The micrometer-scale metallic island, mainly composed of gold, is associated with a continuous electronic density of states and a charging energy  $E_C \simeq k_B \times 0.3$  K (Methods). By thermal annealing, we achieve negligible levels of electron reflection probability at the 2DEG/island interface, as detailed per channel in Methods. This is essential not only to reach the ballistic limit, but also because residual reflections would impede the noise thermometry through additional quantum shot noise. The electron temperature is obtained from electrical current fluctuations, resolved down to a statistical uncertainty of  $\pm 5 \cdot 10^{-32}$  A<sup>2</sup>/Hz at frequencies near 1 MHz, using a homemade preamplifier<sup>27</sup> cooled to 3.9 K. Quantum shot noise measurements provide the in-situ calibrations of the noise amplification chain gain ( $\pm 0.1\%$ , all uncertainties and displayed error bars are statistical standard errors), and of the base electronic temperature  $T \simeq 8$  mK ( $\pm 1\%$ , further confirmed by dynamical Coulomb blockade thermometry<sup>28</sup>, see Methods). At non-zero Joule power, the temperature increase  $T_\Omega - T$  of the metallic island electrons is directly connected to a rise in emitted current noise. In the spirit of the robust Johnson-Nyquist thermometry, the excess noise  $S_{\text{exc}}$  measured on the floating electrode D (Fig. 1a) with respect to the noise

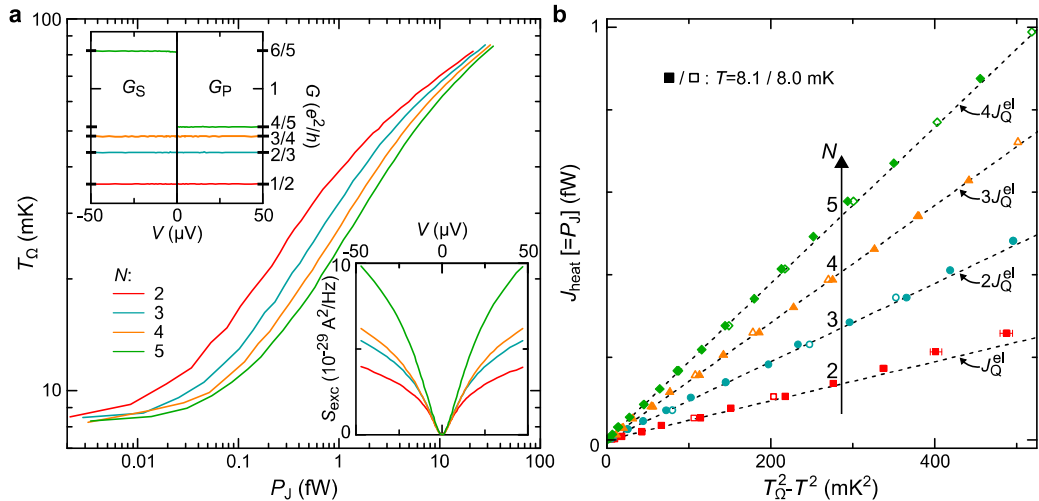


**Figure 2. Heat Coulomb blockade of one ballistic channel.** **a**, The island electron temperature  $T_\Omega$  is plotted versus dissipated Joule power  $P_J$ , for different numbers  $N$  of connected ballistic channels. It is obtained from the excess noise spectral density  $S_{\text{exc}}$  measured electrode D, shown in the bottom-right inset versus the dc voltage  $V$  applied to electrode 1:  $T_\Omega = T + S_{\text{exc}}/(2k_B G_S)$ ,  $P_J = V^2 G_P/2$ . Top-left inset, the device electrical conductances  $G_{S,P}$  (lines, see text) match their expected quantum limited values (superimposed thick ticks on side axis) independently of  $V$ : they are not reduced by Coulomb blockade. **b**, Symbols (statistical uncertainties shown when distinctly larger) represent the overall heat flow ( $J_{\text{heat}} = P_J$ ) displayed versus  $T_\Omega^2 - T^2$ , at low temperatures where electron-phonon interactions are reduced ( $T_\Omega < 25$  mK). The nearby straight dashed lines show  $(N - 1) \times J_Q^{\text{el}}$ , corresponding to a systematic heat current suppression of  $1 \times J_Q^{\text{el}}$ .

at  $V = 0$  reads<sup>5,26,29</sup>:  $S_{\text{exc}} = 2G_S k_B (T_\Omega - T)$ , with  $G_S$  the electrical conductance across the device from electrode 2 to electrodes 1 and 3 (in absence of electrical Coulomb blockade,  $G_S = G_Q^e/[N_2^{-1} + (N_1 + N_3)^{-1}]$ ). Note that further tests made in order to eliminate possible experimental artifacts are described in Methods.

In Fig. 2a we show measurements of the excess noise spectral density  $S_{\text{exc}}$  (bottom-right inset) and of the conductances  $G_S$  (left side of top-left inset) and  $G_P$  (right side of top-left inset), all as a function of the dc voltage  $V$  applied to electrode 1. Each color corresponds to one device configuration  $N [N_1, N_2, N_3] \in \{2 [1, 1, 0], 3 [1, 1, 1], 4 [1, 1, 2], 5 [1, 2, 2]\}$ , with a color code fixed from now on. The island heating is manifested in the increase of  $S_{\text{exc}}$  at finite  $V$ . In contrast, both  $G_S$  and  $G_P$  remain indistinguishable from their maximum quantum limit (respectively  $G_Q^e/[N_2^{-1} + (N_1 + N_3)^{-1}]$  and  $G_Q^e/[N_1^{-1} + (N_2 + N_3)^{-1}]$ , displayed as thick ticks), independently of  $V$ . This demonstrates the absence of Coulomb blockade reduction of the electrical conductance across ballistic channels, at an experimental accuracy better than 0.1% (see also Refs 21–23). Lines in the main panel of Fig. 2a represent, in a log-log scale, the electron temperature in the metallic island,  $T_\Omega$ , versus the injected Joule power  $P_J$ , with  $T_\Omega$  obtained from  $S_{\text{exc}}$  and the separately calibrated base temperature  $T \simeq 8.1$  mK. As generally expected,  $T_\Omega$  is higher when there are fewer electronic channels to evacuate the dissipated  $P_J$ . Figure 2b displays as symbols the same data, as well as a subsequent run at  $T \simeq 8.0$  mK, but now as the net heat flow  $J_{\text{heat}} = P_J$  versus  $T_\Omega^2 - T^2$ , and focusing on low temperat-

ures ( $T_\Omega < 25$  mK) where the phonon contribution  $J_{\text{heat}}^{\text{ph}}$  is reduced and where a full suppression of one electronic thermal channel is predicted<sup>9</sup> (Methods). The straight dashed line closest to the data for  $N$  ballistic channels is  $(N - 1) \times J_Q^{\text{el}}$ , with  $J_Q^{\text{el}} = \pi^2 k_B^2 (T_\Omega^2 - T^2)/6h$  the quantum limit of heat flow per electronic channel. The mere observation that  $J_{\text{heat}}$  is well below predictions for  $N$  independent ballistic channels ( $N \times J_Q^{\text{el}}$ ) directly demonstrates the specific suppression of heat transport from small circuit nodes, whereas electrical transport remains at the maximum quantum limit. Moreover, we find at such low-temperatures a high-precision agreement with heat Coulomb blockade predictions for electronic heat flow, both in the quantitative prediction of a universal suppression of exactly one electronic channel whatever  $N$  and in the temperature power-law  $\propto (T_\Omega^2 - T^2)$ . This direct demonstration of heat Coulomb blockade in the absence of electrical Coulomb blockade constitutes the central result of the present work (see Methods for additional tests establishing the robustness of this observation).

Theory<sup>9</sup> further predicts quantitatively a crossover of the electronic heat flow from  $(N - 1) \times J_Q^{\text{el}}$  to  $N \times J_Q^{\text{el}}$ , which extends mostly over one temperature decade around  $NE_C/\pi k_B$  (Methods). However, the relatively important and rapidly increasing thermal transfers between electrons and phonons at these higher temperatures prevent a direct observation from  $J_{\text{heat}}(T_\Omega)$ . Following Ref. 5, we separately consider the electronic heat current by focusing on the difference to the same value of  $T_\Omega$  between two numbers of connected ballistic channels ( $N \in \{2, 3, 5\}$  and  $N_{\text{ref}} = 4$ ). Indeed, any mechanism that does not depend

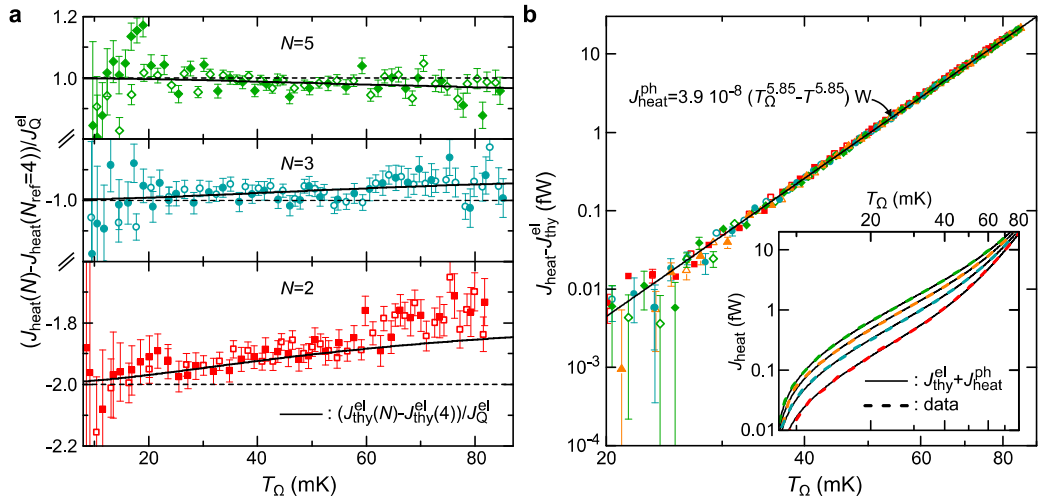


**Figure 3. Heat Coulomb blockade crossover and additional mechanisms.** **a**, Symbols (continuous lines) show the measured (predicted) heat current variation when changing  $N$  from  $N_{\text{ref}} = 4$  at fixed  $T_{\Omega}$ , renormalized by the quantum limit per channel  $J_{\text{Q}}^{\text{el}}$ . The crossover toward the low-temperature heat Coulomb blockade of one ballistic channel specifically shows as a difference with respect to the nearby horizontal dashed line, whereas electron-phonon thermal transfers are canceled out. **b**, Subtracting heat Coulomb blockade predictions, the displayed remaining part of the heat current (symbols) collapse onto a single curve for all  $N \in \{2, 3, 4, 5\}$ , fitted by a  $T_{\Omega}^{5.85}$  functional (line,  $J_{\text{heat}}^{\text{ph}}$ ). Inset, direct comparison between  $J_{\text{thy}}^{\text{el}} + J_{\text{heat}}^{\text{ph}}$  (black continuous lines) and measured total heat current  $J_{\text{heat}}$  (superimposed colored dashed lines).

on  $N$  cancels out in  $J_{\text{heat}}(N, T, T_{\Omega}) - J_{\text{heat}}(N_{\text{ref}}, T, T_{\Omega})$ , including the electron-phonon contribution and the universal low-temperature suppression of one ballistic channel. However, signatures of the  $(N - 1) \times J_{\text{Q}}^{\text{el}}$  to  $N \times J_{\text{Q}}^{\text{el}}$  crossover can be observed since the temperature at which the crossover takes place increases with  $N$  (Methods). Measurements of  $J_{\text{heat}}(N \in \{2, 3, 5\}, T, T_{\Omega}) - J_{\text{heat}}(N_{\text{ref}} = 4, T, T_{\Omega})$ , normalized by the quantum limit of heat flow per channel  $J_{\text{Q}}^{\text{el}}(T, T_{\Omega})$ , are shown as symbols versus  $T_{\Omega}$  in Fig. 3a. In this representation, deviations from  $N - N_{\text{ref}}$  ( $N - 4$ , horizontal dashed lines) are specific signatures of the heat Coulomb blockade crossover. The quantitative prediction, without any fitting parameter, of the full heat Coulomb blockade theory (continuous lines, Methods) closely matches the data. For  $N - N_{\text{ref}} = \pm 1$  ( $N \in \{3, 5\}$ ,  $N_{\text{ref}} = 4$ ) the crossover signal is small, barely discernible at experimental accuracy, although in sign and magnitude agreement with predictions. For  $N - N_{\text{ref}} = -2$  ( $N = 2$ ,  $N_{\text{ref}} = 4$ ) the larger crossover signal precisely follow the theoretical prediction up to  $T_{\Omega} \approx 60$  mK, while at higher  $T_{\Omega} \gtrsim 60$  mK the scatter of the data points rapidly increases due to the overwhelming (subtracted) electron-phonon contribution  $J_{\text{heat}}^{\text{ph}}$ . These observations further establish experiment-

ally the full heat Coulomb blockade theory for ballistic channels at arbitrary temperatures, beyond the universal low-temperature suppression of one quantum channel.

We now investigate the additional heat transfer mechanisms at work in our device. The main panel of Fig. 3b shows as symbols, in a log-log scale versus  $T_{\Omega}$ , the measured  $J_{\text{heat}}(N)$  reduced by the heat Coulomb blockade prediction for  $N$  ballistic electronic channels. We observe that the reduced data collapse for all  $N$  onto a single curve, which is closely reproduced by the functional  $3.9 \cdot 10^{-8} (T_{\Omega}^{5.85} - T^{5.85})$  W (continuous line). This compares well with theoretical expectations for the electron-phonon contribution  $J_{\text{heat}}^{\text{ph}}$  in disordered conductors, where a temperature exponent of 4 or 6 is predicted depending on the nature of disorder<sup>30</sup>. In the inset of Fig. 3b, we directly confront the measured  $J_{\text{heat}}(N \in \{2, 3, 4, 5\}, T_{\Omega})$  (colored dashed lines) with the essentially indistinguishable calculations (black continuous lines) obtained by adding up the full heat Coulomb blockade prediction and the above  $T_{\Omega}^{5.85}$  functional attributed to electron-phonon interactions.

Finally, we point out that the presently observed heat Coulomb blockade of one ballistic channel should be considered when exploiting the total outgoing heat flow from a floating node to investigate elusive exotic states<sup>6</sup>.

[1] Pekola, J. Towards quantum thermodynamics in electronic circuits. *Nat. Phys.* **11**, 118–123 (2015).  
 [2] Vinjanampathy, S. & Anders, J. Quantum thermody-

namics. *Contemp. Phys* **57**, 545–579 (2016).  
 [3] Schwab, K., Henriksen, E., Worlock, J. & Roukes, M. Measurement of the quantum of thermal conductance.

- Nature* **404**, 974–977 (2000).
- [4] Meschke, M., Guichard, W. & Pekola, J. P. Single-mode heat conduction by photons. *Nature* **444**, 187–190 (2006).
- [5] Jezouin, S. *et al.* Quantum Limit of Heat Flow Across a Single Electronic Channel. *Science* **342**, 601–604 (2013).
- [6] Banerjee, M. *et al.* Observed Quantization of Anyonic Heat Flow. *Nature* **545**, 75–79 (2017).
- [7] Cui, L. *et al.* Quantized thermal transport in single-atom junctions. *Science* **355**, 1192–1195 (2017).
- [8] Giazotto, F. & Martínez-Pérez, M. J. The Josephson heat interferometer. *Nature* **492**, 401–405 (2012).
- [9] Slobodeniuk, A., Levkivskiy, I. & Sukhorukov, E. Equilibration of quantum Hall edge states by an Ohmic contact. *Phys. Rev. B* **88**, 165307 (2013).
- [10] Landauer, R. Residual resistivity dipoles. *Z. Phys. B* **21**, 247–254 (1975).
- [11] Büttiker, M. Four-Terminal Phase-Coherent Conductance. *Phys. Rev. Lett.* **57**, 1761–1764 (1986).
- [12] Kulik, I. & Shekhter, R. Kinetic phenomena and charge discreteness effects in granulated media. *Sov. Phys. JETP* **41**, 308–316 (1975).
- [13] Averin, D. & Likharev, K. Coulomb blockade of single-electron tunneling, and coherent oscillations in small tunnel junctions. *J. Low Temp. Phys.* **62**, 345–373 (1986).
- [14] Nazarov, Y. Anomalous current-voltage characteristics of tunnel junctions. *Sov. Phys. JETP* **68**, 561–566 (1989).
- [15] Grabert, H. & Devoret, M. H. (eds.). *Single charge tunneling* (1992), plenum, new york edn.
- [16] Matveev, K. A. Quantum fluctuations of the charge of a metal particle under the Coulomb blockade conditions. *Sov. Phys. JETP* **72**, 892–899 (1991).
- [17] Iftikhar, Z. *et al.* Two-channel Kondo effect and renormalization flow with macroscopic quantum charge states. *Nature* **526**, 233–236 (2015).
- [18] Flensberg, K. Capacitance and conductance of mesoscopic systems connected by quantum point contacts. *Phys. Rev. B* **48**, 11156–11166 (1993).
- [19] Yeyati, A. L., Martin-Rodero, A., Esteve, D. & Urbina, C. Direct Link between Coulomb Blockade and Shot Noise in a Quantum-Coherent Structure. *Phys. Rev. Lett.* **87**, 046802–046805 (2001).
- [20] Kindermann, M. & Nazarov, Y. V. Interaction Effects on Counting Statistics and the Transmission Distribution. *Phys. Rev. Lett.* **91**, 136802–136805 (2003).
- [21] Altimiras, C., Gennser, U., Cavanna, A., Mailly, D. & Pierre, F. Experimental Test of the Dynamical Coulomb Blockade Theory for Short Coherent Conductors. *Phys. Rev. Lett.* **99**, 256805 (2007).
- [22] Parmentier, F. D. *et al.* Strong back-action of a linear circuit on a single electronic quantum channel. *Nat. Phys.* **7**, 935–938 (2011).
- [23] Jezouin, S. *et al.* Tomonaga-Luttinger physics in electronic quantum circuits. *Nat. Comm.* **4**, 1802 (2013).
- [24] Altimiras, C. *et al.* Chargeless Heat Transport in the Fractional Quantum Hall Regime. *Phys. Rev. Lett.* **109**, 026803 (2012).
- [25] Dutta, B. *et al.* Thermal Conductance of a Single-Electron Transistor. *Phys. Rev. Lett.* **119**, 077701 (2017).
- [26] Blanter, Y. M. & Büttiker, M. Shot Noise in Mesoscopic Conductors. *Phys. Rep.* **336**, 1–166 (2000).
- [27] Liang, Y., Dong, Q., Gennser, U., Cavanna, A. & Jin, Y. Input Noise Voltage Below  $1\text{ nV}/\text{Hz}^{1/2}$  at 1 kHz in the HEMTs at 4.2 K. *J. Low Temp. Phys.* **167**, 632–637 (2012).
- [28] Iftikhar, Z. *et al.* Primary thermometry triad at 6 mK in mesoscopic circuits. *Nat. Commun.* **7**, 12908 (2016).
- [29] Blanter, Y. M. & Sukhorukov, E. V. Semiclassical Theory of Conductance and Noise in Open Chaotic Cavities. *Phys. Rev. Lett.* **84**, 1280–1283 (2000).
- [30] Sergeev, A. & Mitin, V. Electron-phonon interaction in disordered conductors: Static and vibrating scattering potentials. *Phys. Rev. B* **61**, 6041–6047 (2000).
- [31] Brouwer, P. W. & Büttiker, M. Charge-relaxation and dwell time in the fluctuating admittance of a chaotic cavity. *Europhys. Lett.* **37**, 441–446 (1997).
- [32] Pierre, F. *et al.* Dephasing of electrons in mesoscopic metal wires. *Phys. Rev. B* **68**, 085413 (2003).
- [33] Rajauria, S. *et al.* Electron and Phonon Cooling in a Superconductor-Normal Metal-Superconductor Tunnel Junction. *Phys. Rev. Lett.* **99**, 047004 (2007).

**Acknowledgments.** This work was supported by the French RENATECH network, the national French program ‘Investissements d’Avenir’ (Labex NanoSaclay, ANR-10-LABX-0035) and the French National Research Agency (project QuTherm, ANR-16-CE30-0010-01). We thank E. Sukhorukov for discussions.

**Author Contributions.** E.S. and F.P. performed the experiment with inputs from A.A.; A.A., E.S. and F.P. analyzed the data; F.D.P. fabricated the sample with inputs from A.A.; A.C., A.O. and U.G. grew the 2DEG; Y.J. fabricated the HEMT used for noise measurements; F.P. led the project and wrote the manuscript with inputs from A.A., E.S. and U.G.

**Author Information.** Correspondence and requests for materials should be addressed to F.P. (frederic.pierre@u-psud.fr).



## METHODS

**Sample.** The sample nanostructuration is performed by standard e-beam lithography in a Ga(Al)As two-dimensional electron gas buried 105 nm below the surface, of density  $2.5 \cdot 10^{11} \text{ cm}^{-2}$  and of mobility  $10^6 \text{ cm}^2 \text{ V}^{-1} \text{ s}^{-1}$ . The central micron-sized island is composed of a metallic multilayer of nickel (30 nm), gold (120 nm) and germanium (60 nm). Its galvanic, ohmic contact with the two-dimensional electron gas is realized by thermal annealing (440 °C for 50 s).

The interface quality between the metallic island and the two-dimensional electron gas is fully characterized, through the individual determination of the electron reflection probability at the interface for each connected quantum Hall channel, with the self-calibrated experimental procedure detailed in Methods of Ref. 17. We find a reflection probability below  $\lesssim 0.001\%$  (the statistical uncertainty) for the three channels closest to the edge (the outer edge channel of each of the three 2DEG branches), 0.08% for the inner edge channel toward electrode 3 used only for  $N \in \{4, 5\}$ , and 0.5% for the inner edge channel toward electrode 2 used only for  $N = 5$ .

The typical electronic level spacing in the metallic island is estimated to be negligibly small ( $\delta \approx k_B \times 0.2 \mu\text{K}$ ), based on the electronic density of states of gold ( $\nu_F \approx 1.14 \cdot 10^{47} \text{ J}^{-1} \text{ m}^{-3}$ ) and the metallic island volume ( $\approx 3 \mu\text{m}^3$ ).

Finally, an important device parameter is the charging energy  $E_C \equiv e^2/2C$ . The value  $E_C \simeq k_B \times 0.3 \text{ K}$  is obtained by standard Coulomb diamond characterization, from the dc voltage height  $V_{\text{diam}}$  of the observed diamonds ( $E_C = eV_{\text{diam}}/2$ ). These measurements are performed in the same cooldown, at the same magnetic field (data not shown, see e.g. Fig. 1c of Ref. 28 for a similar characterization of this sample at a higher quantum Hall filling factor).

**Experimental setup.** The device is fixed to the mixing chamber plate of a cryofree dilution refrigerator. Electrical measurement lines connected to the sample include several filters and thermalization stages. Two shields at base temperature screen spurious high-frequency radiations. Conductances are measured by standard low-frequency lock-in techniques, below 200 Hz. Further details, including on the noise measurement setup used for the electronic thermometry, are provided in the supplementary information of Ref. 28.

**Electronic temperature.** The electronic temperature in the device is extracted from on-chip quantum shot-noise measurements<sup>28</sup>. For this purpose, we effectively short-circuit the central metallic island (equivalent circuit schematic shown bottom-left of Extended Data Fig. 1a) using the lateral continuous gate in the 2DEG branch #2 (gate closest to the bottom in Fig. 1a). The quantum point contact used to set  $N_2$  (bottom-right split gate in Fig. 1a) is here tuned to transmit a single channel with a transmission probability  $\tau \simeq 0.5$ . Extended Data Fig. 1a shows as symbols the measured excess noise versus dc bias voltage  $V$ , and as a red continuous line the theoretical prediction at  $T = 7.97 \text{ mK}$  for the simultaneously measured value  $\tau \simeq 0.515$  (variations of  $\tau$  with  $V$  remain below 0.003 and are ignored). The very low statistical uncertainty of the data shown in the main panel ( $\pm 5 \cdot 10^{-32} \text{ A}^2/\text{Hz}$ , below one tenth of the symbols size) is obtained by averaging 153 sweeps. In practice, we fit each of the individual sweeps separately and extract from the statistical analysis of this ensemble of distinct measurements (shown as symbols in inset) the mean value of the temperat-

ure and the standard error (here  $T = 7.97 \pm 0.06 \text{ mK}$ ). The same shot noise thermometry is performed both just before and just after each run of the full experiment (two runs shown in the manuscript, the first one at  $T \simeq 8.1 \text{ mK}$  and the second at  $T \simeq 8.0 \text{ mK}$ ).

In addition, we consolidate the device electronic temperature  $T$  with a different on-chip thermometry method based on dynamical Coulomb blockade, following Ref. 28. For this purpose, the same quantum point contact (2DEG branch #2) is set to the tunnel regime  $\tau \approx 0.1$  (in absence of dynamical Coulomb blockade renormalization), and the device is tuned to  $N_1 = 0$  and  $N_3 = 2$ , effectively implementing the schematic circuit shown in the bottom-left of Extended Data Fig. 1b with a series resistance  $h/2e^2$ . The temperature is obtained by fitting the conductance data displayed as symbols in the main panel of Extended Data Fig. 1b, using the known values of the series resistance and of  $E_C$ . We find  $T = 8 \text{ mK}$  (corresponding calculation shown as a red line), in agreement with quantum shot noise thermometry within the larger uncertainty of dynamical Coulomb blockade thermometry, which we estimate to  $\pm 1 \text{ mK}$  (grey area).

**Gain calibration of noise amplification chain.** The gain  $G_{\text{amp}}$  of the noise amplification chain is calibrated with the quantum shot noise thermometry described in section ‘Electronic temperature’, from the linear slope of the measured shot noise at  $e|V| \gg k_B T$  (see Ref. 28 for a detailed discussion). As for the determination of  $T$ , we extract a different value of  $G_{\text{amp}}$  from each individual sweep of noise versus dc voltage. From an ensemble of 409 values,  $G_{\text{amp}}$  is extracted with a statistical uncertainty of  $\pm 0.1\%$ . Note that the transmission probability  $\tau$  enters as a factor  $\tau(1-\tau)$  in the determination of  $G_{\text{amp}}$ . Here the value of  $\tau$  is precisely measured simultaneously. Although  $\tau$  exhibits a weak dependence with  $V$  (below 0.003), it is sufficiently small to have a negligible impact on  $G_{\text{amp}}$  at the  $\approx 0.1\%$  level (note the particularly low impact in the vicinity of  $\tau = 0.5$ ) and was not taken into account.

The  $G_{\text{amp}}$  calibration was consolidated at an uncertainty level of  $\approx 1\%$ , by additional quantum shot noise measurements at  $\tau \simeq 0.16$  (for  $T \simeq 8 \text{ mK}$ ) and also at the higher electronic temperature  $T \simeq 16 \text{ mK}$  (for  $\tau \simeq 0.5$ ). The comparison between the different quantum shot noise and dynamical Coulomb thermometry described in the section ‘Electronic temperature’ further establishes the absolute calibration of  $G_{\text{amp}}$ , although at a less precise level of  $\approx 10\%$ . Finally, we point out that the low-temperature heat Coulomb blockade reduction of heat current by precisely one  $J_Q^e$  was also observed at the different integer quantum Hall filling factors  $\nu = 3$  and 4, using specific quantum shot noise calibrations for the modified gain of the noise amplification chain (with our on-chip current to voltage conversion based on the quantum Hall resistance  $1/\nu G_Q^e$ , a larger  $\nu$  therefore results in a lower  $G_{\text{amp}}$ ).

**Dissipated Joule power.** The expression  $P_J = V^2 G_P/2$  is used to calculate the Joule power dissipated in the electronic fluid of the floating metallic node, due to the applied dc bias voltage  $V$  (see Fig. 1a). It corresponds to one half of the standard two-terminal total power  $V^2 G_P$  provided by the voltage generator. This expression can be straightforwardly derived for non-interacting electrons, within the Landauer-Büttiker scattering formalism. Essentially, it amounts to sharing equally the dissipation between cold electrodes, on

the one hand, and central island, on the other hand, as expected in symmetric configurations. In the presence of interactions, one might wonder if the floating character of the central metallic node could possibly break this symmetry. However, the dc voltage of the central island as well as the dc current across it remain unchanged compared to their free-electron values, at experimental accuracy (with the island dc voltage deduced from the measured emitted current through the quantum limited electrical conductance of the connected ballistic channels, see top-left inset of Fig. 2a) and in agreement with theory for the present case of ballistic channels. This provides further evidence that the resulting Joule power dissipated into the central metallic island retains here its standard, non-interacting expression  $P_J = V^2 G_P/2$ . We also point out that the same non-interacting expression for  $P_J$  is specifically expected, on qualitative grounds (a direct quantitative derivation is yet to be done), within the theoretical heat Coulomb blockade framework for ballistic channels of Ref. 9 (Eugene Sukhorukov, private communication).

**Heat Coulomb blockade predictions.** We provide the theoretical expression  $J_{\text{thy}}^{\text{el}}$  derived from Ref. 9 for the net outgoing heat current  $J_{\text{heat}}^{\text{el}}$  through  $N$  ballistic electronic channels connecting a floating metallic node of charging energy  $E_C$  and at the temperature  $T_\Omega$ , to large electrodes at temperature  $T$ , for arbitrary values of  $T_\Omega$  and  $T$ :

$$J_{\text{thy}}^{\text{el}}(N, T_\Omega, T, E_C) = N \frac{\pi^2 k_B^2}{6h} (T_\Omega^2 - T^2) + \frac{N^2 E_C^2}{\pi^2 h} \left[ I\left(\frac{NE_C}{\pi k_B T}\right) - I\left(\frac{NE_C}{\pi k_B T_\Omega}\right) \right], \quad (1)$$

with the function  $I$  given by

$$I(x) = \frac{1}{2} \left[ \ln\left(\frac{x}{2\pi}\right) - \frac{\pi}{x} - \psi\left(\frac{x}{2\pi}\right) \right], \quad (2)$$

where  $\psi(z)$  is the digamma function. All the displayed theoretical predictions of the full heat Coulomb blockade theory (continuous lines in Fig. 3a, inset of Fig. 3b, Extended Data Fig. 2, Extended Data Fig. 3a, inset of Extended Data Fig. 3b and Extended Data Fig. 4) were calculated using Eq. 1, without any fitting parameter. Note that these predictions assume a hot Fermi function characterized by the temperature  $T_\Omega$  for the distribution probability of the electrons in the metallic island. This is expected since the average dwell time of the electrons in the metallic island  $\tau_D = h/\delta N \simeq 200/N \mu\text{s}$  (see e.g. Ref. 31) is estimated to be much larger, by about four orders of magnitude, than the typical timescale of  $\sim 10\text{ns}$  for electron-electron inelastic collisions in similar metals (see e.g. Ref. 32 for the connected measurement of the electron coherence time in gold).

**Asymptotic limits of predictions.** The function  $I$  in Eqs. 1 and 2 has the asymptotic forms

$$I(x \ll 1) \simeq \frac{\pi}{2x}, \quad I(x \gg 1) \simeq \frac{\pi^2}{6x^2}, \quad (3)$$

with a crossover centered on  $x \simeq 1$ .

At  $T, T_\Omega \ll NE_C/\pi k_B$ , Eq. 1 therefore reduces to

$$J_{\text{thy}}^{\text{el}} \simeq (N-1) \frac{\pi^2 k_B^2}{6h} (T_\Omega^2 - T^2) = (N-1) \times J_Q^{\text{el}}, \quad (4)$$

with precisely one electronic channel effectively suppressed for heat conduction.

At  $NE_C/\pi k_B \ll T, T_\Omega$ , Eq. 1 reads

$$J_{\text{thy}}^{\text{el}} \simeq N \frac{\pi^2 k_B^2}{6h} (T_\Omega^2 - T^2) - N \frac{E_C k_B}{2h} (T_\Omega - T), \quad (5)$$

which corresponds to a net reduction of the heat conductance ( $|T - T_\Omega| \rightarrow 0$ ) per ballistic electronic channel by the fixed amount  $\Delta G_{\text{heat}}^{\text{el}} = E_C k_B/2h$  (always small with respect to  $G_Q^{\text{th}}$  in the considered high-temperature limit).

At  $T \ll NE_C/\pi k_B \ll T_\Omega$ , Eq. 1 becomes

$$J_{\text{thy}}^{\text{el}} \simeq \frac{\pi^2 k_B^2}{6h} (NT_\Omega^2 - (N-1)T^2) - N \frac{E_C k_B}{2h} T_\Omega, \quad (6)$$

where the relative reduction due to heat Coulomb blockade progressively vanishes as  $T_\Omega$  increases.

**Control experiment at  $T \simeq 16\text{mK}$ .** We here demonstrate the robustness of our result with respect to base temperature  $T$ . The experiment is performed at a temperature twice as large as before,  $T \simeq 15.9 \pm 0.1\text{mK}$ , for the setting  $N = 2$ . As seen from the  $J_{\text{heat}}$  vs  $T_\Omega^2 - T^2$  data shown as symbols in Extended Data Fig. 3a, this is still sufficiently low to directly and quantitatively establish the heat Coulomb blockade suppression of one ballistic channel. Note that this robustness also further validates the specific tests performed to rule out possible experimental artifacts (additional power injection by the measurement lines, voltage-dependent noise offset, calibration and thermometry issues).

We also find that exactly the same functional  $3.9 \cdot 10^{-8} (T_\Omega^{5.85} - T^{5.85})$ , attributed to electron-phonon (black continuous line in main panel of Extended Data Fig. 3b), matches the present  $T \simeq 16\text{mK}$  data reduced by the predicted electronic heat flow (symbols in main panel of Extended Data Fig. 3b). Note that the observed independence of the electron-phonon coupling with temperature is a commonly used criterion to show that cold electrons and phonons are at the same temperature  $T$  (see e.g. Ref. 33).

**Supplementary experimental tests.** We also performed the following tests:

(i) At  $N = 0$ , the measured noise is found to be independent of dc bias (applied either within the same 2DEG branch or in a disconnected branch, with the current flowing toward cold grounds not shown in Fig. 1), at experimental accuracy. In the language of Ref. 6, the ‘source noise’ is negligible.

(ii) At  $V = 0$ , the absolute measured noise does not change when tuning  $N$  to different values or by connecting the amplification noise chain to an edge channel emitted from a cold ground. This directly shows that the temperature  $T$  is homogeneous (the same  $T$  for all large electrodes and the metallic island, whatever  $N$ ), and also that the power injected into the central island is negligible at  $V = 0$  (in the presence of e.g. significant heating from the measurement lines, the central island temperature and consequently the noise measured would depend on  $N_{1,2,3}$ ; note that such an heating takes place in one of the test configurations discussed in (iii)).

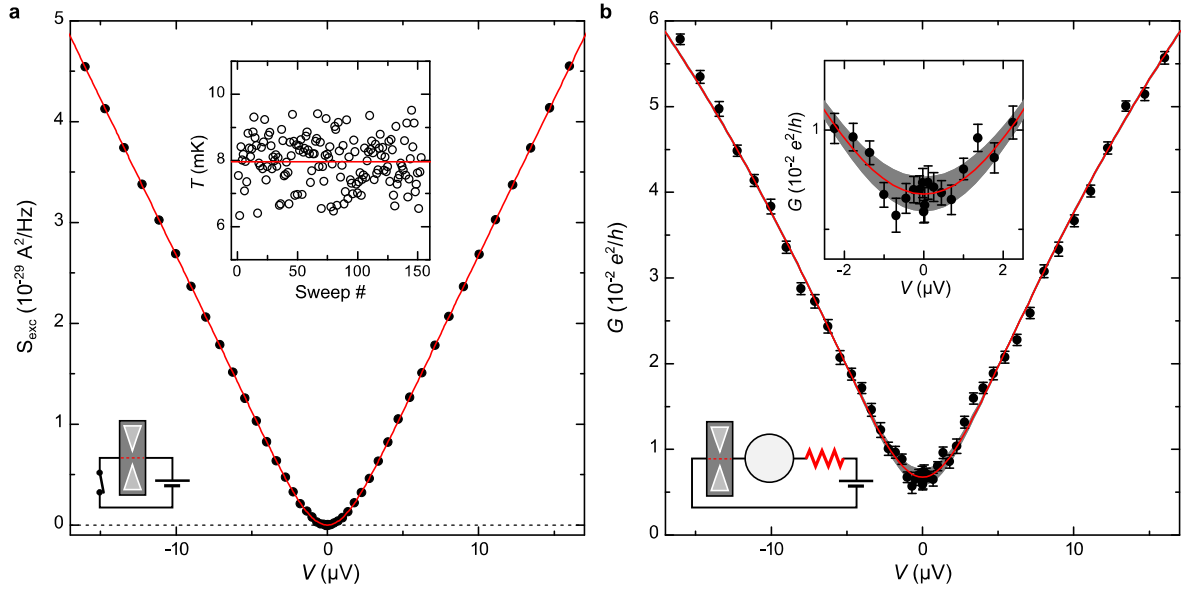
(iii) We checked that the observed heat Coulomb blockade is independent of the specific channel realization, by comparing three different device configurations all corresponding to  $N = 2$  (see Extended Data Fig. 4): ( $N_1 = 1, N_2 = 1, N_3 = 0$ ) (main manuscript, red squares in Extended Data Fig. 4),

( $N_1 = 0, N_2 = 1, N_3 = 1$ ) (violet squares in Extended Data Fig. 4) and ( $N_1 = 1, N_2 = 0, N_3 = 1$ ) (black squares in Extended Data Fig. 4). The first two configurations give exactly the same result at experimental accuracy. The third configuration has the additional complication that, in order to perform the noise thermometry of the central island, we had to make use of an otherwise disconnected measurement line within the 2DEG branch 3, through which a non-negligible power was dissipated into the island even at  $V = 0$  (as seen with measurements as discussed in (ii), and also with other tests including quantum shot noise and dynamical Coulomb blockade measurements). Nonetheless, heat Coulomb blockade predictions (and a full agreement with the first two device configurations) are verified when taking into account the separately calibrated temperature offset  $T_\Omega(V = 0) - T \simeq 5$  mK (obtained through the approach of test (ii)) and the additional dissipated power of 0.06 fW at  $V = 0$ .

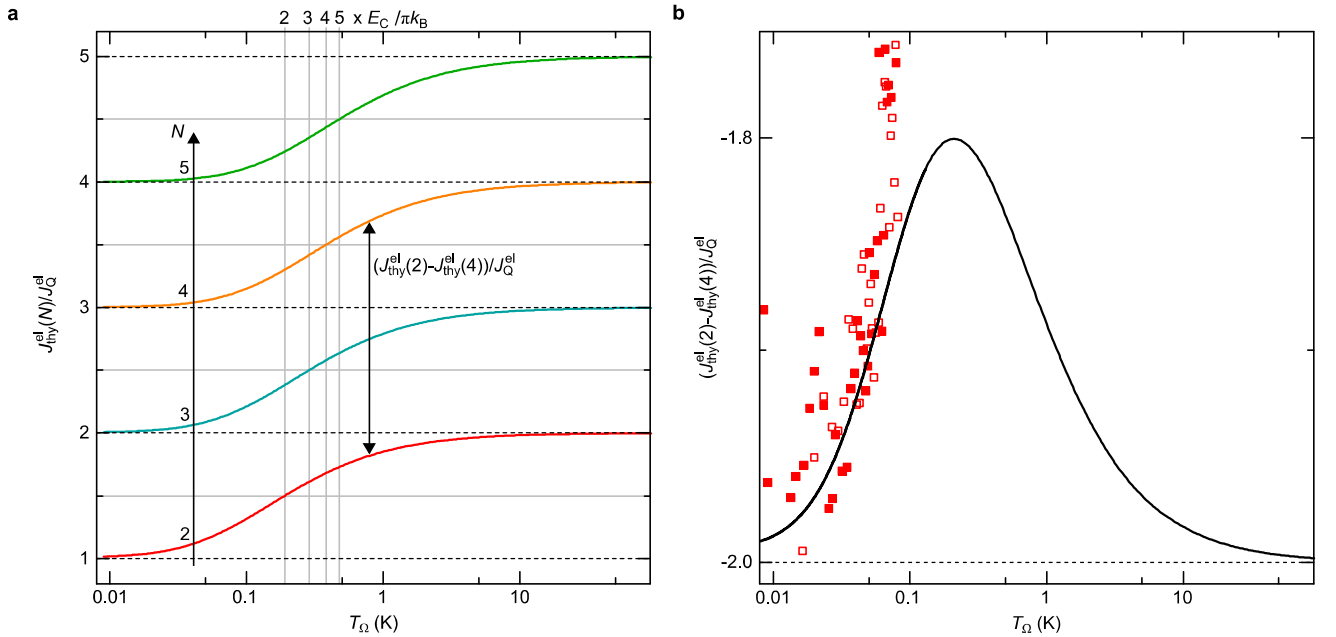
(iv) Finally, we verified the robustness of our results with respect to the integer quantum Hall filling factor  $\nu$  at which the experiment is performed. The heat Coulomb blockade suppression of one ballistic channel was quantitatively observed experimentally not only at  $\nu = 2$  (main manuscript), but also at  $\nu = 3$  and  $\nu = 4$ .

**Comparison with previous experiments.** In the pre-

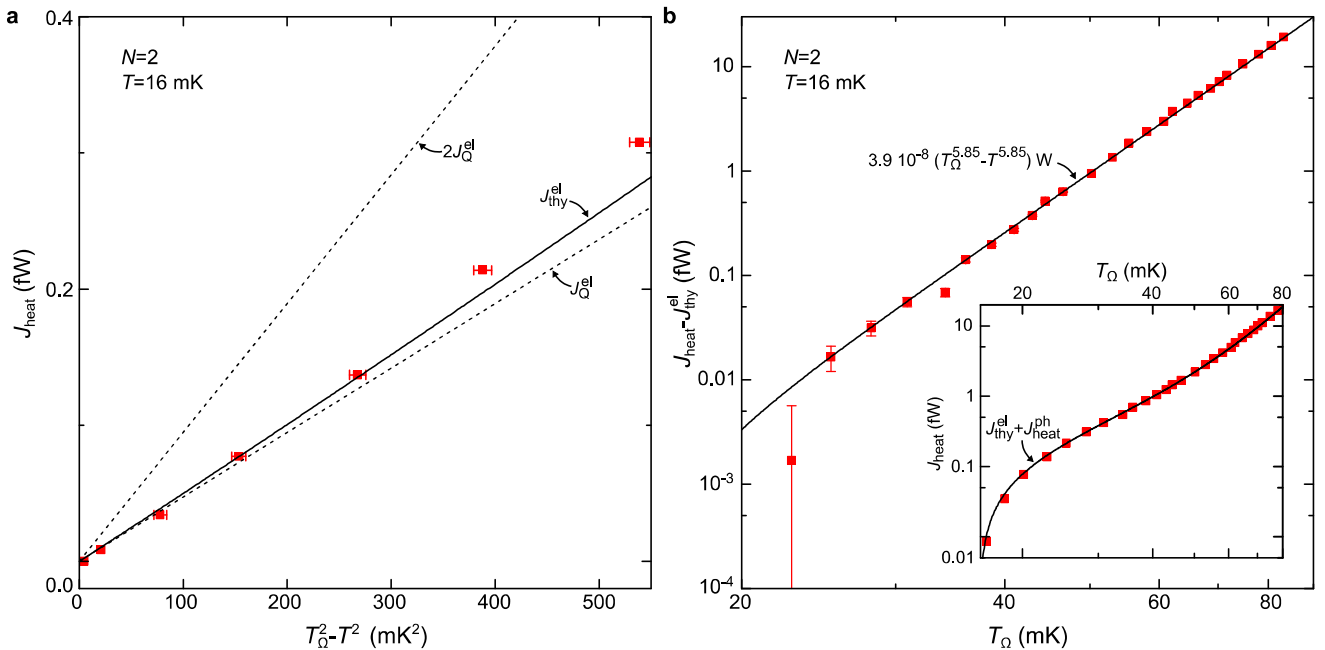
vious works Refs 5,6, besides the robust  $\Delta J_{\text{heat}}$  approach to extract the quantum limit of electronic heat flow  $J_Q^{\text{el}}$ , it was also attempted to determine the full electronic heat flow despite the non-negligible electron-phonon contribution at  $T \gtrsim 25$  mK. For this purpose, a  $T_\Omega^5 - T^5$  power-law was assumed to model the transfer of energy from electrons at  $T_\Omega$  toward phonons at  $T$ . With this model, no heat Coulomb blockade was detected<sup>5,6</sup>. However, we here point out the sensitive influence of the electron-phonon power law exponent in the analysis of these previous experiments. Together with the higher  $T$ , it essentially impeded the observation of the heat Coulomb blockade. We illustrate this with the most accurate data of Ref. 5, obtained at integer quantum Hall filling factor  $\nu = 3$ . As pointed out in the supplementary materials of Ref. 5, fitting the data for reference channel number  $N_{\text{ref}} = 4$  of this previous experiment with the electron-phonon temperature exponent as a free parameter (instead of assuming an exponent of 5) leads to a reduced overall electronic heat flow of  $\approx 3.5 \times J_Q^{\text{el}}$ , a factor in between  $N_{\text{ref}}$  and  $N_{\text{ref}} - 1$ , predicted respectively in the absence and in the presence of a heat Coulomb blockade. Reanalyzing these previous data with the electron-phonon power-law left as a free parameter, we find that they are indeed compatible at experimental accuracy with the present observation of the heat Coulomb blockade of one ballistic channel.



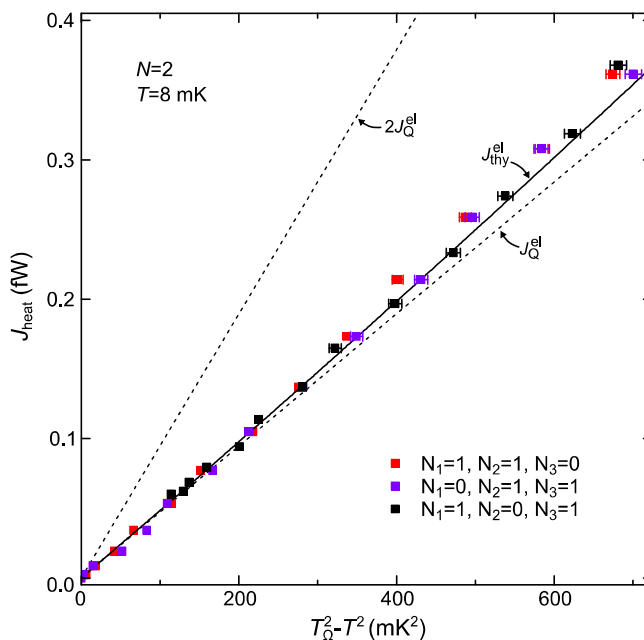
**Extended Data Figure 1. Electronic temperature.** **a**, Quantum shot noise thermometry. Symbols in the main panel represent the measured excess spectral density of the current fluctuations across a quantum point contact set to transmit a single electronic channel with a probability  $\tau \simeq 0.516$ , and biased with the dc voltage  $V$  (see configuration schematic). The statistical uncertainty of  $\pm 5 \cdot 10^{-32} \text{ A}^2/\text{Hz}$  on  $S_{\text{exc}}$  is below one tenth of the symbols size. The red continuous line is the calculated excess current fluctuations for  $T = 7.97$  mK and  $\tau = 0.516$ . Inset: the different electronic temperatures  $T$  shown as symbols are each obtained by fitting a different (successive) voltage bias sweep of the quantum shot noise (symbols in the main panel represent the average of these sweeps). From the statistical analysis of these 153 values, we find  $T \simeq 7.97 \pm 0.06$  mK (horizontal red line). **b**, Dynamical Coulomb blockade thermometry. The electronic temperature is here obtained by fitting the device conductance  $G$  (symbols) versus voltage bias with the dynamical Coulomb blockade theory in the presence of a known series resistance  $R = h/2e^2$  (see configuration schematic). We find  $T \simeq 8$  mK from the fit shown as a continuous line. The estimated uncertainty of  $\pm 1$  mK is displayed as a grey background best visible in the inset showing only low voltages.



**Extended Data Figure 2. Heat Coulomb blockade versus temperature.** **a**, Crossover from  $N \times J_Q^{\text{el}}$  at  $T \gg NE_C/\pi k_B$  to  $(N-1) \times J_Q^{\text{el}}$  at  $T \ll NE_C/\pi k_B$ . Colored continuous lines display the theoretical prediction of Eq. 1 ( $T = 8.07$  mK,  $E_C = 0.3 \times k_B \text{ K}$ ) and versus the metallic node temperature  $T_\Omega$  in log scale. **b**, The normalized difference between heat flows at  $N = 2$  and  $N = 4$  (double arrow in **a**, previously shown in the bottom of Fig. 3a on the experimentally explored temperature range) is displayed on the full temperature range where the crossover takes place. The black continuous line is the prediction of Eq. 1. The same data previously shown in the bottom part of Fig. 3a are displayed as symbols.



**Extended Data Figure 3. Control experiment at  $T \approx 16$  mK.** **a**, Heat Coulomb blockade of one ballistic channel. Measurements at  $N = 2$  of the overall heat flow ( $J_{\text{heat}} = P_J$ ) versus  $T_{\Omega}^2 - T^2$  are displayed as symbols, for low temperatures where the electron-phonon contribution remains relatively small ( $T_{\Omega} < 30$  mK). The bottom dashed line, close to low-temperature data points, corresponds to the low-temperature asymptotic suppression of precisely one  $J_Q^{\text{el}}$ . The quantitative heat Coulomb blockade prediction of Eq. 1 for the electronic thermal transport is shown as a continuous line. The top dashed line corresponds to the prediction for the electronic thermal current across two ballistic channels in the absence of heat Coulomb blockade,  $2J_Q^{\text{el}}$ . **b**, Additional mechanisms. As in Fig. 3b, we display as symbols the measured heat current reduced by the quantitative heat Coulomb blockade prediction ( $N = 2$ ,  $T = 15.9$  mK). We observe an exact match with the same  $T_{\Omega}^{5.85}$  functional (line) obtained at the base temperature of 8 mK. Inset, the sum of heat Coulomb blockade predictions and  $T_{\Omega}^{5.85}$  functional (black continuous line) is directly compared to measured  $J_{\text{heat}}(T_{\Omega})$  (symbols).







**Extended Data Figure 4. Comparison of three device configurations implementing  $N=2$ .** The three sets of symbols, each displayed with a different color, correspond to measurements of  $J_{\text{heat}}$  vs  $T_{\Omega}^2 - T^2$  with the device tuned in different configurations  $[N_1, N_2, N_3]$  (as detailed in the figure), all associated with the same total number of ballistic channels connected to the node ( $N = 2$ ). The bottom and top dashed lines correspond, respectively, to  $J_Q^{\text{el}}$  and  $2 \times J_Q^{\text{el}}$ . The continuous line is the quantitative heat Coulomb blockade prediction for electronic thermal transport given by Eq. 1.

ARTICLE

<https://doi.org/10.1038/s41467-019-13566-8>

OPEN

# Electronic heat flow and thermal shot noise in quantum circuits

E. Sivre <sup>1,3</sup>, H. Duprez <sup>1,3</sup>, A. Anthore<sup>1,2</sup>, A. Aassime<sup>1</sup>, F.D. Parmentier <sup>1</sup>, A. Cavanna<sup>1</sup>, A. Ouerghi<sup>1</sup>, U. Gennser<sup>1</sup> & F. Pierre <sup>1\*</sup>

When assembling individual quantum components into a mesoscopic circuit, the interplay between Coulomb interaction and charge granularity breaks down the classical laws of electrical impedance composition. Here we explore experimentally the thermal consequences, and observe an additional quantum mechanism of electronic heat transport. The investigated, broadly tunable test-bed circuit is composed of a micron-scale metallic node connected to one electronic channel and a resistance. Heating up the node with Joule dissipation, we separately determine, from complementary noise measurements, both its temperature and the thermal shot noise induced by the temperature difference across the channel. The thermal shot noise predictions are thereby directly validated, and the electronic heat flow is revealed. The latter exhibits a contribution from the channel involving the electrons' partitioning together with the Coulomb interaction. Expanding heat current predictions to include the thermal shot noise, we find a quantitative agreement with experiments.

<sup>1</sup>Université Paris-Saclay, CNRS, Centre de Nanosciences et de Nanotechnologies (C2N), 91120 Palaiseau, France. <sup>2</sup>Université de Paris, C2N, 91120 Palaiseau, France. <sup>3</sup>These authors contributed equally: E. Sivre, H. Duprez. \*email: [frederic.pierre@c2n.upsaclay.fr](mailto:frederic.pierre@c2n.upsaclay.fr)

Heating generally drives the crossover from quantum to classical behaviors; nevertheless, heat itself is ruled by quantum mechanics. In recent years, experimental explorations of quantum thermal phenomena have been emerging at a rising pace<sup>1–3</sup>. In particular, the quantum of thermal conductance, a universal basic building block of heat quantum transport, is now firmly established for bosons<sup>1,4</sup>, fermions<sup>5,6</sup>, and quasiparticles that may be anyons<sup>7</sup>, as well as up to macroscopic<sup>8</sup> and room temperature<sup>9,10</sup> scales. However, despite the strong influence of Coulomb interaction on electricity in small quantum circuits<sup>11–14</sup>, its impact on the quantum transport of heat remains barely explored experimentally<sup>15–17</sup>. In a first step for perfectly ballistic circuits, where there is no back-scattering along any of the connected electronic channels, a recent observation<sup>16</sup> was made of the predicted<sup>18</sup> heat Coulomb blockade taking place without any concomitant reduction of the electrical conductance. In this limit and at low temperatures, the Coulomb interaction manifests itself as the systematic suppression of a single channel for the evacuation of heat from a small circuit node<sup>16,18</sup>. Here we address elementary quantum circuits including one generic electronic channel of arbitrary electron transmission probability. An unexpected increase in the flow of heat is observed and quantitatively accounted for by an additional quantum heat transport mechanism, involving the association of shot noise and Coulomb interaction.

We obtain the heat current–temperature characteristics by controllably injecting a dc power into a small floating circuit node connecting a quantum channel to a linear resistance, and by monitoring in situ the resulting increase in the electrons’ temperature. A complication is that the partition of electrons in the generic channel breaks the Johnson–Nyquist proportionality between excess noise and node temperature increase<sup>19,20</sup>, which was previously used for the thermometry of ballistic circuits<sup>5–7,16,17</sup>. We overcome this difficulty with an experimental procedure involving complementary measurements of both the auto- and cross-correlations of electrical fluctuations. This provides us, separately, with the local electronic temperature in the metallic node, as well as with the thermal shot noise. The latter is found in good agreement with predictions derived within the scattering approach<sup>19,21</sup>, in which Coulomb effects have been encapsulated in the temperature-dependent conductance (reduced by the dynamical Coulomb blockade<sup>11</sup>). The node temperature increase, both in terms of injected power and electron transmission probability across the channel, exposes an additional heat current contribution involving thermal shot noise.

## Results

### Test-bed for electronic channels in dissipative environments.

An e-beam micrograph of the device is shown in Fig. 1a together with a schematic representation of the measurement setup. The small floating circuit node that is heated is materialized by the central micron-scale metallic island (in brighter gray), of separately characterized self-capacitance  $C \simeq 3.1$  fF. It is in essentially perfect electrical contact with a standard Ga(Al)As two-dimensional (2D) electron gas underneath the surface. The 2D gas is immersed in a perpendicular magnetic field corresponding to the integer quantum Hall regime at filling factor two. In this regime, the current flows along two adjacent quantum Hall edge channels depicted by lines with arrows indicating the propagation direction. Three quantum point contacts (QPCs) are formed in the 2D electron gas by applying negative voltages on surface split gates coupled capacitively. A single (spin-polarized) short electronic channel of tunable transmission probability  $\tau \in [0, 1]$  is implemented at the left QPC. The top and right QPCs are tuned to a different, ballistic regime: they are set to fully transmit,

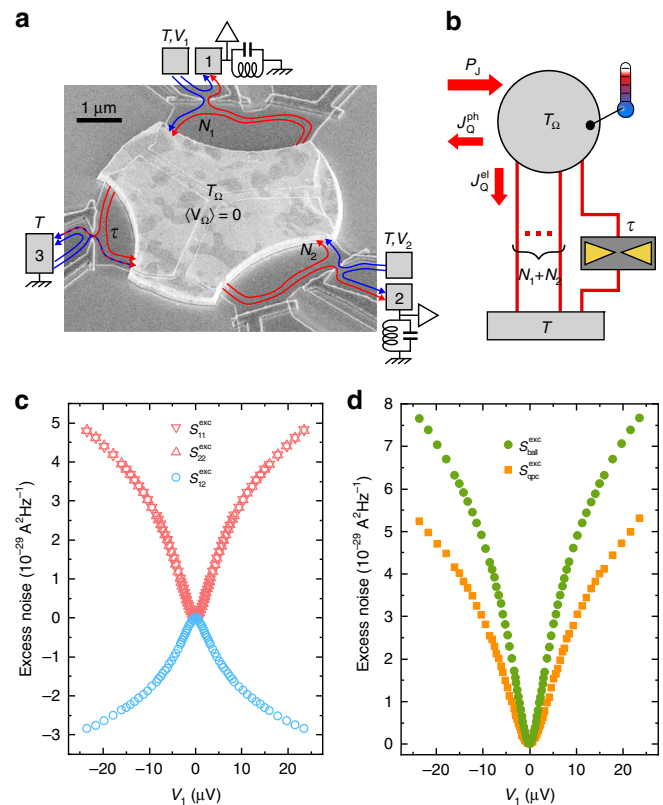


**Fig. 1 Experimental approach.** **a** Device e-beam micrograph with measurement setup schematic. A single generic channel of arbitrary electron transmission probability  $\tau$ , as well as  $N_1$  and  $N_2$  ballistic (perfectly transmitted) channels, are separately connected to a small metallic island. **b** Schematic heat balance representation between injected Joule power ( $P_J$ ) and outgoing heat currents, from electrons to phonons ( $J_Q^{ph}$ ) and through the connected electronic channels ( $J_Q^{el}$ ). **c** Excess auto- and cross-correlation measurements versus  $V_1 = -V_2$ , in the illustrative configuration  $N = 2$  ( $N_1 = N_2 = 1$ ),  $\tau \sim 0.5$ . **d** Extracted excess noise sources per ballistic channel ( $S_{ball}^{exc}$ ) and across the generic single-channel quantum point contact of transmission  $\tau$  ( $S_{qpc}^{exc}$ ), from the data in **c**.

respectively,  $N_1$  and  $N_2$  channels forming together an adjustable linear resistance<sup>22,23</sup>  $R = R_K/N$ , with  $R_K = h/e^2$  the electrical resistance quantum ( $h$  the Planck constant and  $e$  the electron charge) and  $N = N_1 + N_2$ . Further away, the quantum Hall channels are connected to large electrodes at base temperature  $T \simeq 8$  mK, represented in Fig. 1a by gray rectangles.

**Electronic heat flow determination.** The electrons within the central island are heated to  $T_\Omega$  by dissipating a known Joule power  $P_J \simeq (N_1 V_1^2 + N_2 V_2^2)/2R_K$ , with  $V_1$  ( $V_2$ ) the voltage applied to the top (right) large electrode (Methods). The island’s dc voltage is pinned to  $\langle V_\Omega \rangle = 0$ , by imposing  $N_1 V_1 = -N_2 V_2$ , such that the generic channel experiences a pure temperature bias  $T_\Omega - T$  without dc voltage. As illustrated in Fig. 1b, energy conservation in the stationary regime implies  $P_J = J_Q^{el} + J_Q^{ph}$ , with  $J_Q^{el}$  being the heat flow across the connected electronic channels and  $J_Q^{ph}$  the heat transferred from the electrons within the island to the phonons. In practice, electron–phonon heat transfers are negligible only for  $T_\Omega \lesssim 20$  mK<sup>16</sup>. However, as  $J_Q^{ph}$  only depends on temperatures ( $T_\Omega$ ,  $T$ ), and not on the connected electronic channels ( $\tau$ ,  $N$ ), it can be calibrated by tuning the circuit to the ballistic regime ( $\tau \in \{0, 1\}$ ). Using the previously established heat

Coulomb blockade predictions for ballistic channels<sup>16,18</sup>, we find that all the data with  $\tau \in \{0, 1\}$ ,  $N \in \{2, 3, 4\}$  and  $T \in \{8, 16\}$  mK can be accurately reproduced using the same  $J_Q^{\text{ph}} \simeq 2.7 \times 10^{-8} (T_\Omega^{5.7} - T^{5.7})$  W (Methods). At intermediate transmission probability ( $0 < \tau < 1$ ), the unknown electronic heat flow is then obtained by subtracting the above  $J_Q^{\text{ph}}$  from the injected Joule power ( $J_Q^{\text{el}} = P_J - J_Q^{\text{ph}}$ ).

**Local temperature increase measurement.** The island’s electronic temperature  $T_\Omega$  is determined from the low-frequency (MHz) current fluctuations measured on the top (1) and right (2) large electrodes (Methods). The excess auto- and cross-correlation spectral density, from which the zero-bias offset is removed, are plotted in Fig. 1c versus  $V_1$  for the illustrative configuration  $N_1 = N_2 = 1$  at  $\tau \sim 0.5$ . In a nutshell, combining these data gives us access separately to the current noise sources originating from the QPC hosting a single generic channel ( $S_{\text{qpc}}$ ) and from the ballistic channels ( $S_{\text{ball}}$  per channel), both shown in Fig. 1d. This is possible because these two noise sources contribute with the same sign to the experimental autocorrelation signal, while with an opposite sign to the cross-correlation (Methods). The temperature  $T_\Omega$  is then obtained using solely the ballistic noise source  $S_{\text{ball}}$ , directly resulting from the thermal fluctuations of the electronic states’ population in the baths. This robust connection manifests itself as a straightforward, and previously used<sup>5–7,16,17</sup>, generalization of the fluctuation-dissipation relation for the thermal noise  $S_{\text{ball}} = 4k_B \bar{T}/R_K$ , where  $\bar{T} = (T_\Omega + T)/2$  is the average temperature<sup>19,24</sup>. In practice, the excess noise data (with respect to  $V_{1,2} = 0$ ) gives us access to the temperature increase  $T_\Omega - T$ , while  $T$  is separately measured (Methods).

**Shot noise induced by a temperature difference.** Generic channels driven out-of-equilibrium are generally expected to exhibit, in addition to the average thermal noise, a shot noise induced by the electron partitioning into a transmitted electron and a reflected electron<sup>19,21</sup>. In particular, the current noise spectral density at low frequencies ( $\omega \ll k_B T/h$ ), for a single channel of transmission probability  $\tau$ , reads<sup>19</sup>:

$$S_{\text{qpc}}^{\text{thy}} = \frac{4k_B \bar{T} \tau}{R_K} + \frac{2\tau(1-\tau)}{R_K} \int dE [f_{T_\Omega}(E) - f_T(E)]^2, \quad (1)$$

with  $f_{T_\Omega}(E)$  the Fermi distributions in the connected baths at different temperatures and/or voltages. The average thermal noise and the shot noise are, respectively, the first and second term on the right-hand side of Eq. (1). Whereas the shot noise induced by either a voltage difference or a frequency irradiation is experimentally well established (see references in ref. 19 and also ref. 25), the thermal shot noise resulting from the partition of electrons in the sole presence of a temperature difference was observed only recently<sup>20</sup>. Although convincing, this observation did not allow for a one-to-one comparison of the individual data points with the theory, because the possibly multiple electronic channels were incompletely characterized by the measurement of their parallel conductance. In contrast, in the present work with a single generic channel, the QPC conductance  $G_{\text{qpc}} = \tau e^2/h$  completely determines the transmission probability  $\tau$ . In Fig. 2a, following ref. 20, we focus on the thermal shot noise  $\Delta S_{\text{qpc}}$  obtained by removing the average Johnson–Nyquist noise ( $\Delta S_{\text{qpc}} = S_{\text{qpc}} - 4k_B \bar{T}/R_K$ ). The  $\Delta S_{\text{qpc}}$  data at  $N_1 = N_2 = 1$  (symbols) are plotted versus  $T_\Omega$  for several gate voltage tunings of the single-channel QPC. The predictions (continuous lines), calculated without any adjustable parameter using Eq. (1), closely match the data (for control experiments, see Supplementary Fig. 1 at other  $\{N_1, N_2\}$  and

Supplementary Fig. 2 at a larger base temperature  $T \simeq 16$  mK). Note that the simultaneously measured  $G_{\text{qpc}} = \tau e^2/h$  depends on the temperatures  $T$  and  $T_\Omega$ , because of the quantum back-action of the series RC circuit<sup>13</sup> also referred to as the dynamical Coulomb blockade<sup>11</sup>. Remarkably, we find that the effect of Coulomb interaction is accurately encapsulated, at experimental resolution, into the renormalized  $\tau$  injected in Eq. (1). Figure 2b directly reveals the partition origin of the shot noise induced by a temperature difference. The data points represent this experimental shot noise renormalized by the predicted,  $\tau$ -independent temperature function  $\mathcal{F}(T_\Omega, T) = (2/R_K) \int dE [f_{T_\Omega}(E) - f_T(E)]^2$ . The good agreement observed between  $\Delta S_{\text{qpc}}/\mathcal{F}$  and  $\tau(1-\tau)$  attests of the underlying partition mechanism.

**Electronic heat flow from a small quantum circuit node.** We now address the electronic flow of heat across the QPC and ballistic channels. In conductors, the thermal conductance  $G_Q$  is frequently found to be directly proportional to the electrical conductance  $G_{\text{el}}$ , through the so-called Wiedemann–Franz (WF) law  $G_Q = \mathcal{L} G_{\text{el}}$  with  $\mathcal{L} = \pi^2 k_B^2/3e^2$  the Lorenz number. While this relation holds between the quantum of thermal and electrical conductances, it generally breaks down in quantum circuits assembled from several interconnected channels. In particular, it was shown that the thermal conductance from a small, heated circuit node connected by ballistic channels is reduced from the WF expectation by precisely one quantum of thermal conductance at low temperatures<sup>16,18</sup>, whatever the total number of channels. With such a fixed reduction, the increment by  $\mathcal{L}/R_K$  of the thermal conductance when adding an extra ballistic channel (starting from at least one) nevertheless follows the WF relation. Is this also the case if the electrical conductance is increased continuously, by sweeping the transmission probability across an electronic channel from  $\tau = 0$  to 1? The answer is no, as we will now show.

Figure 3a exhibits as symbols, versus  $T_\Omega$ , the experimental electronic heat flow  $J_Q^{\text{el}}$  normalized by the quantum limit per channel  $J_Q^{\text{lim}} = \pi^2 k_B^2 (T_\Omega^2 - T^2)/6h$ , for different circuit settings spanning the full range of  $\tau$  at both  $N = 2$  and  $N = 3$  (see Supplementary Fig. 3b for  $N = 4$ , and Supplementary Fig. 4 for a control experiment at  $T \simeq 16$  mK). The three thick black continuous lines display the full, temperature-dependent heat Coulomb blockade prediction for two (bottom), three (middle), and four (top) ballistic channels<sup>18</sup> (Methods). Note the small, predicted deviations developing with temperature from the complete heat Coulomb blockade of a single channel ( $J_Q^{\text{el}}/J_Q^{\text{lim}} = N - 1$ ) that only applies in the limit of low temperatures  $T_\Omega, T \ll h/k_B RC$ . Open and full circles (full diamonds) are data points obtained for  $N = 2$  ( $N = 3$ ) ballistic channels, with different settings of the generic channel encoded by different colors. The dashed lines represent linear interpolations between ballistic predictions at  $N$  and  $N + 1$  weighted, respectively, by  $1 - \tau$  and  $\tau$  measured for the compared data (same color). For example, the brown dashed line in the top part of Fig. 3a (closest to  $J_Q^{\text{el}}/J_Q^{\text{lim}} \sim 2.5$ ) is given by  $\tau(T_\Omega)$  times the prediction for three ballistic channels (thick black line near  $J_Q^{\text{el}}/J_Q^{\text{lim}} \sim 2$ ; Methods) plus  $1 - \tau(T_\Omega)$  times the prediction for four ballistic channels (thick black line near  $J_Q^{\text{el}}/J_Q^{\text{lim}} \sim 3$ ), with  $\tau(T_\Omega)$  the renormalized conductance simultaneously measured during the acquisition of the top brown data points of corresponding  $T_\Omega$  (in practice a linear interpolation is performed between discrete measurements of  $\tau(T_\Omega)$ ). The difference between dashed lines and data points is particularly significant



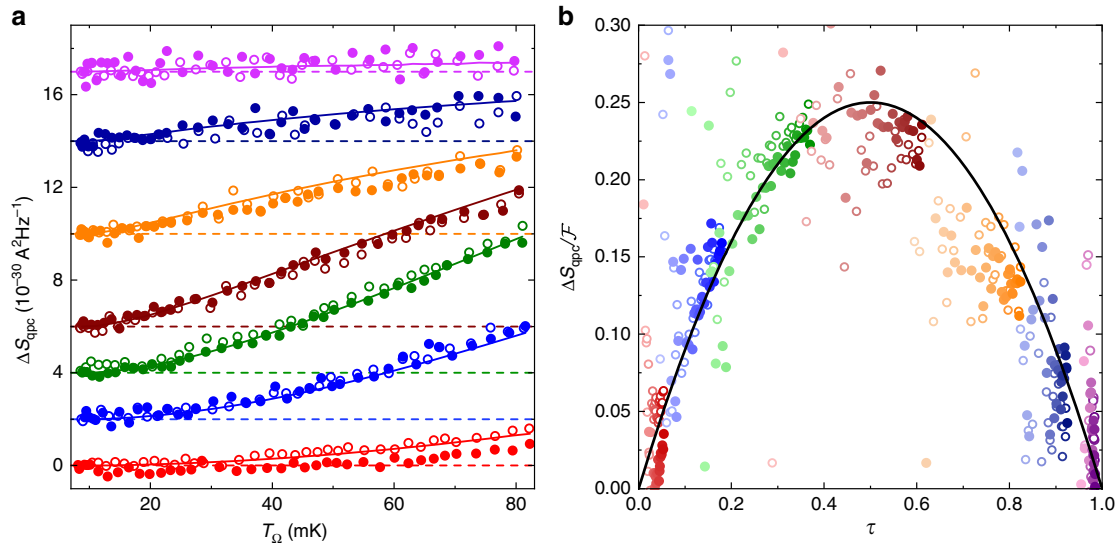


**Fig. 2 Thermal shot noise.** **a** Symbols represent the experimental QPC noise at  $N = 2$  from which the average thermal noise was removed ( $\Delta S_{\text{qpc}} = S_{\text{qpc}} - 4k_{\text{B}}\bar{T}\tau/R_{\text{K}}$ , with  $\bar{T} = (T_{\Omega} + T)/2$ ). Measurements at different gate voltage tunings of the QPC are shifted vertically, with the applied offsets shown as horizontal dashed lines. Open and full symbols distinguish separate sequences of measurements. Continuous lines display Eq. (1) predictions. **b** The  $\tau(1 - \tau)$  partition signature is shown as a continuous line versus  $\tau$ . Symbols represent  $\Delta S_{\text{qpc}}/\mathcal{F}$ , where the  $\tau$ -independent function  $\mathcal{F}(T_{\Omega}, T)$  is the predicted thermal shot noise's temperature dependence (see text). A lighter (darker) symbol coloring indicates a low (large)  $T_{\Omega} - T$  corresponding to a higher (lower) experimental uncertainty.

at intermediate  $\tau$ . This shows that the thermal conductance increase does not reduce to a linear, WF-like, function of the electrical conductance. In contrast, quantitative predictions based on the Langevin approach in ref. 18 but including the partition noise from the generic channel (colored continuous lines, Methods) lie close to the data, without any adjustable parameter. At low temperatures  $T_{\Omega}, T \ll \hbar/k_{\text{B}}RC$ , the difference between theory (thy) predictions  $J_Q^{\text{thy}}$  and the WF extension (linear in  $\tau$ ) of heat Coulomb blockade predictions for ballistic channels  $(N + \tau - 1) \times J_Q^{\text{lim}}$ , reads:

$$J_Q^{\text{thy}} - (N + \tau - 1) \times J_Q^{\text{lim}} \simeq \frac{\tau(1 - \tau)}{N + \tau} \times J_Q^{\text{lim}}. \quad (2)$$

Note that  $J_Q^{\text{thy}} = 0$  for  $N = 0$  at low temperatures, whatever the value of  $\tau$  (see refs. 26–28 for the electrons' state preservation concomitant to the absence of heat transfers). The  $\tau(1 - \tau)$  numerator attests of the role of electron partition in this additional heat transport mechanism. We also point out that this heat current contribution vanishes at higher temperatures, when Coulomb effects become negligible (Methods). This shows straightforwardly the essential role of Coulomb interaction, which combines with electron partition into a different form of quantum heat transport. Figure 3b provides direct experimental evidences for an underlying partition mechanism (see also Supplementary Fig. 3a, c), by subtracting from the renormalized electronic heat flow at  $N = 2$  (symbols in Fig. 3a) the corresponding WF (linear) interpolation (dashed lines in Fig. 3a). Focusing here on the temperature range  $T_{\Omega} \in [17, 65]$  mK where measurements are most accurate (see error bars in Fig. 3a), a convincing agreement is found with  $\tau(1 - \tau)/(2 + \tau)$  plotted as a continuous line versus  $\tau$ .

## Discussion

We have experimentally investigated the heat flow and thermally induced shot noise in an elementary quantum circuit composed of one small metallic node (island) connected by several ballistic channels and by one generic electronic channel of arbitrary electron transmission probability. Applying a temperature bias,

without dc voltage across the generic channel, we measured the thermal shot noise<sup>20</sup> and determined the overall electronic heat flow from the island. The former is found in direct quantitative agreement with thermal shot noise predictions computed using the known transmission probability<sup>19</sup>. The latter displays an additional heat flow contribution. The underlying mechanism involves in particular the Coulomb charging energy of the island, which effectively freezes its total charge at low temperatures and thereby induces correlations between the heat carrying electrical current fluctuations propagating along the connected channels<sup>18</sup> (Methods). In a fully ballistic circuit (without thermal shot noise), these correlations amount to the recently observed systematic blockade of a single channel for the flow of heat, independently of the total number of channels<sup>16,18</sup>. Here, with a generic channel, a thermal shot noise is impinging on the island and fractionalized among all the outgoing channels by the frozen island charge imposed by Coulomb interaction<sup>29</sup>. This combination of Coulomb interaction and thermal shot noise underpins the presently observed additional heat transport mechanism (Methods).

Advancing our understanding of the mechanisms of quantum heat transport and establishing the thermal shot noise contribution is essential for exploiting heat and noise to unveil exotic physics<sup>17,30,31</sup>, and is bound to play a role in the thermal and signal to noise management of future quantum devices. The present work also demonstrates measurement strategies widening the range of experimental systems eligible for thermal explorations: by exploiting complementary auto- and cross-correlation measurements of the electrical fluctuations, we have shown that the different sources of noise can be accessed separately. We expect that such advanced combinations of fluctuation measurements will play an increasing role in the thermal and noise investigations of quantum circuits.

## Methods

**Sample.** The Al(Ga)As 2DEG has an electron density of  $2.5 \times 10^{11} \text{ cm}^{-2}$ , a mobility of  $10^6 \text{ cm}^2 \text{ V}^{-1} \text{ s}^{-1}$  and is located 105 nm below the surface. The central island is formed from a metallic layering of nickel (30 nm), gold (120 nm), and germanium (60 nm), which is thermally annealed at 440 °C for 50 s to make an electrical contact with the 2DEG. The two quantum Hall edge channels at filling factor  $\nu = 2$

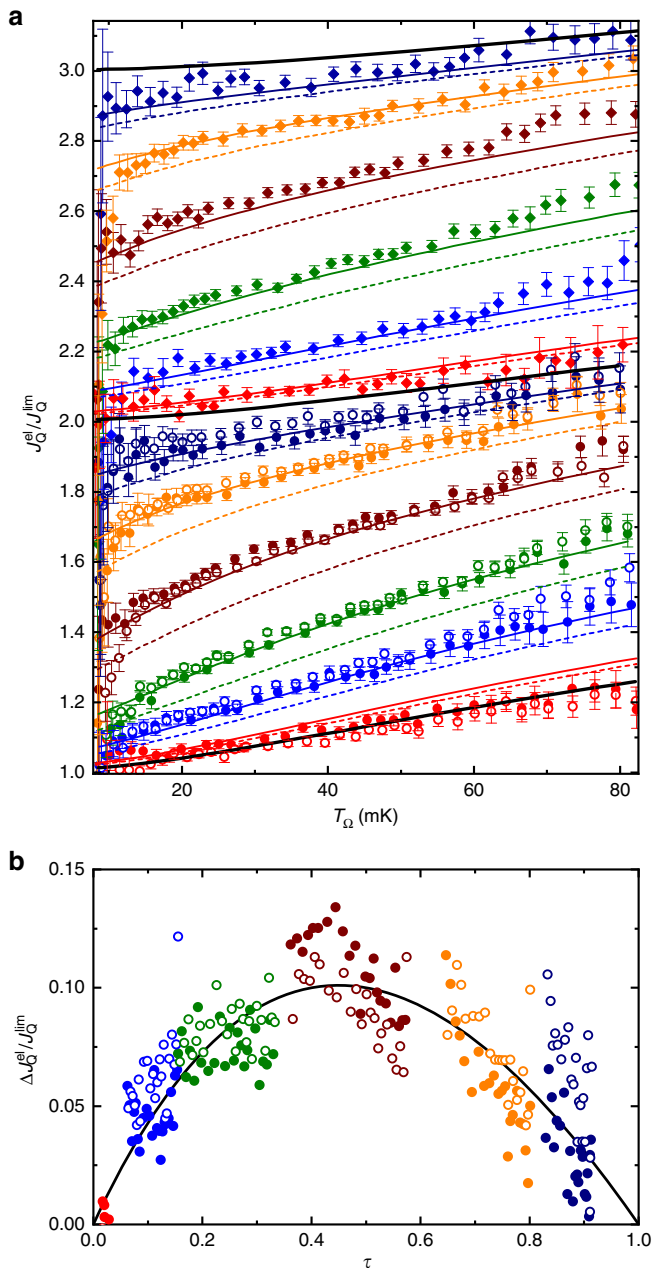


**Fig. 3 Electronic heat flow.** **a** Experimental  $J_Q^{\text{el}}/J_Q^{\text{lim}}$  (with  $J_Q^{\text{lim}} = \pi^2 k_B^2 (T_\Omega^2 - T^2)/6h$ ) are plotted as symbols versus  $T_\Omega$  with  $N = 2$  (circles) and  $N = 3$  (diamonds), for a broad range of QPC tunings (colors). Error bars represent the standard statistical error. Black continuous lines are predictions at  $\tau = 0$  for  $N = 2$  (bottom), 3 (middle), and 4 (top). Dashed lines are interpolations between ballistic predictions, linear in the measured  $\tau$ . Continuous lines are theoretical predictions. **b** Symbols represent the difference  $\Delta J_Q^{\text{el}}$  between experimental  $J_Q^{\text{el}}$  ( $N = 2$ ,  $T_\Omega \in [17, 65]$  mK in panel **a**) and the corresponding interpolation between ballistic predictions, normalized by  $J_Q^{\text{lim}}$ . The continuous line displays versus  $\tau$  the low-temperature prediction  $\tau(1 - \tau)/(N + \tau)$  for  $N = 2$ .

are found in near perfect contact with the island, with a reflection probability below  $6 \times 10^{-3}$  (see Methods in ref. <sup>14</sup> for a detailed description of the characterization procedure). The short  $\sim 1 \mu\text{m}$  distance between metallic island and QPC combined with the low temperatures ( $T_\Omega \lesssim 80$  mK) ascertains that the interaction between co-propagating channels can be safely ignored (see e.g. ref. <sup>32</sup>), as in previous works with the same sample<sup>14,23,33–35</sup>. The self-capacitance of the island  $C \simeq 3.1$  fF (corresponding to a charging energy  $E_C = e^2/2C \approx k_B \times 0.3$  K) is obtained from standard Coulomb diamond measurements (with all channels connected to the device tuned in the tunnel regime).

**Noise measurement setup.** The time-dependent current fluctuations  $\delta I_1(t)$  and  $\delta I_2(t)$  impinging, respectively, on electrodes 1 and 2 are first amplified with a cryogenic amplifier located on the 4K stage of a dilution refrigerator, and with a room temperature amplifier. They are then digitized at 10 Mbit/s and sent to a computer. The Fourier auto- and cross-correlations analysis are performed over a 180 kHz bandwidth centered on 0.855 MHz (the resonant frequency of the LC oscillators shown in Fig. 1a). The amplification gains  $G_{1,2}^{\text{amp}}$  are separately calibrated from the same standard shot-noise vs voltage bias measurements used to determine the base temperature  $T$  (see corresponding section). We find that  $G_{1,2}^{\text{amp}}$  are stable along each run, but slightly different from cooldown to cooldown. Averaging 862 (2840) shot noise vs voltage bias sweeps, the statistical uncertainty on  $G_{1,2}^{\text{amp}}$  is below 0.09% (0.04%) for the first (second) experimental run shown here. The cross-correlation gain  $G_X^{\text{amp}}$  is also impacted by the matching between the two resonators. For a perfect match,  $G_X^{\text{amp}} = \sqrt{G_1^{\text{amp}} G_2^{\text{amp}}}$ . In general, a correction factor  $c_{12}$  needs to be introduced  $G_X^{\text{amp}} = \sqrt{G_1^{\text{amp}} G_2^{\text{amp}}} \times c_{12}$ . This factor  $c_{12}$  is experimentally characterized at  $\tau = 0$  ( $N_{1,2} \neq 0$ ) from the robust relation  $\Delta S_{11} = \Delta S_{22} = -\Delta S_{12}$ , which directly results from the negligible charge accumulation on the island at the measurement frequencies. In practice, we find an essentially perfect resonators' match ( $c_{12} \approx 1.000$  and  $0.993$  for the first and second cooldown, respectively).

**Dissipated Joule power.** The bulk of the Joule power dissipated within the electronic fluid in the metallic island is given by the expression  $P_J \simeq (N_1 V_1^2 + N_2 V_2^2)/2R_K$ . We also include the small additional contributions  $P_J^{\text{ac}}$  due to the extra power dissipated from the small ac voltages  $V_{1,2,3}^{\text{ac}} \simeq 0.23 \mu\text{V}_{\text{rms}}$  applied (at different low frequencies) to the three source electrodes (to simultaneously measure with lock-in the conductances across each of the three QPCs), as well as a separately characterized small triboelectric voltage from the pulse tube vibrations specifically developing on the source electrode 1 (feeding the top QPC)  $V_1^{\text{tribo}} \simeq 0.4 \mu\text{V}_{\text{rms}}$ :

$$P_J^{\text{ac}} = \frac{1}{2R_K(N + \tau)} \times \{ (V_1^{\text{ac}})^2 + (V_1^{\text{tribo}})^2 \} N_1(N_2 + \tau) + (V_2^{\text{ac}})^2 N_2(N_1 + \tau) + (V_3^{\text{ac}})^2 \tau N. \quad (3)$$

In practice,  $P_J^{\text{ac}} \in [2, 6]$  aW is below 1% of  $P_J$  at  $T_\Omega \gtrsim 20$  mK. It corresponds to a temperature increase in the island of  $\sim 0.3$  mK at zero dc bias (see section Base electron temperature). Note that we avoid possible mismatch from the thermoelectric voltage developing along the measurement lines by applying a current dc bias. It is converted onchip into a voltage exploiting the well-defined quantum Hall resistance  $R_K/\nu$  connecting current biased electrodes and cold electrical grounds.

**Base electron temperature.** The base electronic temperature  $T$  is extracted from standard shot-noise measurements, applying a dc bias voltage directly to a QPC set to a transmission probability of one half, with the floating island bypassed using side gates (see Methods in ref. <sup>34</sup> for further details).

Due to the small  $P_J^{\text{ac}}$  (see section Dissipated Joule power), the temperature of the floating island is slightly higher than  $T$  even in the absence of a dc voltage. This small temperature increase is obtained by measuring the cross-correlations at zero dc bias  $V_1 = V_2 = 0$  (carefully calibrating instrumental offsets just before and after each measurement sequence), from the relation:

$$T_\Omega(V_{1,2} = 0) - T \simeq -\frac{R_K}{2k_B} \frac{N + \tau}{N_1 N_2} S_{12}(V_{1,2} = 0), \quad (4)$$

which straightforwardly relies on the generalized fluctuation-dissipation relation. Although there are deviations from the generalized fluctuation-dissipation relation in the presence of a generic channel, as studied in this work, this approximation is excellent for small  $T_\Omega(V_{1,2} = 0) - T \ll T$  such as in the present case. We find  $T_\Omega(V_{1,2} = 0) - T \simeq 0.3$  mK (always below 0.6 mK), consistent with expectations based on the value of  $P_J^{\text{ac}}$  given by Eq. (3). This small temperature difference is included in the experimental determination of  $T_\Omega$ .

**Excess electron temperature and shot noise.** This section details how are obtained the excess electron temperature,  $\Delta T_\Omega = T_\Omega - T_\Omega(V_{1,2} = 0)$ , and the resulting excess noise generated across the generic QPC,  $S_{\text{qpc}}^{\text{exc}} = \langle \delta I_{\text{qpc}}^2 \rangle - \langle \delta I_{\text{qpc}}^2 \rangle(V_{1,2} = 0)$ . A schematic representation of the circuit is shown in Fig. 4 with arrows indicating the chirality also corresponding to the convention used for positive currents. The large electrodes labeled  $E_n$  ( $n \in \{1, 2\}$ ) include each a measurement electrode  $M_n$  and a voltage biased source electrode  $S_n$ . The floating central metallic node is labeled  $\Omega$ .

First, let us separately consider a current fluctuation  $\delta I_{\text{qpc}}$  generated across the generic QPC (see Fig. 4), and determine the resulting current fluctuations  $\delta I_{M_1, M_2}^{\text{qpc}}$  impinging on the measurement electrodes  $M_{1,2}$ . As the corresponding charge accumulated in the island relaxes very fast compared to the measurement frequencies ( $1/R_K C \sim 10$  GHz  $\gg$  1 MHz), the current  $\delta I_{\text{qpc}}$  injected in the island is compensated by the outgoing current from the resulting voltage fluctuation  $\delta V_\Omega$  of the floating island. This reads  $\delta I_{\text{qpc}} = (N + \tau)\delta V_\Omega/R_K$  (for a treatment of

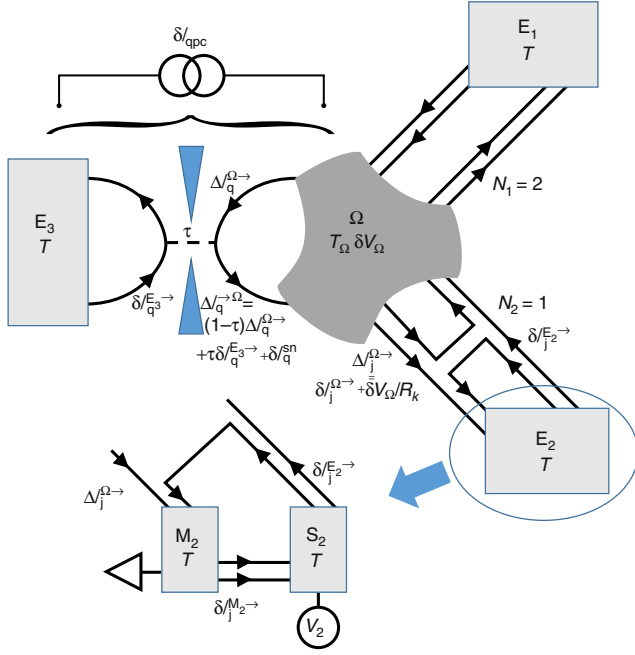


**Fig. 4 Noise schematic.** Graphical representation of the different current and voltage fluctuations discussed in the text.

charge relaxation at arbitrary frequencies see section Heat Coulomb blockade predictions). Then,  $\delta I_{M1(2)}^{qpc} = N_{1(2)} \delta V_{\Omega} / R_K = \delta I_{qpc} N_{1(2)} / (N + \tau)$ . Consequently, the QPC noise’s contribution to the autocorrelation signal is

$$S_{11(22)}^{qpc} = S_{qpc} N_{1(2)}^2 / (N + \tau)^2, \quad (5)$$

and its contribution to the cross-correlation signal is

$$S_{12}^{qpc} = S_{qpc} N_1 N_2 / (N + \tau)^2. \quad (6)$$

Second, we separately consider a current fluctuation  $\delta I_j^{\Omega \rightarrow}$  emitted from the island, by the thermal fluctuations of electronic states’ population at  $T_{\Omega}$ , into a ballistic channel  $j$ . From the fast charge relaxation of the island pointed out in the previous paragraph, one obtains  $\delta V_{\Omega} / R_K = -\delta I_j^{\Omega \rightarrow} / (N + \tau)$ . On the one hand, the current fluctuation measured on the electrode  $M_1$  if the channel  $j$  propagates toward the electrode  $M_2$  ( $j \in M_2$ ) is then  $\delta I_{M1}^{\Omega \rightarrow} = -N_1 / (N + \tau) \delta I_{j \in M_2}^{\Omega \rightarrow}$ . The corresponding autocorrelation signal on  $M_1$ , resulting from the thermal current fluctuations emitted toward  $M_2$  (summing all  $j \in M_2$ ) therefore reads:

$$S_{11}^{\Omega \rightarrow} = \frac{N_1^2}{(N + \tau)^2} \sum_{j=1}^{N_2} \langle (\delta I_j^{\Omega \rightarrow})^2 \rangle = N_2 \times \frac{N_1^2}{(N + \tau)^2} \langle (\delta I^{\Omega \rightarrow})^2 \rangle, \quad (7)$$

where the unimportant channel index  $j$  is omitted in  $\langle (\delta I^{\Omega \rightarrow})^2 \rangle \equiv \langle (\delta I_j^{\Omega \rightarrow})^2 \rangle$  (independent of  $j$ ). On the other hand, the current fluctuation measured on the electrode  $M_1$  if the channel  $j$  is also connected to the electrode  $M_1$  ( $j \in M_1$ ) includes both the direct term  $\delta I_{j \in M_1}^{\Omega \rightarrow}$  and the smaller  $\delta V_{\Omega}$  contribution:  $\delta I_{M1}^{\Omega \rightarrow} = [1 - N_1 / (N + \tau)] \delta I_{j \in M_1}^{\Omega \rightarrow}$ . As a result

$$S_{11}^{\Omega \rightarrow} = \left(1 - \frac{N_1}{N + \tau}\right)^2 \sum_{j=1}^{N_1} \langle (\delta I_j^{\Omega \rightarrow})^2 \rangle = N_1 \times \left(1 - \frac{N_1}{N + \tau}\right)^2 \langle (\delta I^{\Omega \rightarrow})^2 \rangle, \quad (8)$$

and

$$S_{12}^{\Omega \rightarrow} = -N_1 \times \left(1 - \frac{N_1}{N + \tau}\right) \frac{N_2}{N + \tau} \langle (\delta I^{\Omega \rightarrow})^2 \rangle. \quad (9)$$

Summing up the independent contributions from the QPC ( $\delta I_{qpc}$ ) and from all ballistic channels (emitted  $\delta I_j^{\Omega \rightarrow}$  and absorbed  $\delta I_j^{E_n \rightarrow}$ ), one straightforwardly

obtains for the autocorrelation signal:

$$S_{11(22)} = N_{1(2)} \left[ \left(1 - \frac{N_{1(2)}}{N + \tau}\right)^2 + \frac{N_1 N_2}{(N + \tau)^2} \right] \langle (\delta I^{\Omega \rightarrow})^2 \rangle + \frac{N_{1(2)}^2}{(N + \tau)^2} S_{qpc} + \frac{N_{1(2)}^2 N}{(N + \tau)^2} \langle (\delta I^{E \rightarrow})^2 \rangle + S_{offset1(2)}, \quad (10)$$

with  $S_{offset1(2)}$  a noise offset mostly corresponding to the amplification chain, and also including the thermal noise along the  $2 - N_{1(2)}$  reflected channels and along the 2 quantum Hall channels propagating from measurement ( $M$ ) to source ( $S$ ) contacts (for the experimental bulk filling factor  $\nu = 2$ ; see Fig. 4). Similarly, one gets for the cross-correlation signal:

$$S_{12} = \frac{N_1 N_2}{(N + \tau)^2} [-(N + 2\tau) \langle (\delta I^{\Omega \rightarrow})^2 \rangle + S_{qpc} + N \langle (\delta I^{E \rightarrow})^2 \rangle]. \quad (11)$$

Focusing on the excess signal with respect to  $V_{1,2} = 0$ , one obtains from Eqs. (10) and (11):

$$S_{ball}^{exc} = \frac{S_{11}^{exc}}{2N_1} + \frac{S_{22}^{exc}}{2N_2} - \frac{S_{12}^{exc} N}{2N_1 N_2}, \quad (12)$$

with  $S_{ball}^{exc} = \langle (\delta I^{\Omega \rightarrow})^2 \rangle - \langle (\delta I^{\Omega \rightarrow})^2 \rangle (V_{1,2} = 0)$  the excess noise generated across one ballistic channel. From the Johnson–Nyquist-type relation well established in the ballistic case<sup>5-7,16-18</sup>  $\langle (\delta I^{\Omega \rightarrow})^2 \rangle = 2k_B T_{\Omega} / R_K$ , the excess island’s temperature reads:

$$\Delta T_{\Omega} = \frac{R_K}{2k_B} \left( \frac{S_{11}^{exc}}{2N_1} + \frac{S_{22}^{exc}}{2N_2} - \frac{S_{12}^{exc} N}{2N_1 N_2} \right). \quad (13)$$

Solving Eqs. (10) and (11) also provides  $S_{qpc}^{exc}$ :

$$S_{qpc}^{exc} = (N + 2\tau) \left( \frac{S_{11}^{exc}}{2N_1} + \frac{S_{22}^{exc}}{2N_2} \right) + S_{12}^{exc} \frac{(N + \tau)^2 + \tau^2}{2N_1 N_2}. \quad (14)$$

**Heat Coulomb blockade predictions.** In this section we derive the predictions shown as continuous lines in Fig. 3 and Supplementary Figs. 3 and 4, for the electronic flow of heat  $J_Q^E$  in the presence of a generic quantum channel. We follow the Langevin approach developed for ballistic systems in ref. 18, and expand it to the case where the current is partially reflected with a probability  $1 - \tau$  on a QPC inserted along one of the channels (the other channels remaining ballistic, see schematic in Fig. 4). The three main differences with ref. 18 are: (i) the symmetry between channels is broken, (ii) a partition noise emerges at the generic QPC, (iii) the transmission probability  $\tau$  depends on the temperatures due to dynamical Coulomb blockade.

The heat flow  $J_{Qj}^{\rightarrow}$  propagating in one direction ( $\rightarrow$ ) along one electronic channel ( $j$ ) is obtained from the time-dependent electrical current fluctuations  $\Delta I_j^{\rightarrow}$  propagating in the same direction at the considered location<sup>18</sup>:

$$J_{Qj}^{\rightarrow} = \frac{\hbar}{2e^2} \int_{-\infty}^{\infty} d\omega \left( \langle (\Delta I_j^{\rightarrow})^2 \rangle - \langle (\Delta I_j^{\rightarrow})^2 \rangle_{vacuum} \right), \quad (15)$$

with  $\langle \rangle_{vacuum}$  referring to the vacuum fluctuations at zero temperature.

If  $\Delta I_j^{\rightarrow}$  directly originates from the large, voltage biased electrodes ( $S_{1,2,3}$  in  $E_{1,2,3}$ ), then it only includes the emitted thermal current fluctuation  $\delta I_j^{E_n \rightarrow}$  (see Fig. 4). These thermal fluctuations are assumed uncorrelated ( $\langle \delta I_j^{E_n \rightarrow} \delta I_k^{E_m \rightarrow} \rangle = 0$  for  $j \neq k$  even at  $m = n$ ) and of variance given by the usual thermal noise expression at the base temperature  $T$ <sup>18</sup>:

$$\langle (\delta I_j^{E_n \rightarrow})^2 \rangle(\omega) = \frac{\hbar \omega / R_K}{-1 + \exp[\hbar \omega / k_B T]}. \quad (16)$$

Note the factor two difference with the standard low-frequency expression  $2k_B T / R_K$ , in which the contribution at positive and negative frequencies are added. Injecting Eq. (16) into Eq. (15), one obtains the usual expression  $J_{Qj}^{\rightarrow} = (\pi k_B T)^2 / 6\hbar$ .

In contrast to the voltage biased electrodes, the floating metallic node’s electrochemical potential exhibits fluctuations  $\delta V_{\Omega}$  (related to charge fluctuations as, e.g., in the voltage probe and dephasing probe models, see ref. 19 and references therein). These result in the emission of identical current fluctuations  $\delta V_{\Omega} / R_K$  in all outgoing channels<sup>18,19</sup>. Such current fluctuations add up with the thermal emission  $\delta I_j^{\Omega \rightarrow}$  of electrons from the central node:  $\Delta I_j^{\rightarrow} = \delta I_j^{\Omega \rightarrow} + \delta V_{\Omega} / R_K$ , with  $\langle \delta I_j^{\Omega \rightarrow} \delta I_k^{\Omega \rightarrow} \rangle = 0$  for  $j \neq k$  and a variance  $\langle (\delta I_j^{\Omega \rightarrow})^2 \rangle$  given by the same Eq. (16) but with the island temperature  $T_{\Omega}$  instead of  $T$ . The integrand in Eq. (15) therefore includes such correlations as  $\langle \delta I_j^{\Omega \rightarrow} \delta V_{\Omega} \rangle$ . These can be obtained from the connection to the island’s charge fluctuations  $\delta Q = C \delta V_{\Omega}$  ( $\delta Q = Q - \langle Q \rangle$  with  $Q$  the overall charge of the island, and  $C$  its self-capacitance), which obey the charge

conservation relation:

$$\begin{aligned}
 i\omega\delta Q &= \sum_{j=1}^{N+1} (\Delta I_j^{-\Omega} - \Delta I_j^{\Omega-\}) \\
 &= \Delta I_q^{-\Omega} - \delta I_q^{\Omega-\} - \delta Q/R_K C \\
 &\quad + \sum_{j=1}^N (\delta I_j^{E\rightarrow} - \delta I_j^{\Omega-\}) - N\delta Q/R_K C,
 \end{aligned} \tag{17}$$

where we separated in the second equality the generic channel labeled with the index  $q$  (first line) from the  $N$  ballistic channels (second line). In channel  $q$ , the incoming current fluctuations toward the island  $\Delta I_q^{-\Omega}$  include three contributions:

$$\Delta I_q^{-\Omega} = \tau\delta I_q^{E_3\rightarrow} + (1-\tau)(\delta I_q^{\Omega-\} + \delta Q/R_K C) + \delta I_q^{sn}, \tag{18}$$

with the third term corresponding in the Langevin description to an uncorrelated noise source induced by the electrons' partition at the QPC. At equilibrium ( $T = T_\Omega$ ), the Johnson-Nyquist relation at low frequencies imposes  $2\langle(\delta I_q^{sn})^2\rangle = \tau(1-\tau) \times 4k_B T/R_K$  (the factor two is because positive and negative frequencies are included for this comparison). In the non-equilibrium regime ( $T \neq T_\Omega$ ), the information needed on  $\delta I_q^{sn}$  for the heat current will be directly obtained from energy flow conservation at the input and output of the QPC (see below). Note that we neglect in Eq. (18) the small time delay associated with the round loop path island-QPC-island (a delay of about 20 ps using a typical velocity of  $10^5$  m/s), and that the transmission probability  $\tau$  is taken as a frequency independent value (that depends on  $T$  and  $T_\Omega$  due to dynamical Coulomb blockade, see e.g. ref. 23). Combining Eqs. (17) and (18) allows us to write  $\delta Q$  as a function of uncorrelated noise sources:

$$\begin{aligned}
 (i\omega + \tau_\Omega/R_K C)\delta Q &= \tau(\delta I_q^{E_3\rightarrow} - \delta I_q^{\Omega-\}) \\
 &\quad + \delta I_q^{sn} + \sum_{j=1}^N (\delta I_j^{E\rightarrow} - \delta I_j^{\Omega-\}),
 \end{aligned} \tag{19}$$

where we introduced  $\tau_\Omega$  defined as the sum of the transmission probabilities of the channels connected to the island:

$$\tau_\Omega = N + \tau. \tag{20}$$

This straightforwardly makes it possible to formulate the integrands  $\langle(\Delta I_q^{-\Omega})^2\rangle$  and  $\langle(\Delta I_q^{\Omega-\})^2\rangle$  as functions of uncorrelated noise sources (independently of  $\delta V_\Omega$ ). As an illustration, we obtain for the latter:

$$\begin{aligned}
 \langle(\Delta I_q^{\Omega-\})^2\rangle &= \frac{\langle(\delta I_q^{sn})^2\rangle + (\tau_\Omega - \tau(1-\tau))\langle(\delta I_q^{E\rightarrow})^2\rangle}{\tau_\Omega^2 + (\omega R_K C)^2} \\
 &\quad + \left(1 + \frac{\tau_\Omega - \tau(1-\tau) - 2\tau\tau_\Omega}{\tau_\Omega^2 + (\omega R_K C)^2}\right)\langle(\delta I_q^{\Omega-\})^2\rangle,
 \end{aligned} \tag{21}$$

where the arbitrary index  $j$  is omitted. The only missing ingredient is  $\delta I_q^{sn}$ . As pointed out above, the required information can be obtained most robustly from global heat conservation at the QPC:  $J_{Qq}^{E_3\rightarrow} + J_{Qq}^{\Omega-\} = J_{Qq}^{E_3\rightarrow} + J_{Qq}^{\Omega-\}$ , with  $J_{Qq}^{E_3\rightarrow}$  the flow of heat from the large electrode  $E_3$  toward the QPC,  $J_{Qq}^{\Omega-\}$  the flow of heat from the island toward the QPC,  $J_{Qq}^{E_3\rightarrow}$  the flow of heat from the QPC toward  $E_3$ , and  $J_{Qq}^{\Omega-\}$  the flow of heat from the QPC toward the island. Using Eq. (15), this equality reads:

$$\begin{aligned}
 \int_{-\infty}^{\infty} d\omega \langle(\delta I_q^{sn})^2\rangle &\times \left[1 + \frac{\tau_\Omega - \tau(1-\tau) - 2\tau\tau_\Omega}{\tau_\Omega^2 + (\omega R_K C)^2}\right] \\
 &= \int_{-\infty}^{\infty} d\omega \tau(1-\tau) \left[1 + \frac{\tau_\Omega - \tau(1-\tau) - 2\tau\tau_\Omega}{\tau_\Omega^2 + (\omega R_K C)^2}\right] \\
 &\quad \times \left\{\langle(\delta I_q^{E_3\rightarrow})^2\rangle + \langle(\delta I_q^{\Omega-\})^2\rangle\right\}.
 \end{aligned} \tag{22}$$

Summing up the contributions of all channels and performing the integration in Eq. (15), we obtain for the net heat flow from the metallic island:

$$\begin{aligned}
 J_Q^{\text{thy}} &= \sum_{j=1}^{N+1} (J_{Qj}^{\Omega-\} - J_{Qj}^{\Omega-}) \\
 &= \tau_\Omega \frac{\pi^2 k_B^2}{6h} (T_\Omega^2 - T^2) - \tau_\Omega \frac{h(\tau_\Omega - \tau(1-\tau))}{(2\pi R_K C)^2} \\
 &\quad \times \left[ \Im\left(\frac{h\tau_\Omega/R_K C}{2\pi k_B T_\Omega}\right) - \Im\left(\frac{h\tau_\Omega/R_K C}{2\pi k_B T}\right) \right],
 \end{aligned} \tag{23}$$

with the function  $\Im$  given by

$$\Im(x) = \frac{1}{2} \left[ \ln\left(\frac{x}{2\pi}\right) - \frac{\pi}{x} - \psi\left(\frac{x}{2\pi}\right) \right], \tag{24}$$

with  $\psi(z)$  the digamma function. Equation (23) was used to calculate the

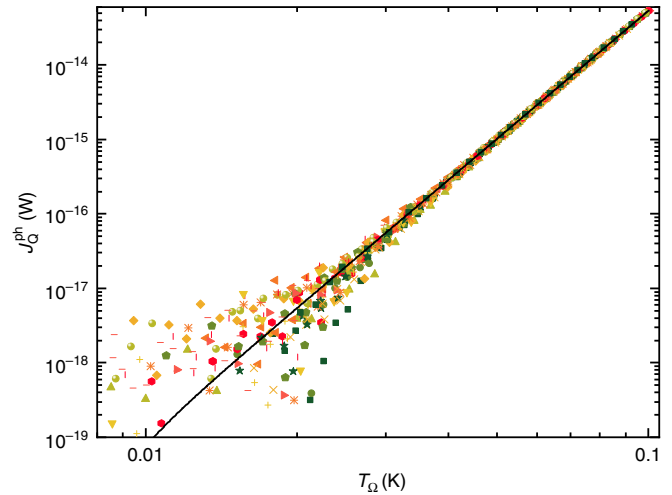


**Fig. 5 Electron-phonon heat transfers.** Symbols represent the flow of heat  $J_Q^{\text{ph}}$  from the electrons within the metallic island to the phonons at  $T \simeq 8$  mK. Different symbols represent data points from different configurations  $N \in \{2, 3, 4\}$  and  $\tau \in \{0, 1\}$ , including measurements performed in two different cooldowns. All the data collapse on  $J_Q^{\text{ph}} = 2.752 \times 10^{-8} (T_\Omega^{5.709} - T^{5.709})$  W (continuous line).

predictions shown as continuous lines in Fig. 3a, Supplementary Fig. 3b and Supplementary Fig. 4.

At  $\tau = 0$  or 1, Eq. (23) reduces to the expression derived for a ballistic system<sup>18</sup> (see Methods in ref. 16 for a similar formulation). At high temperatures, Eq. (23) reduces to the non-interacting result matching the widespread Wiedemann-Franz law (without additional contribution from the partition noise):

$$\begin{aligned}
 J_Q^{\text{thy}} \left( T, T_\Omega \gg \frac{h\tau_\Omega}{k_B R_K C} \right) &\simeq \tau_\Omega \frac{\pi^2 k_B^2}{6h} (T_\Omega^2 - T^2) \\
 &\simeq \tau_\Omega J_Q^{\text{lim}}.
 \end{aligned} \tag{25}$$

At low temperatures, Eq. (23) simplifies into:

$$\begin{aligned}
 J_Q^{\text{thy}} \left( T, T_\Omega \ll \frac{h\tau_\Omega}{k_B R_K C} \right) &\simeq \left( \tau_\Omega - 1 + \frac{\tau(1-\tau)}{\tau_\Omega} \right) \frac{\pi^2 k_B^2}{6h} (T_\Omega^2 - T^2) \\
 &\simeq \left( \tau_\Omega - 1 + \frac{\tau(1-\tau)}{\tau_\Omega} \right) J_Q^{\text{lim}}.
 \end{aligned} \tag{26}$$

In this case, in addition to the systematic blockade of one ballistic channel ( $-1$ ) with respect to the non-interacting case ( $\tau_\Omega$ ), we find an additional contribution to the flow of heat whose partition character is signaled by the characteristic  $\tau(1-\tau)$  dependence.

**Electron-phonon heat transfers.** The Fig. 5 displays the amount of heat transferred from electrons in the metallic island to cold phonons at base temperature  $T \simeq 8$  mK. It is obtained by subtracting from the injected Joule power  $P_j$  the known electronic heat flow  $J_Q^{\text{el}}$  when the circuit is tuned in the ballistic regime (for the subtracted expression of  $J_Q^{\text{el}}$ , see Eq. (23) with  $\tau \in \{0, 1\}$  or refs. 16,18). The data from all ballistic configurations ( $N \in \{2, 3, 4\}$ ,  $\tau \in \{0, 1\}$ ) collapse on the same curve, fitted by  $J_Q^{\text{ph}} = \Sigma(T_\Omega^\alpha - T^\alpha)$  with  $\Sigma = 2.752 \times 10^{-8}$  W K $^{-\alpha}$  and  $\alpha = 5.709$ . We checked that this power law also precisely accounts for  $J_Q^{\text{ph}}$  at the larger temperature  $T \simeq 16$  mK (data not shown).

### Data availability

The data that support the findings of this study are available from the corresponding author upon reasonable request.

Received: 4 July 2019; Accepted: 8 November 2019;

Published online: 10 December 2019

### References

- Schwab, K., Henriksen, E., Worlock, J. & Roukes, M. Measurement of the quantum of thermal conductance. *Nature* **404**, 974–977 (2000).

2. Giazotto, F. & Martínez-Pérez, M. J. The Josephson heat interferometer. *Nature* **492**, 401–405 (2012).
3. Ronzani, A. et al. Tunable photonic heat transport in a quantum heat valve. *Nat. Phys.* **14**, 991–995 (2018).
4. Timofeev, A. V., Helle, M., Meschke, M., Möttönen, M. & Pekola, J. P. Electronic refrigeration at the quantum limit. *Phys. Rev. Lett.* **102**, 200801 (2009).
5. Jezouin, S. et al. Quantum limit of heat flow across a single electronic channel. *Science* **342**, 601–604 (2013).
6. Srivastav, S. et al. Universal quantized thermal conductance in graphene. *Sci. Adv.* **5**, eaaw5798 (2019).
7. Banerjee, M. et al. Observed quantization of anyonic heat flow. *Nature* **545**, 75–79 (2017).
8. Partanen, M. et al. Quantum-limited heat conduction over macroscopic distances. *Nat. Phys.* **12**, 460 (2016).
9. Mosso, N. et al. Heat transport through atomic contacts. *Nat. Nanotechnol.* **12**, 430–433 (2017).
10. Cui, L. et al. Quantized thermal transport in single-atom junctions. *Science* **355**, 1192–1195 (2017).
11. Grabert, H. & Devoret, M. (eds) *Single Charge Tunneling* (Plenum, New York, 1992).
12. Likharev, K. Single-electron devices and their applications. *Proc. IEEE* **87**, 606–632 (1999).
13. Parmentier, F. D. et al. Strong back-action of a linear circuit on a single electronic quantum channel. *Nat. Phys.* **7**, 935–938 (2011).
14. Jezouin, S. et al. Controlling charge quantization with quantum fluctuations. *Nature* **536**, 58–62 (2016).
15. Dutta, B. et al. Thermal conductance of a single-electron transistor. *Phys. Rev. Lett.* **119**, 077701 (2017).
16. Sivre, E. et al. Heat Coulomb blockade of one ballistic channel. *Nat. Phys.* **14**, 145–148 (2018).
17. Banerjee, M. et al. Observation of half-integer thermal Hall conductance. *Nature* **559**, 205–210 (2018).
18. Slobodeniuk, A., Levkivskiy, I. & Sukhorukov, E. Equilibration of quantum Hall edge states by an Ohmic contact. *Phys. Rev. B* **88**, 165307 (2013).
19. Blanter, Y. & Büttiker, M. Shot noise in mesoscopic conductors. *Phys. Rep.* **336**, 1–166 (2000).
20. Lumbroso, O., Simine, L., Nitzan, A., Segal, D. & Tal, O. Electronic noise due to temperature differences in atomic-scale junctions. *Nature* **562**, 240–244 (2018).
21. Martin, T. & Landauer, R. Wave-packet approach to noise in multichannel mesoscopic systems. *Phys. Rev. B* **45**, 1742–1755 (1992).
22. Jezouin, S. et al. Tomonaga-Luttinger physics in electronic quantum circuits. *Nat. Commun.* **4**, 1802 (2013).
23. Anthore, A. et al. Circuit quantum simulation of a Tomonaga-Luttinger liquid with an impurity. *Phys. Rev. X* **8**, 031075 (2018).
24. Blanter, Y. M. & Sukhorukov, E. V. Semiclassical theory of conductance and noise in open chaotic cavities. *Phys. Rev. Lett.* **84**, 1280–1283 (2000).
25. Reydellet, L.-H., Roche, P., Glattli, D. C., Etienne, B. & Jin, Y. Quantum partition noise of photon-created electron-hole pairs. *Phys. Rev. Lett.* **90**, 176803 (2003).
26. Duprez, H. et al. Transmitting the quantum state of electrons across a metallic island with Coulomb interaction. Preprint at <https://arXiv.org/abs/1902.07569> (2019).
27. Idrisov, E., Levkivskiy, I. & Sukhorukov, E. Dephasing in a Mach-Zehnder Interferometer by an Ohmic Contact. *Phys. Rev. Lett.* **121**, 026802 (2018).
28. Clerk, A., Brouwer, P. & Ambegaokar, V. Interaction-induced restoration of phase coherence. *Phys. Rev. Lett.* **87**, 186801 (2001).
29. Idrisov, E., Levkivskiy, I. & Sukhorukov, E. Quantum ammeter. Preprint at <https://arXiv.org/abs/1906.10902> (2019).
30. Altimiras, C. et al. Chargeless heat transport in the fractional quantum hall regime. *Phys. Rev. Lett.* **109**, 026803 (2012).
31. Inoue, H. et al. Proliferation of neutral modes in fractional quantum Hall states. *Nat. Commun.* **5**, 4067 (2014).
32. leSueur, H. et al. Energy relaxation in the integer quantum Hall regime. *Phys. Rev. Lett.* **105**, 056803 (2010).
33. Iftikhar, Z. et al. Two-channel Kondo effect and renormalization flow with macroscopic quantum charge states. *Nature* **526**, 233–236 (2015).
34. Iftikhar, Z. et al. Primary thermometry triad at 6 mK in mesoscopic circuits. *Nat. Commun.* **7**, 12908 (2016).
35. Iftikhar, Z. et al. Tunable quantum criticality and superballistic transport in a ‘charge’ Kondo circuit. *Science* **360**, 1315–1320 (2018).

## Acknowledgements

This work was supported by the French RENATECH network, the national French program Investissements d’Avenir (Labex NanoSaclay, ANR-10-LABX-0035) and the French National Research Agency (projects QuTherm, ANR-16-CE30-0010, and SIM-CIRCUIT, ANR-18-CE47-0014-01). We thank Y. Jin for providing the cryogenic HEMTs used for the noise measurements, and E. Sukhorukov for fruitful discussions.

## Author contributions

E.S. and H.D. performed the experiment with inputs from A. Aassime, A. Anthore, and F.P.; A. Anthore, E.S., F.P. and H.D. analyzed the data and expanded the theory with help from A. Aassime; F.D.P. fabricated the sample using developments from A. Anthore; A.C., A.O., and U.G. grew the 2DEG; F.P. led the project and wrote the manuscript with contributions from A. Aassime, A. Anthore, E.S., H.D., and U.G.

## Competing interests

The authors declare no competing interests.

## Additional information


Supplementary information is available for this paper at <https://doi.org/10.1038/s41467-019-13566-8>.

Correspondence and requests for materials should be addressed to F.P.

Peer review information *Nature Communications* thanks Tomonori Arakawa, Liliana Arrachea and Elke Scheer for their contribution to the peer review of this work.

Reprints and permission information is available at <http://www.nature.com/reprints>

Publisher’s note Springer Nature remains neutral with regard to jurisdictional claims in published maps and institutional affiliations.

 **Open Access** This article is licensed under a Creative Commons Attribution 4.0 International License, which permits use, sharing, adaptation, distribution and reproduction in any medium or format, as long as you give appropriate credit to the original author(s) and the source, provide a link to the Creative Commons license, and indicate if changes were made. The images or other third party material in this article are included in the article’s Creative Commons license, unless indicated otherwise in a credit line to the material. If material is not included in the article’s Creative Commons license and your intended use is not permitted by statutory regulation or exceeds the permitted use, you will need to obtain permission directly from the copyright holder. To view a copy of this license, visit <http://creativecommons.org/licenses/by/4.0/>.

© The Author(s) 2019

**Macroscopic Electron Quantum Coherence in a Solid-State Circuit**H. Duprez,<sup>1,\*</sup> E. Sivre,<sup>1,\*</sup> A. Anthore,<sup>1,2</sup> A. Aassime,<sup>1</sup> A. Cavanna,<sup>1</sup> A. Ouerghi,<sup>1</sup> U. Gennser,<sup>1</sup> and F. Pierre<sup>1,†</sup><sup>1</sup>*Centre de Nanosciences et de Nanotechnologies (C2N), CNRS, Univ Paris Sud, Université Paris-Saclay, 91120 Palaiseau, France*<sup>2</sup>*Université de Paris, Univ Paris Diderot, 75013 Paris, France*

(Received 18 December 2018; published 14 May 2019)

The quantum coherence of electronic quasiparticles underpins many of the emerging transport properties of conductors at small scales. Novel electronic implementations of quantum optics devices are now available with perspectives such as “flying-qubit” manipulations. However, electronic quantum interferences in conductors remained up to now limited to propagation paths shorter than  $30\ \mu\text{m}$  independent of the material. Here we demonstrate strong electronic quantum interferences after a propagation along two  $0.1\text{-mm}$ -long pathways in a circuit. Interferences of visibility as high as 80% and 40% are observed on electronic analogues of the Mach-Zehnder interferometer of, respectively,  $24\text{-}\mu\text{m}$  and  $0.1\text{-mm}$  arm length, consistently corresponding to a  $0.25\text{-mm}$  electronic phase coherence length. While such devices perform best in the integer quantum Hall regime at filling factor 2, the electronic interferences are restricted by the Coulomb interaction between copropagating edge channels. We overcome this limitation by closing the inner channel in micron-scale loops of frozen internal degrees of freedom combined with a loop-closing strategy providing an essential isolation from the environment.

DOI: [10.1103/PhysRevX.9.021030](https://doi.org/10.1103/PhysRevX.9.021030)

Subject Areas: Condensed Matter Physics, Mesoscopics, Quantum Physics

**I. INTRODUCTION**

Ballistic electrons allow for advanced quantum manipulations at the single-electron level in circuits, in the spirit of the manipulation of photons in quantum optics [1–3]. Perspectives notably include a different paradigm for quantum-information processing with a nonlocal architecture based on “flying-qubits” encoded, for example, by the presence or absence of an electron within a propagating wave packet [1,2,4–7]. Electronic edge states topologically protected against disorder constitute promising solid-state platforms. In particular, the emblematic chiral edge channels propagating along a two-dimensional (2D) conductor in the quantum Hall regime are generally considered ideal 1D conductors. Their analogy with light beams, their *in situ* tunability by field effect, and the availability of single-electron emitters were exploited to implement the electronic analogues of optical devices, such as the interferometers of types Fabry-Perot [8], Mach-Zehnder [9], Hanbury-Brown and Twiss [10], and Hong-Ou-Mandel [11]. In contrast to photons, the Coulomb interaction

between charged electrons provides a natural correlation mechanism to realize, e.g., CNOT gates [1,2,4,5]. However, the same Coulomb interaction generally entangles the propagating electrons efficiently with numerous degrees of freedom, including the surrounding electrons, which gives rise to quantum decoherence [12] (see Ref. [13] for a notable exception).

In practice, the maximum electron phase coherence length  $L_\phi$  was previously found to reach remarkably similar values at the lowest accessible temperatures in very diverse systems, from diffusive metal ( $L_\phi \simeq 20\ \mu\text{m}$  reported in Ref. [14] at 40 mK) to near ballistic two-dimensional electron gas ( $L_\phi \simeq 20\ \mu\text{m}$  reported in Ref. [15] at 30 mK) and graphene ( $L_\phi \simeq 3\text{--}5\ \mu\text{m}$  estimated in Ref. [16] at 260 mK). Along the ballistic quantum Hall edge channels of specific interest for electron quantum optics,  $L_\phi \simeq 24\ \mu\text{m}$  was demonstrated at 20 mK [17] at the most advantageous magnetic field tuning corresponding to filling factor  $\nu = 2$  in a Ga(Al)As 2D electron gas. We also point out two promising findings: An important temperature robustness of small conductance oscillations measured across a  $6\text{-}\mu\text{m}$ -long Ga(Al)As device, from which a large value of  $L_\phi \sim 86\ \mu\text{m}$  was indirectly inferred [18] and conductance oscillations of very high visibility along a graphene *p-n* junction [19]. Here, we establish a macroscopic electron phase coherence length of  $0.25\ \text{mm}$  achieved along quantum Hall channels by nanocircuit engineering.

\*These authors contributed equally to this work.

†frederic.pierre@c2n.upsaclay.fr

Published by the American Physical Society under the terms of the [Creative Commons Attribution 4.0 International license](https://creativecommons.org/licenses/by/4.0/). Further distribution of this work must maintain attribution to the author(s) and the published article's title, journal citation, and DOI.

At low temperatures, short-range electron-electron interactions within the *same* chiral edge channel of the integer quantum Hall regime are predicted to increase the electrons' propagation velocity but not to limit their coherence [20,21]. The dominant dephasing mechanism is generally attributed to the interaction between electrons located in *adjacent* edge channels [20,22] (except at  $\nu = 1$  and fractional filling factors where the stronger decoherence [23,24] is not clearly understood). This picture is established by complementary signatures including energy transfers [25,26], charge fractionalization [27–29], and Hong-Ou-Mandel characterizations [30]. However, additional dissipative mechanisms yet unidentified were also evidenced experimentally, even in the most canonical  $\nu = 2$  case [25–27]. In this work, we demonstrate a circuit design strategy that very efficiently suppresses the essential decoherence mechanisms.

## II. NANOENGINEERING THE PHASE COHERENCE LENGTH

The electronic version of the Mach-Zehnder interferometer [MZI, schematically depicted in Fig. 1(a)] essentially consists in a quantum Hall edge channel following two separate paths, and in two quantum point contacts (QPCs) used as tunable beam splitters [9]. The quantum Hall regime is realized in a Ga(Al)As 2D electron gas immersed in a perpendicular magnetic field of 4.3 T corresponding to a filling factor  $\nu = 2$ , with two copropagating edge channels. The interfering MZI paths involve only the outer edge channel [thick black lines in Fig. 1(a)]. The two beam-splitter QPCs are formed by field effect using split gates [colored orange in Fig. 1(a) with suspended bridges to contact the top parts]. The quantum phase difference between the two paths is proportional to the enclosed magnetic flux. It is here controlled by fine-tuning the lower edge path with the voltage  $V_{pl}$  applied to a lateral plunger gate [colored green in Figs. 1(a) and 1(b)]. The quantum interferences are evidenced by sweeping  $V_{pl}$  from the resulting oscillations of the transmitted current impinging on the metallic electrode labeled *D* in Fig. 1(a). Their energy dependence with respect to the bias voltage  $V_{dc}$  applied to the source electrode is obtained from a concomitant noise in the transmitted current. The second MZI output is connected to the central metallic electrode (elongated yellow disk in Fig. 1), which is electrically grounded through a suspended bridge. In contrast to previous MZI implementations, our devices include two long surface gates [light gray in Figs. 1(a) and 1(b)] with a particular comb shape with both shafts and teeth placed over the 2D electron gas. This shape is essential for the presently demonstrated strong increase of the electron coherence. As illustrated in Fig. 1(a), these gates can be biased to form inner channel loops along the interfering outer edge channel paths. In order to unambiguously demonstrate and accurately measure very large phase

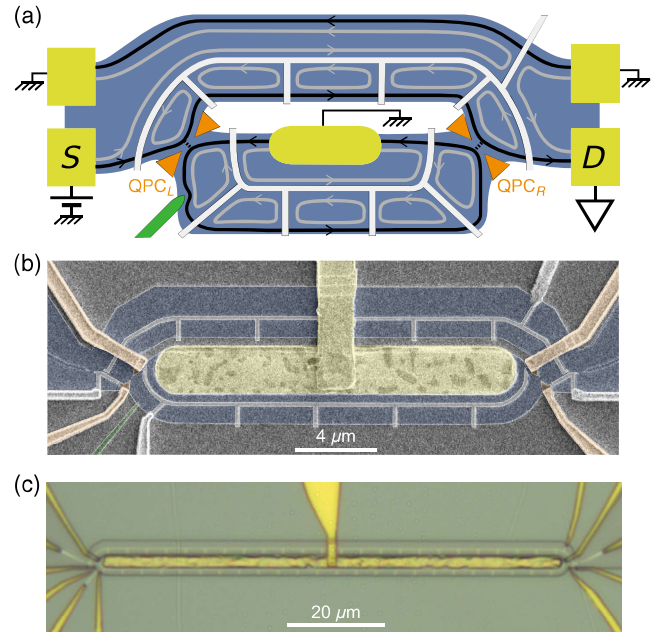


FIG. 1. Nanocircuit engineering of electronic coherence. (a) Sample schematic. Two chiral edge channels (black and gray lines with arrows) propagate along a 2D electron gas (blue) set in the integer quantum Hall regime at filling factor  $\nu = 2$ . The outer channel (black) follows two separate paths between tunable beam splitters implemented by quantum point contacts (orange), thereby forming a Mach-Zehnder interferometer. The inner edge channel (gray) can be closed into well-separated loops with specific comb-shaped gates (light gray) voltage biased to reflect only this channel. Sweeping the voltage on a lateral plunger gate (green) results in MZI oscillations of the current transmitted from source (*S*) to detector (*D*). (b) Colored scanning electron micrograph of the sample with MZI arms of symmetric length  $L \simeq 24 \mu\text{m}$ . (c) Optical image of the  $L \simeq 0.1 \text{ mm}$  MZI. The inner edge channel loops have nominally identical perimeters of  $9 \mu\text{m}$ , except one of  $5 \mu\text{m}$  for the lower left loop of each sample.

coherence lengths, we fabricate two MZIs with extraordinarily long symmetric arms of length  $L \simeq 24 \mu\text{m}$  [Fig. 1(b)] and  $0.1 \text{ mm}$  [Fig. 1(c)]. For a straightforward comparison at different  $L$ , the two devices are made concurrently (a few millimeters away on the same chip) with identical designs except for the length of the elongated central area and are simultaneously cooled down to 10 mK.

How can  $L_\phi$  be increased? It was initially shown that most of the electrons' energy relaxation can be frozen within the outer edge channel at  $\nu = 2$  (along an  $8\text{-}\mu\text{m}$  path) by closing into a loop the inner channel [31]. This freezing was explained by the electronic levels' quantization within the loop, which effectively quenches the phase space for inelastic collisions with the inner loop's electrons (for a level spacing larger than the available energy) [31,32]. As inelastic collisions also result in decoherence, a similar approach was subsequently tested on  $L_\phi$  using an electronic MZI [33]. However, the increase in  $L_\phi$  by forming inner channel loops was limited to a factor of 2 [33], relatively

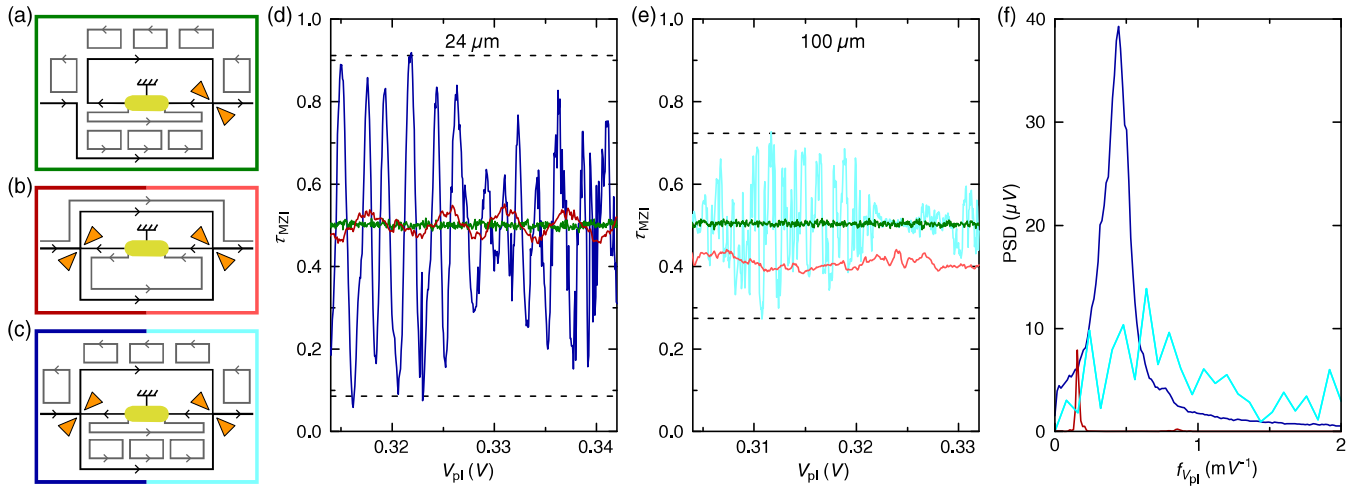


FIG. 2. Quantum oscillations. (a)–(c) Schematics of the different configurations. (d),(e) Continuous lines show versus plunger gate voltage  $V_{\text{pl}}$ , the measured fraction  $\tau_{\text{MZI}}$  of current transmitted from  $S$  to  $D$  along the outer channel of the  $L \approx 24 \mu\text{m}$  (d) and  $0.1 \text{ mm}$  (e) MZI [same color as the box enclosing the corresponding schematic in panels (a), (b), or (c); darker shade for the shorter device]. Horizontal dashed lines display the predicted  $\tau_{\text{MZI}}$  extrema for the same  $L_\phi = 0.25 \text{ mm}$  in both MZIs. (f) Continuous lines show the power spectral density of  $\tau_{\text{MZI}}(V_{\text{pl}})$  determined along large  $V_{\text{pl}}$  sweeps (extending between 50 and 80 mV) measured several times [same color code as in panels (d),(e)]. For the challenging case of  $L \approx 0.1 \text{ mm}$  in configuration (c) (light blue line), the Fourier analysis is restricted to plunger gate-voltage windows exhibiting oscillations larger than 66% of their maximum amplitude.

modest compared to the freezing of energy relaxation. Our conjecture is that the weaker impact on  $L_\phi$  reflects a fundamental design limitation in the MZI implementation of Ref. [33], where an otherwise negligible coupling between two different *outer* edge channels could be mediated by the rigid displacements of the inner loops. These rigid displacements provide an additional mechanism for both decoherence and energy relaxation: Even if the inner loops' electronic degrees of freedom are not excited, the loops' presence can strongly enhance the capacitive coupling between different propagative edge channels adjacent to separate portions of the same loops. The present MZI implementation suppresses this mechanism while preserving a 2D bulk at  $\nu = 2$  through a gate design allowing for a much larger separation of the inner loops from additional quantum Hall channels (see Fig. 4 for an illustration, and Sec. II in the Appendix for further discussion).

### III. QUANTUM OSCILLATIONS VERSUS LOOP FORMATION

We present in Fig. 2 illustrative MZI oscillations versus plunger gate voltage  $V_{\text{pl}}$  (a positive bias of  $+0.35 \text{ V}$  is applied during cooldown). The displayed  $\tau_{\text{MZI}}$  corresponds to the transmission probability across the MZI from source  $S$  to detector  $D$ . It is given by the fraction measured at the electrode  $D$  of the current injected into the outer edge channel at the electrode  $S$ . The two  $L \approx 24 \mu\text{m}$  and  $0.1 \text{ mm}$  MZIs are each tuned in three different configurations [Figs. 2(a)–2(c)]. The green lines in Figs. 2(d) and 2(e) are data obtained with both devices set in the configuration

shown in Fig. 2(a). Their flatness demonstrates directly in the presence of inner channel loops the absence of  $\tau_{\text{MZI}}$  oscillations when all the transmitted current goes through a single MZI arm (the lower arm; in this specific case  $\tau_{\text{MZI}} = \tau_{\text{QPC}}^R$  since  $\tau_{\text{QPC}}^L = 1$ ). The red and blue lines in Figs. 2(d) and 2(e) are obtained with both QPC beam splitters set to half transmission probability for the outer edge channel ( $\tau_{\text{QPC}}^L \approx \tau_{\text{QPC}}^R \approx 0.5$ , the inner edge channel being always fully reflected at the QPCs) in the configurations illustrated in Figs. 2(b) and 2(c). In the conventional MZI configuration [no loops, Fig. 2(b)], small oscillations of period  $6.4 \text{ mV}$  are observed only on the  $L \approx 24 \mu\text{m}$  device [dark red lines in Figs. 2(d) and 2(f)]. Their visibility  $\mathcal{V} \equiv (\tau_{\text{MZI}}^{\text{max}} - \tau_{\text{MZI}}^{\text{min}}) / (\tau_{\text{MZI}}^{\text{max}} + \tau_{\text{MZI}}^{\text{min}}) \approx 6\%$  corresponds to a typical phase coherence length value of  $L_\phi \approx 17 \mu\text{m}$  (despite a relatively low temperature  $T \approx 10 \text{ mK}$ ) obtained from the standard relationship for a symmetric MZI:

$$\mathcal{V} = 4 \sqrt{\tau_{\text{QPC}}^R (1 - \tau_{\text{QPC}}^R) \tau_{\text{QPC}}^L (1 - \tau_{\text{QPC}}^L)} \exp\left(\frac{-2L}{L_\phi}\right), \quad (1)$$

which assumes a perfect absorption of the outer edge channel by the central metallic contact connected to electrical ground (separately checked; see the Appendix). In contrast, for the  $L \approx 0.1 \text{ mm}$  device, no oscillations can be detected without inner channel loops as expected from Eq. (1) ( $\mathcal{V} \approx 10^{-5}$  calculated with  $L = 0.1 \text{ mm}$  and  $L_\phi = 17 \mu\text{m}$ ). Instead, we observe a slowly evolving  $\tau_{\text{MZI}}$ , which is markedly below 0.5. This low mean value reflects the tunneling of electrons from outer to inner edge channels, which becomes significant over



such a long propagation distance. As a result, a larger (smaller) fraction of the current injected into the outer edge channel is absorbed by the grounded central Ohmic contact (detected at  $D$ ). Specific measurements of the tunneling between copropagating channels are discussed in the Appendix (Sec. V).

With inner channel loops formed [Fig. 2(c)], high-amplitude oscillations of maximum visibility  $\mathcal{V} \approx 80\%$  and  $40\%$  are observed for the  $L \simeq 24 \mu\text{m}$  and  $0.1 \text{ mm}$  MZIs, respectively. Their sinusoidal shape is, however, perturbed by jumps as well as amplitude modulations, which are attributed to fluctuators such as moving charges in the MZI vicinity. A sudden variation in surrounding charges will indeed appear as a phase jump. In contrast, relatively rapid fluctuations with respect to the experimental integration time (approximately 1 s) but slow with respect to the electron quantum coherence time will artificially reduce the amplitude of MZI oscillations, below their intrinsic value limited by  $L_\phi$  according to Eq. (1). As illustrated with the emblematic single-electron transistor, individual charge fluctuators are usually influenced by surrounding gate voltages. Accordingly, we observe modulations of the phase jump density and of the amplitude of oscillations with gate voltages. Note that two sources of moving charges are specific to the present MZI implementation with inner channel loops: (i) the voltage bias applied to the very long surface gates used to form the loops and (ii) jumps in the number of electrons within each of the many inner channel loops (from the possible tunneling of electrons between outer channel and inner loops). We now further establish by a train of evidence that the large

oscillations observed with inner channel loops result from the quantum interferences between the two MZI paths and that their maximum visibility accurately reflects  $L_\phi$ .

#### IV. OSCILLATION CHARACTERIZATION

First, a well-defined plunger gate-voltage period of 2.2 mV is observed for the smaller  $L \simeq 24 \mu\text{m}$  MZI, as directly evidenced from the power spectral density [dark blue lines in Figs. 2(d) and 2(f)]. A compatible but broader oscillation periodicity can also be perceived for the  $L \simeq 0.1 \text{ mm}$  MZI but only if the FFT analysis is restricted to plunger gate-voltage windows where the oscillation amplitude is relatively large [light blue line in Fig. 2(f)]. The period for  $L \simeq 24 \mu\text{m}$  with loops is shorter than without, as expected from the stronger influence of the plunger gate voltage. This reduction is a consequence of the quenched screening from isolated inner channel loops hosting a discrete number of electrons as compared to a copropagative inner channel. It also implies that any nearby moving charges will have a stronger impact on the MZI quantum phase.

Second, as shown in Fig. 3(a), the maximum oscillation visibility (highest symbols) follows the hallmark MZI signature  $\sqrt{\tau_{\text{QPC}}^L(1 - \tau_{\text{QPC}}^L)}$  (continuous lines) when varying the outer edge channel transmission probability across the left QPC beam splitter  $\tau_{\text{QPC}}^L$ . For this purpose, we measure  $\tau_{\text{MZI}}(V_{\text{pl}})$  over many periods on both devices and for various settings of  $\tau_{\text{QPC}}^L$  at fixed  $\tau_{\text{QPC}}^R \simeq 0.5$  (see the Appendix). Each symbol in Fig. 3(a) (full and open

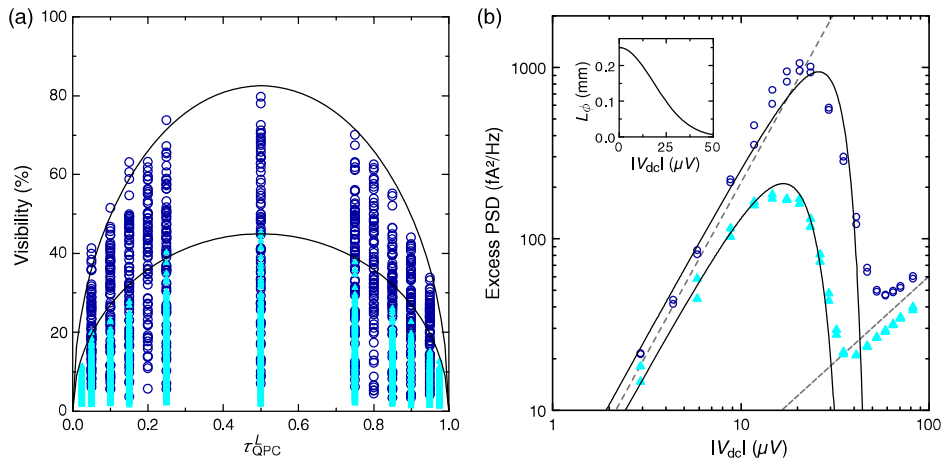


FIG. 3. Beam-splitter and bias-voltage tunings. Open (full) symbols are data points obtained on the  $L \simeq 24(100) \mu\text{m}$  MZI. (a) The local quantum oscillations' visibility in the presence of inner channel loops [Fig. 2(c)] separately extracted period per period along large  $V_{\text{pl}}$  sweeps is displayed as symbols versus the transmission probability  $\tau_{\text{QPC}}^L$  of the outer channel across the left QPC (at fixed  $\tau_{\text{QPC}}^R \simeq 0.5$ ). Continuous lines are Eq. (1)'s predictions for  $L_\phi = 0.25 \text{ mm}$  with  $L = 24 \mu\text{m}$  or  $0.1 \text{ mm}$ . (b) The excess power spectral density of temporal fluctuations in the transmitted MZI current with respect to zero dc bias and averaged in  $V_{\text{pl}}$  is shown versus source ( $S$ ) dc voltage  $V_{\text{dc}}$ . The gray straight lines represent a quadratic (dashed) and linear (dash-dotted) increase. The black continuous lines in the main panel display the noise contribution from phase fluctuations calculated with  $L_\phi(V_{\text{dc}}) = (0.25 \text{ mm}) \times \exp[-(V_{\text{dc}}/26 \mu\text{V})^2]$  (shown in the inset).

corresponding to the  $L \simeq 24 \mu\text{m}$  and  $0.1 \text{ mm}$  MZIs, respectively) displays the “locally” extracted visibility of the oscillations obtained by analyzing a restricted plunger gate-voltage window of one period ( $2.2 \text{ mV}$ ). The close agreement between the highest data points and MZI expectations confirms that the observed oscillations result from the two-path quantum interferences.

Third, we find a quantitative data or theory agreement with the *same*  $L_\phi \approx 0.25 \text{ mm}$  for both devices, despite a factor of 4 in their size. The continuous lines in Fig. 3(a) are calculated using Eq. (1) with  $L_\phi = 0.25 \text{ mm}$ , the corresponding MZI length  $L = 24 \mu\text{m}$  or  $0.1 \text{ mm}$ , and  $\tau_{\text{QPC}}^R = 0.5$ . This agreement provides strong evidence that the measured maximum “local” visibility closely captures the intrinsic MZI visibility determined solely by  $L_\phi$  (note that  $L_\phi$  will otherwise be underestimated).

Fourth, as shown in Fig. 3(b), out-of-equilibrium measurements of the transmitted current noise around  $0.86 \text{ MHz}$  further confirm the presence of MZI interferences accompanied by phase fluctuations and allow probing the energy dependence of  $L_\phi$ . The displayed data points represent measurements of the excess power spectral density of the current impinging on the electrode  $D$  versus the dc bias voltage  $V_{\text{dc}}$  applied to the source electrode  $S$ . MZI phase variations, such as those produced by nearby charge fluctuators, are expected to manifest as a quadratic increase of the noise power at low  $V_{\text{dc}}$  (see the Appendix and Ref. [34]), as we experimentally observe. At larger bias, the generally expected reduction of  $L_\phi$  also progressively diminishes the influence of the quantum phase and, consequently, the current noise induced by phase fluctuations. Experimentally, such a collapse is observed and can be accounted for using the *same*  $L_\phi(V_{\text{dc}})$  for both devices: The two black continuous lines (main panel) are calculations based on Eq. (1) (see the Appendix, Eq. (A2)) using the empirically determined  $L_\phi = (0.25 \text{ mm}) \times \exp[-(V_{\text{dc}}/26 \mu\text{V})^2]$  (shown in the inset). Ultimately, a linear noise increase is recovered as expected for the shot-noise contribution [34] (see the Appendix).

## V. DISCUSSION

The large phase coherence length presently achieved provides information for the design of novel quantum Hall devices. It sets an upper bound to possibly relevant decoherence mechanisms along the quantum Hall edges in addition to the dominant interchannel coupling and narrows down the mechanisms for a frequently observed but still mysterious additional dissipation [25–27,35].

We establish that nearby metallic gates are completely compatible with large phase coherence lengths, despite the presence of many diffusive electrons. Note their beneficial screening of the long-range part of Coulomb interaction (to approximately  $3.5 \mu\text{m}$ , the loop-gates’ period, whether the loops are formed or not), which could otherwise provide an effective decoherence mechanism [36–39] as well as an

unwanted coupling to spurious low-energy modes and distant channels [35,40,41]. In practice, a strong capacitive shortcut ( $100 \text{ nF}$ ) is included at the low-temperature end of the electrical lines controlling the gates of our samples in order to further suppress both extrinsic and thermal noise sources.

We also find that the additional neutral modes predicted for a realistic smooth confinement potential at the edge [42–44] can essentially be ignored. Either these neutral modes are missing in the outer channel along our etched-defined edges or they are very weakly coupled to the usual charge mode of the same channel. This finding is consistent with thermal conductance measurements across narrow constrictions perfectly transmitting one or several quantum Hall channels at integer bulk filling factors, where the extra heat transfer that would be expected from additional edge modes is not observed [45–47].

Finally, we mention that the two-dimensional quantum Hall bulk does not provide here a substantial path to quantum decoherence, at least when broken into small areas of a few micron squares (within the inner channel loops) and with the long-range part of Coulomb interaction screened by metallic gates. This finding contrasts with the observations of an unexpected heat flow away from the edge at lower filling factors [48–50] and of a long-distance capacitive coupling across the two-dimensional bulk [40,41].

## VI. CONCLUSION

We demonstrate that the electron quantum coherence in solid-state circuits can be extended to the macroscopic scale by strongly suppressing through circuit nanoengineering the dominant decoherence mechanism. The present implementation on quantum Hall edge channels is particularly well suited for the coherent control and long-distance entanglement of propagative electrons. Future optimizations include the understanding and suppression of the slow electron phase fluctuations here often, although not systematically, observed. Our work gives access to electron quantum optics devices of a higher complexity level, in line with the direction taken by this field of research [1–3,18]. More generally, increasing the electron phase coherence is essential to progress toward functional quantum devices involving multiple quantum manipulations, such as information processing with electronic flying qubits.

## ACKNOWLEDGMENTS

This work is supported by the French RENATECH network, the national French program “Investissements d’Avenir” (Labex NanoSaclay, Grant No. ANR-10-LABX-0035), and the French National Research Agency (project QuTherm, Grant No. ANR-16-CE30-0010-01).

E. S. and H. D. performed the experiment and analyzed the data with inputs from A. Aa., A. An., and F. P.; F. P.

fabricated the sample with input from E. S. and H. D.; A. C., A. O., U. G. grew the 2DEG; F. P. led the project and wrote the manuscript with input from A. Aa., A. An., E. S., H. D. and U. G.; H. D. and E. S. contributed equally to this work.

## APPENDIX: EXPERIMENTAL METHODS

### 1. Samples

Both samples are made of the same Ga(Al)As heterojunction hosting a two-dimensional electron gas of mobility  $10^6 \text{ cm}^2 \text{ V}^{-1} \text{ s}^{-1}$  and density  $2.510^{11} \text{ cm}^{-2}$  located 105 nm underneath the surface. They are nano-fabricated by *e*-beam lithography, dry etching, and metallic deposition. The central metallic electrode (nickel [30 nm], gold [120 nm], and germanium [60 nm]) forms an Ohmic contact with the 2DEG obtained by thermal annealing (at 440 °C for 50 s) and is set to electrical ground through a suspended bridge. The two arms of each MZI are designed to be as symmetric as possible, such that the thermal smearing of the visibility induced by an asymmetry remains negligible by a large margin as previously observed [17,33]. The elongated shape of the central area is chosen to limit the overall magnetic flux enclosed between the two arms and, hence, the effect of environmental magnetic noise (e.g., from the pulse tube vibrations) on the particularly sensitive MZI phase in these very large devices. Note that a positive bias voltage of +0.35 V is applied to all used gates during cooldown. This is a widespread procedure in Ga(Al)As devices to reduce the charge noise induced by biasing the gates, although it is probably not essential here due to the relatively low bias voltages used to form inner channel loops.

### 2. Loop gate design

Figure 4 recapitulates the different kinds of inner channel loops in the energy-relaxation experiment [31] [one inner loop enclosed only by the outer channel; see Fig. 4(a)] in the first MZI implementation [33] [inner loops enclosed by a metallic gate, the MZI outer channel, and another counterpropagating outer channel; see Fig. 4(b)] and in the present MZI implementation [inner loops enclosed by a metallic gate and the MZI outer channel; see Fig. 4(c)]. Now focusing on the present implementation, the gates'

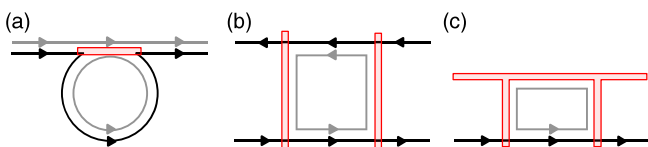


FIG. 4. Loop design. Inner loop design in previous energy-relaxation experiment [31] (a), previous MZI experiment [33], (b) and in the present implementation (c). The outer (inner) edge channel is represented by a black (gray) line. A schematic of the gates used to reflect the inner edge channel is displayed in red.

width of 200 nm reflects a compromise between the separation with additional quantum Hall channels on the other side of the gates, which should be sufficiently large to result in a negligible coupling, and the wish to limit the  $\nu = 1$  area underneath the gates, as very weak interferences are often observed if the whole 2D bulk is set to  $\nu = 1$  (either by tuning  $B$  without gates or using a broad top gate fully covering the 2D bulk; see, e.g., Ref. [24]). The distance between the inner channel loops and the propagative (inner) quantum Hall channel on the other side of the gates (opposite the MZI outer channel) should therefore be larger than 200 nm. This is more than 1 order of magnitude larger than the narrow incompressible strip normally separating adjacent edge channels (typically 10 nm [51]). The loops' perimeter should also be chosen small enough such that the separation between the quantized electronic levels is larger than the available energy of approximately  $k_B T$ . Assuming a typical drift velocity between  $10^4$  and  $10^5$  m/s along the sample edges, we find that the 9- $\mu\text{m}$  loop perimeter corresponds to a level spacing within 4.6 and 46  $\mu\text{eV}$ , always larger than the thermal energy ( $3k_B T \simeq 2.6 \mu\text{eV}$  at 10 mK) and comparable to the characteristic 26- $\mu\text{V}$  dc bias voltage over which  $L_\phi(V_{\text{dc}})$  is found to decrease [Fig. 3(b)]. Finally, the gates are designed elongated to minimize their overlap with the outer MZI edge channel, as at these locations their capacitive coupling is maximal and the lateral edge confinement is modified. Note also that one should be particularly careful about the electrical noise introduced by the measurement lines connected to the very long gates used to form the inner channel loops. These gates are indeed much more strongly coupled to the MZI phase than typical lateral plunger gates due to their very long size and because the inner loop efficiently mediates the capacitive coupling between the metallic gate and the MZI outer edge channel.

### 3. Experimental setup

The two simultaneously cooled devices are thermally anchored to the mixing chamber of a cryo-free dilution refrigerator. Electrical lines connected to the samples include multiple filters and thermalization stages. Note the important  $RC$  filter (200 k $\Omega$ , 100 nF) implemented at base temperature on the lines connected to the gates, including the long gates used to form the inner channel loops. Spurious high-frequency radiation is screened by two shields at base temperature. The fraction of transmitted current  $\tau_{\text{MZI}}$  is measured with lock-ins at a frequency below 200 Hz and using an effective integration time close to 1 s per point (corresponding to equivalent noise bandwidth of 0.8 Hz). The power spectral density of temporal current fluctuations is measured over a much larger bandwidth of 180 kHz around 0.86 MHz, using a homemade cryogenic amplifier and a tank circuit based on a superconducting coil. The temperature of electrons in the devices is extracted

from the quantum shot noise across a quantum point contact (the right beam splitter QPC of the  $L \simeq 24 \mu\text{m}$  MZI set to  $\tau_{\text{QPC}}^R \simeq 0.5$ ). See Ref. [52] for further details on the same experimental setup.

#### 4. Central Ohmic contacts characterization

The quality of the grounded central Ohmic contact is characterized by the ratio of reflected to impinging current. Ideally, there should be no reflected current. In practice, if the impinging current is carried only by the outer edge channel (used for the interferometer), the reflected current is found to be negligible for both devices (below 1%). If the impinging current is carried by both the inner and outer edge channels, we find a reflected current in the range of 11%–21% corresponding to a 22%–42% reflection of the inner edge channel from the central Ohmic contact of the  $L \simeq 24 \mu\text{m}$  paths' MZI, whereas for the  $L \simeq 0.1 \text{ mm}$  MZI, the reflected current remains essentially negligible (below 1%). Note that a good Ohmic contact with the outer channel is assumed in Eq. (1) (an imperfect contact will further limit the amplitude of MZI oscillations).

#### 5. Tunneling between inner and outer channels

Tunneling of electrons between adjacent copropagating channels is usually negligible at filling factor  $\nu = 2$ . However, the propagation distances in the present devices can be considerable. Following standard procedures [53], we determine the electron interchannel tunneling along the MZI arms between the two QPC beam splitters when the inner edge channel is not formed into small loops. Note that the tunneling of electrons in the presence of small inner channel loops is expected to be much smaller because of the electronic level quantization within the loops and because of the Coulomb blockade of tunneling into (nearly) isolated islands (although this tunneling cannot be measured because there is no dc current toward closed loops). The tunneling between copropagative inner and outer edge channels is obtained by applying a small bias selectively on one of the two channels and by measuring at the end of the path the current in the other channel. We find that the tunneling remains small for the  $L \simeq 24 \mu\text{m}$  MZI [between 2.5% and 5% (approximately 0%) of the injected current is detected on the second channel after propagating along the lower (upper) MZI arm]. The tunneling is more important for the  $L \simeq 0.1 \text{ mm}$  MZI [between 30% and 48% (between 10% and 26%) of the injected current is detected on the second channel after propagating along the lower (upper) MZI path].

#### 6. Cross-talk characterization

Changing a gate voltage also slightly influences the other nearby gates. We take into account this small capacitive cross-talk correction on the beam-splitter quantum point

contacts (of at most 6% attained for the lateral plunger gate effect on the nearby left QPC).

#### 7. Formation of inner channel loops

The comb-shaped gates of homogeneous width (200 nm) are polarized with a positive voltage of +0.35 V during the cooldown from room temperature. A broad gate-voltage window is found to fully reflect the inner quantum Hall channel while completely letting through the outer channel (with a minimal common window from 0 to 0.13 V that applies simultaneously to each arm of both devices). Such a behavior is usually observed on similar 2DEGs, thanks to the large energy separation between the two lowest Landau levels at filling factor  $\nu = 2$ . Note that the results corresponding to closed inner channel loops that we present in the manuscript are not specific to a precise gate-voltage setting (chosen within the minimal common window) but representative of the general behavior observed when the inner edge channel loops are completely closed while the outer edge channel is fully propagative.

#### 8. Visibility of conductance oscillations versus QPC transmission

Here we provide more details on the procedure followed to extract the oscillations visibility data displayed in Fig. 3(a). We perform relatively large plunger gate-voltage sweeps of 50 mV corresponding to approximately 21 periods (with a step of 50  $\mu\text{V}$  corresponding to 1/46 of a period) and repeat several times the same sweep (twice for the  $L \simeq 24 \mu\text{m}$  MZI, 14 times for the more challenging  $L \simeq 0.1 \text{ mm}$  MZI). Each sweep is then decomposed into one-period intervals with half a period of overlap between consecutive intervals, and a local visibility of the oscillations in  $\tau_{\text{MZI}}$  is extracted from  $\mathcal{V} \equiv (\tau_{\text{MZI}}^{\text{max}} - \tau_{\text{MZI}}^{\text{min}}) / (\tau_{\text{MZI}}^{\text{max}} + \tau_{\text{MZI}}^{\text{min}})$  in each of these intervals. The symbols in Fig. 3(a) display the many different values of  $\mathcal{V}$  obtained by this procedure.

#### 9. Temporal noise spectral density

Here we provide more details on the noise data and calculations displayed in Fig. 3(b). The data points represent the excess power spectral density of the current detected on electrode  $D$  [see Fig. 1(a)], i.e., the total noise from which is subtracted the equilibrium noise offset at  $V_{\text{dc}} = 0$  (that includes the contribution of the amplification chain). To make sure that the noise dependence in the MZI quantum phase is fully averaged out, the displayed data represent the average of many noise measurements equally distributed in a range of the plunger gate voltage corresponding to several periods (240 [40] values of  $V_{\text{pl}}$  distributed over approximately five [2] periods for the  $L \simeq 24[100] \mu\text{m}$  MZI). The displayed calculations (continuous lines) include only the contribution of “slow” fluctuations in the MZI quantum phase  $\delta\phi(t)$  detected

within a 180-kHz window around 0.86 MHz and not the quantum shot-noise contribution that we further discuss below. From the relationship  $\tau_{\text{MZI}}(t) = 0.5\{1 + \mathcal{V} \sin[\langle\phi\rangle + \delta\phi(t)]\}$ , it is straightforward to obtain that the resulting noise in the transmitted current is given by [34]

$$\langle I_{\delta\phi}^2 \rangle \propto \frac{V_{\text{dc}}^2 e^4}{h^2} \mathcal{V}^2, \quad (\text{A1})$$

with  $h$  the Planck constant and  $e$  the elementary electron charge. At low  $V_{\text{dc}}$  bias (as long as the oscillation visibility  $\mathcal{V}$  is not significantly reduced), one thus expects a quadratic increase. Using the relationship between visibility and phase coherence length given Eq. (1), this expression becomes

$$\langle I_{\delta\phi}^2 \rangle \propto \frac{V_{\text{dc}}^2 e^4}{h^2} \exp\left(\frac{-4L}{L_\phi}\right). \quad (\text{A2})$$

The calculations displayed as black continuous lines are obtained from Eq. (A2) using for both devices the same empirical expression  $L_\phi(V_{\text{dc}}) = 0.25 \text{ mm} \times \exp[-(V_{\text{dc}}/26 \mu\text{V})^2]$  (displayed in the inset) the corresponding MZI length  $L = 24 \mu\text{m}$  or  $0.1 \text{ mm}$  and where the unknown prefactor (depending on the number and coupling strength of the phase noise sources) is considered here as a free parameter for each device. The smaller quantum shot-noise contribution [not included in Eq. (A2)] is linear in  $V_{\text{dc}}$  and does not rely on the presence of MZI quantum interferences. As expected, if the vanishing current noise results from a quantum decoherence by “fast” phase fluctuations [34] (compared to the electron quantum coherence), the amplitude of the linear noise is found strongly suppressed compared to the naive expectation  $\langle I^2 \rangle = 2e(V_{\text{dc}}e^2/h)\langle\tau_{\text{MZI}}\rangle(1 - \langle\tau_{\text{MZI}}\rangle)$  by a factor of 4 (6) for the MZI of arm length  $L \simeq 24(100) \mu\text{m}$ .

### 10. Comparison of voltage-bias robustness with and without inner channel loops

In the absence of inner channel loops, the negligible MZI phase noise does not allow us to probe  $L_\phi(V_{\text{dc}})$  through the power spectral density of the transmitted current’s temporal fluctuations. However, on the  $L \simeq 24 \mu\text{m}$  MZI where quantum oscillations are visible without loops, it is possible to determine, versus dc voltage bias, their visibility  $\mathcal{V}_{\text{diff}}$  in the transmitted differential current  $dI_{\text{MZI}}/dV_{\text{dc}}$ . The “diff” subscript is introduced here to clearly distinguish between, on the one hand, this usually measured  $\mathcal{V}_{\text{diff}}$  and, on the other hand, the visibility  $\mathcal{V}$  of oscillations in the total transmitted current  $I_{\text{MZI}}$  that is probed through noise measurements [Fig. 3(b)]. These two quantities are simply connected by the relation [54]

$$\mathcal{V}_{\text{diff}} = |\mathcal{V} + V_{\text{dc}} \partial\mathcal{V}/\partial V_{\text{dc}}|. \quad (\text{A3})$$

Measurements of  $\mathcal{V}_{\text{diff}}(V_{\text{dc}})$  on the  $L \simeq 24 \mu\text{m}$  MZI without loops are shown in Fig. 5 as open red circles. We find that  $\mathcal{V}_{\text{diff}}$  displays a single side lobe with a first minimum at  $|V_{\text{dc}}| \simeq 5 \mu\text{V}$  and becomes negligible below our experimental resolution at  $|V_{\text{dc}}| \gtrsim 15 \mu\text{V}$ . The data can be reproduced by the simple single side-lobe expression derived in Ref. [54] assuming a Gaussian phase averaging (continuous line in Fig. 5):

$$\mathcal{V}_{\text{diff}}^{\text{Gaussian}} = \mathcal{V}_0 \left| 1 - \frac{V_{\text{dc}}^2}{V_0^2} \right| \exp\left(-\frac{V_{\text{dc}}^2}{2V_0^2}\right), \quad (\text{A4})$$

with  $\mathcal{V}_0 = 0.06$  the zero bias visibility and  $V_0 = 5 \mu\text{V}$  the characteristic voltage scale also corresponding to the position of the intermediate minimum. In order to compare the robustness of MZI interferences with and without inner channel loops, we convert the noise data in Fig. 3(b) into the corresponding  $\mathcal{V}_{\text{diff}}$ . The resulting  $\mathcal{V}_{\text{diff}}$  is displayed in Fig. 5 as open dark blue circles and full light blue triangles for, respectively, the  $L \simeq 24$  and  $100 \mu\text{m}$  MZI with loops. This conversion first involves the determination of  $\mathcal{V}$  from Eq. (A1) (using the measured noise spectral density from which the linear shot-noise contribution observed at large  $V_{\text{dc}}$  is subtracted). The unknown proportionality coefficient in Eq. (A1) is fixed by adjusting the visibility at low bias with its direct  $V_{\text{dc}} \approx 0$  measurement displayed in Fig. 3(a). The resulting  $\mathcal{V}$  is then injected into Eq. (A3) to obtain  $\mathcal{V}_{\text{diff}}$ .

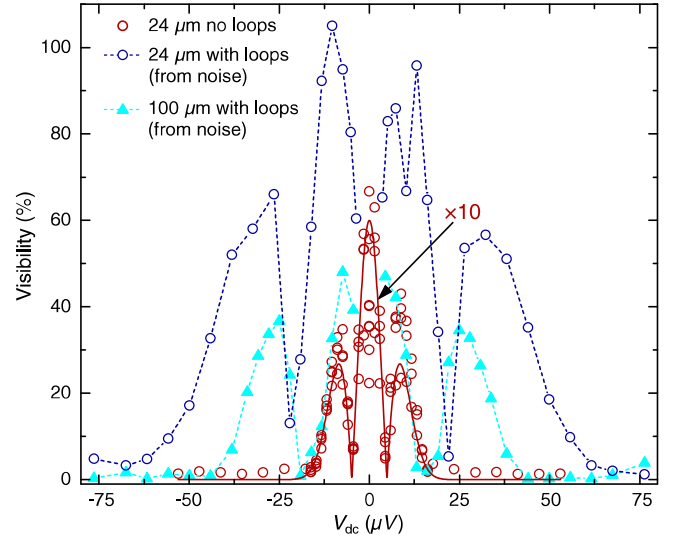


FIG. 5. Out-of-equilibrium visibility in the differential current  $\mathcal{V}_{\text{diff}}$ . The red circles represent measurements of the visibility of the oscillations in the differential transmitted current across the  $L \simeq 24 \mu\text{m}$  MZI without inner channel loops as a function of the applied dc bias voltage. The continuous red line is calculated from Eq. (A4) (see text). The dark blue circles (light blue full triangles) connected by dashed lines represent the differential visibility on the  $L \simeq 24(100) \mu\text{m}$  MZI with formed inner channel loops, which is extracted from the noise measurements displayed in Fig. 3(b) (see text).

Comparing the two datasets at the same  $L \simeq 24 \mu\text{m}$  (open circles), we find that the robustness of the MZI visibility with  $V_{\text{dc}}$  is approximately 4 times larger in the presence of loops (dark blue) than without them (red).

- 
- [1] D. Glattli and P. Roulleau, *Levitons for Electron Quantum Optics.*, *Phys. Status Solidi B* **254**, 1600650 (2017).
- [2] C. Bäuerle, D. C. Glattli, T. Meunier, F. Portier, P. Roche, P. Roulleau, S. Takada, and X. Waintal, *Coherent Control of Single Electrons: A Review of Current Progress*, *Rep. Prog. Phys.* **81**, 056503 (2018).
- [3] E. Bocquillon *et al.*, *Electron Quantum Optics in Ballistic Chiral Conductors*, *Ann. Phys. (Berlin)* **526**, 1 (2014).
- [4] A. Bertoni, P. Bordone, R. Brunetti, C. Jacoboni, and S. Reggiani, *Quantum Logic Gates Based on Coherent Electron Transport in Quantum Wires*, *Phys. Rev. Lett.* **84**, 5912 (2000).
- [5] R. Ionicioiu, G. Amaratunga, and F. Udrea, *Quantum Computation with Ballistic Electrons*, *Int. J. Mod. Phys. B* **15**, 125 (2001).
- [6] T. Stace, C. Barnes, and G. Milburn, *Mesoscopic One-Way Channels for Quantum State Transfer via the Quantum Hall Effect*, *Phys. Rev. Lett.* **93**, 126804 (2004).
- [7] T. Bautze, C. Sussmeier, S. Takada, C. Groth, T. Meunier, M. Yamamoto, S. Tarucha, X. Waintal, and C. Bäuerle, *Theoretical, Numerical, and Experimental Study of a Flying Qubit Electronic Interferometer*, *Phys. Rev. B* **89**, 125432 (2014).
- [8] B. J. van Wees, L. P. Kouwenhoven, C. J. P. M. Harmans, J. G. Williamson, C. E. Timmering, M. E. I. Broekaart, C. T. Foxon, and J. J. Harris, *Observation of Zero-Dimensional States in a One-Dimensional Electron Interferometer*, *Phys. Rev. Lett.* **62**, 2523 (1989).
- [9] Y. Ji, Y. Chung, D. Sprinzak, M. Heiblum, D. Mahalu, and H. Shtrikman, *An Electronic Mach-Zehnder Interferometer*, *Nature (London)* **422**, 415 (2003).
- [10] I. Neder, N. Ofek, Y. Chung, M. Heiblum, D. Mahalu, and V. Umansky, *Interference between Two Indistinguishable Electrons from Independent Sources*, *Nature (London)* **448**, 333 (2007).
- [11] E. Bocquillon, V. Freulon, J.-M. Berroir, P. Degiovanni, B. Placais, A. Cavanna, Y. Jin, and G. Fève, *Coherence and Indistinguishability of Single Electrons Emitted by Independent Sources*, *Science* **339**, 1054 (2013).
- [12] Y. Nazarov and Y. Blanter, *Quantum Transport* (Cambridge University Press, Cambridge, England, 2009).
- [13] H. Duprez *et al.*, *Transferring the Quantum State of Electrons across a Fermi Sea with Coulomb Interaction*, [arXiv:1902.07569](https://arxiv.org/abs/1902.07569).
- [14] F. Pierre, A. B. Gougam, A. Anthore, H. Pothier, D. Esteve, and N. O. Birge, *Dephasing of Electrons in Mesoscopic Metal Wires*, *Phys. Rev. B* **68**, 085413 (2003).
- [15] Y. Niimi, Y. Baines, T. Capron, D. Mailly, F. Y. Lo, A. D. Wieck, T. Meunier, L. Saminadayar, and C. Bäuerle, *Quantum Coherence at Low Temperatures in Mesoscopic Systems: Effect of Disorder*, *Phys. Rev. B* **81**, 245306 (2010).
- [16] F. Miao, S. Wijeratne, Y. Zhang, U. C. Coskun, W. Bao, and C. N. Lau, *Phase-Coherent Transport in Graphene Quantum Billiards*, *Science* **317**, 1530 (2007).
- [17] P. Roulleau, F. Portier, D. C. Glattli, P. Roche, A. Cavanna, G. Faini, U. Gennser, and D. Mailly, *Direct Measurement of the Coherence Length of Edge States in the Integer Quantum Hall Regime*, *Phys. Rev. Lett.* **100**, 126802 (2008).
- [18] M. Yamamoto, S. Takada, C. Bäuerle, K. Watanabe, A. D. Wieck, and S. Tarucha, *Electrical Control of a Solid-State Flying Qubit*, *Nat. Nanotechnol.* **7**, 247 (2012).
- [19] D. Wei, T. van der Sar, J. D. Sanchez-Yamagishi, K. Watanabe, T. Taniguchi, P. Jarillo-Herrero, B. I. Halperin, and A. Yacoby, *Mach-Zehnder Interferometry Using Spin- and Valley-Polarized Quantum Hall Edge States in Graphene*, *Sci. Adv.* **3**, e1700600 (2017).
- [20] I. P. Levkivskyi and E. V. Sukhorukov, *Dephasing in the Electronic Mach-Zehnder Interferometer at Filling Factor  $\nu = 2$* , *Phys. Rev. B* **78**, 045322 (2008).
- [21] T. Giamarchi, *Quantum Physics in One Dimension* (Oxford University Press, New York, 2003).
- [22] P. Roulleau, F. Portier, P. Roche, A. Cavanna, G. Faini, U. Gennser, and D. Mailly, *Noise Dephasing in Edge States of the Integer Quantum Hall Regime*, *Phys. Rev. Lett.* **101**, 186803 (2008).
- [23] L. V. Litvin, A. Helzel, H.-P. Tranitz, W. Wegscheider, and C. Strunk, *Edge-Channel Interference Controlled by Landau Level Filling.*, *Phys. Rev. B* **78**, 075303 (2008).
- [24] I. Gurman, R. Sabo, M. Heiblum, V. Umansky, and D. Mahalu, *Dephasing of an Electronic Two-Path Interferometer*, *Phys. Rev. B* **93**, 121412(R) (2016).
- [25] H. le Sueur, C. Altimiras, U. Gennser, A. Cavanna, D. Mailly, and F. Pierre, *Energy Relaxation in the Integer Quantum Hall Regime*, *Phys. Rev. Lett.* **105**, 056803 (2010).
- [26] K. Itoh, R. Nakazawa, T. Ota, M. Hashisaka, K. Muraki, and T. Fujisawa, *Signatures of a Nonthermal Metastable State in Copropagating Quantum Hall Edge Channels*, *Phys. Rev. Lett.* **120**, 197701 (2018).
- [27] E. Bocquillon, V. Freulon, J.-M. Berroir, P. Degiovanni, B. Placais, A. Cavanna, Y. Jin, and G. Fève, *Separation of Neutral and Charge Modes in One-Dimensional Chiral Edge Channels*, *Nat. Commun.* **4**, 1839 (2013).
- [28] H. Inoue, A. Grivnin, N. Ofek, I. Neder, M. Heiblum, V. Umansky, and D. Mahalu, *Charge Fractionalization in the Integer Quantum Hall Effect*, *Phys. Rev. Lett.* **112**, 166801 (2014).
- [29] M. Hashisaka, N. Hiyama, T. Akiho, K. Muraki, and T. Fujisawa, *Waveform Measurement of Charge- and Spin-Density Wavepackets in a Chiral Tomonaga-Luttinger Liquid*, *Nat. Phys.* **13**, 559 (2017).
- [30] A. Marguerite, C. Cabart, C. Wahl, B. Roussel, V. Freulon, D. Ferraro, C. Grenier, J. M. Berroir, B. Placais, T. Jonckheere *et al.*, *Decoherence and Relaxation of a Single Electron in a One-Dimensional Conductor*, *Phys. Rev. B* **94**, 115311 (2016).
- [31] C. Altimiras, H. le Sueur, U. Gennser, A. Cavanna, D. Mailly, and F. Pierre, *Tuning Energy Relaxation along Quantum Hall Channels*, *Phys. Rev. Lett.* **105**, 226804 (2010).

- [32] C. Cabart, B. Roussel, G. Fève, and P. Degiovanni, *Taming Electronic Decoherence in 1D Chiral Ballistic Quantum Conductors*, *Phys. Rev. B* **98**, 155302 (2018).
- [33] P. A. Huynh, F. Portier, H. le Sueur, G. Faini, U. Gennser, D. Mailly, F. Pierre, W. Wegscheider, and P. Roche, *Quantum Coherence Engineering in the Integer Quantum Hall Regime*, *Phys. Rev. Lett.* **108**, 256802 (2012).
- [34] F. Marquardt and C. Bruder, *Effects of Dephasing on Shot Noise in an Electronic Mach-Zehnder Interferometer*, *Phys. Rev. B* **70**, 125305 (2004).
- [35] T. Krähenmann *et al.*, *Auger-Spectroscopy in Quantum Hall Edge Channels: A Possible Resolution to the Missing Energy Problem*, arXiv:1902.10065.
- [36] E. Sukhorukov and V. Cheianov, *Resonant Dephasing in the Electronic Mach-Zehnder Interferometer*, *Phys. Rev. Lett.* **99**, 156801 (2007).
- [37] J. Chalker, Y. Gefen, and M. Veillette, *Decoherence and Interactions in an Electronic Mach-Zehnder Interferometer*, *Phys. Rev. B* **76**, 085320 (2007).
- [38] D. Kovrizhin and J. Chalker, *Multiparticle Interference in Electronic Mach-Zehnder Interferometers*, *Phys. Rev. B* **81**, 155318 (2010).
- [39] M. Schneider, D. Bagrets, and A. Mirlin, *Theory of the Nonequilibrium Electronic Mach-Zehnder Interferometer.*, *Phys. Rev. B* **84**, 075401 (2011).
- [40] M. Hashisaka, K. Washio, H. Kamata, K. Muraki, and T. Fujisawa, *Distributed Electrochemical Capacitance Evidenced in High-Frequency Admittance Measurements on a Quantum Hall Device*, *Phys. Rev. B* **85**, 155424 (2012).
- [41] N.-H. Tu, M. Hashisaka, T. Ota, Y. Sekine, K. Muraki, T. Fujisawa, and N. Kumada, *Coupling between Quantum Hall Edge Channels on Opposite Sides of a Hall Bar*, *Solid State Commun.* **283**, 32 (2018).
- [42] A. MacDonald, S. Yang, and M. Johnson, *Quantum Dots in Strong Magnetic Fields: Stability Criteria for the Maximum Density Droplet*, *Aust. J. Phys.* **46**, 345 (1993).
- [43] C. Chamon and X. Wen, *Sharp and Smooth Boundaries of Quantum Hall Liquids*, *Phys. Rev. B* **49**, 8227 (1994).
- [44] I. Aleiner and L. Glazman, *Novel Edge Excitations of Two-Dimensional Electron Liquid in a Magnetic Field*, *Phys. Rev. Lett.* **72**, 2935 (1994).
- [45] S. Jezouin, F. D. Parmentier, A. Anthore, U. Gennser, A. Cavanna, Y. Jin, and F. Pierre, *Quantum Limit of Heat Flow Across a Single Electronic Channel*, *Science* **342**, 601 (2013).
- [46] M. Banerjee, M. Heiblum, A. Rosenblatt, Y. Oreg, D. E. Feldman, A. Stern, and V. Umansky, *Observed Quantization of Anyonic Heat Flow*, *Nature (London)* **545**, 75 (2017).
- [47] E. Sivre, A. Anthore, F. D. Parmentier, A. Cavanna, U. Gennser, A. Ouerghi, Y. Jin, and F. Pierre, *Heat Coulomb Blockade of One Ballistic Channel*, *Nat. Phys.* **14**, 145 (2018).
- [48] C. Altimiras, H. le Sueur, U. Gennser, A. Anthore, A. Cavanna, D. Mailly, and F. Pierre, *Chargeless Heat Transport in the Fractional Quantum Hall Regime*, *Phys. Rev. Lett.* **109**, 026803 (2012).
- [49] V. Venkatachalam, S. Hart, L. Pfeiffer, K. West, and A. Yacoby, *Local Thermometry of Neutral Modes on the Quantum Hall Edge*, *Nat. Phys.* **8**, 676 (2012).
- [50] H. Inoue, A. Grivnin, Y. Ronen, M. Heiblum, V. Umansky, and D. Mahalu, *Proliferation of Neutral Modes in Fractional Quantum Hall States*, *Nat. Commun.* **5**, 4067 (2014).
- [51] D. B. Chklovskii, B. I. Shklovskii, and L. I. Glazman, *Electrostatics of Edge Channels*, *Phys. Rev. B* **46**, 4026 (1992).
- [52] Z. Iftikhar, A. Anthore, S. Jezouin, F. D. Parmentier, Y. Jin, A. Cavanna, A. Ouerghi, U. Gennser, and F. Pierre, *Primary Thermometry Triad at 6 mK in Mesoscopic Circuits*, *Nat. Commun.* **7**, 12908 (2016).
- [53] B. van Wees, E. M. M. Willems, C. J. P. M. Harmans, C. W. J. Beenakker, H. van Houten, J. G. Williamson, C. T. Foxon, and J. J. Harris, *Anomalous Integer Quantum Hall Effect in the Ballistic Regime with Quantum Point Contacts*, *Phys. Rev. Lett.* **62**, 1181 (1989).
- [54] P. Roulleau, F. Portier, D. C. Glattli, P. Roche, A. Cavanna, G. Faini, U. Gennser, and D. Mailly, *Finite Bias Visibility of the Electronic Mach-Zehnder Interferometer*, *Phys. Rev. B* **76**, 161309(R) (2007).

# Transferring the quantum state of electrons across a Fermi sea with Coulomb interaction

H. Duprez,<sup>1,\*</sup> E. Sivre,<sup>1,\*</sup> A. Anthore,<sup>1,2</sup> A. Aassime,<sup>1</sup> A. Cavanna,<sup>1</sup> U. Gennser,<sup>1</sup> and F. Pierre<sup>1,†</sup>

<sup>1</sup>*Centre de Nanosciences et de Nanotechnologies (C2N), CNRS, Univ Paris Sud, Université Paris-Saclay, 91120 Palaiseau, France*

<sup>2</sup>*Univ Paris Diderot, Sorbonne Paris Cité, 75013 Paris, France*

The Coulomb interaction generally limits the quantum propagation of electrons. However, it can also provide a mechanism to transfer their quantum state over larger distances. Here, we demonstrate such a form of teleportation, across a metallic island within which the electrons are trapped much longer than their quantum lifetime. This effect originates from the low temperature freezing of the island's charge  $Q$  which, in the presence of a single connected electronic channel, enforces a one-to-one correspondence between incoming and outgoing electrons. Such high-fidelity quantum state imprinting is established between well-separated injection and emission locations, through two-path interferences in the integer quantum Hall regime. The added electron quantum phase of  $2\pi Q/e$  can allow for strong and decoherence-free entanglement of propagating electrons, and notably of flying qubits.

A disordered environment, with a large number of interacting degrees of freedom, is generally considered as the nemesis of quantum technologies. This is exemplified by a metallic island, often pictured as a reservoir of thermal electrons, with its large energy density of states  $1/\delta$  and limited number  $N$  of connected electronic channels. Indeed, the interval between inelastic collisions destroying the quantum coherence of the electrons [1, 2] is typically much smaller than their dwell time inside the island ( $\tau_D = h/N\delta$  for perfect channels [3], with  $h$  the Planck constant). However, we show experimentally that the Coulomb interaction in such an island can, under the right circumstances, lead to a near perfect preservation of the quantum state of electrons transferred across it. In the employed quantum Hall regime implementation, where injection and emission points are physically separated by chirality, this constitutes a form of teleportation of the electrons' states without transmitting the physical particles themselves. This phenomenon is different from the standard 'quantum teleportation' protocol [4], and similar to the 'electron teleportation' proposed in [5].

The voltage probe model of a metallic Fermi sea [6] is widely used to mimic the electrons' quantum decoherence and energy relaxation toward equilibrium (see e.g. [7] and references therein). However, independent absorption and emission of electrons result in fluctuations of the total island charge  $Q$ , with a characteristic charging energy  $E_C = e^2/2C$  (with  $C$  the geometrical capacitance of the island and  $e$  the elementary electron charge). At low temperatures  $T \ll E_C/k_B$  (with  $k_B$  the Boltzmann constant) this energy is not available, and the macroscopic quantum charge state  $Q$  is effectively frozen [8, 9] (although not quantized in units of  $e$  as long as one channel is perfectly connected [10–12]). Consequently, correlations develop between absorbed and emitted elec-

trons. These culminate if only one transport channel is connected to the island, in which case theory predicts that the electrons entering it and those exiting it are in identical quantum states [9, 13]. Effectively, the electronic states within the connected quantum channel are decoupled from the many quasiparticles within the island, despite the fact that the incoming (outgoing) physical electron particles penetrate into (originate from) the island. Another consequence is that heat evacuation from the island's internal states along the channel is fully suppressed [8]. In contrast, in the presence of two or more open channels the coherence is lost [9], and heat evacuation is restored in agreement with the recently observed systematic heat Coulomb blockade of one ballistic channel [14]. Interestingly, the 'electron teleportation' proposed in [5] also relies on the 'all-important' Coulomb charging energy of a small island, although combined in that case with Majorana bound states in an altogether different mechanism.

We demonstrate the high-fidelity replication of electron quantum states across a metallic island through quantum interferences. For this purpose, an injected current is first split along two separate paths that are subsequently recombined, thereby realizing an electronic Mach-Zehnder interferometer (MZI). In contrast with usual MZI implementations [15–19], one of the paths can controllably be diverted toward a small floating metallic island (see Fig. 1). In that case, any two-path quantum interferences involve both the initial electrons (direct left path) and the reemitted ones (interrupted right path, assuming a perfect contact with the island). Therefore a high interference visibility directly ascertains a high fidelity of the electron state replication.

A colorized e-beam micrograph of the measured device is shown in Fig. 1. The sample was nanofabricated from a high-mobility Ga(Al)As two dimensional electron gas, and immersed in a perpendicular magnetic field  $B \simeq 5$  T corresponding to the integer quantum Hall filling factor  $\nu = 2$ . In this regime, two quantum Hall channels co-

\* These authors contributed equally to this work.

† e-mail: frederic.pierre@c2n.upsaclay.fr



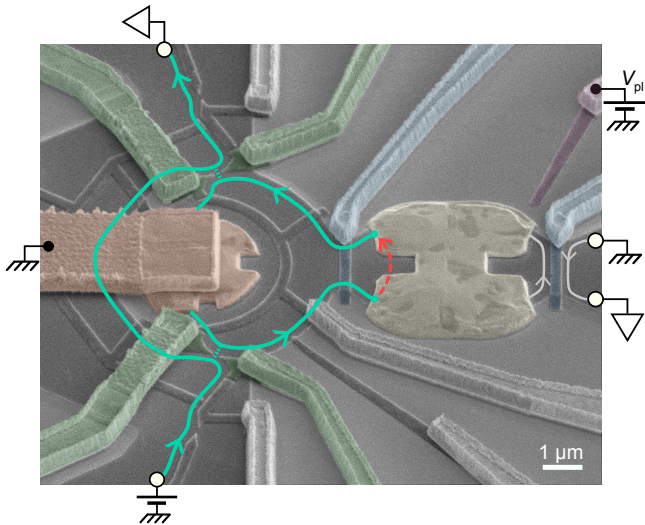


FIG. 1. Device e-beam micrograph. Areas with a Ga(Al)As two-dimensional electron gas underneath the surface appear darker. The applied perpendicular magnetic field  $B \approx 5$  T corresponds to the integer quantum Hall regime at filling factor two. Capacitively coupled gates colored green and blue control, respectively, the Mach-Zehnder interferometer beam splitters for the outer quantum Hall edge channel (lines with arrow, here corresponding to the schematic in Fig. 2(b)) and the connection to the floating metallic island (yellow) in good ohmic contact with the buried 2D electron gas. One of the two MZI outputs is the central small ohmic contact (orange) connected to ground through a suspended bridge. The second one, larger and located further away, is schematically represented by the top white circle. The MZI phase difference is controlled through  $B$  or the plunger gate voltage  $V_{PI}$ . The red dashed line visually represents the non-local quantum state transfer across the island, between electrons' injection (starting point) and emission (arrow).

propagate along the edges (the electron gas was etched away in the brighter areas), and the MZI is formed using only the outer edge channel. The followed paths are represented by thick lines with arrows for the configuration where one MZI arm goes through the floating metallic island (corresponding schematic shown in Fig. 2(b)). The two MZI beam splitters, each tuned to half transmission, are realized with quantum point contacts formed by field effect using split gates (colored green; the inner quantum Hall channel, not shown, is fully reflected). One of the two MZI outputs is the small central metallic electrode (orange), which is grounded through a suspended bridge. The quantum interferences are characterized by the oscillations of the current transmitted to the second MZI output formed by a much larger electrode  $60 \mu\text{m}$  away (represented in Fig. 1 by the top white circle), while sweeping either the magnetic field  $B$  or the voltage  $V_{PI}$  applied to a lateral plunger gate (purple). The floating metallic island (yellow) consists of  $2 \mu\text{m}^3$  of a gold-germanium-nickel alloy diffused into the Ga(Al)As heterojunction by thermal annealing. From the typical

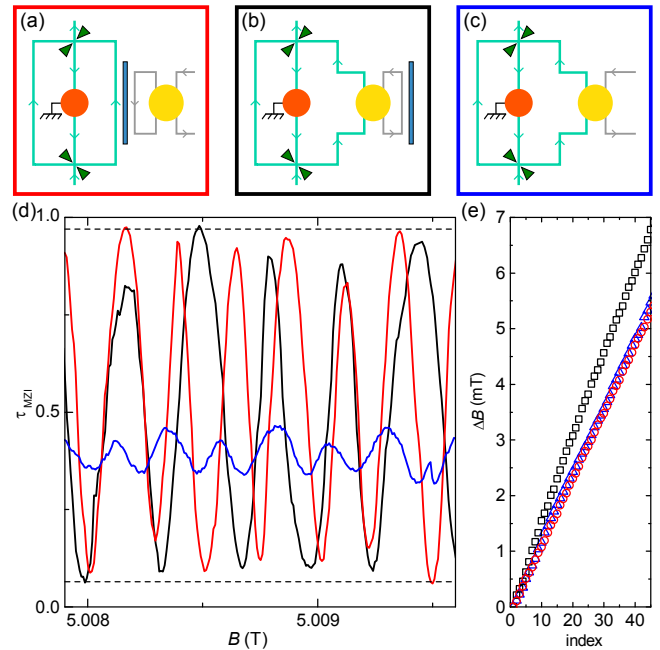


FIG. 2. Quantum oscillations versus magnetic field. (a,b,c), Schematics of implemented MZI configurations. (d), Fraction  $\tau_{\text{MZI}}$  of the outer edge channel current transmitted across the MZI as a function of  $B$ . Continuous lines are measurements performed in the configuration framed by a box of the same color in (a,b,c). The horizontal black dashed lines represent the  $\tau_{\text{MZI}}$  extrema for the standard and floating island MZI configurations (schematics in (a) and (b), respectively), corresponding to a high quantum oscillations visibility of  $\mathcal{V} \sim 90\%$ . With a second channel connected to the floating island (configuration shown Fig. 2(c)), the quantum oscillations are strongly reduced to a visibility  $\mathcal{V} \sim 20\%$ , consistent with the separately characterized small residual reflection of  $\sim 3\%$  (see text and [20]), and the average  $\langle \tau_{\text{MZI}} \rangle$  is diminished as part of the current is transmitted across the island toward a remote electrical ground. (e), Symbols display the magnetic field position of consecutive extrema (both peaks and dips increment the index number). The larger slope for the floating island MZI configuration (black squares) corroborates the electron quantum state transfer between different injection and emission locations across the floating metallic island.

metallic density of states of such metals  $\nu_F \approx 10^{47} \text{ J}^{-1} \text{ m}^{-3}$  ( $1.14 \times 10^{47}$  for gold, the main constituent), the electronic dwell time is  $\tau_D \approx 60 \mu\text{s}$ . This is much longer, by more than three orders of magnitude, than the energy relaxation and phase decoherence times of electrons observed in similar metals, which is at most in the  $20 \text{ ns}$  range [2, 21]. In the absence of Coulomb-induced correlations, no interferences would therefore be expected from the reemitted electrons, by a wide margin. The gates barring the broad way on each side of the floating island (blue) are normally tuned to either fully reflect or fully transmit the outer edge channel, in order to implement the MZI configurations schematically represented Figs. 2(a,b,c).

Note that the second (inner) quantum Hall edge channel is always completely reflected at the barring gate, and can therefore be ignored [9]. The island charging energy  $E_C \simeq k_B \times 0.3\text{K}$  was obtained from standard Coulomb diamond measurements (in a specifically tuned tunnel regime, see Fig. 3(b) and [20]). At the experimental electronic temperature  $T \simeq 10\text{mK}$  (measured on-chip from shot noise [22]), the criterion  $k_B T \ll E_C$  for fully developed Coulomb-induced correlations is therefore well verified. Note the previous experiments performed in the opposite ‘high-temperature’ regime  $k_B T \gg E_C$  of negligible Coulomb correlations, in which case, unsurprisingly, a complete quantum decoherence [23] and energy relaxation [24] of electrons were observed with a single connected channel. Finally, the transparency of the contact between the floating island and the outer quantum Hall edge channel plays an essential role since, if it is poor, many electrons would simply be reflected at the interface. Here,  $\geq 97\%$  of the incoming current penetrates into the floating island [20], which is also ascertained by the striking changes of behavior detailed later.

In Fig. 2, we show illustrative MZI oscillations versus  $B$  of  $\tau_{\text{MZI}}$ , the fraction of outer edge channel current transmitted across the device. The measurements were performed in the three configurations depicted in Figs. 2(a,b,c). The red continuous line in Fig. 2(d) corresponds to a standard electronic MZI, with the floating metallic island bypassed (schematic in Fig. 2(a)). In that case, the oscillations are of high visibility  $\mathcal{V} \equiv (\tau_{\text{MZI}}^{\text{max}} - \tau_{\text{MZI}}^{\text{min}}) / (\tau_{\text{MZI}}^{\text{max}} + \tau_{\text{MZI}}^{\text{min}}) \approx 90\%$  and, as expected for the Aharonov-Bohm phase, the magnetic field period of  $241 \pm 3 \mu\text{T}$  (red symbols in Fig. 2(e) show consecutive extrema positions) closely corresponds to one flux quantum ( $241 \mu\text{T} \times S \simeq 0.98h/e$  using the nominal area  $S \simeq 16.8 \mu\text{m}^2$ ). A small asymmetry in the  $\tau_{\text{MZI}}$  data (the average is slightly above 0.5) results from a small reflection of the outer edge channel on the grounded central ohmic contact (of  $\approx 5\%$ , see [20]). The black continuous line in Fig. 2(d) was measured with the right MZI arm deviated to go through the floating ohmic island (edge channel paths displayed in Fig. 1, and schematic in Fig. 2(b)). We observe first that the quantum interferences’ visibility remains of the same high amplitude, which corresponds to a perfect fidelity (at experimental accuracy) of the replicated quantum states imprinted on the electrons reemitted from the island, in agreement with low temperature predictions [9, 13]. Second, the magnetic field period of  $305 \pm 4 \mu\text{T}$  is found to be larger than in the standard MZI configuration of Fig. 2(a) (see black symbols in Fig. 2(e)). This increase is *opposite* to the reduction that would be expected from the Aharonov-Bohm period with the larger surface enclosed by the outer channel path and the inner boundary of the floating metallic island (see [20] for a graphical representation,  $S \simeq 18.4 \mu\text{m}^2$  would correspond to an Aharonov-Bohm period of  $225 \mu\text{T} \simeq h/eS$ ). Such opposite evolution and relatively important discrepancy (36%) establish that the MZI phase does not reduce to the usual Aharonov-Bohm phase acquired by a single

electron propagating along two different paths. Instead, the larger period corroborates the transfer of the electrons’ state across the island, thereby amputating the electron path from a section (the 2DEG/metal interface) and making the Aharonov-Bohm notion of enclosed surface ill-defined.

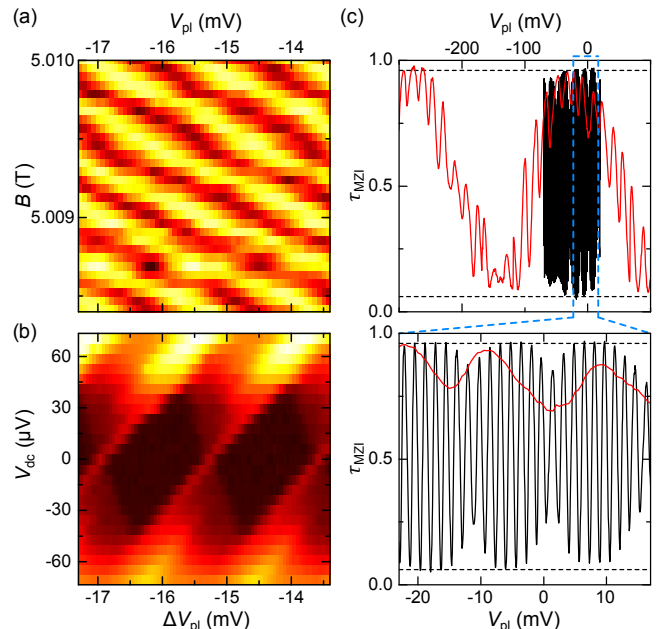


FIG. 3. Quantum phase versus island charge. (a), Color plot of  $\tau_{\text{MZI}}(B, V_{\text{pl}})$  in the floating island MZI configuration (schematic in Fig. 2(b)), with the larger values shown brighter, which establishes the equivalent role of  $B$  and  $V_{\text{pl}}$ . (b), Coulomb diamonds characterization of the floating island (larger differential conductance shown brighter, with the island here weakly coupled on both sides and  $V_{\text{dc}}$  the applied dc bias voltage). A comparison with panel (a), plotted using the same  $V_{\text{pl}}$  scale, reveals that the addition of a charge of  $e$  on the island precisely corresponds, in the floating island MZI configuration, to an electron quantum phase of  $2\pi$  (one quantum oscillation period). (c), The top and bottom panels display measurements of  $\tau_{\text{MZI}}(V_{\text{pl}})$  with the device set in the floating island MZI configuration (black line) and in the standard MZI configuration (red line, schematic in Fig. 2(a)). The MZI oscillations’ period in  $V_{\text{pl}}$  is shorter by a factor of  $1/160$  when the island is connected. Note an additional modulation of fixed period ( $\approx 15\text{mV}$ ).

The blue continuous line in Fig. 2(d) was measured with one MZI arm going through the floating island, and in the presence of a second electronic channel connected to it (configuration schematically displayed in Fig. 2(c)). We find strongly suppressed conductance oscillations corresponding to a full decoherence of the electrons going through the island. The residual visibility  $\mathcal{V} \lesssim 0.2$  is consistent with the proportion  $1 - \tau_{\text{island}} \lesssim 3\%$  of reflected electrons, not penetrating into the island. Indeed, the MZI contribution of the reflected electrons at small  $1 - \tau_{\text{island}} \ll 1$  reads  $\mathcal{V}_0(4/3)\sqrt{1 - \tau_{\text{island}}} \lesssim 0.21$ , with  $\mathcal{V}_0 \approx 90\%$  the MZI visibility in the standard configura-

tion [20, 23]. The magnetic field period of  $246 \pm 4 \mu\text{T}$  for these smaller oscillations (see blue symbols in Fig. 2(e)) is found close to the period observed in the standard MZI configuration shown in Fig. 2(a), suggesting that the residual reflections take place at the level of the barring gate (colored blue, left of island in Fig. 1). Note that the average  $\langle\tau_{\text{MZI}}\rangle \simeq 0.39$  is shifted below 0.5 because part of the injected current is evacuated toward a remote electrical ground through the second channel connected to the floating island ( $\langle\tau_{\text{MZI}}\rangle = 0.375$  expected from current conservation for a floating island and a central ohmic contact both perfectly connected).

We now investigate the relation between the island's charge and the electron phase shift associated with the quantum state transfer. For this purpose, Fig. 3 focuses on the influence on  $\tau_{\text{MZI}}$  of the voltage  $V_{\text{pl}}$  applied to a plunger gate (colored purple in Fig. 1) which is relatively far from the MZI outer quantum Hall channel, but close to the island. The equivalent role on the MZI phase of  $V_{\text{pl}}$  and  $B$  is first directly established, in Fig. 3(a), with the device set in the floating island MZI configuration (schematic in Fig. 2(b)). Figure 3(b) displays Coulomb diamond measurements of the conductance across the island as a function of the same plunger gate voltage  $V_{\text{pl}}$ , with here the island weakly connected through tunnel barriers such that  $Q$  is quantized in units of  $e$  (only in that specific case) and without two-path interferences (see device schematic in [20]). Remarkably, the MZI gate voltage period in Fig. 3(a) precisely matches the Coulomb diamonds' period in Fig. 3(b), as can be seen by directly comparing the two panels plotted using the same  $V_{\text{pl}}$  scale. In the floating MZI limit of strongly connected channels  $Q = eV_{\text{pl}}/\Delta$ , with  $\Delta \simeq 1.7\text{mV}$  the Coulomb diamond period [10–12]. A quantum phase shift of  $2\pi Q/e$  therefore applies to the transferred electrons, as specifically predicted theoretically [9, 13], and in agreement with Friedel's sum rule. Comparing with the device set

in the standard MZI configuration, we show in Fig. 3(c) that the  $\tau_{\text{MZI}}$  oscillations (red line) are of identical maximum visibility  $\mathcal{V} \simeq 90\%$  than with one arm going through the metallic island (black line), as also seen versus magnetic field in Fig. 2(d). However, the  $V_{\text{pl}}$  period is increased by a large factor of 160, from 1.7mV to 270mV, which reflects the weak coupling of the plunger gate voltage to the MZI outer edge channel (see [20] for an extended  $V_{\text{pl}}$  range). This provides a final evidence that the electrons contributing to the quantum oscillations in the floating island configuration indeed penetrate into the metal. Note the presence of an additional, smaller signal of fixed period 15mV visible in both configurations (in the form of direct oscillations or of an amplitude modulation), which might originate from the progressive charging of a nearby defect.

This experimental work demonstrates that the Coulomb interaction has two facets. It can both destroy and preserve quantum effects. Although a metallic island is often pictured as a floating reservoir of uncorrelated electrons [6, 25], we establish that a high-fidelity electron quantum state transfer can take place across it, enforced by the Coulomb charging energy. This provides a mean to overcome limitations imposed by the decoherence of individual electrons. Moreover, the observed universal  $2\pi$  electron phase shift for one elementary charge  $e$  on the island allows for a strong entanglement of single-electron states, both between themselves or with other quantum degrees of freedom, with a negligible loss of coherence. Such controllable, strong-coupling mechanism constitutes a key element in the context of quantum Hall edges envisioned as platforms for the manipulation and transfer of quantum information via propagating electrons [19, 26–31]. In particular, it is remarkably well suited to implement quantum gates for these ‘flying qubits’, such as the CNOT proposal involving a conditional phase shift of  $\pi$  described in [30].

- 
- [1] Nazarov, Y. & Blanter, Y. *Quantum Transport* (Cambridge University Press, 2009).
- [2] Pierre, F. *et al.* Dephasing of electrons in mesoscopic metal wires. *Phys. Rev. B* **68**, 085413 (2003).
- [3] Brouwer, P. & Büttiker, M. Charge-relaxation and dwell time in the fluctuating admittance of a chaotic cavity. *Europhys. Lett.* **37**, 441–446 (1997).
- [4] Bennett, C. *et al.* Teleporting an unknown quantum state via dual classical and Einstein-Podolsky-Rosen channels. *Phys. Rev. Lett.* **70**, 1895–1899 (1993).
- [5] Fu, L. Electron Teleportation via Majorana Bound States in a Mesoscopic Superconductor. *Phys. Rev. Lett.* **104**, 056402 (2010).
- [6] Büttiker, M. Coherent and Sequential Tunneling in Series Barriers. *IBM J. Res. Dev.* **32**, 63–75 (1988).
- [7] Blanter, Y. M. & Büttiker, M. Shot Noise in Mesoscopic Conductors. *Phys. Rep.* **336**, 1–166 (2000).
- [8] Slobodeniuk, A., Levkivskiy, I. & Sukhorukov, E. Equilibration of quantum Hall edge states by an Ohmic contact. *Phys. Rev. B* **88**, 165307 (2013).
- [9] Idrisov, E., Levkivskiy, I. & Sukhorukov, E. Dephasing in a Mach-Zehnder Interferometer by an Ohmic Contact. *Phys. Rev. Lett.* **121**, 026802 (2018).
- [10] Matveev, K. A. Coulomb blockade at almost perfect transmission. *Phys. Rev. B* **51**, 1743–1751 (1995).
- [11] Nazarov, Y. Coulomb Blockade without Tunnel Junctions. *Phys. Rev. Lett.* **82**, 1245–1248 (1999).
- [12] Jezouin, S. *et al.* Controlling charge quantization with quantum fluctuations. *Nature* **536**, 58–62 (2016).
- [13] Clerk, A., Brouwer, P. & Ambegaokar, V. Interaction-Induced Restoration of Phase Coherence. *Phys. Rev. Lett.* **87**, 186801 (2001).
- [14] Sivre, E. *et al.* Heat Coulomb blockade of one ballistic channel. *Nat. Phys.* **14**, 145–148 (2018).
- [15] Ji, Y. *et al.* An electronic Mach-Zehnder interferometer. *Nature* **422**, 415–418 (2003).
- [16] Roulleau, P. *et al.* Finite bias visibility of the electronic Mach-Zehnder interferometer. *Phys. Rev. B* **76**, 161309

- (2007).
- [17] Litvin, L., Tranitz, H., Wegscheider, W. & Strunk, C. Decoherence and single electron charging in an electronic Mach-Zehnder interferometer. *Phys. Rev. B* **75**, 033315 (2007).
- [18] Bieri, E. *et al.* Finite-bias visibility dependence in an electronic Mach-Zehnder interferometer. *Phys. Rev. B* **79**, 245324 (2009).
- [19] Duprez, H. *et al.* Macroscopic electron quantum coherence in a solid-state circuit. *submitted* (2019).
- [20] Supplementary materials and methods.
- [21] Bäuerle, C. *et al.* Experimental Test of the Numerical Renormalization-Group Theory for Inelastic Scattering from Magnetic Impurities. *Phys. Rev. Lett.* **95**, 266805 (2005).
- [22] Iftikhar, Z. *et al.* Primary thermometry triad at 6 mK in mesoscopic circuits. *Nat. Commun.* **7**, 12908 (2016).
- [23] Roulleau, P. *et al.* Tuning decoherence with a voltage probe. *Phys. Rev. Lett.* **102**, 236802 (2009).
- [24] Altimiras, C. *et al.* Tuning Energy Relaxation along Quantum Hall Channels. *Phys. Rev. Lett.* **105**, 226804 (2010).
- [25] de Jong, M. & Beenakker, C. Semiclassical theory of shot noise in mesoscopic conductors. *Physica A* **230**, 219–248 (1996).
- [26] Bertoni, A., Bordone, P., Brunetti, R., Jacoboni, C. & Reggiani, S. Quantum Logic Gates based on Coherent Electron Transport in Quantum Wires. *Phys. Rev. Lett.* **84**, 5912–5915 (2000).
- [27] Ionicioiu, R., Amaratunga, G. & Udreă, F. Quantum Computation with Ballistic Electrons. *Int. J. Mod. Phys. B* **15**, 125–133 (2001).
- [28] Stace, T., Barnes, C. & Milburn, G. Mesoscopic One-Way Channels for Quantum State Transfer via the Quantum Hall Effect. *Phys. Rev. Lett.* **93**, 126804 (2004).
- [29] Bocquillon, E. *et al.* Electron quantum optics in ballistic chiral conductors. *Ann. Phys. (Berlin)* **526**, 1–30 (2014).
- [30] Glattli, D. & Roulleau, P. Levitons for electron quantum optics. *Phys. Status Solidi B* **254**, 1600650 (2017).
- [31] Bäuerle, C. *et al.* Coherent control of single electrons: a review of current progress. *Rep. Prog. Phys.* **81**, 056503 (2018).

### Acknowledgments

This work was supported by the French RENATECH network, the national French program ‘Investissements d’Avenir’ (Labex NanoSaclay, ANR-10-LABX-0035) and the French National Research Agency (project QuTherm, ANR-16-CE30-0010).

E.S. and H.D. performed the experiment and analyzed the data with inputs from A.Aa., A.An. and F.P.; F.P. fabricated the sample with inputs from E.S and H.D.; A.C., and U.G. grew the 2DEG; F.P. led the project and wrote the manuscript with inputs from A.Aa., A.An., E.S., H.D. and U.G.

We thank P. Brouwer, L. Glazman, C. Mora, Y. Oreg and E. Sukhorukov for illuminating discussions.



**Titre :** Fluctuations électriques et flux de chaleur dans un circuit composite quantique

**Mots clés :** transport quantique, flux de chaleur, fluctuations de courant

**Résumé :** L'interaction de Coulomb influence fortement toutes les propriétés de transport des circuits composites quantique à basse température. Dans cette thèse, nous étudions les fluctuations de courant et le flux de chaleur dans un circuit quantique, composé de plusieurs canaux de conduction élémentaires. Nous utilisons la mesure combinée des corrélations croisées et des auto-corrélations des fluctuations de courant, ce qui nous permet d'extraire séparément, d'une part, le bruit de grenaille provenant du partitionnement des électrons via un canal partiellement transmis et, d'autre part, la température des électrons dans le dispositif. Nous commençons notre investigation dans le cas où un canal quantique élémentaire arbitraire est inséré dans un circuit linéaire. Dans ce cas, nous établissons expérimentalement une relation

reliant la suppression de conductance induite par l'interaction de Coulomb et la variation du bruit de grenaille en fonction de la tension. Deuxièmement, dans le même circuit, nous mesurons le bruit de grenaille au travers d'un canal élémentaire unique résultant du transfert de charges induit par un pur gradient thermique. Troisièmement, nous étudions l'effet de l'interaction de Coulomb sur le flux de chaleur électronique. Dans un circuit composé exclusivement de canaux balistiques, nous démontrons expérimentalement le blocage de Coulomb de la chaleur systématique de l'un des canaux. Au-delà de la limite balistique, nous observons un nouveau mécanisme sur le flux de chaleur relié à la fois au partitionnement électronique à travers un canal non balistique et à l'interaction de Coulomb.

**Title:** Electrical fluctuations and heat flow in a quantum composite circuit

**Keywords:** quantum transport, heat flow, current fluctuations

**Abstract:** The Coulomb interaction strongly influences all transport properties of quantum composite circuits at low temperature. In this thesis, we investigate the current fluctuations and the flow of heat in a quantum circuit, composed of several elementary conduction channels. We use combined measurement of cross-correlations and auto-correlations of the current fluctuations, allowing us to extract separately, on the one hand, the current shot noise coming from the partitions of electrons through a partially transmitted channel and, on the other hand, the temperature of the electrons in the device. We start our investigation with an arbitrary elementary quantum channel embedded in a linear circuit. In this case, we establish experimentally a relation connecting

the conductance suppression induced by the Coulomb interaction and the shot noise variation as a function of the voltage. Second, in the same circuit, we measure the shot noise through a single elementary channel resulting from the transfer of charge induced by a pure thermal bias. Third, we investigate the effect of Coulomb interaction on the electronic heat flow. In a circuit exclusively composed of ballistic channels, we demonstrate experimentally the systematic heat Coulomb blockade of one of the channels. Beyond the ballistic limit, we observe a new heat flow mechanism connected to both the electron-partition through a non-ballistic channel and to the Coulomb interaction.